

UC Berkeley

UC Berkeley Electronic Theses and Dissertations

Title

Development of Superconducting High-Resolution Gamma-Ray Spectrometers for Nuclear Safeguards

Permalink

<https://escholarship.org/uc/item/0wf1p1mr>

Author

Dreyer, Jonathan

Publication Date

2012

Peer reviewed|Thesis/dissertation

**Development of
Superconducting High-Resolution Gamma-Ray Spectrometers
for Nuclear Safeguards**

by

Jonathan Glen Dreyer

A dissertation submitted in partial satisfaction of the
requirements for the degree of
Doctor of Philosophy

in

Engineering-Nuclear Engineering

in the

Graduate Division
of the
University of California, Berkeley

Committee in charge:

Professor Stanley Prussin, Chair
Professor Kai Vetter
Professor James Siegrist
Dr. Stephan Friedrich

Fall 2012

**Development of
Superconducting High-Resolution Gamma-Ray Spectrometers
for Nuclear Safeguards**

Copyright 2012
by
Jonathan Glen Dreyer

Abstract

Development of Superconducting High-Resolution Gamma-Ray Spectrometers for Nuclear Safeguards

by

Jonathan Glen Dreyer

Doctor of Philosophy in Engineering-Nuclear Engineering

University of California, Berkeley

Professor Stanley Prussin, Chair

Superconducting high-resolution gamma-ray spectrometers based on molybdenum/copper transition edge sensors (TES) with tin absorbers have been developed for nuclear safeguard applications. This dissertation focuses on plutonium analysis, specifically the direct measurement of the ^{242}Pu gamma-ray signature at 44.915 keV. As existing nondestructive analysis methods cannot directly measure this or any other ^{242}Pu gamma ray, the feasibility of making such a measurement using a TES based system is presented. Analysis from Monte Carlo simulations and analytical noise models shows that the direct detection of this gamma-ray line is possible and can be quantified in the presence of a ^{240}Pu gamma-ray line with a line separation of 324 eV, even if the emission from the ^{240}Pu is several orders of magnitude stronger. Spectroscopic measurements conducted in a liquid cryogen system offered an energy resolution of 180 eV, adequate for the measurement of ^{242}Pu ; however, TES operation in a liquid-cryogen-free pulse tube refrigerator degraded sensor performance such that this measurement was no longer possible. The numerical noise model indicates that the energy resolution of this device is adequate to demonstrate a direct measurement of ^{242}Pu if the noise pickup from the mechanical cooler can be suppressed. This work shows that the precise measurement of low-intensity gamma-ray signatures, such as the 44.915 keV gamma ray from ^{242}Pu , will require arrays of low-noise TES sensors and that such a system would offer invaluable information in the analysis of plutonium bearing materials.

To Grandma and Grandpa

Contents

List of Figures	v
List of Tables	vii
Abbreviations and Acronyms	viii
1 Introduction	1
1.1 Introduction	2
1.2 The Plutonium Threat	2
1.3 Safeguards and Nuclear Forensics	5
1.4 Current Methodology and Limitations	6
1.5 Previous Work	8
1.6 Dissertation Outline	9
2 Plutonium Isotopic Analysis	11
2.1 Background	12
2.2 Plutonium Production	13
2.3 Isotope Correlation for Safeguards	16
2.4 Current Methodology for Plutonium Assay	17
2.4.1 Calorimetry	17
2.4.2 Passive Neutron Coincidence Counting	20
2.4.3 High-Resolution Gamma Spectrometry	20
2.5 Limitations	26
3 Foundations	30
3.1 Foundations	31
3.2 Energy Thermalization in Superconductors	32
3.2.1 Photoelectric Absorption	33
3.2.2 Compton Scattering	34
3.2.3 Thermalization	35
3.3 Transition Edge Sensors and Electrothermal Feedback	39
3.4 Noise Contributions	43

3.4.1	Phonon Noise	43
3.4.2	Thermometer Johnson Noise	43
3.5	Intrinsic Noise and Energy Resolution	44
4	Calorimeter Theory	48
4.1	Basic Calorimeter Theory	49
4.2	Noise Analysis in Frequency Domain	53
4.3	Noise Equivalent Power and Energy Resolution	55
4.4	Calorimeter Noise Example	56
4.5	Complex Calorimeter	58
4.6	Complex Calorimeter Noise Example	63
4.7	Transition Edge Sensors for Isotopic Measurements	66
4.7.1	Sensor Performance	66
4.7.2	Quantifying Measurement Sensitivity	66
4.7.3	Direct Measurement of ^{242}Pu	72
5	Experimental Apparatus	74
5.1	Sensor Design	75
5.2	Sensor Fabrication	75
5.3	Detection Efficiency	77
5.4	Cryostat Design	81
5.4.1	Two-stage pulse tube refrigerator	82
5.4.2	Adiabatic Demagnetization Refrigerator	86
5.5	Cryostat performance	90
6	Transition Edge Sensor Modeling	92
6.1	Simulation Methodology	93
6.2	Simplified Absorber Model	93
6.3	Detector and Cryostat Model	100
7	Experimental Results	106
7.1	Measurements in Liquid Cryogen Dewar	107
7.1.1	Noise Performance	107
7.1.2	Measurements	107
7.2	Measurements in Pulse Tube Cryostat	111
7.2.1	Noise Performance	111
7.2.2	Gamma-ray Measurements	115
7.3	Discussion	117
8	Summary and Conclusions	121
8.1	Findings	122
8.2	Future Efforts	123

Bibliography	125
A Derivations	138
A.1 Temperature Response of a Simple Transition Edge Sensor	139
A.2 Simplification of the Simple Calorimeter Phonon and Johnson Noise	140
A.3 Power Spectrum of TES Signal Current	141
A.4 Thevenin Equivalent Bias Circuit	142
A.5 Simplification of the Basic Calorimeter Thermal and Current Response . .	143
A.6 Calculation of Energy Resolution from Noise Equivalent Power	150
B Calculation of Sensor Parameters	153
B.1 Heat Capacity of Tin and Transition Edge Sensor	154
B.1.1 Heat Capacity of Tin Absorber	154
B.1.2 Heat Capacity of Molybdenum-Copper Transition Edge Sensor . . .	155
B.2 Heat Capacity of Stycast Epoxy	157
B.3 Thermal Conductance of Stycast Epoxy	157
B.4 Thermal Conductance of Silicon Nitride Membrane	159
B.5 Electron-Phonon Coupling	159
B.6 Material Properties of Transition Edge Sensors	159
C Optimum Filtering	161
D Sensor Modeling	163
D.1 Simple Calorimeter	164
D.2 Basic Calorimeter	165
D.3 Complex Calorimeter	167
E Precision of Isotopic Ratio Measurement	170

List of Figures

1.1	World wide stockpiles of plutonium.	3
1.2	World wide nuclear capacity and plutonium production.	4
1.3	Correlation of Pu isotopes in BWR as a function of burnup.	8
1.4	Spectrum of uranium oxide fuel	9
2.1	Nuclide chain for the production of plutonium	14
2.2	Capture-to-fission ratio of plutonium isotopes	15
2.3	Production of plutonium in PWR fuel as function of burnup	16
2.4	Reactor type disclosure by isotopic correlation	18
2.5	Schematic of coaxial and planar HPGe detectors.	21
2.6	Spectrum from 530 g plutonium as PuO ₂ taken with coaxial HPGe detector.	22
2.7	Spectrum of a plutonium solution taken with a planar HPGe detector.	24
2.8	Correlation of Pu isotopes in BWR as a function of burnup	29
3.1	Schematic of a simple calorimeter	32
3.2	The temperature response of a TES to the absorption of a photon	33
3.3	Diagram illustrating the photoelectric absorption of a photon	34
3.4	Diagram illustrating the scattering of a photon on an electron	35
3.5	Flow chart of electrons and phonons in a superconducting absorber.	37
3.6	Phonon and unbound electron energy in a superconducting tin film.	38
3.7	Schematic of the resistance vs temperature for a transition-edge sensor	40
3.8	The bias power input into the TES as a function of temperature	41
3.9	Signal and current noise of a simple calorimeter.	47
4.1	Schematic of a basic calorimeter.	50
4.2	Current noise in a basic calorimeter.	57
4.3	Noise equivalent power (NEP) of a basic calorimeter.	58
4.4	Schematic of a complex calorimeter	59
4.5	Current noise in a complex calorimeter.	64
4.6	Noise equivalent power (NEP) of a complex calorimeter.	65
4.7	Energy resolution dependence on sensor parameters.	67
4.8	Simulated sensor response to a 10 mg sample of reactor grade Pu.	68
4.9	Sample case for quantifying measurement sensitivity.	69

4.10	Example of fitting peaks using analytical model.	70
4.11	Precision of the ^{242}Pu gamma ray line for increasing number of detector·days.	73
5.1	Transition sensor dependence on Mo/Cu ratio and total thickness.	75
5.2	Surface roughness measurements of the Si_3N_4 layer for TES fabrication.	76
5.3	TEM image of an eight layer TES.	77
5.4	Schematic of the TES fabrication process	78
5.5	Schematic of a transition edge sensor.	79
5.6	Photograph of transition edge sensor.	80
5.7	Quantum efficiency of transition edge sensor and cryostat.	81
5.8	Schematic of a liquid cryogen dewar.	83
5.9	Schematic of a single-stage pulse tube refrigerator.	84
5.10	The pressure and temperature of a PTR during a cooling cycle.	85
5.11	Schematic of two-stage pulse tube refrigerator	87
5.12	Entropy as a function of temperature for GGG and FAA.	89
5.13	Cooldown cycle of the pulse-tube ADR for regulation at 0.1 K.	91
6.1	Schematic of simplified absorber Geant4 model	94
6.2	Fraction of incident energy deposited or lost with absorber thickness	95
6.3	Simulated energy spectrum from a 45 keV photon source incident on tin.	96
6.4	Performance of a $0.25 \times 2 \times 2$ mm tin absorber.	97
6.5	Fraction of incident energy deposited or lost from photon or electron escape.	98
6.6	The fraction of attenuated photon for different sized absorbers.	99
6.7	Schematic of the cryostat modeled in the Geant4 simulation.	101
6.8	Schematic of the encapsulated ^{241}Am used for the Geant4 simulations.	102
6.9	Comparison of a measured ^{241}Am spectrum and a Geant4 simulation.	103
6.10	Geant4 simulation of 10 mg of reactor grade plutonium.	104
6.11	Geant4 simulation of 10 mg of weapons grade plutonium.	105
7.1	Measured current noise from TES operated in a liquid dewar.	108
7.2	HPGe and TES spectra of uranium oxide material	111
7.3	Reduction in noise after modifications to cryostat.	113
7.4	The noise contribution from the PTR compressor.	114
7.5	Current noise measured from PTR system.	114
7.6	Comparison of experimental and modeled pulse shapes.	115
7.7	Expanded view of Figure 7.6	116
7.8	Spectrum of an ^{241}Am source.	117
7.9	Spectrum of a ^{133}Ba source.	118
7.10	Precision of the ^{242}Pu gamma-ray line for increasing detector·days	120
A.1	Transition edge sensor bias circuit and Thevenin equivalent.	143
A.2	Schematic of a basic calorimeter.	144

List of Tables

1.1	Nuclear forensics and attribution time line.	7
2.1	Properties of plutonium isotopes commonly found in nuclear fuels.	12
2.2	Nuclear decay properties of plutonium isotopes.	13
2.3	Percentage of plutonium composition of reactor fuel at discharge	17
2.4	The typical percentage of specific power by isotope.	19
2.5	Isotopic compositions for example plutonium samples.	21
2.6	Gamma rays emitted in the decay of ^{242}Pu	23
2.7	Gamma-ray signatures used for isotopic analysis.	26
2.8	Performance values for $^{240}\text{Pu}_{\text{eff}}$ and P_{eff}	27
2.9	Uncertainties in isotopic measurements from the Pu-2000 exercise	28
3.1	Material properties and characteristic decay constants for tin	36
3.2	Simplified transition edge sensor parameters	46
4.1	Basic calorimeter modeling parameters	57
4.2	Complex calorimeter modeling parameters	63
4.3	Description of symbols used for analytical peak fitting.	70
5.1	Properties of FAA and GGG magnetic cooling salts	90
6.1	Energies of x-ray from the principle K- and L-shell emission lines for tin . .	96
6.2	Approximate isotopic composition (wt %) of various grades of plutonium. .	100
7.1	Complex calorimeter modeling parameters	109
7.2	Atomic composition of Y-12 uranium oxide sample.	110
B.1	Phonon and electron heat capacities of a TES	157
B.2	Heat capacity and effective thermal conductance of Stycast epoxy dots . .	158
B.3	Properties of commonly used TES materials	160

Abbreviations and Acronyms

ADR	Adiabatic demagnetization refrigerator
BWR	Boiling water reactor
CANDU	CANada Deuterium Uranium reactor
DA	Destructive Analysis
ESARDA	European Safeguards Research and Development Association
FAA	Ferric Ammonium Alum
FWHM	Full width at half maximum
Geant4	Monte Carlo simulation toolkit
GGG	Gadolinium Gallium Garnet
HPGe	High-Purity Germanium
HRGS	High-Resolution Gamma Spectrometry
ICT	Isotopic correlation techniques
NDA	Non-destructive Analysis
NEP	Noise Equivalent Power
PNCC	Passive Neutron Coincidence Counting
PR	Photoresist
PSD	Position Sensitive Detector
PTR	Pulse Tube Refrigerator
PWR	Pressurized water reactor
SQUID	Superconducting Quantum Interference Device
TES	Transition Edge Sensor
TIMS	Thermal Ionization Mass Spectrometry
UHV	ultra-high vacuum
wt%	Weight Percent

Acknowledgments

First and foremost, I would like to convey my utmost gratitude to my committee. My faculty advisor, Professor Stanley Prussin, has offered exemplary guidance and unwavering support throughout my graduate career. Stan's passion for scientific understanding is an inspiration and has shaped my growth, both as his student and as a fellow scientist. Thank you for your insightful advice and constructive criticisms. To my research advisor, Dr. Stephan Friedrich, I am grateful to have had the opportunity to work in the cryogenic detector group. Your guidance, expertise and encouragement were invaluable throughout the course of my research. The members of my dissertation committee, Professors Kai Vetter and James Siegrist, gave generously of their time and expertise; thank you for the contributions and many valuable suggestions.

A great deal of thanks goes to those in my research group at LLNL. I am incredibly fortunate to have been able to learn from such a talented group of researchers. To Owen Drury, who generously donated his time and expertise to this project: thank you for your support over these years. I have always enjoyed our discussions and appreciated your insightful comments. Thanks also to Miguel Velazquez, for his help with the liquid cryostats and the noise model, and to Sergey Pereverzev, whose knowledge of SQUIDS and noise reduction techniques were invaluable. Special thank you to Jan Bautteux, who assisted in the design and fabrication of numerous components. We have been fortunate to have someone with your expertise on the team. To Cameron Bates, many thanks for your valuable advice; I wish you much success in your graduate studies. I also owe much to Andrea Robles for developing the Geant4 modeled used for device simulations. Lastly, I would like to acknowledge Thomas Niedermayr, Stephane Terracol, and Dragos Hau, all of whom I had to pleasure of working with during my undergraduate summer internships at LLNL.

In addition to the cryogenic detector group, numerous individuals at Livermore have provided assistance. In particular, I owe thanks to Larry Hiller for lending his coding expertise, Martin Robel for assistance with ORIGIN-ARP, Marianne Ammendolia for her technical expertise, Tom Gosnell for the discussions on measuring ^{242}Pu , and to Roger Henderson for preparing the plutonium samples.

I am grateful to all my fellow graduate students in Stan's research group. It has been an honor to work with you all. Thanks to Brett I. for his generous support and for providing SEM images. My thanks to Brian Q., Joseph D., Christina L., and Dan C., in particular. Your advice has always been appreciated.

Early in my graduate career I had the opportunity to collaborate with UC Berkeley's Cosmology Group, thanks to Professor Adrian Lee and Professor William Holzapfel allowing me to work in their laboratories. The graduate students in their groups were exceptionally welcoming and I learned a great deal about cryogenics from them; I owe many thanks to Kam A., Martin L., Mike M., and Tom P. for their help.

Sincere thanks are due to Lisa Zelman and Kris Petersen. Dealing with the numerous administration and bureaucratic matters at Berkeley and LLNL during my studies

would have been infinitely more difficult, if possible at all, without both of your assistance.

I would like to gratefully acknowledge the financial support that made this work possible. The UC Berkeley Domestic Nuclear Threat Security project, the U.S. Department of Homeland Security Fellowship and the Lawrence Scholar Program Fellowship provided support for my studies and the U.S. Department of Energy for providing funding for this research. Thanks also to Lawrence Livermore National Laboratory for providing me with the necessary facilities to conduct this work.

I would like to thank two of my undergraduate professors, Kimberlee Kearfott and David Wehe, at the University of Michigan. They provided the opportunity to work in their laboratories, introducing me to the possibilities of academic research, and their mentorship inspired me to pursue a graduate degree.

My time at Berkeley has been enriched in a large part from the many friends that have become a part of my life. I am grateful for the friendship and support all of you have given me. Your words of encouragement and understanding have helped me through many difficult times and I am unable to express how grateful I am. I especially thank Peter B., Amy C., Jesse E., Lauren F., Jackie M., Sam M., Jeremy O., Will R., Mark S., Theo S., and Kurt T.

Special thanks to my family: my mother, Julie, and my brothers, Nathaniel, Christopher, and Benjamin. To my mother: thank you for your support and love throughout this long process. Many thanks also to my brothers, for being supportive and caring siblings, in as much as can be expected from younger brothers.

To Shuai: thank you for your patient understanding and persistent encouragement. I can never express how fortunate I am to have you in my life. Finishing my research and writing this dissertation would not have been possible without your unconditional love and support. 我爱你。

Lastly, I would like to thank my grandparents, Edward and Patricia, to whom this work is dedicated. You are my greatest inspiration and I cannot express enough how much your love and unwavering support have shaped my life. Grandpa, I wish you were here to read this, as it was your confidence in me that has made this journey possible. I can only pray to one day be as thoughtful and wise as you.

There are, of course, many others who have supported me and this research, and they are too numerous to individually thank here. To all of you who have helped me along the way: thank you.

Chapter 1

Introduction

1.1 Introduction

On July 16, 1945 the detonation of the first nuclear weapon in the desert of New Mexico heralded the beginning of the atomic age. Although the potential of this technology for energy generation was realized early in the weapons program, fears of the inherent military dimension required that this knowledge remain classified. Efforts to use nuclear energy for peaceful civil applications began in 1953 with the Atoms for Peace program introduced by President Eisenhower. This initiative led to the creation of the International Atomic Energy Agency (IAEA) charged with promoting nuclear energy while ensuring that this technology was not used for military applications. The inherent proliferation risk from the use of nuclear energy required controls or *safeguards* be implemented such that the IAEA could verify a state's compliance with international agreements [1]. The hopes of inexpensive and safe nuclear energy were quickly overshadowed by the Cold War as the prevailing deterrence strategies led the United States and USSR to stockpile enormous quantities of weapons and nuclear materials. At the end of the Cold War it was these legacy materials that were the target of smuggling.

Today, nuclear security is significantly more complex as the Soviet-American rivalry has been replaced with the concern that states and independent non-state groups might proliferate nuclear materials and weapons as well as traffic nuclear materials. The events of September 11, 2001 and the subsequent war on terrorism have brought these issues to the forefront of the US national security policy. The National Security Strategy of May 2010 stresses the critical importance of nuclear security, stating that there is “no greater threat to the American people than weapons of mass destruction, particularly the danger posed by the pursuit of nuclear weapons by violent extremists and their proliferation to additional states.”[2] Despite this renewed effort to limit the nuclear threat the path is fraught with challenges and the risks to national and international security are compounded as the peaceful pursuits of nuclear energy increase throughout the world [3].

1.2 The Plutonium Threat

George Perkovich writing for Foreign Affairs [4] stated “plutonium is one of the most dangerous materials on earth.” The risk of proliferation, the environmental cost and the detriments to human health are substantial, and renewed calls have been made for safe disposal [5]. However, at present, substantial quantities of plutonium exist in the military stockpiles and continue to be produced during commercial power generation.

The United States and Russia hold $\sim 90\%$ of the total military stockpiles of weapons grade plutonium (Figure 1.1). Following the collapse of the Soviet Union, many of the production facilities used during the Cold War were neglected, leaving nuclear materials vulnerable to theft. Incomplete production records at these plants compounded the challenges of accounting and securing loose nuclear material [6]. Although joint US-Russian security initiatives have dramatically improved the security of these sites, concerns still

remain. Terrorist organizations actively seek to obtain these materials, either through force or bribery. The latter is of particular concern as corruption and insider theft are widespread in Russia, and the outdated material accounting methods used at these facilities provide opportunities for smuggling [7].

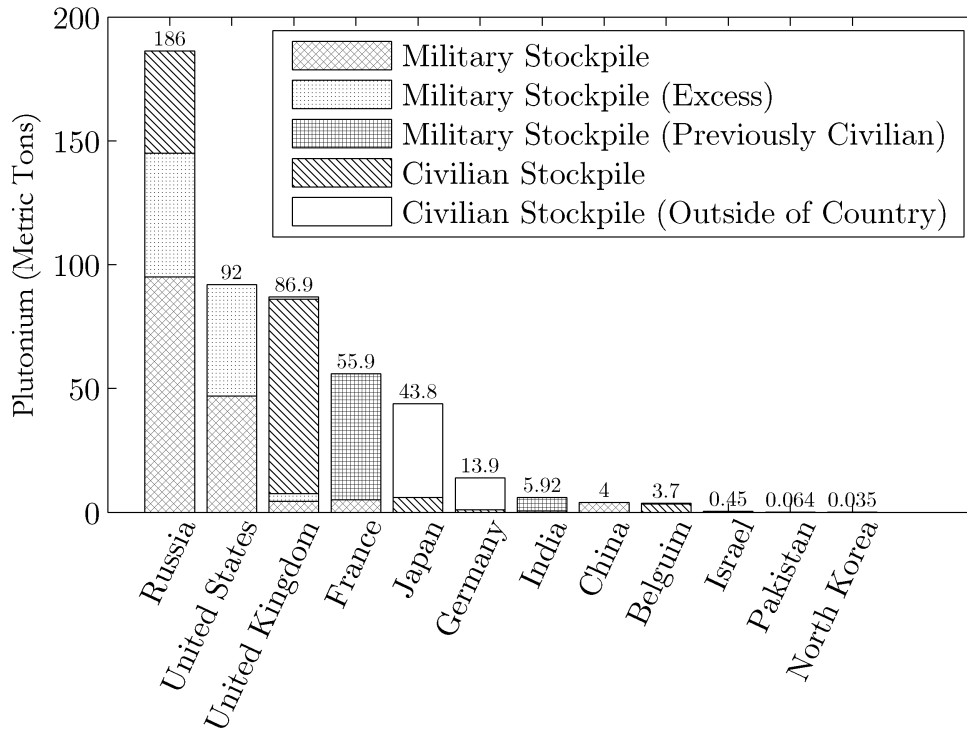


Figure 1.1: Quantities of plutonium in civilian and military stockpiles. Weapons stockpiles consist of plutonium enriched to $\geq 94\%$ ^{239}Pu [8].

As of 2008, the worldwide capacity of the 439 operating nuclear power plants was approximately 400 GWe [9]. This global generating capacity is projected to increase to 600 GWe by 2030 (Figure 1.2)[10]. The spent fuel produced during reactor operation contains plutonium and a third of this spent fuel is expected to be reprocessed with the plutonium separated and used in mixed oxide (MOX) fuels. Even with reprocessing the plutonium inventory in spent fuel will approach nearly 2.5×10^6 g by 2030. Although not ideal, the plutonium produced in nuclear power plants can be used for fission weapons, and 2.5×10^6 g is enough by some estimates to make more than 150,000 crude nuclear explosives [11]. Precise accounting for and monitoring of the amount of plutonium in the existing stockpile is therefore essential to prevent the transfer of nuclear weapons to other states and reduce the threat of nuclear terrorism.

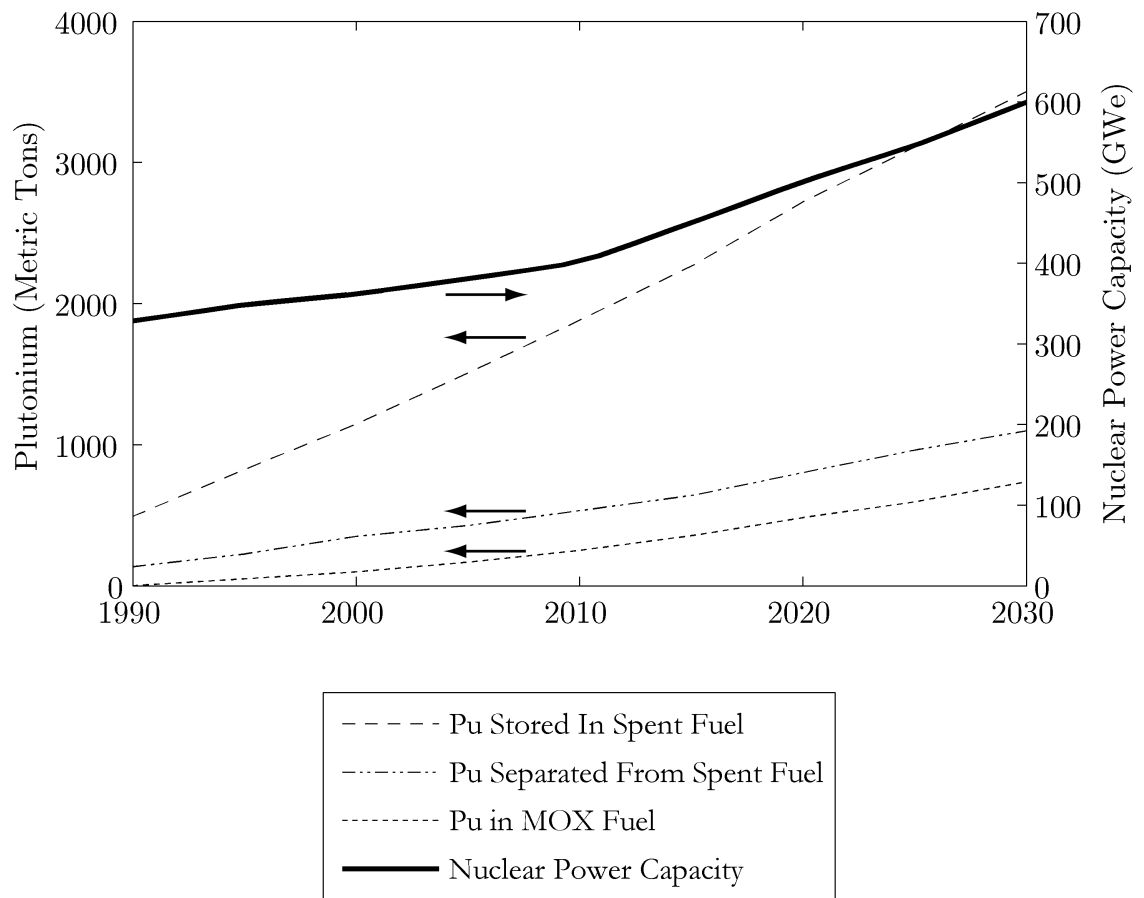


Figure 1.2: World wide nuclear capacity (solid line) and plutonium production [10].

1.3 Safeguards and Nuclear Forensics

Safeguards are a system of material accounting, containment, and surveillance designed to detect the diversion of nuclear materials [12, 13, 14]. In this process a state declares the inventory of nuclear materials present at facilities and provides records as to the operation of these facilities. This information is used as a guide for nuclear material accountancy (NMA), in which independent measurements are made to verify the disclosed quantities of nuclear material [15]. The difference between the declared amounts and these measurements is an accounting *defect*.

Depending on the quantity of material missing defects can be categorized as either gross, partial, or a bias [16]. A *gross defect* arises when all or most of the declared material is missing. These are identified by checking the physical inventory through item counting and gross defect radiation measurements. A missing fuel assembly or the presence of a skeleton assembly are examples of gross defects [17]. *Partial defects* refer to items in which some fraction of the declared amount of material is unaccounted; for example, a portion of a fuel assembly has been removed or replaced with non-fuel material. Visual inspection is not adequate to detect these defects. An inspection is required using neutron counting and gamma ray spectroscopy capable of measuring the material content to within a few percent of the declared value [18]. *Bias defects* occur when a small fraction of the declared material is missing, and arise from the diversion of small amounts of material over a long period of time. These are difficult to detect during an inspection and require material samples be taken for chemical analysis. These techniques offer the highest accuracy, often less than one percent [19, 20].

Nuclear forensic analysis is the process by which nuclear materials are analyzed to provide information as to the origins of the sample, and allows for interpretations to be made about the method of production and the intended use of the materials [21]. These techniques are crucial for attribution of interdicted nuclear materials and in providing more robust nuclear safeguards [22]. The attribution process includes a suite of techniques used for the physical, chemical, elemental, and isotopic characterization of the material [23]. These are intended to provide a signature that can be used to identify the material. A time line for how these techniques could be used for sample analysis is shown in Table 1.1. Such a sequence can be used in the analysis of unknown samples, provided the material is already in an easily measurable form [24]. In addition to the traditional forensics tools, i.e. visual inspection, fingerprinting, etc. there are isotopic signatures that require separate methods for analysis.

The methods employed in safeguards and nuclear forensics to determine the distinct isotopic details of a sample can be classified as either destructive analysis (DA) or non-destructive analysis (NDA). Destructive analysis is a measurement technique which introduces a significant change to the sample being measured such that it cannot be returned to the batch from which it was taken [25, 26]. DA methods are generally considered to be the most accurate measurement techniques available; however, dissolution and chemical separation often can be needed and substantial time is required for sample preparation

[18]. Nondestructive analysis often measures the radiation emitted from the bulk nuclear materials without alteration of the item under analysis [3]. While not necessarily as accurate as DA, these methods are more rapid and allow for the measurements on a large variety of material configurations such as nuclear waste and production materials where obtaining small samples for DA would be prohibitive or not representative of the entire sample.

1.4 Current Methodology and Limitations

Nondestructive measurements for the quantitative assay of plutonium are of great importance in both safeguards and nuclear forensics [28]. These NDA techniques, discussed in detail in Chapter 2, measure the thermal power generation or neutron emission to determine the quantity of the plutonium present in a material. However these methods require isotopic information, provided by gamma-ray spectroscopy, in order to interpret the response in terms of plutonium mass and this interpretation is affected by the uncertainty in the isotopic measurement. Isotopic information is also valuable in nuclear forensics, as the isotopic composition of plutonium produced in a nuclear reactor will vary according to the reactor design and operating conditions. The isotopic profile of the plutonium provides insight as to the initial fuel enrichment, reactor neutron flux and energy spectrum. The ratio of the plutonium isotopes produced in a boiling water reactor (BWR) as a function of burnup for different initial enrichments of ^{235}U is shown as an example in Figure 1.3. Knowledge of the plutonium isotopic composition is useful in determining the provenance of an unknown nuclear material.

One significant challenge in using NDA techniques for quantitative plutonium analysis is the inability to measure ^{242}Pu directly. This isotope has a long half-life, $t_{1/2} = 3.73 \times 10^5$ yr, and only three gamma-ray lines, all with energies below 200 keV. Measuring this weak gamma ray signature is further complicated by overlap from gamma ray lines of other isotopes and the background produced by the scatter of higher-energy radiation. Current spectroscopic techniques do not offer energy resolutions sufficiently high to adequately resolve the ^{242}Pu signature in samples containing a mixture of plutonium isotopes separated from nuclear fuel. The inability to measure this isotope has been addressed by developing tools that interpret the measurable quantities in the sample to infer the concentration of ^{242}Pu . However, these techniques are valid for a narrow range of isotopic compositions when the reactor type is known and thus are of limited use in analyzing completely unknown samples.

An example of how the uncertainty in the plutonium isotopic measurement affects the determination of initial fuel composition is shown in Figure 1.3. The measurement uncertainty using current spectroscopic techniques is discussed in detail in Chapter 2 and in Figure 1.3 these values are used to show the corresponding uncertainty in the initial ^{235}U enrichment of a nuclear fuel from the BWR. An improvement in the measurement of the $^{238}\text{Pu}/^{242}\text{Pu}$ atom ratio would reduce the uncertainty in the initial ^{235}U enrichment

Table 1.1: Time line for nuclear forensics analysis techniques. Destructive analysis methods are italicized [27].

Technique/Method	24 Hours	1 Week	1 Month
Radiological	Estimated total activity Dose Rate (α , γ , n) Surface Contamination		
Physical characterization	Visual Inspection Weight Radiography Photography Dimension Optical Microscopy Density	<i>SEM (EDS)</i> <i>XRD</i> Organics	<i>TEM (EDS)</i>
Traditional forensic analysis	Fingerprints Fibers		
Isotope analysis	Alpha-spectroscopy Gamma-spectroscopy	<i>Mass spectrometry</i> (<i>SIMS</i> , <i>TIMS</i> , <i>ICP-MS</i>)	<i>Radiochemical separations for mass spectrometry of trace impurities:</i> <i>Pb, stable isotopes</i>
Chemical/Elemental		<i>ICP-MS</i> <i>XRF</i> <i>ICP-OES</i>	<i>GC/MS</i>

Note: SEM: scanning electron microscopy; TEM: transmission electron microscopy; EDS: energy dispersive x-ray spectrometry; XRD: x-ray diffraction; SIMS: secondary ion mass spectrometry; TIMS: thermal ionization mass spectrometry; ICP-MS: inductively coupled, plasma source mass spectrometry; XRF: x-ray fluorescence; GC/MS: gas chromatography mass spectrometry; ICP-OES: inductively coupled plasma source optical emission spectroscopy

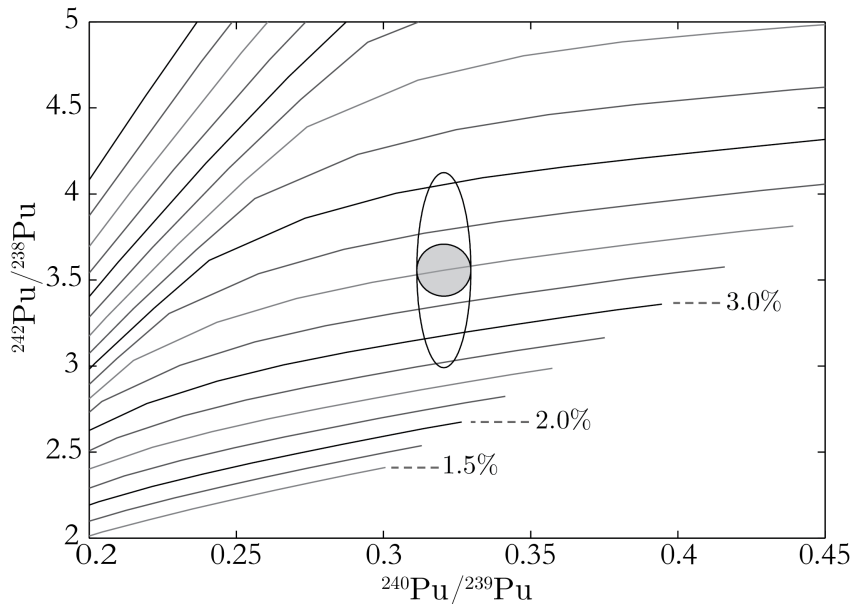


Figure 1.3: Correlation of Pu isotopes in BWR as a function of burnup for an initial enrichment of ^{235}U from 1.5% to 6% in 0.25% steps. The oval indicates the uncertainty in the measurement using current technology. The shaded region indicates the uncertainty for improved measurement ^{238}Pu and ^{242}Pu .

by a factor of ~ 3 , indicated by the shaded circular region. For this reason, a measurement system with an energy resolution sufficient to directly measure ^{242}Pu would prove invaluable to nuclear analysis. This thesis details the efforts to develop such a detector.

1.5 Previous Work

In the 1930s it was recognized that the sensitivity of calorimetric measurements would improve when made at low temperatures, $T < 10\text{ K}$ [29]. In the following decade sensors based on the superconducting-to-normal transition were first developed for the measurement of infrared photons [30] and alpha particles [31]. The difficulty in obtaining such low temperatures limited the use of these devices until the 1980s when x-ray astronomy [32], the search for neutrinos [33], and neutrinoless double-beta decay [34] required sensitivities only achievable using these low-temperature sensors, motivating the necessity to develop cryogenic detector technology. The technological advances resulting from these scientific endeavors were crucial in the efforts to use this technology for gamma-ray spectroscopy.

In the last decade transition edge sensors for gamma-ray spectroscopy have been demonstrated with energy resolutions of 50 – 100 eV. Lawrence Livermore National Laboratory (LLNL) is developing tin absorber superconducting gamma ray and LiF absorber fast-neutron calorimeters for fundamental science and national security applica-

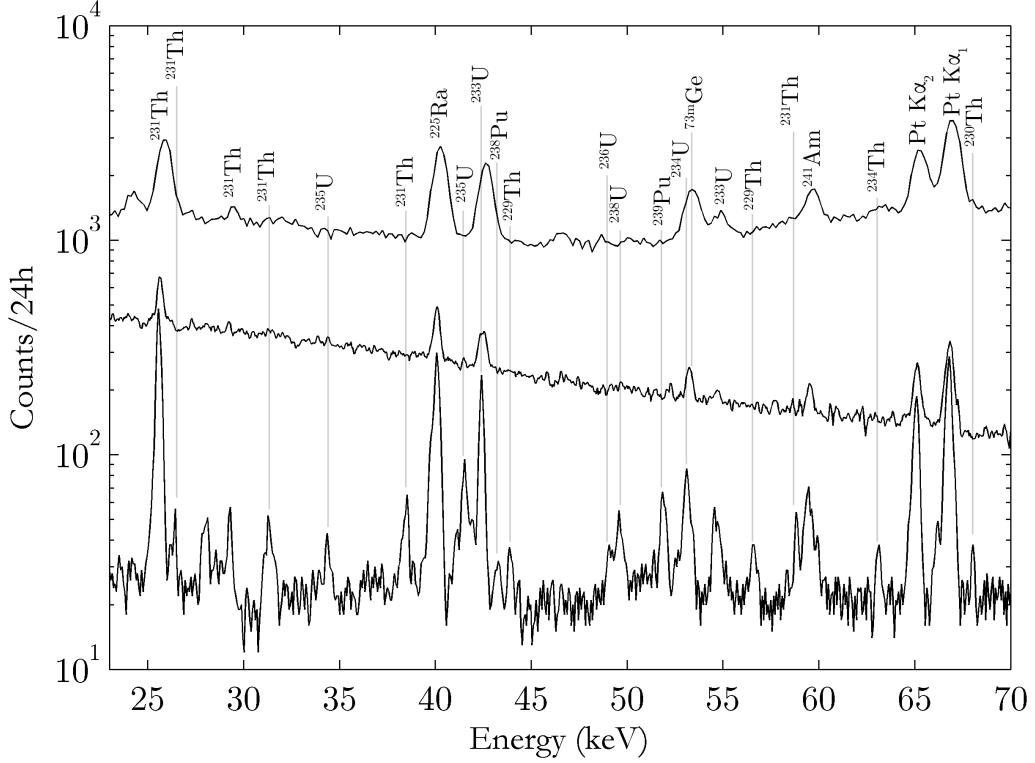


Figure 1.4: Spectrum of uranium oxide fuel taken using a coaxial HPGe detector (upper spectrum), a planar HPGe detector (middle spectrum), and a superconducting transition edge sensor (lower spectrum) [39].

tions [35, 36, 37]. Spectroscopic measurements of uranium yellowcake [38], uranium fuel oxides [39], and plutonium and uranium samples [40, 41] have shown the gains in isotopic analysis from the improved energy resolution. A spectrum taken using a single transition edge sensor (TES) spectrometer of a mixed uranium oxide fuel is shown in Figure 1.4. Recent work has focused on developing arrays of sensors [42, 43, 44, 45]. To maintain the low temperatures required for detector operation, the number of wires used for reading out these multiple sensors must be limited. These efforts have been promising for making isotopic measurements in reasonable timescales [46].

1.6 Dissertation Outline

This dissertation discusses the development of a gamma spectrometer for direct measurement of the ^{242}Pu gamma-ray signature using transition edge sensors. Chapter 2 provides a discussion of the relevant properties of plutonium and current methodologies for determining the plutonium concentration in mixed isotope samples. Chapter 3 pro-

vides a brief introduction to the theory of TES calorimeters from photon absorption to the signal generation. The fundamental sources of noise and the contribution to the overall performance are also discussed. Chapter 4 expands the theory with the inclusion of additional sources of noise. The model of the calorimeter noise developed in this chapter provides the basis for the measurement analysis in Chapter 7. Chapter 5 describes the cryostat systems and cryogenic methods used to operate at millikelvin temperatures. Cryostats operated using liquid cryogens and modern pulse tube refrigeration technology are discussed. Chapter 6 describes the Monte Carlo simulations used to assess the feasibility of plutonium isotopic measurements using a TES. Chapter 7 describes the results for operation of a transition edge sensor in a pulse tube refrigeration system. Noise reduction techniques to improve performance are discussed. Best performance of the system is presented with the measured noise analyzed using the model developed in Chapter 4. Chapter 8 summarizes this work and discusses future research. Appendix A includes the derivations referenced in Chapter 3 and 4. Appendix B provides material properties and the calculation of heat capacities, thermal conductivities, and coupling constants for materials used in transition edge sensors. Appendix C presents an overview of the optimum filtering method used for TES analysis. Appendix D documents the MATLAB code used in Chapters 3 and 4 for analyzing the TES noise. Appendix E presents the analytical derivation of the precision of measuring two closely spaced gamma ray lines in a spectrum.

Chapter 2

Plutonium Isotopic Analysis

2.1 Background

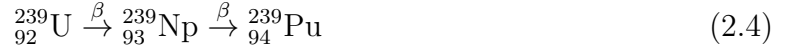
Plutonium (Pu) is the 94th element of the periodic table, belonging to the actinide series of elements. The first isotope of plutonium, ^{238}Pu , was discovered in 1940 by Seaborg, McMillan, Kennedy and Wahl by bombarding uranium with deuterons using the 60-inch cyclotron at University of California, Berkeley [47]. In this process the absorption of a deuteron by $^{238}_{92}\text{U}$ would produce the nuclide $^{238}_{93}\text{Np}$, which then decayed by β - emission to ^{238}Pu as



In 1941, ^{241}Pu was discovered by Kennedy, Segre, Wahl, and Seaborg by producing ^{239}U through neutron absorption in ^{238}U [48]



The subsequent decay of $^{239}_{92}\text{U}$ by beta emission produced $^{239}_{94}\text{Pu}$



Shortly thereafter ^{239}Pu was found to have a thermal neutron fission cross section higher than ^{235}U [49]. This is a crucial parameter in weapons design and consequently publication of this discovery was delayed until after World War II. Of the twenty plutonium isotopes that have been identified since 1940, six are relevant to this thesis. Their nuclear properties are summarized in Table 2.1. Unlike uranium which can be mined in large quantities, plutonium is one of the least abundant elements found in nature [50]. Natural ^{239}Pu exists in minute quantities in uranium ore from neutron capture in ^{238}U described in (2.3). Trace quantities of ^{244}Pu have been found in bastnasite ore, the presence of this long lived Pu isotope, $t_{1/2} = 8.28 \times 10^7$ yr, is a remnant from the formation of the solar system [51].

Table 2.1: Properties of plutonium isotopes commonly found in nuclear fuels [52][53].

Isotope	Mass (amu)	Half-life (yr)	Specific Activity (Ci/g)	Specific Power (mW/g)	Decay Mode
^{238}Pu	238.0495	87.7	17.1	567.6	α
^{239}Pu	239.0521	2.41×10^4	0.06	1.9	α
^{240}Pu	240.0538	6564	0.22	7.1	α
^{241}Pu	241.0568	14.35	103.4	3.4	β
^{242}Pu	242.0587	3.73×10^5	0.004	0.1	α

Table 2.2: Thermal and fast fission cross sections, average number of neutrons per fission ν , and spontaneous fission yields for plutonium. Cross section values calculated using the data plotted in Figure 2.2.

Isotope	0.025 eV		1 MeV		ν [57]	Spontaneous fission yield [56] (neutrons/g.s)
	σ_c (b)	σ_f (b)	σ_c (b)	σ_f (b)		
^{238}Pu	5.1×10^2	17	0.2	2.1	2.21	2.59×10^3
^{239}Pu	2.7×10^2	752	0.03	1.7	2.16	2.18×10^{-2}
^{240}Pu	2.9×10^2	0.06	0.08	1.5	2.16	1.02×10^3
^{241}Pu	32.7×10^2	1×10^3	0.11	1.6	2.25	5.0×10^{-2}
^{242}Pu	19	< 0.01	0.1	1.4	2.15	1.72×10^3

2.2 Plutonium Production

Plutonium is produced in reactors fueled with uranium. A majority of the fuel is ^{238}U enriched to a few percent in ^{235}U . The production of plutonium in uranium fuel is shown in Figure 2.1. During operation, ^{235}U fissions to produce neutrons that are absorbed in ^{238}U producing short-lived ^{239}U , which beta decays to ^{239}Np and subsequently into fissile ^{239}Pu . ^{235}U can also produce ^{238}Pu through successive neutron absorption and beta decay [54].

The neutron capture and fission cross sections of plutonium influence the isotopic composition of plutonium produced in a reactor. These properties are isotope dependent and determine the probability that a nucleus will undergo fission, thereby reducing the quantity of plutonium in the fuel, or absorption, thereby producing an isotope of plutonium with an increased mass number by unity. The capture-to-fission ratios for the various plutonium isotopes are shown in Figure 2.2 as a function of neutron energy, with the average values for thermal and fast neutrons listed in Table 2.2. The differing cross sections of the plutonium isotopes can be used to determine several key reactor parameters: fuel utilization (burn-up), initial fuel composition, and the neutron energy spectrum.

The amount of energy that is produced per unit mass of fuel is termed burn-up [58]. In low burn-up situations, where the fuel is irradiated for a short period of time or exposed to a low flux of neutrons, the plutonium produced is almost entirely ^{239}Pu . With increasing irradiation times the quantity of ^{240}Pu from neutron absorption increases, and subsequent neutron capture results in the production of higher mass number Pu isotopes (Table 2.3). As an example, the isotopic composition of plutonium in a PWR as a function of burn up is shown in Figure 2.3.

The quantity of ^{235}U used in a reactor can vary from natural abundance of 0.711%, used in Canada Deuterium Uranium (CANDU) reactors, to several weight percent ^{235}U , for light water reactors. Successive neutron captures in ^{235}U results in the production of ^{238}Pu , and as a result increasing initial fuel enrichment will increase the abundance of ^{238}Pu produced in the reactor.

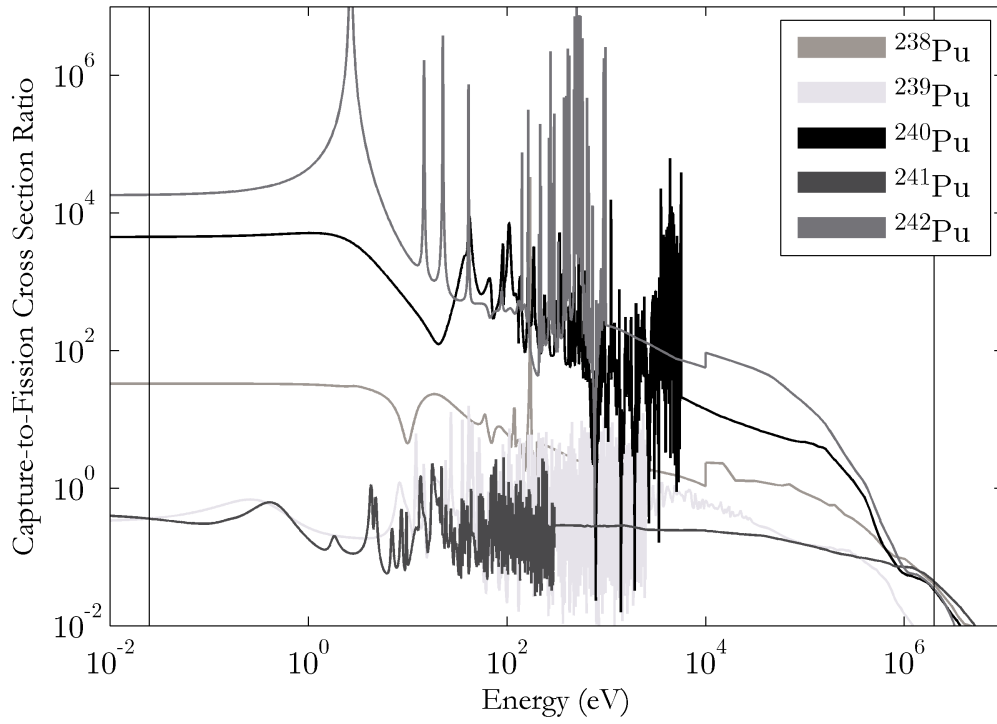


Figure 2.2: Capture-to-fission ratio of plutonium isotopes calculated using the ENDF/B-VII.0 cross-section library. The vertical lines indicate the 0.025 eV (thermal) and 1 MeV(fast) values listed in Table 2.2.

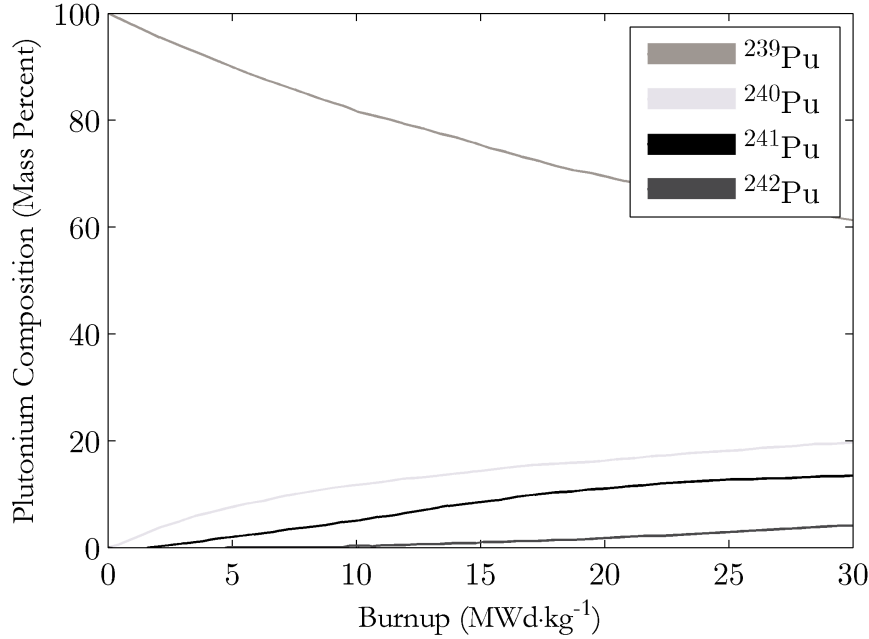


Figure 2.3: The isotopic composition of plutonium produced in a PWR fuel as a function of burn-up [59].

The fission cross section for plutonium at higher neutron energies is substantial; consequently the plutonium produced in reactors with higher neutron energies, such as a Magnox reactor, will have a higher concentration of ^{239}Pu . For fuel exposed to a thermal energy spectrum, such as CANDU systems, ^{239}Pu more readily captures neutrons allowing for the formation isotopes of higher mass. The difference in the isotopic abundances can be seen in Table 2.3. Plutonium continues to be produced even after the fuel has been discharged from the reactor. As shown in Figure 2.1, the alpha decay of curium produces additional Pu in the spent fuel.

2.3 Isotope Correlation for Safeguards

In the late 1960s it was recognized that the isotopic composition of nuclear fuels was dependent on parameters including the initial enrichment, burnup, neutron flux and energy spectrum [61]. The fission product abundances are correlated to the specifics of the fuel irradiation and provide information useful in determining the provenance of an unknown nuclear material. This method of using isotope ratio correlations is referred to as Isotopic safeguards techniques (IST) or Isotopic correlation techniques (ICT).

Early efforts focused on using single isotope ratios (e.g. $^{134}\text{Cs}/^{137}\text{Cs}$, $^{242}\text{Pu}/^{241}\text{Pu}$) to prevent diversion of spent fuel at reprocessing facilities [62]. Recent work has found

Table 2.3: Plutonium composition (wt%) of reactor fuel at discharge [60].

Reactor	Burnup (GWd/MTU)	^{238}Pu	^{239}Pu	^{240}Pu	^{241}Pu	^{242}Pu
PWR	30	1.1	56.6	25.7	12.8	3.7
	45	2.4	50.4	26.0	14.8	6.4
	65	4.8	45.1	24.9	15.5	9.7
BWR	30	1.2	55.7	25.9	13.1	4.1
	45	2.7	49.5	26.0	14.9	6.9
	65	5.5	44.2	24.7	15.3	10.3
Magnox	7	0.3	59.8	28.2	9.0	2.7
CANDU	25	0.7	46.5	34.4	10.0	8.5

isotopic correlations for the age of a sample, which is useful for determining when the material was last chemically separated [63]. Other works have developed ICT methodologies to determine the source of interdicted nuclear materials, unknown fuels, and samples found in the environment [64, 65]. One such relationship is shown in Figure 2.4, which shows the correlation between the $^{242}\text{Pu}/^{240}\text{Pu}$ and $^{238}\text{Pu}/\text{Pu}_{\text{Total}}$ as a function of burnup [66]. From this example it can be seen that such ratios in the plutonium isotopes can help determine the type of reactor in which it was produced. The following section discusses the nondestructive analysis methods used to determine the mass and isotopic composition of plutonium in a material.

2.4 Current Methodology for Plutonium Assay

The three most common NDA techniques used to assay the plutonium content in a sample are Passive Neutron Coincidence Counting (PNCC), calorimetry, and High-Resolution Gamma Spectrometry (HRGS). The first two methods, PNCC and calorimetry provide the rate of neutron emission and energy release from the sample, respectively. However, both methods are unable to measure isotope-specific nuclear properties and require HRGS to provide the plutonium isotopic composition in order to interpret the response to determine the total mass of plutonium in a sample. Consequently uncertainty in the HRGS measurement will affect the accuracy of the result. The following sections will discuss the methodologies used for PNCC and calorimetry, followed by a more thorough discussion of HRGS.

2.4.1 Calorimetry

Calorimetry determines the amount of plutonium in a sample by measuring the heat produced by the radioactive decay of the plutonium and its daughter isotopes. As the

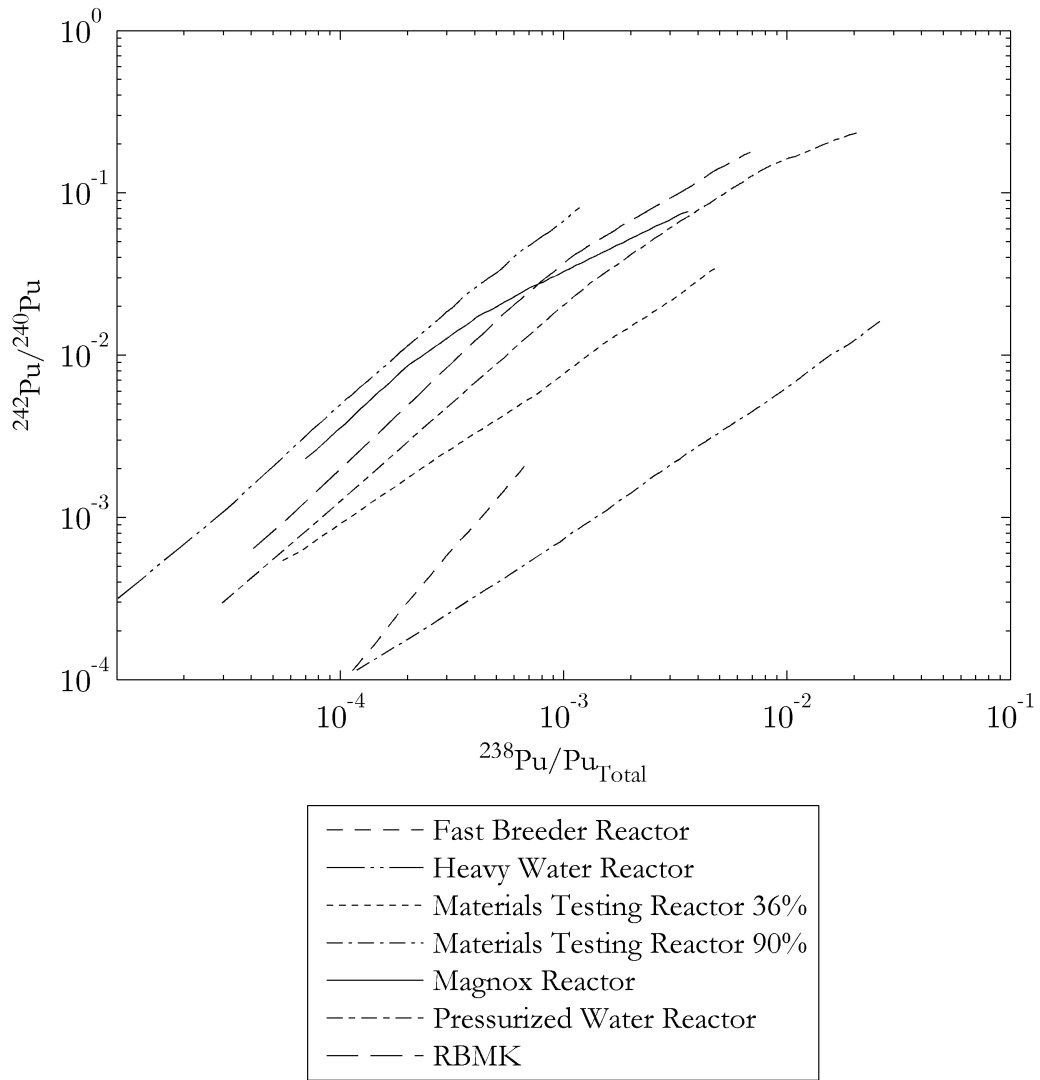


Figure 2.4: Reactor type disclosure by isotopic correlation [66].

thermal power generated per unit amount of material depends on the plutonium isotopic composition and the ^{241}Am content, calorimetry requires knowledge of the relative abundances to infer the corresponding plutonium mass [57]. The uncertainties in the isotopic composition are often the largest errors in the measurement [67]. As shown in Table 2.4, the majority of the heat measured by calorimetry results from the spontaneous alpha decay of ^{239}Pu . The concentration of ^{241}Am , produced by the beta decay of ^{241}Pu ($t_{1/2} = 13.2\text{yr}$), depends on the irradiation conditions and the age of the material after discharge from the reactor and therefore must be accounted for prior to calorimetric analysis. ^{242}Pu can not be directly measured using this method as its contributions to the total measured thermal power is negligible [53].

Table 2.4: The typical percentage of decay power for plutonium separated from the fuel. Values calculated using compositions listed in Table 2.3 and isotopic information from Table 2.1.

Isotope	Percent of Total Heat Generated			
	PWR	BWR	Magnox	CANDU
^{238}Pu	63.8	64.5	29.8	49.8
^{239}Pu	10.7	9.8	20.1	11.4
^{240}Pu	17.8	16.8	35	31.0
^{241}Pu	4.3	4.1	5.4	4.3
^{242}Pu	0	0	0.1	0.1
^{241}Am	3.3	4.6	9.6	3.4

The specific thermal power of a plutonium sample as measured by calorimetry is given by summing the power produced by the n constituent isotopes contributing to the sample heat [67]

$$W_S = \sum_{i=1}^n M_i P_i = M \sum_{i=1}^n R_i P_i = M P_{\text{eff}} \quad (2.5)$$

where M_i is the mass of the i th isotope, M is the total mass of plutonium, P_i is the specific power of the i th isotope, R_i is the ratio of the mass of the i th isotope to the total plutonium mass (mass fraction), and P_{eff} is the effective specific power of the sample.

The thermal power measurement is highly accurately, with uncertainties typically less than 0.1%. However, to interpret the results of calorimetric assay and determine the mass of radioactive material present requires knowledge of the isotopic composition, determined by gamma-ray spectroscopy [57]. The uncertainty in the isotopic ratios greatly outweighs the calorimetric uncertainties, and in most situations an approximate estimate of the order of the total precision of the overall measurement will be $\pm 1\%$ of the precision of the gamma-ray isotopic measurement [68].

2.4.2 Passive Neutron Coincidence Counting

Passive Neutron Coincidence Counting (PNCC) is an NDA technique used to determine the mass of plutonium in an unknown sample by measuring the neutrons released by spontaneous fission. The spontaneous fission yields of the even-isotopes of plutonium (^{238}Pu , ^{240}Pu , ^{242}Pu), listed in Table 2.1, are dominant in the measurement. As the neutrons from each isotope are emitted simultaneously they are correlated in time and the count rate is a complex function of the Pu mass and isotopic composition [69]. The quantity determined using PNCC is an effective ^{240}Pu mass, $m_{240\text{eff}}$. This value is the equivalent mass of ^{240}Pu that would provide the same neutron coincidence response as obtained from all of the even isotopes present in the sample, and can be expressed as [70]

$$m_{240\text{eff}} = \gamma_{238}m_{238} + m_{240} + \gamma_{242}m_{242} \quad (2.6)$$

where coefficients γ_{238} and γ_{242} are 2.573 and 1.708, respectively [71]. The γ coefficients scale the neutron coincidence response of ^{238}Pu and ^{242}Pu to the equivalent amount from ^{240}Pu . As PNCC can only provide a weighted sum of the three isotopes, the total amount of plutonium m_{Pu} requires the isotopic mass fractions f_{238} , f_{240} and f_{242} of ^{238}Pu , ^{240}Pu , and ^{242}Pu , which must be determined through gamma ray spectroscopy. With the mass fractions known, the total mass of plutonium m_{Pu} is given by

$$m_{\text{Pu}} = \frac{m_{240\text{eff}}}{\gamma_{238}f_{238} + f_{240} + \gamma_{242}f_{242}} \quad (2.7)$$

A discussion of the complete methodology can be found in the literature [72]. As with calorimetric analysis, PNCC requires an additional independent measurement, namely from gamma spectroscopy, to interpret the neutron measurements. In many situations the inaccuracies in the isotopic abundances are substantially greater than the total random and systematic uncertainties from PNCC measurement itself [57]. For high accuracy measurements of plutonium it is essential to have accurate spectrometric measurements.

2.4.3 High-Resolution Gamma Spectrometry

The isotopic information required for PNCC and calorimetry is provided using high-resolution gamma spectroscopy (HRGS). As the accuracy of the other NDA measurement techniques rely on the precision of the spectroscopic measurement, high resolution spectra are required. Of the currently available radiation detection systems, only semiconductor detectors, specifically high-purity germanium (HPGe) detectors, offer the efficiency and energy resolution needed for these measurements.

Schematics of the two most common HPGe detector configurations are shown in Figure 2.5. The detector consists of a single crystal of germanium with electrodes on either side. The crystals are machined into either a disk for planar detectors or a cylinder with an axial hole for coaxial detectors. Radiation absorbed in the germanium produces ionizations. On the average one electron-hole pair is produced for about 3 eV of energy absorbed. The

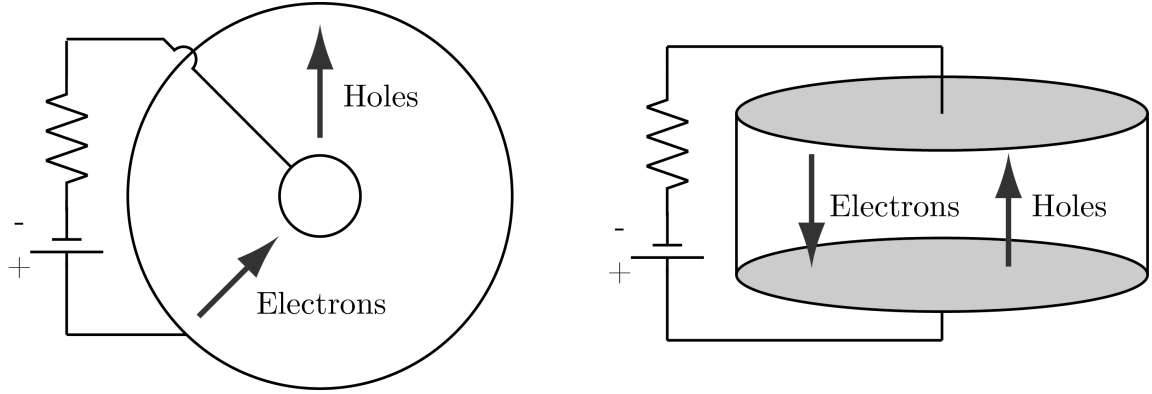


Figure 2.5: Schematic of coaxial (left) and planar (right) germanium detectors.

electron energy is sufficient to cross the germanium band gap (~ 1 eV) into the conduction band where the applied electric field draws the charges to the electrodes producing a voltage pulse.

The larger, coaxial systems are used for larger bulk samples and are useful for measuring the gamma spectrum above 200 keV. An example spectrum taken using a coaxial HPGe detector is shown in Figure 2.6. Indicated on the spectrum are the plutonium gamma-ray lines commonly used for isotopic ratio calculations. The methodology for determining the isotopic ratios from the spectrum will be discussed in following section; however, note that none of the three gamma ray lines from ^{242}Pu appear in the spectrum. These lines, summarized in Table 2.6, are all below 200 keV. The 44.915-keV and 103.50-keV gamma ray are indistinguishable amongst the other plutonium and ^{241}Am lines while the 158.8 keV line is too weak to be observed above the background.

Table 2.5: Isotopic compositions for samples measured in Figure 2.6 and 2.7.

Isotope	Isotopic Composition (wt%)	
	Figure 2.6	Figure 2.7
^{238}Pu	0.202	0.649
^{239}Pu	82.49	67.01
^{240}Pu	13.75	21.80
^{241}Pu	2.69	8.11
^{242}Pu	0.76	2.44
^{241}Am	11800 $\mu\text{g/g}_{\text{Pu}}$	Not reported

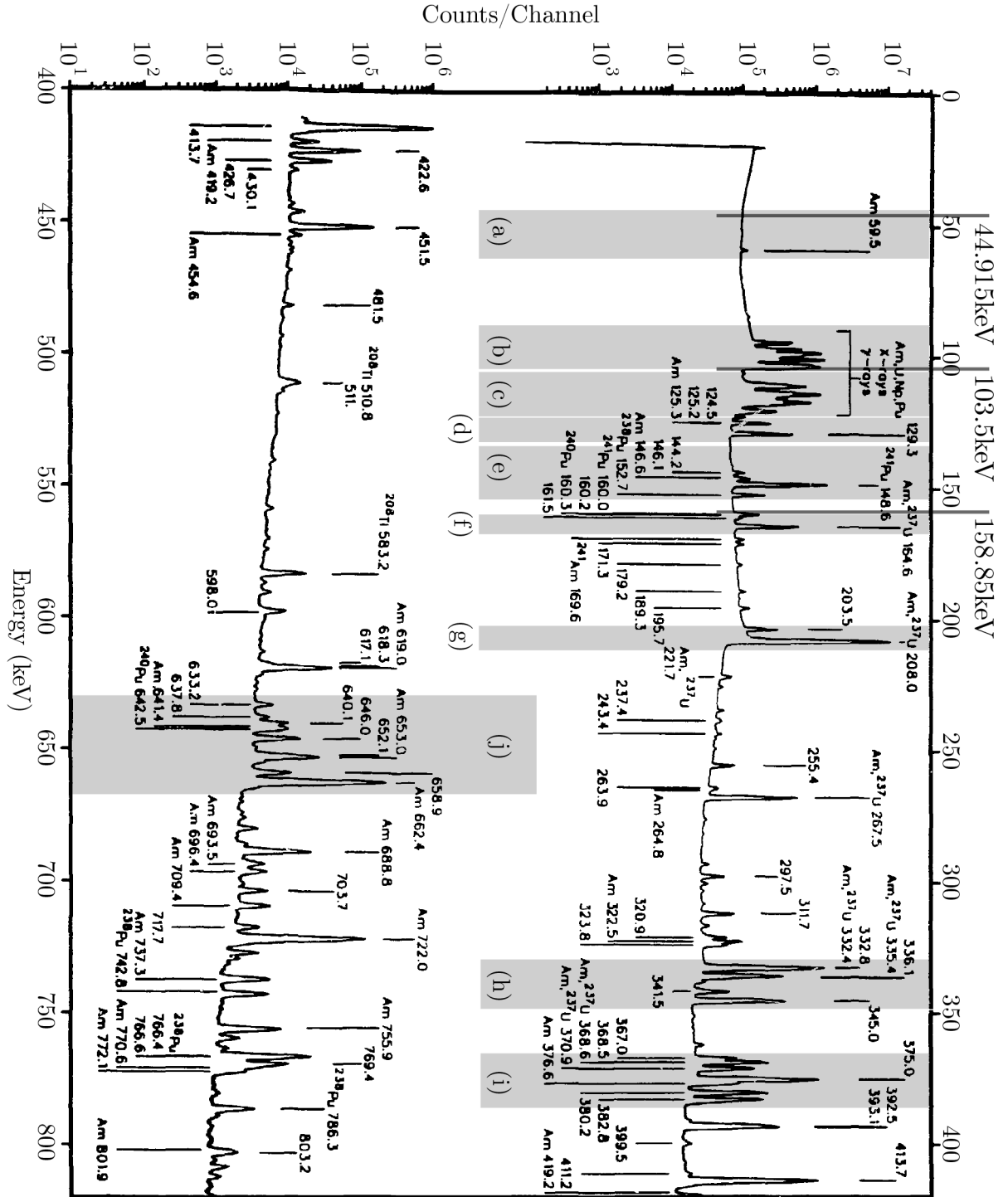


Figure 2.6: Spectrum from 530 g plutonium as PuO_2 with isotopic composition (wt%) listed in Table 2.5. The spectrum is taken using is a 10.2% relative efficiency coaxial HPGe detector with 1.65 keV resolution at 1332 keV. Energies not labeled with a specific isotope are from ^{239}Pu . The energy regions commonly used for plutonium isotopic analysis are indicated with gray shading [73].

Table 2.6: Gamma rays emitted in the decay of ^{242}Pu .

Energy	Intensity
44.915 keV	0.036
103.50 keV	0.0078
158.8 keV	0.00045

Planar germanium detectors have a smaller active volume and therefore lower efficiency than coaxial detectors for photons whose mean free path exceeds the dimensions of the detector. For a 7 mm germanium crystal this is ~ 150 keV. Above this energy the efficiency decreases proportionally to $\log(1/E)$ [74, 75]. However, such detectors offer higher energy resolution and the smaller volume reduces the Compton continuum from the interaction of high-energy photons and allows for improved measurements for photons with energies less than 150 keV. A spectrum taken of a solution containing 3 g of Pu measured using a 200 mm² by 7 mm intrinsic planar germanium detector is shown in Figure 2.7. The activity of ^{241}Am contributes substantially to the count rate and therefore was separated from the solution to make the measurement. With the planar system the low-energy lines from the plutonium isotopes are visible, with the exception of the ^{242}Pu line at 44.915 keV. Although the sample preparation removed the ^{241}Am contribution to the Compton background, which is substantial in aged plutonium samples [76], and the system offered an improved energy resolution, the 45.230 keV ^{240}Pu line with ~ 450 eV FWHM prevents the measurement of the ^{242}Pu line.

Isotopic Ratio Determination

The plutonium isotopic ratios are determined using the gamma ray spectrum obtained from HRGS. A radionuclide with N atoms in a sample will produce a peak of intensity I [counts/sec] in a spectrum when measured using a detector with a total photopeak efficiency ε at an energy E . This can be expressed as

$$I = \varepsilon P \lambda N \quad (2.8)$$

where P is the probability per decay for emission of the photon of interest and λ is the decay constant of the radionuclide. The detection efficiency ε is dependent on numerous factors, including the source-detector geometry, self-attenuation of the source, shielding around the source, and the detector efficiency. As many characteristics of the sample are often unknown, the uncertainty arising from ε can be reduced by calculating the ratio of the isotopic abundances from two peaks of similar energies. The atom ratio of two isotopes N_1/N_2 is given by

$$\frac{N_1}{N_2} = \frac{I_1 \varepsilon_2 P_2 T_1}{I_2 \varepsilon_1 P_1 T_2} \quad (2.9)$$

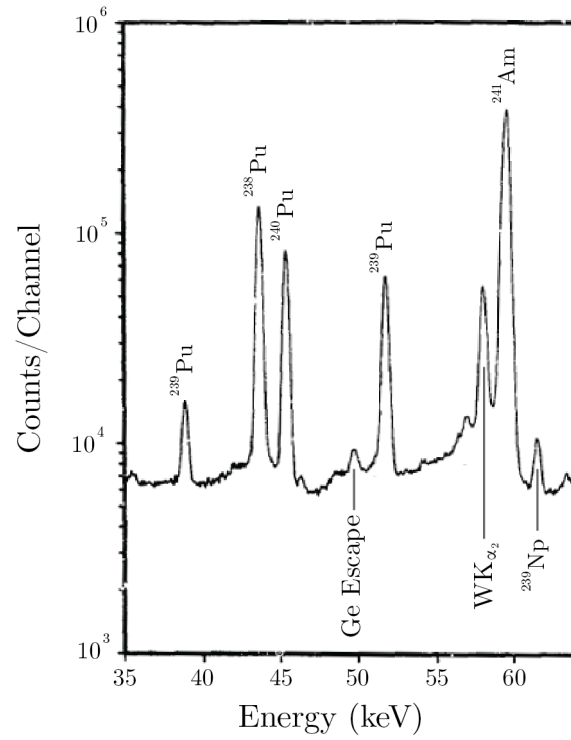


Figure 2.7: Spectrum of a nitric acid solution containing 185 g/L plutonium. The measurement was made using a 200 mm² by 7 mm intrinsic planar germanium detector with an energy resolution of 0.5 keV at 100 keV. The tungsten x-ray line is the result of the detector shielding. The isotopic composition of the sample is listed in Table 2.5. [73, 77]

where T_1 , T_2 are the half-lives, I_1 , I_2 are the peak intensities, ε_1 , ε_2 are the counting efficiencies, and P_1 , P_2 are the branching probabilities as described in equation (2.8). As this method relies on the half-lives and gamma-ray emission probabilities, it does not need to be calibrated with known standards. With this ratio method the dominant sources of uncertainty are no longer the values of ε , but rather the precision of the intensities I_1 and I_2 . The process of calculating these ratios has been automated using computer codes such as Multi-Group Analysis (MGA) and FRAM [78, 79]. In the following we summarize the methodology used in MGA.

Regions of Interest

There are ten regions in a gamma spectrum with closely spaced gamma lines that are used to determine the isotopic ratios of plutonium. These are listed in Table 2.7. The peaks commonly used for this analysis are indicated in the PuO₂ spectrum in Figure 2.6 and range from 40 to 600 keV. The gamma ray peaks in each region are fit with a Gaussian and two exponential decay terms to account for the low-energy tailing of the peak [80]. The fitting of the X-ray peaks is more complex as the Gaussian detector response and exponential decay terms must be convolved with the Lorentzian shaped X-ray distribution [81]. The intensity of the Compton continuum at the boundaries of the energy region is determined and the background contribution for each channel is interpolated and subtracted from the spectrum. The total efficiency for each region includes the intrinsic efficiency of the detector, the self-attenuation of the sample, and, if present, the attenuation by the cadmium used to suppress the 59 keV line from ²⁴¹Am. The peak fits and efficiency curve provide a set of equations that must be iteratively solved for the isotopic ratios of interest. Of the isotopes with measurable gamma ray lines, ²³⁹Pu and ²⁴¹Pu have lines at multiple energies from which the abundances can be measured accurately. Abundance calculations for ²⁴⁰Pu and ²³⁸Pu are commonly less accurate because many of the lines from ²⁴⁰Pu are obscured by line overlap and can be difficult to resolve properly. The ²³⁸Pu in many samples is a small fraction of the total plutonium, and with fewer lines available for analysis the uncertainty can be quite large [67, 73].

²⁴²Pu Isotopic Correlation

As discussed earlier in this section, the ²⁴²Pu gamma-ray signature cannot be directly measured using current HPGe detector systems. Instead the ²⁴²Pu content is estimated from correlations of the other isotopes present in the sample. The correlation used by many early analysis codes was given by [82]

$$[^{242}\text{Pu}] = C \frac{[^{240}\text{Pu}] \cdot [^{241}\text{Pu}]}{[^{239}\text{Pu}]^2} \quad (2.10)$$

where the brackets indicate the weight percent of the given isotope and C is a coefficient empirically determined using the isotopic compositions for five PWRs, six BWRs and

Table 2.7: Isotopes in each energy region used for isotopic analysis.

Region	Energy Range	^{238}Pu	^{239}Pu	^{240}Pu	^{241}Pu	^{242}Pu
(a)	38 – 59 keV	1	1	1	0	1
(b)	94 – 104 keV	3	5	3	5	1
(c) ¹	110 – 120 keV	0	4	0	1	0
(d) ²	123 – 129 keV	0	0	0	1	0
(e)	129 – 152 keV	1	1	1	0	0
(f) ¹	160 – 165 keV	0	2	0	2	0
(g)	203 – 208 keV	0	1	0	1	0
(h)	332 – 345 keV	0	4	0	2	0
(i)	367 – 382 keV	0	7	0	2	0
(j)	632 – 664 keV	0	10	1	0	0

¹Region used for efficiency calculations.

²Used for measuring the $^{241}\text{Am}/^{241}\text{Pu}$ ratio

one CANDU reactor with isotopic information provided by the Battelle Northwest data bank [83, 84, 85]. A value of $C = 52$ was found to give good agreement with the data base values, independent of reactor type. Unfortunately the correlation shown in (2.10) is dependent on the short-lived ^{241}Pu , and therefore the ^{242}Pu abundance will be biased for high burn-up fuels and for spent fuel with long cooling times prior to the chemical separation of the plutonium. This results in errors in the ^{242}Pu content as large as 20% for high burn-up fuels [86]. To address this issue another ratio, independent of ^{241}Pu , was developed

$$\frac{[^{242}\text{Pu}]}{[^{239}\text{Pu}]} = C_0 \left(\frac{[^{238}\text{Pu}]}{[^{239}\text{Pu}]} \right)^{C_1} \left(\frac{[^{240}\text{Pu}]}{[^{239}\text{Pu}]} \right)^{C_2} \quad (2.11)$$

where the coefficients C_0 , C_1 , and C_2 are dependent on reactor type and fuel enrichment [87]. In the chemical analysis of over 4000 samples of BWR and PWR fuel, C_1 and C_2 were found to be independent of reactor type and initial enrichment, with values of 0.33 and 1.7, respectively. The selection of C_0 is chosen from twenty possible values and requires knowledge of the reactor type. Provided the type and initial fuel enrichment of the reactor which produced the plutonium is known, the average uncertainty for this correlation technique is approximately 3% and 6% for ^{242}Pu produced in PWR and BWR, respectively [88].

2.5 Limitations

The significant limitation of the current NDA methodology is the lack of information of the ^{242}Pu abundance. As both PNCC and calorimetry require the isotopic composition

Table 2.8: Uncertainties (%) of the $m_{240\text{eff}}$ and P_{eff} values for different fuels. The first column lists the percent uncertainty in the ^{242}Pu correlation. The italicized columns are uncertainties when the ^{242}Pu abundance is provided from thermal ionization mass spectrometry, the adjacent column is the case when ^{242}Pu abundance is determined from correlation [57].

	^{242}Pu Correlation Uncertainty (%)	$m_{240\text{eff}}$		P_{eff}	
Low Burnup	2	<i>1.17</i>	1.19	<i>0.35</i>	0.34
Magnox	2.5	<i>1.14</i>	1.17	<i>0.64</i>	0.64
PWR	3	<i>0.92</i>	1.35	<i>0.99</i>	1.06
AGR	4	<i>1.00</i>	1.28	<i>0.78</i>	0.85
BWR	6	<i>1.00</i>	1.77	<i>0.85</i>	0.92

to interpret the system responses to determine the total amount of plutonium, $m_{240\text{eff}}$ and P_{eff} , respectively, the uncertainties in the ^{242}Pu correlation will affect the quality of these conclusions. Table 2.8 lists the uncertainties the $m_{240\text{eff}}$ and P_{eff} values calculated for several reactor fuels. The second column lists the uncertainties in the ^{242}Pu correlation for each type of fuel. The two columns below $m_{240\text{eff}}$ and P_{eff} are the uncertainties in the value when the ^{242}Pu abundance is provided using thermal ionization mass spectrometry (TIMS) and through correlation. Thermal ionization mass spectrometry is a destructive analysis technique which provides abundance values with an uncertainty of approximately 0.1%. The uncertainties in the second column are for measurements in which the ^{242}Pu abundance is determined from correlations of the other isotopes present in the sample. As expected, the correlation method shows good agreement with low burnup fuels and Magnox reactors for which ^{242}Pu is less than 1% of the total plutonium produced in the fuel. The uncertainty for AGR, BWR, and PWR fuels is larger when using correlated abundances, resulting from the decreased accuracy of the ^{242}Pu correlation.

The limitations of the ^{242}Pu correlation technique are more apparent when the provenance of the fuel is not known. In early 2000 the Working Group on Standards and Non-Destructive Assay of the European Safeguards Research and Development Association (ESARDA), organized an exercise among eight different research facilities in Europe and the United States with the goal of assessing the current performance in determining plutonium isotopic abundances. The laboratories were provided with a set of plutonium bearing samples and were asked to determine the plutonium isotopic composition [89]. For each sample the composition was determined using a ^{242}Pu abundance provided by ESARDA and another using a ^{242}Pu calculated using isotopic correlation. The average relative uncertainties for the plutonium abundances are listed in Table 2.9.

The results of the study showed the least uncertainty for isotopes with the strongest gamma-ray signatures, ^{239}Pu and ^{241}Pu , and conversely poorer performance for those with lines that are weak or are obscured by overlap. The uncertainty in determining the ^{242}Pu abundance when using a correlation method was substantial, with an average

Table 2.9: Mean of the relative uncertainties (%) in isotopic measurements from the Pu-2000 exercise [89].

Isotope	^{242}Pu Provided	^{242}Pu Calculated
^{238}Pu	7.7	7.6
^{239}Pu	0.5	0.6
^{240}Pu	2.8	2.8
^{241}Pu	1.6	1.6
^{242}Pu	-	13

of 13%. This uncertainty highlights an inherent limitation in using correlation methods with mixed samples and materials of unknown origin. The uncertainty in the determination of ^{242}Pu will affect quality of the conclusions drawn from the measurements of both the isotopic abundances and the quantitative determination of the plutonium mass [90].

As discussed in Section 2.3, isotope correlations are useful in ascertaining the age of the sample and the type of reactor used to produce the plutonium. These correlations can also be used to determine the initial enrichment of the fuel, as shown in Figure 2.8. In this figure the plutonium isotopic compositions were computed using SCALE/ORIGEN-ARP [91]. The code calculates the change in fuel composition during operation, providing an averaged composition representative of a fuel assembly as a whole [92]. The results of a SCALE simulation for a BWR with 30 GWd/MTU burn-up for 1.5% to 6.0% initial ^{235}U enrichment in 0.25% steps is shown in Figure 2.8. The oval in the figure indicates the current uncertainty performance values, representing a one-sigma uncertainty in the initial enrichment of approximately 1.5%. The gray shaded circle indicates the uncertainty in the case where the concentrations of ^{238}Pu and ^{242}Pu are known to 2%, reducing the uncertainty in the initial abundance to 0.5%. Current gamma-ray detector technology does not provide the energy resolution and Compton continuum suppression required to measure ^{242}Pu . This thesis describes an effort to build a gamma detector capable of directly measuring the 44.915 keV gamma ray from ^{242}Pu .

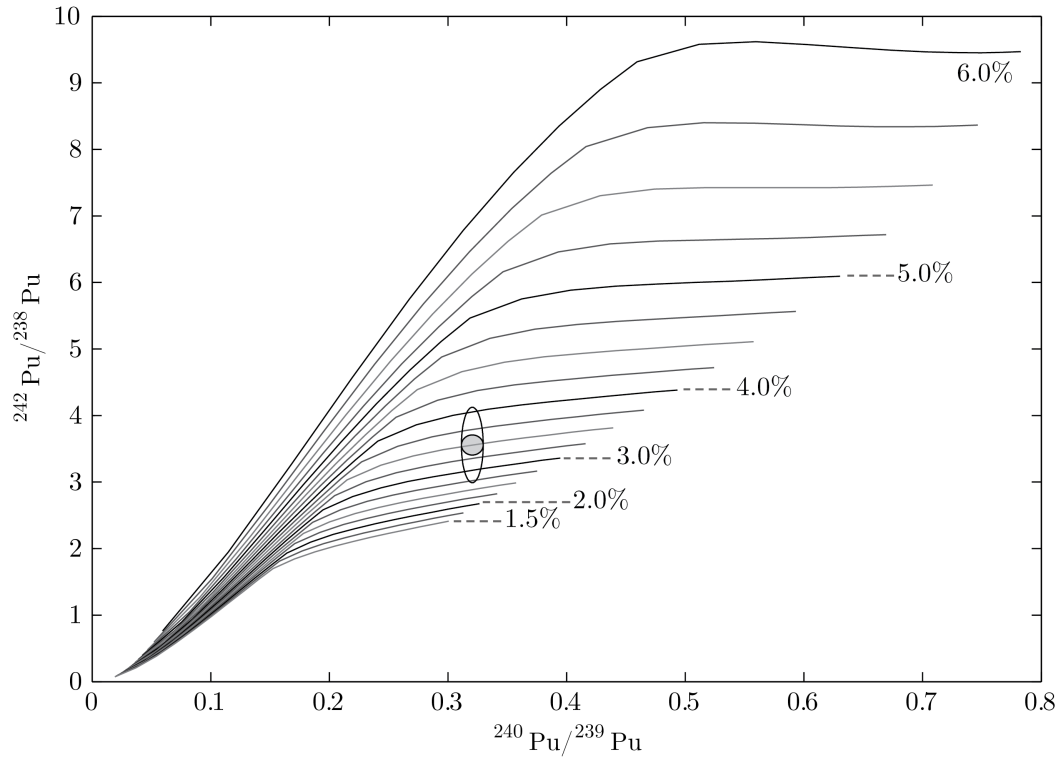


Figure 2.8: Correlation of Pu isotopes in BWR as a function of burnup for initial enrichment of ^{235}U from 1.5% to 6.0% in 0.25% steps. The oval indicates the current uncertainty for the performance values listed in Table 2.9, the shaded circle for the uncertainty in the case where ^{238}Pu and ^{242}Pu are known to 2%.

Chapter 3

Foundations

In this chapter we introduce the fundamentals of the transition-edge sensor (TES) calorimeter. After a brief summary of the relevant theoretical aspects of superconductivity, we describe the process of photon absorption and thermalization and continue with a discussion of the detector operation. Lastly we describe the fundamental sources of noise that limit the energy resolution of the sensor. This discussion provides the groundwork for the analysis in Chapter 4.

3.1 Foundations

Calorimeters are used to measure heat, either from a chemical process or a physical change in a system. TES calorimeters are a subset of these thermal sensors used to measure the temperature change resulting from the absorption of radiation. The specific design of the calorimeter must be tailored to the type of radiation of interest; however, the fundamentals of the operation are the same. In this discussion we will focus on using TES calorimeters for measuring gamma rays with energies up to 200 keV.

An ideal TES calorimeter, as shown in Figure 3.1, consists of three components: an absorber, a thermometer, and a weak thermal link. The absorber is a thermal mass at a temperature T and a heat capacity C [J/K] that absorbs and thermalizes the energy of the incident photon. Perfectly coupled to the absorber is a thermometer that measures the temperature increase. The excess heat from the absorption event is then removed through a weak thermal link with a thermal conductance G [W/K] to a heat sink. The heat sink, commonly referred to as the cold bath, is at a temperature T_b , less than T . With the excess heat removed from absorber and thermometer, the sensor cools back to the steady state temperature. Without any external power applied, the temperature of the absorber equals that of the cold bath, $T = T_b$.

For the calorimeter shown in Figure 3.1, we can express the time-dependent energy transfer in the system as

$$C \frac{dT}{dt} = E_\gamma \delta(t - t_0) - P_{\text{bath}}(T, T_b) \quad (3.1)$$

where $E_\gamma \delta(t - t_0)$ [W] is the instantaneous power deposited at time t from the absorption of a photon at time t_0 and $P_{\text{bath}}(T, T_b)$ [W] is the heat flow from the absorber to the cold bath. The functional form of $P_{\text{bath}}(T, T_b)$ is device dependent and for this simple calorimeter we will assume it varies linearly with the difference between the bath and absorber temperature.

$$P_{\text{bath}}(T, T_b) = G(T - T_b) \quad (3.2)$$

With this approximation equation (3.1) is linear and can be solved taking $t_0 = 0$ (See Appendix A.1). The temperature evolution in the absorber is given by

$$T(t) = T_b + \frac{E_\gamma}{C} e^{-t/\tau_0} \quad (3.3)$$

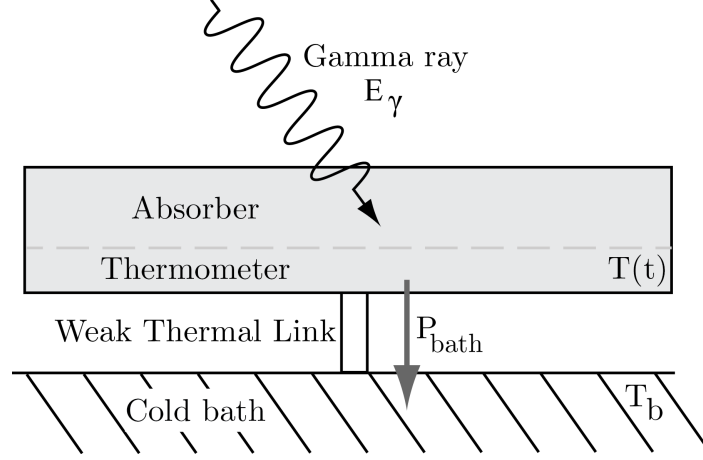


Figure 3.1: Schematic of a simple calorimeter. The energy deposited from an incident gamma ray increases the temperature of the absorber. This temperature increase is measured by a sensitive thermometer. The absorber cools via a thermal link to a cold bath.

where the steady state temperature of the absorber is T_b and the time constant $\tau_0 = C/G$. Figure 3.2 shows the thermal response of the sensor to the absorption of the photon. The absorber temperature increases $\Delta T = E_\gamma/C$ with the absorption and then cool backs to the quiescent temperature with a time constant of τ_0 . By measuring this change in temperature, ΔT , the energy of the incident photon can be determined.

We can now make a qualitative argument why thermal detectors can offer superior energy resolution. What we experience macroscopically as heat, consists microscopically of a multitude of independent lattice vibrations, termed *phonons*, that moved through the crystal lattice of the detector. If we have a detector with heat capacity C at a temperature T , the total thermal energy stored in this detector will be approximately CT . In thermal equilibrium, a phonon has an average energy of $E_{ph} = k_B T$, where k_B is the Boltzmann constant (see e.g. [93]). The average number of phonons is therefore give by $N_{ph} = \frac{CT}{k_B T} = \frac{C}{k_B}$, with a fluctuation in this number of order $\sigma = \sqrt{N_{ph}} = \sqrt{C/k_B}$. The resulting RMS fluctuations in energy therefore have a magnitude $E_{RMS} = \sigma \cdot E_{ph} = k_B T \sqrt{\frac{C}{k_B}} = \sqrt{k_B T^2 C}$. For a sensor made of 1 mm^3 tin with a heat capacity of 5.4 pJ/K at the temperature of 100 mK the limiting resolution is $\sim 25 \text{ eV}$.

3.2 Energy Thermalization in Superconductors

Radiation detection systems consist of two parts: a material to absorb the radiation and a system to measure the physical effects of the absorption. In a TES calorimeter these are the absorber and thermometer, respectively. As with all radiation detectors,

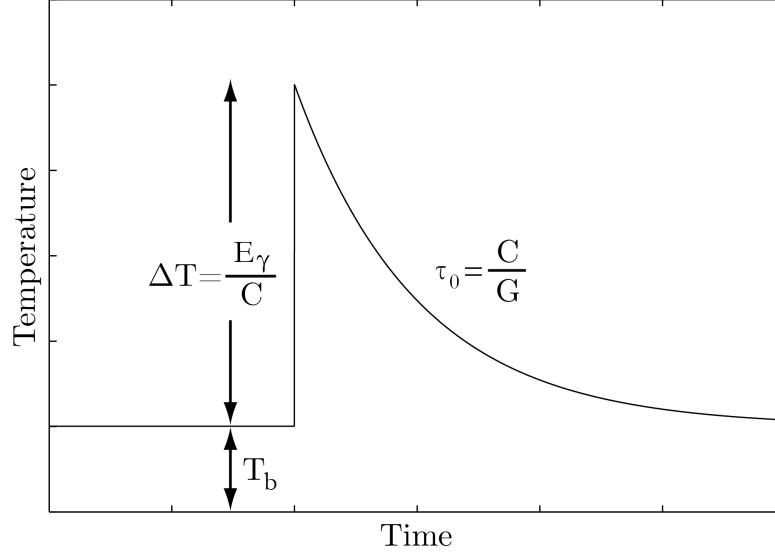


Figure 3.2: The temperature response of a TES to the absorption of a photon. The absorption of a photon will increase the temperature of the absorber by $\Delta T = E_\gamma / C$ above the quiescent temperature after which the system will cool back down with a time constant of $\tau_0 = C / G$.

the material selected for the absorber must be sensitive to the radiation of interest. The following discusses the processes governing photon absorption and thermalization in a TES calorimeter.

Photons are electrically neutral and travel some distance before interacting within a medium. This is governed by a probability of interaction per unit distance, which depends on the specific material and the energy of the photon E_γ . The principal mechanisms for interactions of photons in matter include photoelectric absorption, Compton scattering, and pair production. For photons with the energies of up to 200 keV, the dominant interactions are photoelectric absorption and Compton scattering. We discuss these two mechanisms in the following section.

3.2.1 Photoelectric Absorption

In photoelectric absorption a single photon is completely absorbed by a bound electron followed by the emission of an electron with a kinetic energy E_{e-} given by $E_{e-} = h\nu - \varphi$ where $h\nu$ is the energy of the absorbed photon and φ is the binding energy of the electron. This process is shown in Figure 3.3. The ejected electron is often from an inner shell and this vacancy is filled by a free electron in the system or from the rearrangement of the remaining bound electrons. This can result in the emission of a characteristic X-ray whose energy is equal to the difference between the initial and final electron energy levels or in the emission of an electron, referred to as an Auger electron, whose energy will be the

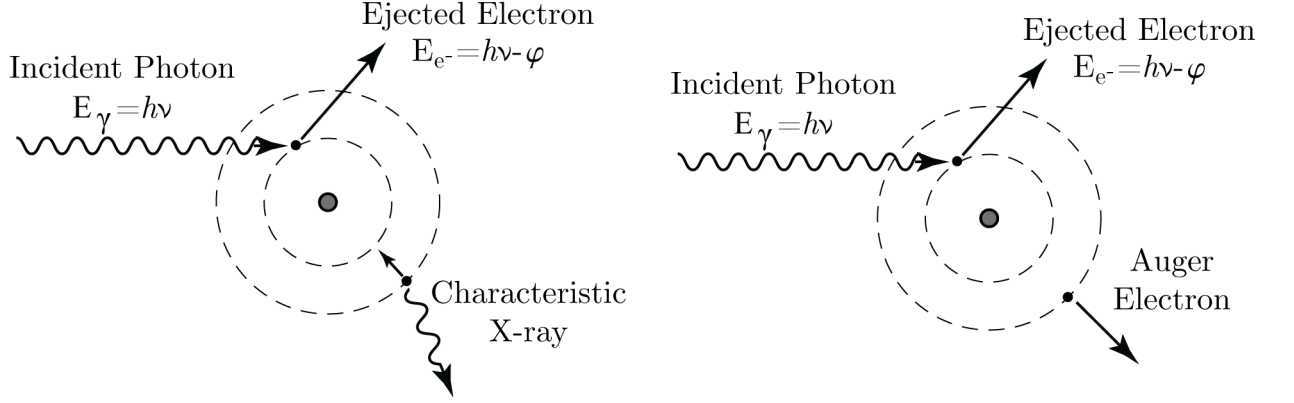


Figure 3.3: Photoelectric absorption of a photon. A single electron with binding energy φ absorbs a photon, ejecting the electron with an energy E_{e^-} . This process leaves the atom in an ionized state and will de-excite by emission of a characteristic X-ray (left) or the emission of an Auger electron (right).

difference between the original atomic excitation energy and the binding energy of shell from which the electron was ejected. The probability that a photon or X-ray will create a photoelectron is dependent on the incident energy E and the atomic number Z of the absorbing material. The probability of interaction is roughly proportional to Z^4/E^3 [94].

The photoelectron, characteristic x-ray, and Auger electron are often of energies less than a tens of keV and can travel only a short distance before being absorbed and therefore the full energy of the incident photon is deposited within the volume. However, if one of these secondary particles escapes from the absorber only a portion of the energy of the incident photon will be absorbed.

3.2.2 Compton Scattering

Compton scattering is an interaction in which a photon is scattered by an electron at rest in the rest frame of reference. This is an approximation to the scattering of a photon on an atomic electron in the limit that the photon energy is very large compared to the binding energy of the electron. This process results in a less energetic photon and a scattered free electron with kinetic energy dependent on the scattering angle, shown in Figure 3.4. The Compton scatter model of this process assumes that the electron is initially at rest and with the conservation of momentum and energy we find that the energy of scattered photon is given by

$$h\nu' = \frac{h\nu}{1 + (h\nu/mc^2)(1 - \cos \theta)} \quad (3.4)$$

and the kinetic energy of electron T_e is

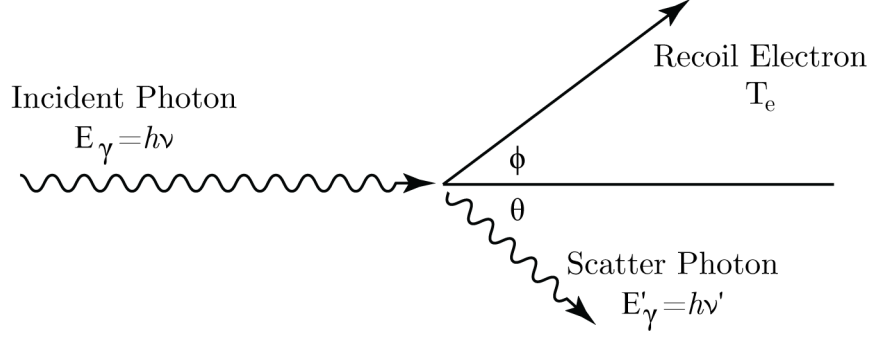


Figure 3.4: Diagram illustrating the Compton scattering of a photon on an electron. After the collision the photon is scattered at an angle θ with an energy of $h\nu'$. The electron recoils at an angle ϕ with an energy T_e .

$$T_e = h\nu \frac{1 - \cos \theta}{mc^2/h\nu + 1 - \cos \theta} \quad (3.5)$$

For small scattering angles only a small fraction of the energy is transferred to the electron. The maximum kinetic energy transferred occurs for $\theta = 180^\circ$, and from equation (3.5) we find

$$T_{e,\max} = \frac{2h\nu}{2 + mc^2/h\nu} \quad (3.6)$$

that is less than the energy of incident photon. Unless the scattered photon is subsequently absorbed, which is unlikely for small detector volumes, it will scatter out of the absorber, depositing less than its total energy. The partial energy deposition of high energy photons creates a Compton continuum in a spectrum and this low-energy background increases the difficulty in measuring low-energy photons. The contribution of Compton scatter in TES measurements is discussed in Chapter 6.

3.2.3 Thermalization

Before discussing the thermalization process in a TES, we briefly discuss the concept of superconductivity. Superconductivity is a property of certain materials that when cooled below a critical temperature T_C they enter a state of zero resistivity to direct current. Kamerling Onnes in Leiden, Netherlands first observed this phenomenon in 1911. Onnes discovered that in cooling a sample of mercury from 14K to 3K the electrical resistance would rapidly decrease to an immeasurable value [95]. The phenomenon of superconductivity is now understood to be the result of a phonon-mediated electron-electron coupling, first realized by Leon Cooper in 1956. Cooper described the interaction between a pair of electrons within Debye energy, E_D , of the Fermi surface [96], where the Debye energy is the maximum energy of a phonon in the system. Cooper found that a

Table 3.1: Material properties and characteristic decay constants for tin

Parameter	Symbol	Value
Debye energy [93]	E_D	200 K \rightarrow 17 meV
Fermi energy [93]	E_F	10.03 eV
Superconducting gap (at 0 K) [100]	Δ_0	0.58 meV
Cooper pair breaking [101]	τ_B	10 ps
Quasiparticle recombination time [102]	τ_R	\sim 1 ns

pair of electrons would be unstable in the presence of a weak attractive force and would result in the formation of a bound state whose total energy was less than the Fermi energy, $2E_F$, the energy of the highest filled electronic state in a system. Electrons in this bound pair have equal and opposite momentum and spin and are referred to as Cooper pairs. The concept of a single pair of bound electrons was expanded by Bardeen, Cooper, and Schrieffer (BCS) in 1957 whereby they were able to describe a cooperative condensation process in which many pairs of electrons of the normal Fermi sea are formed, minimizing the total energy of the system [97]. Once the electrons bind to form Cooper pairs their energy is reduced by a value Δ , resulting in a gap of 2Δ in the energy spectrum between the ground state and the lowest-lying excited states. This superconducting energy gap can be likened to the band gap found in traditional semiconductor detectors; however, 2Δ is \sim meV, several orders of magnitude smaller than that of a semiconductor band gap. As a result, once the energy of an electron is shared by the lattice in a conventional semiconductor detector, electron excitation by phonons does not occur, as the Debye energy is less than the band gap (55 meV and 1.12 eV, respectively for silicon [98]). As a result the process of energy dispersion after the initial photon interaction is different from that found in semiconductor detection systems.

Transition edge sensors operate at about 100 mK, well below the 3 K transition temperature of the tin absorber. In this qualitative discussion we summarize the photon thermalization process in superconductors found in literature [101, 104, 99, 103]. A schematic diagram of the thermalization process is shown in Figure 3.5 with important properties and time scales listed in Table 3.1. A photon is absorbed within the material on timescales less than 10 fs [103]. The energy lost through Compton scattering and photoelectric processes produce high energy electrons, $E > \sim$ keV, which decay very rapidly via electron-electron interactions, scattering several times until the energy is \sim eV. Below this energy the dominant relaxation process is through electron-phonon interactions, in which the electron transfers energy to the lattice and excites a lattice vibration (phonon). The electron energy will continue to decrease via this process, producing on average at least 15 phonons, until the energy of the electron is less than the Debye energy, E_D and is insufficient for phonon production [104]. These high energy phonons (\sim 10 meV) are not in thermal equilibrium and lose energy in the production of lower-energy phonons, propagate through the sensor to produce the measured thermal signal, or break Cooper pairs

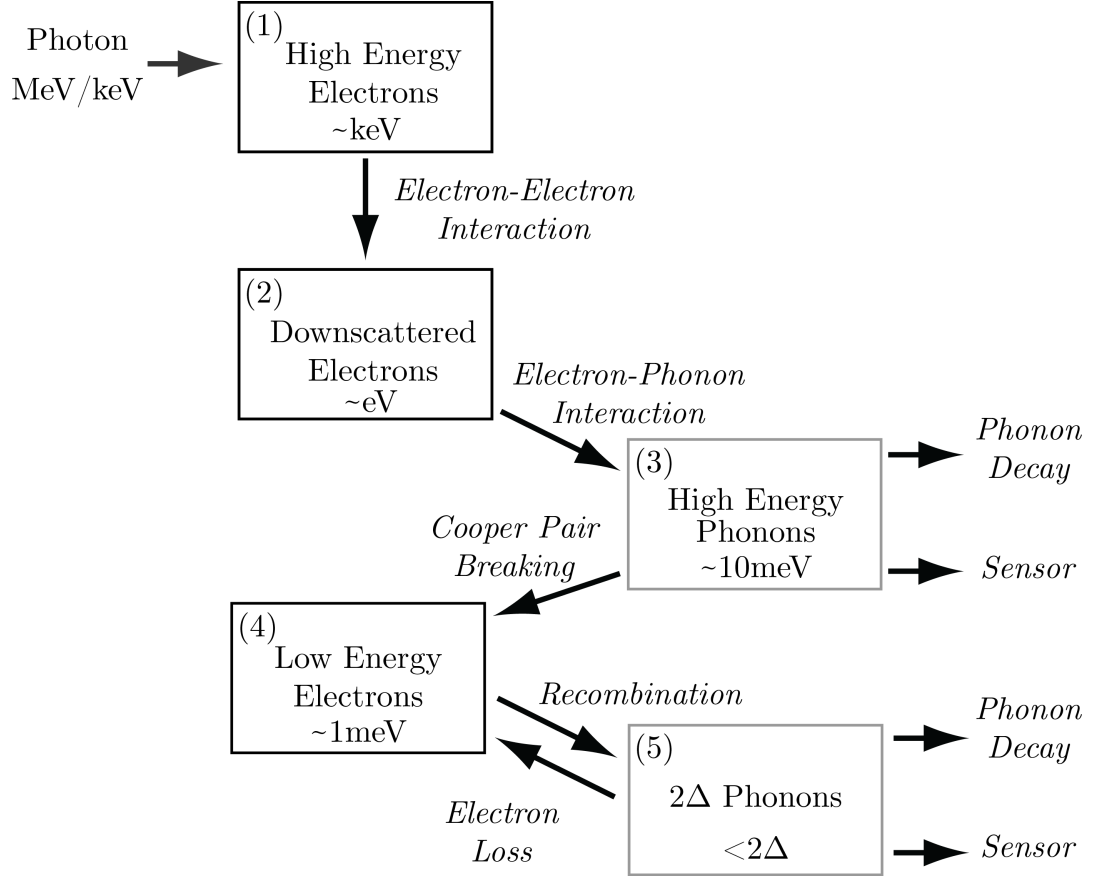


Figure 3.5: Flow chart of photon thermalization in a superconductor. The high electrons produced from photon interactions will downscatter via electron-electron interactions until reaching an energy $\sim \text{eV}$ where electron-phonon interactions will produce phonons. At energies of $\sim \text{meV}$ these phonons will break cooper pairs producing unbound electrons. The phonons that escape the material produce the thermal signal measured in the transition edge sensor [99].

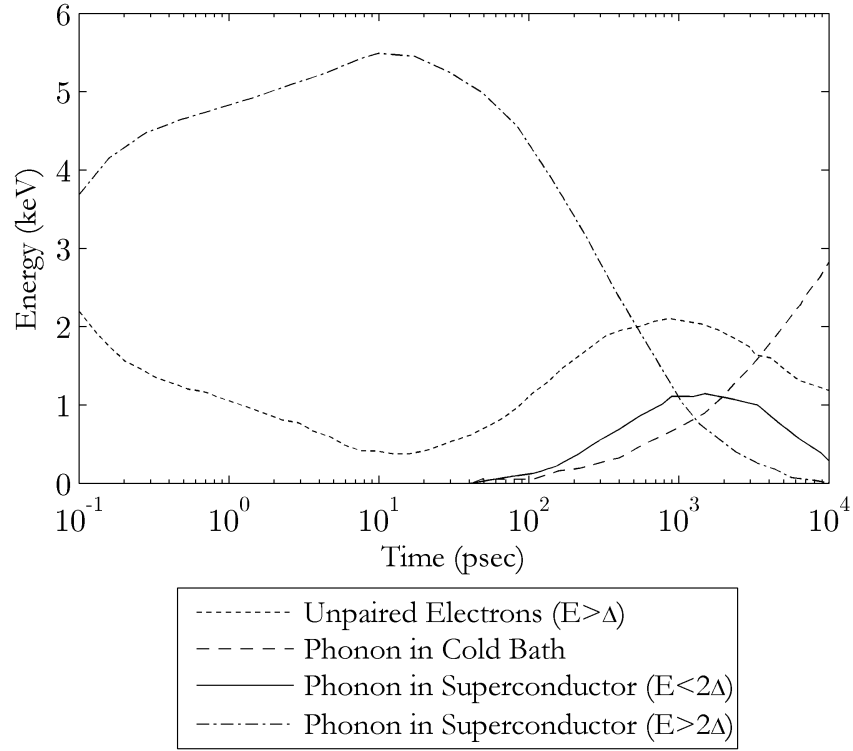


Figure 3.6: The distribution of energy in tin at $T = 0.5$ K after the absorption of a 5.89 keV photon. Within ~ 1 ns the high energy phonons and electrons have relaxed and the energy of the phonon system will escape into the cold bath [103].

adding to the population of unpaired electrons. Cooper pair breaking is only available to phonons having energies larger than 2Δ and occurs on a time scale on the order of $\tau_B \approx 10^{-10}$ s [101]. The additional unpaired electrons relax forming Cooper pairs with the emission of phonons with an intrinsic recombination time $\tau_R \approx 10^{-9}$ s [102]. As the energy of these phonons is less than the 2Δ required to break a Cooper pair, no unpaired electrons are created. Phonons that reach the material surface can traverse into the transition edge sensor, producing a thermal signal while those remaining will propagate throughout the crystal losing energy through lattice interactions, producing additional phonons. The time dependent distribution of energy in the unpaired electrons and phonon systems for a tin absorber at $T = 0.5$ K after the absorption of a 5.89 keV photon is shown in Figure 3.6. Within ~ 10 ns the energy absorbed from the incident photon is thermalized within the absorber and this added heat will increase the temperature of the TES at a rate determined by the thermal link between the absorber and transition edge sensor. For tin absorbers attached using Stycast epoxy, described in Chapter 5, the rise time of in the TES will be $\sim 100 \mu\text{s}$. Eventually the absorber-TES system will return to thermal equilibrium with the surrounding cold bath at a rate of $\tau_{\text{eq}} = C/G$, ~ 1 ms for SiN membranes [105].

3.3 Transition Edge Sensors and Electrothermal Feedback

A transition edge sensor (TES) is a thermal sensor that measures the change in temperature resulting from a photon absorption through increase of resistance in a thin superconducting material that is operated within the superconducting to normal transition. The resistance of a transition edge sensor as a function of temperature is shown schematically in Figure 3.7. The device has a normal state resistance of R_N for temperature greater than the transition temperature $T > T_C$ and zero resistance below the transition temperature. The steepness of the transition is expressed by the dimensionless parameter α , given by

$$\alpha = \frac{T}{R} \frac{\partial R}{\partial T} \quad (3.7)$$

As discussed in Section 3.1 the sensor will be in thermal equilibrium with the cold bath, $T = T_b$ and its temperature will increase with an applied power P . Transition edge sensors are operated with a bath temperature well below the transition temperature, $T_b < T_C$, and an applied power heats the sensor into the transition. To maintain the sensor at a given *bias point* within the transition a constant DC voltage is applied across the sensor. This produces a Joule heating P given by

$$P = \frac{V^2}{R(T)} \quad (3.8)$$

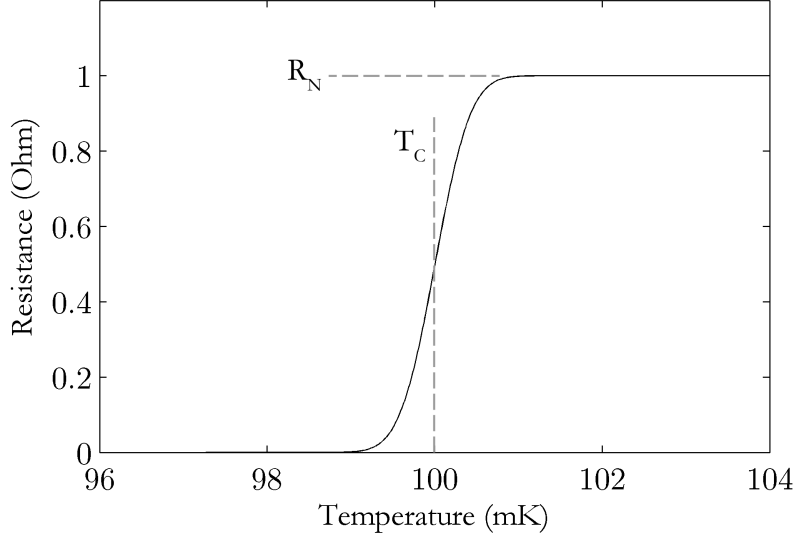


Figure 3.7: Schematic of the resistance vs temperature for a transition-edge sensor. When operated within the superconducting to normal transition a small change in temperature creates large change in resistance. Within this small range of temperatures a TES is an extremely sensitive thermometer.

and the heat flow into the cold bath is given by equation 3.2. The bias and cooling powers expressed by equations 3.8 and 3.2 are plotted in Figure 3.8. The absorption of a photon increases the temperature of the sensor, in turn increasing its resistance R . For a constant bias voltage V the joule heating decreases, lowering the temperature until it is in equilibrium with the heat loss through the cold bath. This restoring action from the change in the Joule heating is termed negative *electrothermal feedback* (ETF) [106]. With electrothermal feedback a TES is stably self-regulated within the transition.

We can now add the power contribution from electrothermal feedback into the thermal model described in Section 3.1. The heat flow P_{bath} varies with the difference in temperature between the TES and the cold bath and can therefore be written as

$$P_{\text{bath}}(T, T_b) = K(T^n - T_b^n) \quad (3.9)$$

where K is the thermal conductivity coefficient and n is a coefficient which depends on the dominant mechanism of heat transport, the geometry of the link, and the material [107]. For a TES, n is typically between 3 – 4. From equation (3.9) we define the thermal conductance G across the weak thermal link as

$$G = \frac{dP}{dT} = nKT^{n-1} \quad (3.10)$$

Substituting equations (3.9) and (3.8) into equation (3.1) gives

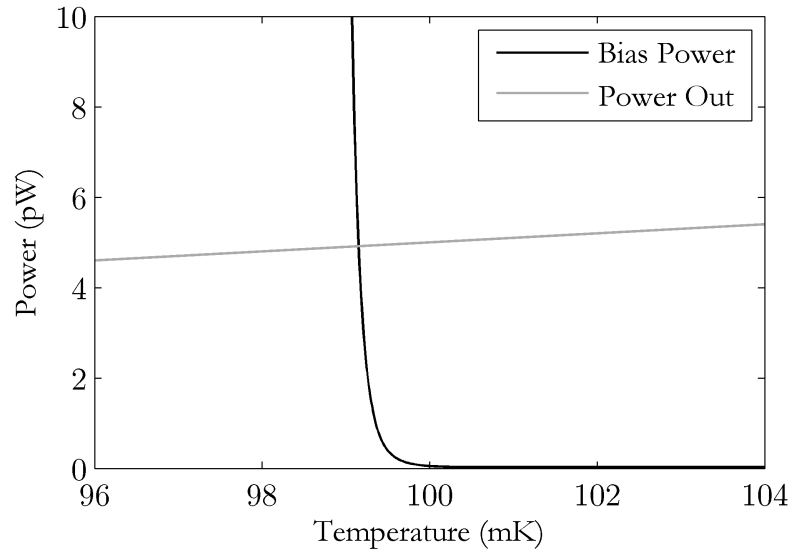


Figure 3.8: The bias power input into the TES as a function of temperature. The input power, given by V^2/R is constant above the TES transition temperature and rapidly increases as the resistance of the device decreases to zero as the temperature falls below T_C . The power dissipated through the thermal link to the cold bath varies with the difference between the sensor and bath temperature. The TES operates stably at the intersection of the input bias power and output power.

$$C \frac{dT(t)}{dt} = \frac{V^2}{R(T)} - K(T^n - T_b^n) + E_\gamma \delta(t - t_\gamma) \quad (3.11)$$

To analytically solve this non-linear differential equation (3.11) we must first linearize the system using a Taylor expansion about the equilibrium temperature. Recall that in steady state the ETF bias voltage injects a power equal to that dissipated through the weak link

$$\frac{V^2}{R} = K(T^n - T_b^n) \quad (3.12)$$

and expanding to first order in ΔT we arrive a

$$C \Delta \dot{T}(t) = \overbrace{\frac{V^2}{R} - K(T^n - T_b^n)}^0 + E_\gamma \delta(t - t_\gamma) - \frac{V^2}{R^2} \frac{\partial R}{\partial T} \Delta T - nKT^{n-1} \Delta T \quad (3.13)$$

$$= E_\gamma \delta(t - t_\gamma) - \left(\frac{V^2}{R^2} \frac{\partial R}{\partial T} + nKT^{n-1} \right) \Delta T \quad (3.14)$$

where V , R , and T are steady state values and ΔT is the variable. Using equations (3.12), (3.7), and (3.10) we find equation (3.14) can be expressed as

$$\Delta \dot{T}(t) = - \left(\frac{\alpha P}{TC} + \frac{G}{C} \right) \Delta T + \frac{E_\gamma}{C} \delta(t - t_\gamma) \quad (3.15)$$

whose solution is a decaying exponential of the same form as equation (3.3)

$$\begin{aligned} \Delta T(t) &= \frac{E_\gamma}{C} e^{-\left(\frac{\alpha P}{TC} + \frac{G}{C}\right)t} \\ &= \frac{E_\gamma}{C} e^{-\left(\frac{\alpha P}{TG} + 1\right)\frac{G}{C}t} \\ &= \frac{E_\gamma}{C} e^{-\frac{t}{\tau_{\text{eff}}}} \end{aligned} \quad (3.16)$$

where the time effective time constant is

$$\tau_{eff} = \frac{\tau_0}{1 + \frac{\alpha P}{TG}} \quad (3.17)$$

With equations (3.12) and (3.10) we can express equation (3.17) as

$$\begin{aligned} \tau_{eff} &= \frac{\tau_0}{1 + \frac{\alpha}{T} \left(\frac{K(T^n - T_b^n)}{nKT^{n-1}} \right)} \\ &= \frac{\tau_0}{1 + \frac{\alpha}{n} \left(\frac{T^n - T_b^n}{T^n} \right)} \\ &= \frac{\tau_0}{1 + \frac{\alpha}{n} \left(1 - \frac{T_b^n}{T^n} \right)} \end{aligned} \quad (3.18)$$

As α and n are positive and $T_b^n < T^n$, the decay time for a pulse will be shorter for a voltage biased sensor due to ETF, $\tau_{eff} < \tau_0$. The reduction of Joule heating from the voltage bias allows the sensor to cool more rapidly than by phonon transport through the weak thermal link itself. ETF therefore has the same effect as an additional thermal conductance in parallel with the weak link. This additional thermal conductance can be expressed by

$$G_{ETF} = \frac{\alpha P}{T} \quad (3.19)$$

while the effective ETF decay time τ_{ETF} is

$$\tau_{ETF} = \frac{C}{G_{ETF}} = \frac{C}{\frac{\alpha P}{T}} = \frac{\alpha P}{TG} \tau_0 \quad (3.20)$$

3.4 Noise Contributions

We will look at simple model of a simple TES calorimeter where all amplifier and other external noise sources are assumed to be small enough to be negligible. In this case we only have two sources of noise: Johnson noise of the transition edge sensor and phonon noise from the connection to the cold bath.

3.4.1 Phonon Noise

Phonon noise (also referred to as thermodynamic fluctuation noise) results from fluctuations in the energy content of the detector as phonons are exchanged between the cold bath and the transition edge sensor via the weak thermal link. These statistical fluctuations in energy create temperature fluctuations in the calorimeter. As the mean free path of the phonon is much larger than the length of the thermal link, the spectral density of the phonon noise is given by [108]

$$P_{ph}^2(\omega) = 2k_B (T_b^2 + T^2) G \quad (3.21)$$

where k_B is the Boltzmann constant, T is the temperature of the sensor, T_b is the bath temperature, and G is the thermal conductance between the bath and sensor.

3.4.2 Thermometer Johnson Noise

Johnson noise is caused by random fluctuations in the motion of the electrons in the TES. This motion creates fluctuations in voltage producing a variation in the measured resistance of the TES. At a temperature T , the Johnson noise in the sensor is given by [109]

$$v_{jh}^2(\omega) = 4k_B T R \quad (3.22)$$

The frequency distribution of the Johnson noise is constant (white) within the frequencies of interest for TES operation.

3.5 Intrinsic Noise and Energy Resolution

With the noise sources discussed in Section 3.4 we can now develop an analytical model to quantify the spectral distribution of noise in a transition edge sensor. We begin with equation (3.15) without the absorption of a photon

$$\Delta \dot{T}(t) = - \left(\frac{\alpha P}{TC} + \frac{G}{C} \right) \Delta T \quad (3.23)$$

substituting equation (3.19) and adding terms for the Johnson and phonon noise, equation (3.23) becomes

$$C \Delta \dot{T}(t) = - (G_{ETF} + G) \Delta T + P_{jh}(t) + P_{ph}(t) \quad (3.24)$$

For a given voltage V , the Johnson noise can be expressed as

$$P_{jh}(t) = i_{jh}(t)V \quad (3.25)$$

For noise analysis it is convenient to work in the frequency domain. Taking the Fourier transform of equation (3.24) we can solve for $\Delta \dot{T}(t)$. Recall that for a signal $x(t)$ with a Fourier transform $X(j\omega)$

$$\frac{dx(t)}{dt} \xleftrightarrow{\mathcal{F}} j\omega X(j\omega) \quad (3.26)$$

with this we can evaluate equation (3.24) to solve for ΔT

$$j\omega C \Delta T(\omega) = - (G_{ETF} + G) \Delta T(\omega) + I_{jh}(\omega)V + P_{ph}(\omega) \quad (3.27)$$

$$\Delta T(\omega) (j\omega C + (G_{ETF} + G)) = i_{jh}(\omega)V + P_{ph}(\omega) \quad (3.28)$$

Rearranging gives

$$\Delta T(\omega) = \frac{i_{jh}(\omega)V + P_{ph}(\omega)}{G_{ETF} + G + j\omega C} \quad (3.29)$$

The temperature variations $\Delta T(\omega)$ produce fluctuations in the current through the sensor. Substituting equation (3.7) and recalling $I = V/R$ we find these fluctuations are given by

$$\Delta i_{ph}(\omega) = - \frac{V}{R^2} \frac{dR}{dT} \Delta T(\omega) \quad (3.30)$$

$$= - \frac{\alpha I}{T} \Delta T(\omega) \quad (3.31)$$

Substituting equation (3.29) the current fluctuations are given by

$$\begin{aligned} \Delta i_{ph}(\omega) &= \frac{-I\alpha (i_{jh}(\omega)V + P_{ph}(\omega))}{T(G_{ETF} + G + j\omega C)} \\ &= \frac{-I\alpha \left(\frac{v_{jh}(\omega)}{R} V + P_{ph}(\omega) \right)}{T(G_{ETF} + G + j\omega C)} \\ &= \frac{-I\alpha (v_{jh}(\omega)I + P_{ph}(\omega))}{T(G_{ETF} + G + j\omega C)} \end{aligned} \quad (3.32)$$

The Johnson noise and phonon noise are the only sources of noise considered here, and since they are uncorrelated, they can be summed in quadrature to give

$$|\Delta i_{total}(\omega)|^2 = |\Delta i_{jh}(\omega)|^2 + |\Delta i_{ph}(\omega)|^2 \quad (3.33)$$

where the Johnson noise is expressed as

$$\Delta i_{jh}(\omega) = \frac{v_{jh}(\omega)}{R} \quad (3.34)$$

and the phonon noise $\Delta i_{ph}(\omega)$ is given by equation (3.32). With these terms equation (3.33) yields

$$\langle |\Delta i_{total}(\omega)|^2 \rangle = v_{jh}^2(\omega) \left| \frac{1}{R} - \frac{I^2 \alpha}{T(G_{ETF} + G + j\omega C)} \right|^2 + P_{ph}^2(\omega) \left| \frac{I \alpha}{T(G_{ETF} + G + j\omega C)} \right|^2 \quad (3.35)$$

For the phonon noise term we substitute $P_{ph}^2(\omega)$ with equation (3.21) and find

$$\langle |\Delta i_{ph}(\omega)|^2 \rangle = 2k_b (T_b^2 + T^2) G \left| \frac{-I \alpha}{(G_{ETF} + G + j\omega C) T} \right|^2 \quad (3.36)$$

and after some algebraic manipulation (Appendix A.2) we arrive at

$$\langle |\Delta i_{ph}(\omega)|^2 \rangle = 2k_b (T_b^2 + T^2) \cdot \frac{G}{V^2} \left(\frac{\alpha P}{TG} \right)^2 \left(\frac{\tau_{eff}}{\tau_0} \right)^2 \frac{1}{1 + \omega^2 \tau_{eff}^2} \quad (3.37)$$

where

$$\tau_{eff} = \frac{C}{G_{eff}} = \frac{C}{G + G_{ETF}} \quad (3.38)$$

Similarly substituting equation (3.22) into the Johnson noise is give

$$\langle |\Delta i_{jh}(\omega)|^2 \rangle = 4k_b T R \left| \frac{1}{R} + \frac{-I^2 \alpha}{(G_{ETF} + G + j\omega C) T} \right|^2 \quad (3.39)$$

and again, after some algebraic manipulation (Appendix A.2), we find

$$\langle |\Delta i_{jh}(\omega)|^2 \rangle = \frac{4k_b T}{R} \left(\frac{\tau_{eff}}{\tau_0} \right)^2 \frac{1 + \omega^2 \tau_0^2}{1 + \omega^2 \tau_{eff}^2} \quad (3.40)$$

The frequency spectrum of the signal current $\Delta I(\omega)$ can be determined by taking the Fourier transform of equation (3.14). This is evaluated in Appendix A.3 and is given by

$$|\Delta I(\omega)| = \left(\frac{1}{\tau_{eff}} - \frac{1}{\tau_0} \right) \frac{E_\gamma}{V} \frac{\tau_{eff}}{\sqrt{1 + \omega^2 \tau_{eff}^2}} \quad (3.41)$$

Table 3.2: Parameters for simplified transition edge sensor.

Parameter	Symbol	Value
Bias temperature	T	100 mK
Heat sink temperature	T_B	50 mK
Operating point voltage	V	$3 \mu\text{V}$
Absorber heat capacity	C	10 pJ/K
Thermal conductance	G	1 nW/K
Temperature sensitivity	α	190
Operating point resistance	R	0.2Ω
	n	3.2
Operating point current	I	$15 \mu\text{A}$

With these expressions we can now model the spectral response of the detector with parameters listed in Table 3.2. Figure 3.9 shows the sensor signal in comparison to the Johnson and phonon noise. The signal and phonon noise are both damped at frequencies greater than $1/2\pi\tau_{eff}$. Both the signal and phonon noise represent thermal power in the system, and although the noise component is frequency independent (see equation (3.21)), the TES response to thermal fluctuations is limited by its intrinsic time constant $1/2\pi\tau_{eff}$. As a result both the signal and phonon noise are suppressed above this frequency. The Johnson noise is suppressed by the ETF at frequencies below $1/2\pi\tau_{eff}$, and above this frequency it is given by equation (3.22).

In the following chapter we will discuss the additional sources of noise that can limit TES calorimeters from achieving this energy resolution.

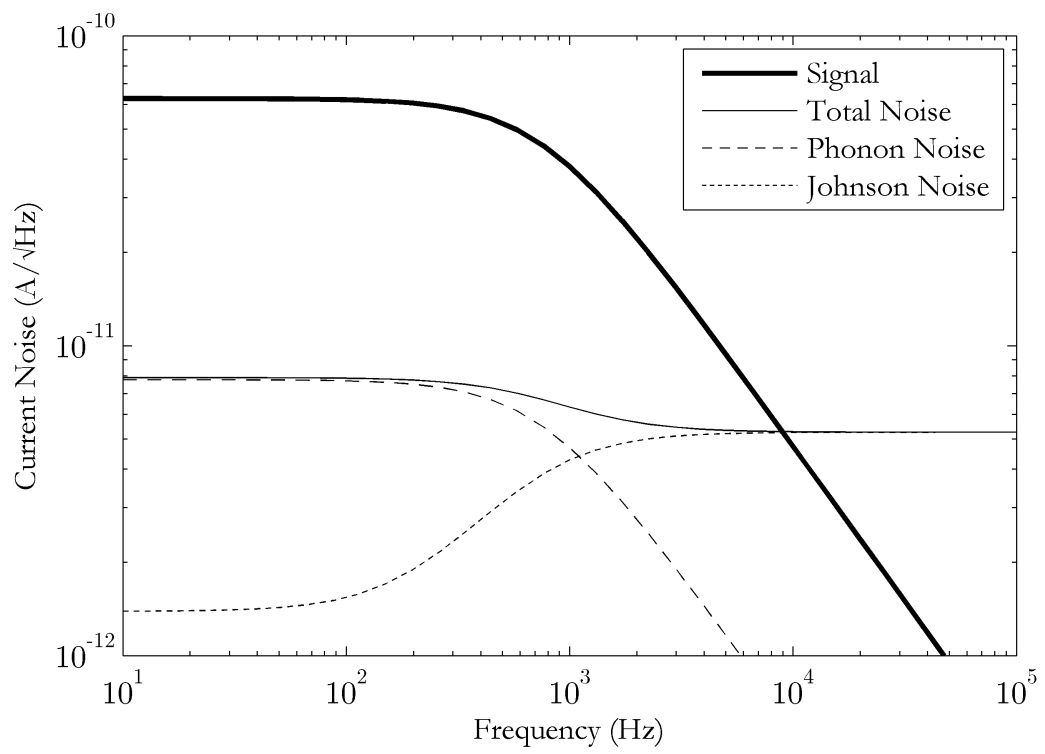


Figure 3.9: Signal and current noise of a simple calorimeter.

Chapter 4

Calorimeter Theory

The following chapter develops a comprehensive model for the response of the calorimeter and its system noise. The model presented here follows the calorimeter theory developed by Irwin [110], Lindeman [111], Figueroa [112], and Cunningham [42]. We first evaluate a basic calorimeter, which models the thermal and electrical system, and then apply the model to a sample TES. In later sections we present a complex calorimeter model that allows for variable noise sources and more accurately reproduces the noise measured in our devices.

4.1 Basic Calorimeter Theory

The following section discusses the thermal detector and its electrical bias circuit with a basic model of a TES. This model produces equations to describe the sensor response, its noise characteristics and the optimal energy resolution. Lastly, we consider these equations for typical TES parameters.

The response of the TES is governed by two coupled equations describing the thermal and electrical circuits. The schematic of the transition edge sensor and the Thevenin equivalent bias circuit is shown in Figure 4.1. The equivalent bias circuit is discussed in Appendix A.4. The electrical circuit includes a voltage bias V_{bias} , load resistor R_L , and circuit noise source v_{cn} . The thermal circuit within the calorimeter includes the absorber with heat capacity $C(T)$ at a temperature $T(t)$ connected to the cold bath at temperature T_b via a weak link with thermal conductance $G(T)$. Thermal power can be introduced into the sensor with absorption of a gamma ray P_γ or as phonon noise from the weak thermal link p_{ph} . The detector noise coupled into the electrical circuit is given by v_{dn} . The transition edge sensor is indicated as a variable resistor with a value dependent on temperature T and current I .

In this model, the bias voltage heats the absorber, and the associated bias power is dissipated through the weak thermal link. Thermal fluctuations across the weak link introduce variations in power via p_{ph} and the absorption of a photon will deposit an energy P_γ . The thermal differential equation that describes the detector shown in Figure 4.1 is

$$C(T) \frac{dT(t)}{dt} = I(t)V(t) - P_{\text{bath}}(T, T_b) + p_{ph} + P_\gamma \quad (4.1)$$

From equation (3.9) the thermal link can be expressed as

$$P_{\text{bath}}(T, T_b) = K (T^n - T_b^n) \quad (4.2)$$

The voltage $V(t)$ across the sensor is given by the bias voltage in addition to the voltage noise

$$V(t) = I(t)R(T, I) + v_{dn}(t) \quad (4.3)$$

Substituting equations (4.2) and (4.3) into equation (4.1) we find

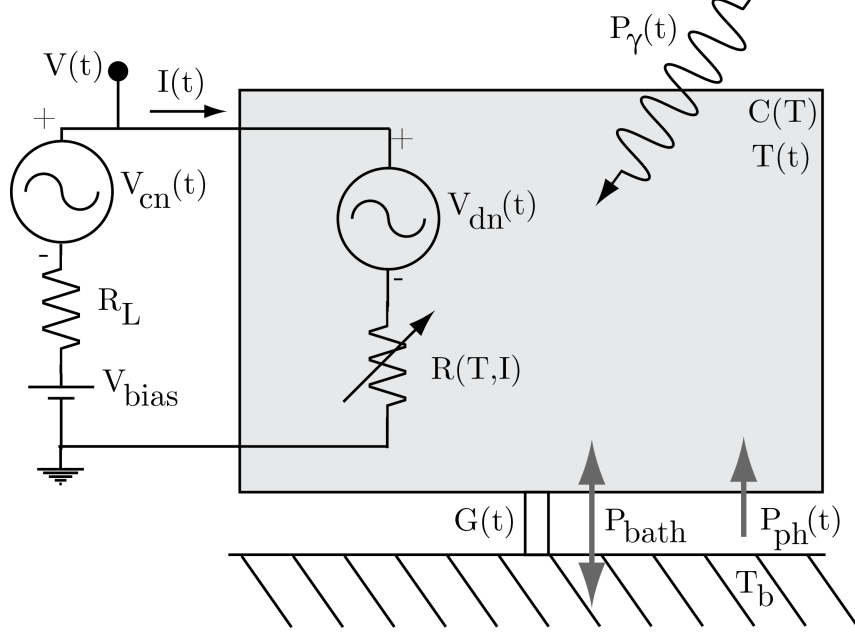


Figure 4.1: Schematic of a basic calorimeter. The electrical and thermal systems can be expressed as two coupled equations which govern the sensor response. The individual components are described in the text.

$$C(T) \frac{dT(t)}{dt} = I(t)^2 R(T, I) + I(t) v_{dn}(t) - K (T^n - T_b^n) + p_{ph} + P_\gamma \quad (4.4)$$

For the electrical equation we apply Kirchhoff's voltage law, the sum of the voltages in a closed network is zero, $\sum_k^n V_k = 0$ and find

$$\sum_k^n V_k = V_{bias} - I(t) R_L + v_{cn}(t) - v_{dn} - I(t) R(T, I) = 0 \quad (4.5)$$

Solving equation (4.5) for $I(t)$ and substituting into equation (4.4) we find

$$\begin{aligned} 0 &= V_{bias} - I(t) R_L + v_{cn}(t) - v_{dn}(t) - I(t) R(T, I) \\ &= V_{bias} + v_{cn}(t) - v_{dn}(t) - I(t) (R_L + R(T, I)) \end{aligned} \quad (4.6)$$

To solve equations (4.6) and (4.4) we must first linearize the system using a Taylor expansion. Recall that for a function of n variables $(x_1, x_2, x_3, \dots, x_n)$ the linear expansion around point $a = (a_1, a_2, a_3, \dots, a_n)$ is given by

$$f(x) = f(a) + \sum_{i=1}^n (x_i - a_i) \frac{\partial f}{\partial x_i} (a_1, a_2, \dots, a_n) + \sum_{i=1}^n O(|x_i - a_i|^2) \quad (4.7)$$

Linearizing equation (4.6) around R_0 , T_0 , and I_0 we arrive at

$$\begin{aligned}
0 = & V_{\text{bias}} + v_{cn}(t) - v_{dn}(t) - (R_L + R_0) I \\
& + \frac{\partial}{\partial I} (V_{\text{bias}} + v_{cn}(t) - v_{dn}(t) - I(t) (R_L + R(T, I))) \Big|_{\substack{I_0 \\ T_0}} \Delta I \\
& + \frac{\partial}{\partial T} (V_{\text{bias}} + v_{cn}(t) - v_{dn}(t) - I(t) (R_L + R(T, I))) \Big|_{\substack{I_0 \\ T_0}} \Delta T
\end{aligned} \quad (4.8)$$

Taking the derivatives we find

$$0 = v_{cn}(t) - v_{dn}(t) - \left(R_L + R_0 + I_0 \frac{\partial R(T, I)}{\partial I} \right) \Delta I - \left(I_0 \frac{\partial R(T, I)}{\partial T} \right) \Delta T \quad (4.9)$$

We can define the quantity

$$\alpha \equiv \frac{T_0}{R_0} \frac{\partial R(T, I)}{\partial T} \Big|_{\substack{I_0 \\ T_0}} \quad (4.10)$$

as a measure of the sensitivity of the TES resistance to changes in temperature, and introduce the β parameter, a measure of the current sensitivity at the operating point

$$\beta \equiv \frac{I_0}{R_0} \frac{\partial R(T, I)}{\partial I} \Big|_{\substack{I_0 \\ T_0}} \quad (4.11)$$

With equations (4.10) and (4.11), equation (4.9) becomes

$$0 = (v_{cn}(t) - v_{dn}(t)) - (R_L + R_0 + R\beta) \Delta I - \left(\frac{I_0 R_0}{T_0} \alpha \right) \Delta T \quad (4.12)$$

Solving equation (4.12) for ΔT we arrive at

$$\begin{aligned}
\Delta T &= \frac{T_0}{I_0 R_0 \alpha} ((v_{cn}(t) - v_{dn}(t)) - (R_L + R_0 (1 + \beta)) \Delta I) \\
&= \frac{T_0}{I_0 R_0 \alpha} (v_{cn}(t) - v_{dn}(t)) - \frac{T_0 R_0}{I_0 R_0 \alpha} \left(1 + \beta + \frac{R_L}{R_0} \right) \Delta I \\
&= \frac{T_0}{V \alpha} (v_{cn}(t) - v_{dn}(t)) - \frac{T_0}{I_0 \alpha} \left(1 + \beta + \frac{R_L}{R_0} \right) \Delta I
\end{aligned} \quad (4.13)$$

The thermal equation equation (4.4), is solved in a similar manner. Expanding about the operating point we find

$$\begin{aligned}
\frac{d}{dt} \Delta T &= \frac{1}{C} \left(I_0^2 R - K (T^n - T_b^n) + I_0 v_{dn}(t) + p_{ph}(t) + P_\gamma \right) \\
&+ \frac{1}{C} \frac{\partial}{\partial I} \left(I(t)^2 R(T, I) + I(t) v_{dn}(t) - K (T(t)^n - T_b^n) + p_{ph}(t) + P_\gamma \right) \Big|_{\substack{I_0 \\ T_0}} \Delta I \\
&+ \frac{\partial}{\partial T} \left(\frac{1}{C(t)} \left(I(t)^2 R(T, I) + I(t) v_{dn}(t) - K (T(t)^n - T_b^n) + p_{ph}(t) + P_\gamma \right) \right) \Big|_{\substack{I_0 \\ T_0}} \Delta T
\end{aligned} \quad (4.14)$$

Recall from equation (3.12) that in steady state $I^2 R = K (T^n - T_b^n)$ and evaluating

$$\begin{aligned} \frac{d}{dt} \Delta T = & \frac{1}{C} (I v_{dn}(t) + p_{ph}(t) + P_\gamma) + \frac{1}{C} \left(2I_0 R_0 + I_0^2 \frac{\partial R(T, I)}{\partial T} + v_{dn}(t) \right) \Delta I \\ & + \left(\frac{1}{C} \left(I_0^2 \frac{\partial R(T, I)}{\partial T} - K n T^{n-1} \right) \right. \\ & \left. - \frac{1}{C^2} \frac{\partial C(T)}{\partial T} \right) \bigg|_{T_0} (I_0^2 R_0 - K (T^n - T_b^n) + I_0 v_{dn}(t) + p_{ph}(t) + P_\gamma) \Delta T \quad (4.15) \end{aligned}$$

Simplifying we find

$$\begin{aligned} \frac{d}{dt} \Delta T = & \frac{1}{C} \left((I_0 v_{dn}(t) + p_{ph}(t) + P_\gamma) + ((2 + \beta) I_0 R_0 + v_{dn}(t)) \Delta I \right. \\ & \left. + \left(I_0^2 \frac{R_0}{T_0} \alpha - K n T^{n-1} \right) \Delta T \right) - \frac{1}{C^2} \frac{\partial C(T)}{\partial T} \bigg|_{T_0} (I_0 v_{dn}(t) + p_{ph}(t) + P_\gamma) \Delta T \quad (4.16) \end{aligned}$$

If we take all second order derivatives to zero and with equation (3.10) for the thermal conductance G we arrive at

$$C \frac{d}{dt} \Delta T = I_0 v_{dn}(t) + p_{ph}(t) + P_\gamma + (2 + \beta) I_0 R \Delta I + \left(\frac{I_0^2 R_0 \alpha}{T_0} - G \right) \Delta T \quad (4.17)$$

substituting $P = I^2 R$ and $V = IR$

$$C \frac{d}{dt} \Delta T = I_0 v_{dn}(t) + p_{ph}(t) + P_\gamma + V (2 + \beta) \Delta I + \left(\frac{P \alpha}{T_0} - G \right) \Delta T \quad (4.18)$$

The temperature and current of the system are linearly dependent, and therefore we substitute equation (4.13) into equation (4.18) and solve for the current. This is solved in Appendix A.5 with the result of

$$\begin{aligned} \frac{C}{G} \frac{d}{dt} \left(\Delta I + \frac{-v_{cn}(t) + v_{dn}(t)}{(R_0 (1 + \beta) + R_L)} \right) = \\ - \left(L \frac{\left(1 - \frac{R_L}{R_0} \right)}{\left(1 + \beta + \frac{R_L}{R_0} \right)} + 1 \right) \Delta I + (1 - L) \frac{v_{cn}(t)}{R_0 (1 + \beta) + R_L} \\ - \frac{v_{dn}(t)}{(R_0 (1 + \beta) + R_L)} - L \frac{(P_{ph}(t) + P_\gamma)}{I_0 (R_0 (1 + \beta) + R_L)} \quad (4.19) \end{aligned}$$

where $L \equiv \frac{P \alpha}{G T_0}$ is the low-frequency loop gain of the sensor. This equation can be solved analytically to obtain the calorimeter current response to a photon absorption. We set

all noise terms to zero and use $P_\gamma = E_\gamma \delta(t - t_\gamma)$

$$\frac{d}{dt} \Delta I = -\frac{G}{C} \left(L \frac{\left(1 - \frac{R_L}{R_0}\right)}{\left(1 + \beta + \frac{R_L}{R_0}\right)} + 1 \right) \Delta I - \frac{\alpha P}{CT_0 I_0 R_0} \frac{E_\gamma \delta(t - t_\gamma)}{\left(1 + \beta + \frac{R_L}{R_0}\right)} \quad (4.20)$$

$$= -\frac{G}{C} \left(L \frac{\left(1 - \frac{R_L}{R_0}\right)}{\left(1 + \beta + \frac{R_L}{R_0}\right)} + 1 \right) \Delta I - \frac{\alpha I_0}{T_0 \left(1 + \beta + \frac{R_L}{R_0}\right)} \frac{E_\gamma}{C} \delta(t - t_\gamma) \quad (4.21)$$

Solving for ΔI , following the same method as that in Section 3.1, we find

$$\Delta I = \frac{\alpha I_0}{T_0 \left(1 + \beta + \frac{R_L}{R_0}\right)} \frac{E_\gamma}{C} e^{\frac{-t}{\tau_{\text{eff}}}} \quad (4.22)$$

where

$$\tau_{\text{eff}} = \frac{\frac{C}{G}}{1 + L \frac{\left(1 - \frac{R_L}{R_0}\right)}{\left(1 + \beta + \frac{R_L}{R_0}\right)}} = \frac{\tau_0}{1 + L \frac{\left(1 - \frac{R_L}{R_0}\right)}{\left(1 + \beta + \frac{R_L}{R_0}\right)}} \quad (4.23)$$

This result can be compared to that derived in Section 3.3. In the limit of $\beta \rightarrow 0$ and $R_L \ll R_0$ the results reduce to those found in Section 3.3. To increase the count rate τ_{eff} should be as small as possible. As the value of β is sensor specific and not easily adjusted and $R_L/R_0 \rightarrow 0$ for voltage biased sensors, the loop gain L should be made as large as possible. The loop gain is maximized for sensors with high temperature sensitivity (large α) operated with a low bath temperature and a large bias power. The thermal conductance G should be made as large as possible; however, the phonon noise increases with the thermal conductance given in equation (3.21) and therefore G must be optimized for the desired count rate and necessary noise performance.

4.2 Noise Analysis in Frequency Domain

To calculate the noise spectrum we will follow the method introduced in Section 3.5 and continue the analysis in the frequency domain. Using equation (3.26) we take the Fourier transform of equation (4.19) and arrive at

$$\begin{aligned} \left(j\omega \frac{C}{G} + 1 + L \frac{1 - \frac{R_L}{R_0}}{1 + \beta + \frac{R_L}{R_0}} \right) \Delta I &= \left(1 - L + j\omega \frac{C}{G} \right) \frac{v_{cn}(\omega)}{R_0(1 + \beta) + R_L} \\ &\quad - \left(1 + j\omega \frac{C}{G} \right) \frac{v_{dn}(\omega)}{R_0(1 + \beta) + R_L} \\ &\quad - L \frac{P_\gamma(\omega) + p_{tn}(\omega)}{I(R_0(1 + \beta) + R_L)} \end{aligned} \quad (4.24)$$

Sensor Responsivity

The analysis of the current noise first requires the calculation of the sensor responsivity. The responsivity is the change in sensor current per absorbed signal power, and is given by [113]

$$S(\omega) = \frac{\partial I}{\partial P_\gamma} \quad (4.25)$$

With equation (4.25) we can calculate the sensor responsivity to photon absorption P_γ from equation (4.24)

$$S(\omega) = \frac{\partial I}{\partial P_\gamma} = \frac{-1}{V \left(1 + \beta + \frac{R_L}{R_0}\right)} \frac{L}{\left(1 + L \frac{1 - \frac{R_L}{R_0}}{1 + \beta + \frac{R_L}{R_0}}\right)} \frac{1}{(1 + j\omega\tau_{\text{eff}})} \quad (4.26)$$

Using the definition of τ_{eff} from equation (4.23) we find

$$S(\omega) = \frac{-L}{\left(1 + \beta + \frac{R_L}{R_0}\right)} \frac{\tau_{\text{eff}}}{\tau_0} \frac{1}{(1 + j\omega\tau_{\text{eff}})} \frac{1}{V} \quad (4.27)$$

Current Noise

We now calculate the current noise of the spectrometer. The current noise for a given noise source $n(\omega)$ is the average of the magnitude of the noise

$$\langle |\Delta I_n|^2 \rangle = \left\langle \left| \frac{\partial I}{\partial n} \cdot n(\omega) \right|^2 \right\rangle \quad (4.28)$$

With equation (4.28) the current noise for the individual sources can be calculated. First we calculate $\frac{\partial I}{\partial n}$ for each noise source.

$$\frac{\partial I}{\partial v_{dn}} = \frac{-1}{1 + \beta + \frac{R_L}{R_0}} \frac{1}{\left(1 + L \frac{1 - \frac{R_L}{R_0}}{1 + \beta + \frac{R_L}{R_0}}\right)} \frac{(1 + j\omega\tau_0)}{(1 + j\omega\tau_{\text{eff}})} \quad (4.29)$$

$$\frac{\partial I}{\partial v_{cn}} = \frac{-1}{1 + \beta + \frac{R_L}{R_0}} \frac{1}{\left(1 + L \frac{1 - \frac{R_L}{R_0}}{1 + \beta + \frac{R_L}{R_0}}\right)} \frac{(1 - L + j\omega\tau_0)}{(1 + j\omega\tau_{\text{eff}})} \quad (4.30)$$

Simplifying with equation (4.23) we arrive at

$$\frac{\partial I}{\partial v_{dn}} = \frac{-1}{1 + \beta + \frac{R_L}{R_0}} \frac{\tau_{\text{eff}}}{\tau_0} \frac{(1 + j\omega\tau_0)}{(1 + j\omega\tau_{\text{eff}})} \frac{1}{R} \quad (4.31)$$

$$\frac{\partial I}{\partial v_{cn}} = \frac{-1}{1 + \beta + \frac{R_L}{R_0}} \frac{\tau_{\text{eff}}}{\tau_0} \frac{(1 - L + j\omega\tau_0)}{(1 + j\omega\tau_{\text{eff}})} \frac{1}{R} \quad (4.32)$$

The thermal noise enters in to the model in same pathway as P_γ and we can therefore use equation (4.27) for the derivative. The current noise of each source is therefore

$$\langle |\Delta i_{tn}(\omega)|^2 \rangle = \frac{(L)^2}{\left(1 + \beta + \frac{R_L}{R_0}\right)^2} \left(\frac{\tau_{eff}}{\tau_0}\right)^2 \frac{1}{1 + \omega^2 \tau_{eff}^2} \left(\frac{P_{tn}(\omega)}{R_0}\right)^2 \quad (4.33)$$

$$\langle |\Delta i_{dn}(\omega)|^2 \rangle = \frac{1}{\left(1 + \beta + \frac{R_L}{R_0}\right)^2} \left(\frac{\tau_{eff}}{\tau_0}\right)^2 \frac{1 + \omega^2 \tau_0^2}{1 + \omega^2 \tau_{eff}^2} \left(\frac{v_{dn}(\omega)}{R_0}\right)^2 \quad (4.34)$$

$$\langle |\Delta i_{cn}(\omega)|^2 \rangle = \frac{1}{\left(1 + \beta + \frac{R_L}{R_0}\right)^2} \left(\frac{\tau_{eff}}{\tau_0}\right)^2 \frac{(1 - L)^2 + \omega^2 \tau_0^2}{1 + \omega^2 \tau_{eff}^2} \left(\frac{v_{cn}(\omega)}{R_0}\right)^2 \quad (4.35)$$

These individual noise terms can be summed in quadrature to give the total noise

$$\langle |\Delta i_{total}(\omega)|^2 \rangle = \langle |\Delta i_{dn}(\omega)|^2 \rangle + \langle |\Delta i_{tn}(\omega)|^2 \rangle + \langle |\Delta i_{cn}(\omega)|^2 \rangle \quad (4.36)$$

The noise current for a sample sensor are plotted in Section 4.4.

4.3 Noise Equivalent Power and Energy Resolution

The sensitivity of a transition edge sensor can also be expressed in terms of the noise equivalent power (NEP). The NEP is equal to the input power for which the signal-to-noise ratio is one. For a known current noise $\Delta i_n(\omega)$ and its responsivity $S_n(\omega)$, the NEP can be expressed as [114]

$$\text{NEP}(\omega) = \frac{\langle |\Delta i_n(\omega)|^2 \rangle}{S_n(\omega)} \quad (4.37)$$

The NEP for the noise sources of the basic calorimeter can be calculated using the responsivity from equation (4.27) and equations (4.33), (4.34), and (4.35). The NEP for these sources of noise are

$$\text{NEP}_{tn}(\omega) = p_{tn}(\omega) \quad (4.38)$$

$$\text{NEP}_{dn}(\omega) = \frac{1 + j\omega\tau_0}{-L} \cdot I_0 v_{dn}(\omega) \quad (4.39)$$

$$\text{NEP}_{cn}(\omega) = \frac{1 - L + j\omega\tau_0}{-L} \cdot I_0 \cdot v_{cn}(\omega) \quad (4.40)$$

The total NEP, NEP_{total} , is determined by summing the individual noise terms in quadrature. The total NEP is used to determine the limiting energy resolution that be achieved. For a signal processed using optimum (Wiener) filtering as described in Appendix C, the

theoretical resolution can be calculated by integrating the NEP over all frequencies as the following [32, 115]

$$\Delta E_{FWHM} = 2\sqrt{2\ln 2} \left(\int_0^\infty \frac{4}{\text{NEP}_{total}^2(f)} df \right)^{-\frac{1}{2}} \quad (4.41)$$

From equations (4.38), (4.39), and (4.40) we find

$$\text{NEP}_{total}^2(\omega) = p_{tn}^2(\omega) + \frac{1 + \omega^2 \tau_0^2}{L^2} \cdot I_0^2 v_{dn}^2(\omega) + \frac{(1 - L)^2 + \omega^2 \tau_0^2}{L^2} \cdot I_0^2 v_{cn}^2(\omega) \quad (4.42)$$

where $p_{tn}(\omega)$ and $v_{dn}(\omega)$ are defined by equations (3.21) and (3.22). The Johnson noise of the load resistor is given as

$$v_{cn}^2(\omega) = 4k_b T_L R_L \quad (4.43)$$

The integration of equation (4.42) is found in Appendix A.6 and results in

$$\Delta E_{FWHM} = 2\sqrt{2\ln 2} \sqrt{\frac{\tau_0 I_0}{L} \sqrt{\left(p_{tn}^2 + \frac{I_0^2}{L^2} (v_{dn}^2 + v_{cn}^2 (1 - L)^2) \right) (v_{dn}^2 + v_{cn}^2)}} \quad (4.44)$$

For the case of strong electrothermal feedback where $R_L \ll R_0$, $T_b \ll T_0$, and $L \gg 1$ the result from equation (4.44) can be simplified (See Appendix A.6) to

$$\Delta E_{FWHM} = 2\sqrt{2\ln 2} \sqrt{\frac{4k_B T_0^2 C}{\alpha}} \sqrt{\frac{n}{2}} \quad (4.45)$$

in agreement with the equation found in the literature [106].

4.4 Calorimeter Noise Example

The current noise and noise equivalent power for a basic gamma-ray microcalorimeter using typical parameters are shown in Figures 4.2 and 4.3. The values used for this example are listed in Table 4.1 and calculated in Appendix B. As with the simple calorimeter described in Chapter 3, both the signal and phonon noise are damped at frequencies greater than the thermal time constant τ_{eff} calculated from equation (4.23). At low frequencies the noise contribution from the sensor and load resistor are similar; however above $1/2\pi\tau_{eff}$ the Johnson current noise is no longer suppressed by ETF and becomes the dominate source of detector noise. From equation (4.44) the energy resolution for this example is 8.7 eV, in the case of strong ETF, where $R_L \ll R_0$ and $T_b \ll T_0$ the resolution is improved to 6.8 eV.

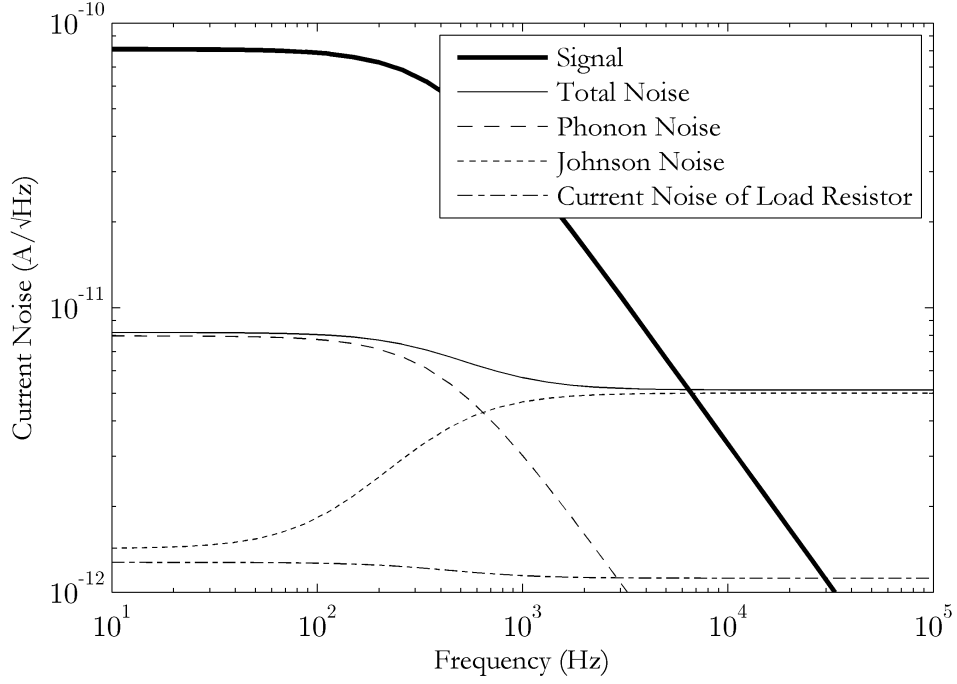


Figure 4.2: Current noise in a basic calorimeter. Sensor parameters listed in Table 4.1.

Table 4.1: Basic Calorimeter Modeling Parameters

Parameter	Symbol	Value
Bias temperature	T_0	100 mK
Heat sink temperature	T_B	50 mK
Temperature of load resistor	T_L	100 mK
Operating point voltage	V	$2.5 \mu\text{V}$
Absorber heat capacity	C	5.4 pJ/K
Thermal conductance	G	0.63 nW/K
Temperature sensitivity	α	10
Current sensitivity	β	0
Operating point resistance	R_0	0.2Ω
Load resistor	R_L	0.01Ω
Operating point current	I_0	$12 \mu\text{A}$

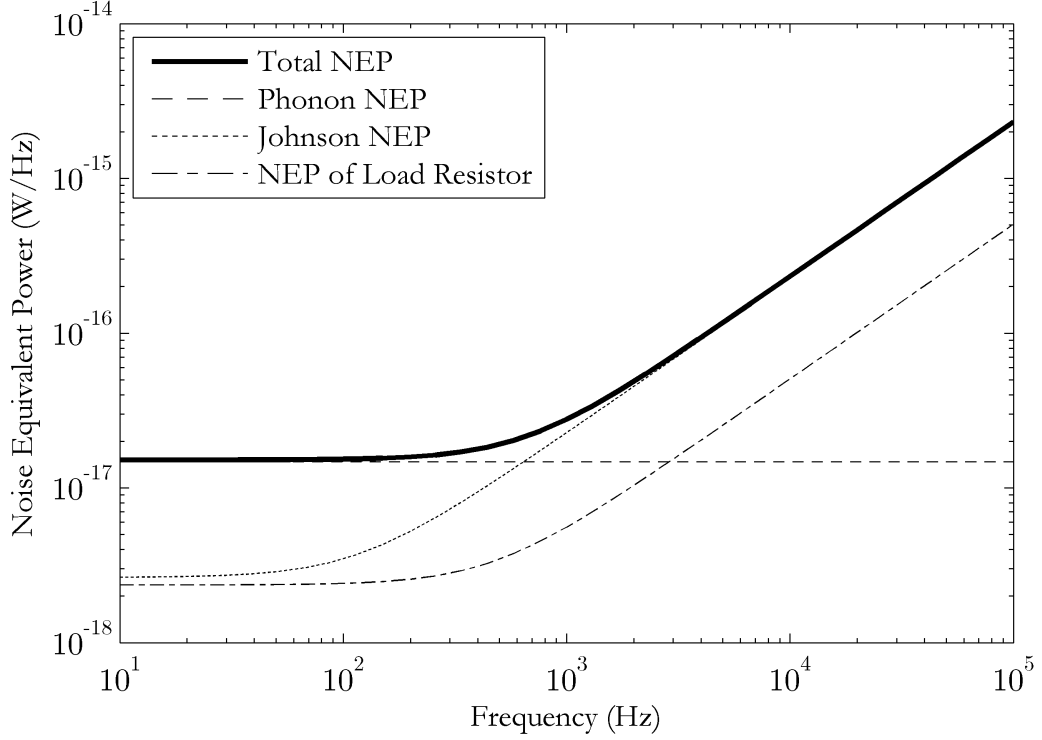


Figure 4.3: Noise equivalent power (NEP) of a basic calorimeter.

4.5 Complex Calorimeter

In the following section we improve upon the model by separating the absorber and TES sensor and divide the TES into two subsystems, one for the electron and another for the phonons of the TES. Both the electron and phonon system of the absorber are assumed to be strongly coupled and are therefore considered as one system. Each of these systems is defined by a heat capacity C and temperature T identified by a subscript. The electrical system has been improved with the inclusion of a circuit noise source I_{cn} , capacitor C_{cap} and inductor L . In most cases the capacitance C_{cap} can be neglected as the RC time constant is much faster than the L/R of the electrical circuit. Thermal energy can be deposited into each system via P_{tn} , where the subscript n is the system. The thermal subsystems are connected to one another by different thermal conductances G . The TES phonon system is connected to the cold via a thermal conductance G_{pb} . The electron system of the TES is coupled to the readout through R with a voltage noise source v_{dn} . These additional elements provide a more accurate representation of the actual system.

As with the previous sections, the electrical and thermal systems can be expressed by a set of differential equations. According to Kirchhoff's laws the current and voltage of

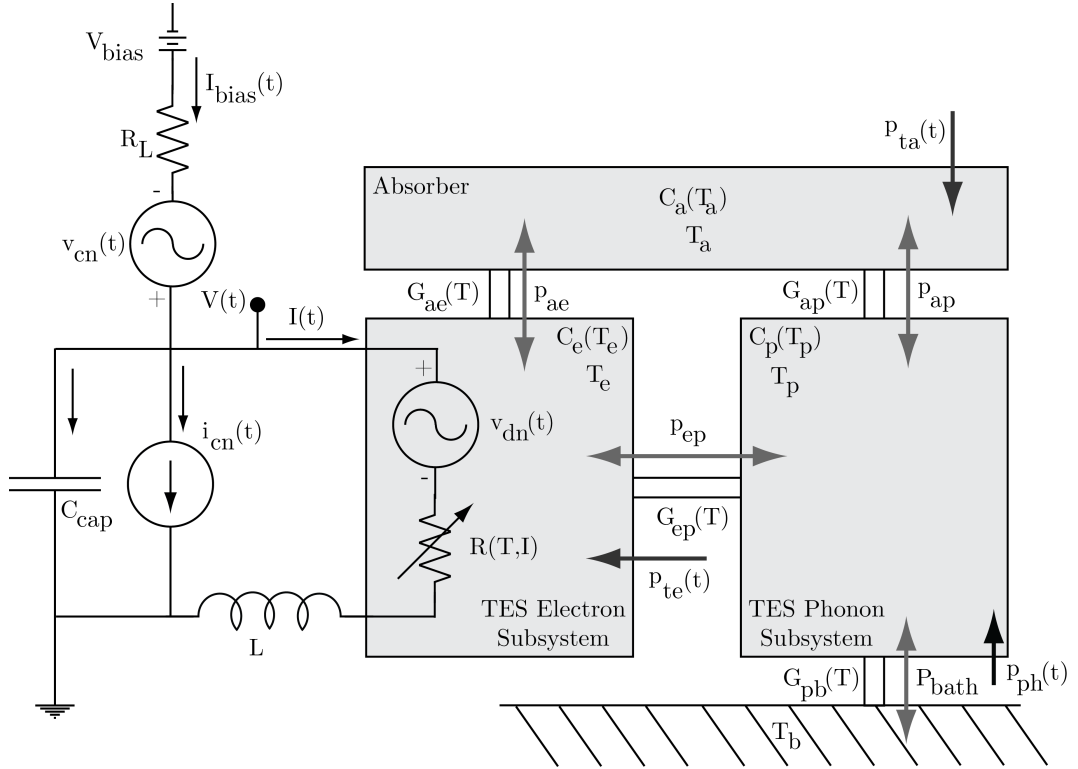


Figure 4.4: Schematic of a complex calorimeter. The sensor consists of a TES separated into a phonon and electron system with attached absorber. The bias circuit includes voltage bias V_{bias} , load resistor R_L , capacitor C_{cap} , and inductor L . The circuit voltage and current noise sources are indicated by v_{cn} and i_{cn} .

the system can be expressed as

$$L \frac{dI(t)}{dt} = -I(t)R(T, I) + V(t)R(T, I) - v_{dn}(t)R(T, I) \quad (4.46)$$

$$R_L C_{\text{cap}} \frac{dV(t)}{dt} = -R_L I(t) - V(t) + V_{\text{bias}} + v_{cn}(t) - R_L i_{cn}(t) \quad (4.47)$$

For the TES electron system, power is deposited by the bias, the voltage noise, and the thermal noise between the TES-phonon and absorber systems. The power is dissipated through the thermal links to the other systems. This can be expressed as

$$C_e \frac{dT_e(t)}{dt} = I(t)^2 R(T, I) - K_{ep} (T_e^{n_{ep}} - T_p^{n_{ep}}) - K_{ae} (T_e^{n_{ae}} - T_a^{n_{ae}}) + p_{te}(t) + I(t)v_{dn}(t) + p_{ep} + p_{ae} \quad (4.48)$$

For the TES-phonon and absorber systems, the power is exchanged between the adjacent systems via thermal links. These are given by

$$C_p \frac{dT_p(t)}{dt} = K_{ep} (T_p^{n_{ep}} - T_e^{n_{ep}}) - K_{pb} (T_p^{n_{pb}} - T_b^{n_{pb}}) - K_{ap} (T_p^{n_{ap}} - T_a^{n_{ap}}) + p_{tp}(t) + p_{ap} + p_{ep} \quad (4.49)$$

$$C_a \frac{dT_a(t)}{dt} = K_{ae} (T_a^{n_{ae}} - T_e^{n_{ae}}) - K_{ap} (T_a^{n_{ap}} - T_p^{n_{ap}}) + p_{ta}(t) - p_{ae} - p_{ap} \quad (4.50)$$

These five equations must now be expanded about the operating point (I, V, T_e, T_p, T_a). This process is the same as with the earlier sections, with the added complication of the three thermal subsystems, each with an independent temperature. In the linearization process, these temperatures must be taken into consideration when taking the derivatives. For example, the thermal conductance between the absorber and TES-phonon system is given by

$$G_{ap}^a = \left. \frac{d}{dT_a} K_{ap} (T_a^{n_{ap}} - T_p^{n_{ap}}) \right|_{T_a} \quad (4.51)$$

$$= K_{ap} n_{ap} T_a^{n_{ap}-1} \quad (4.52)$$

when taken with respect to the absorber temperature and

$$G_{ap}^p = \left. \frac{d}{dT_p} K_{ap} (T_a^{n_{ap}} - T_p^{n_{ap}}) \right|_{T_p} \quad (4.53)$$

$$= K_{ap} n_{ap} T_p^{n_{ap}-1} \quad (4.54)$$

with respect to the TES-phonon temperature. For systems at the same temperature, the values will be the same. With this notation equations (4.46)-(4.50) can be linearized and then translated into the frequency domain yielding

$$j\omega L \Delta I = -R(1 + \beta) \Delta I + \Delta V - \frac{\alpha V}{T_e} \Delta T_e - v_{dn} \quad (4.55)$$

$$j\omega R_L C_{\text{cap}} \Delta V = -R_L \Delta I - \Delta V + v_{cn}(\omega) - R_L i_{cn}(\omega) \quad (4.56)$$

$$j\omega C_e \Delta T_e = (2 + \beta) V \Delta I - (G_{ep}^e + G_{ae}^e) \Delta T_e + G_{ep}^p \Delta T_p + G_{ep}^a \Delta T_a + p_{te}(\omega) + p_{ep} - p_{ae} \quad (4.57)$$

$$j\omega C_p \Delta T_p = - (G_{ep}^p + G_{pb}^p + G_{ap}^p) \Delta T_p + G_{ep}^e \Delta T_e + G_{ap}^a \Delta T_a + p_{tp}(\omega) + p_{ap} - p_{ep} \quad (4.58)$$

$$j\omega C_a \Delta T_a = (G_{ae}^a + G_{ap}^a) \Delta T_a + G_{ae}^e \Delta T_e + G_{ap}^p \Delta T_p + p_{ta}(\omega) - p_{ae} - p_{ap} \quad (4.59)$$

Solving this set of equations algebraically would be impractical; however it can be easily converted into matrices and, for a given ω , solved analytically using a computer. The equations can be arranged in the form

$$X \Delta = N \quad (4.60)$$

where

$$X = \begin{bmatrix} R(1 + \beta) + j\omega L & -1 & \frac{\alpha V}{T} \\ R_L & 1 + j\omega R_L C_{\text{cap}} & 0 \\ -(2 + \beta) V & 0 & G_{ep}^e + G_{ae}^e - \frac{\alpha P}{T} + j\omega C_e \dots \\ 0 & 0 & -G_{ep}^e \\ 0 & 0 & -G_{ae}^e \\ & 0 & 0 \\ & 0 & 0 \\ & -G_{ep}^p & -G_{ae}^e \\ G_{ep}^p + G_{ep}^p + G_{pb}^p + j\omega C_p & & -G_{ap}^a \\ & -G_{ap}^p & G_{ae}^a + G_{ap}^a + j\omega C_a \end{bmatrix} \quad (4.61)$$

$$\Delta = \begin{bmatrix} \Delta I \\ \Delta V \\ \Delta T_e \\ \Delta T_p \\ \Delta T_a \end{bmatrix} \quad (4.62)$$

$$N = \begin{bmatrix} v_{dn}(\omega) \\ v_{cn}(\omega) - R_L i_{cn}(\omega) \\ p_{te}(\omega) - I v_{dn}(\omega) + p_{ep} - p_{ae} \\ p_{tp}(\omega) + p_{ap} - p_{ep} \\ p_{ta}(\omega) - p_{ae} - p_{ap} \end{bmatrix} \quad (4.63)$$

With equation (4.60) we can solve for Δ as

$$\Delta = N X^{-1} \quad (4.64)$$

The first parameter of interest is the responsivity. From the definition given in equation (4.25), the responsivity for a power input at location p with readout method r is given by

$$S_{r,p} = \frac{\partial \Delta_r}{\partial N_p} \quad (4.65)$$

For example, the current responsivity of the sensor to power input into the absorber is given by

$$S_{I,A} = S_{1,5} = \frac{\partial \Delta V}{p_{ta}} = \frac{\partial \Delta_1}{\partial N_5} = X_{1,5}^{-1} \quad (4.66)$$

where the subscript numbers indicate the row of interest (i.e. Row 1→Current, Row 2→Voltage,...). Similar to equation (4.28) the contribution from the noise source N to the readout R is given by

$$\langle |\Delta_r|^2 \rangle = \left\langle \left| \sum_k S_{r,k} \cdot N_k \right|^2 \right\rangle \quad (4.67)$$

Recall from equation (4.37) that the noise equivalent power for each noise term can be calculated as

$$\text{NEP}_{r,p} = \left| \frac{1}{S_{r,p}} \sum_k S_{r,k} \cdot N_k \right| \quad (4.68)$$

$$= \left| \frac{1}{S_{r,p}} \sum_k \frac{\partial \Delta_r}{\partial N_k} \cdot N_k \right| \quad (4.69)$$

as this considers only those elements of N_k for which the noise term of interest is present. For example, a current readout, $r = 1$, the NEP from the electron-phonon noise p_{ep} referred to the energy input in the absorber, $p = 5$, would be given as

$$p_{ep} = \begin{bmatrix} 0 \\ 0 \\ p_{ep} \\ p_{ep} \\ 0 \end{bmatrix} \quad (4.70)$$

$$\text{NEP}_{1,5}(p_{ep}) = \left| \frac{1}{S_{1,5}} \sum_k \frac{\partial \Delta_r}{\partial N_k} \cdot N_k(p_{ep}) \right| \quad (4.71)$$

$$= \left| \frac{1}{S_{1,5}} \left(\frac{\partial \Delta_1}{\partial N_3} p_{ep} - \frac{\partial \Delta_1}{\partial N_4} p_{ep} \right) \right| \quad (4.72)$$

$$= \left| \frac{1}{S_{1,5}} (S_{1,3} p_{ep} - S_{1,4} p_{ep}) \right| \quad (4.73)$$

As with the previous section, the total NEP is calculated by summing the individual noise terms in quadrature. With the summed NEP the energy resolution can be calculated using equation (4.41), numerical integrating over the range of frequencies.

Table 4.2: Complex calorimeter modeling parameters

Parameter	Symbol	Value
Bias temperature	T	100 mK
Temperature sensitivity	α	25
Current sensitivity	β	0
Capacitor	C_{cap}	0
Inductor	L	0
Bias Temperature	T	100 mK
Heat Sink Temperature	T_b	50 mK
Absorber Temperature	T_a	100 mK
Detector Electron System Temperature	T_e	100 mK
Detector Phonon System Temperature	T_p	100 mK
Temperature of load resistor	T_L	100 mK
Cold bath-Phonon Thermal Conductance	G_{pb}	0.62 nW/K
Electron-Phonon Thermal Conductance	G_{ep}^e and G_{ep}^p	31.2 nW/K
Absorber-Electron Thermal Conductance	G_{ae}^a and G_{ae}^e	0 nW/K
Absorber-Phonon Thermal Conductance	G_{ap}^a and G_{ap}^p	7.2 nW/K
Absorber Heat Capacity	C_a	5.4 pJ/K
Detector Electron Heat Capacity	C_e	5.1×10^{-3} pJ/K
Detector Phonon Heat Capacity	C_p	1.3 pJ/K
Operating point resistance	R	0.2 Ω
Load resistor	R_L	0.01 Ω
Operating point voltage	V_{bias}	3 μ V
Operating point current	I	15 μ A

4.6 Complex Calorimeter Noise Example

The current noise and NEP for an example complex calorimeter is shown in Figures 4.5 and 4.6. The parameters for this example are listed in Table 4.2. Similar to the basic calorimeter discussed in Section 4.4, the thermal noise between the cold bath and the sensor dominates at low frequencies and detector Johnson noise at high frequencies. The addition of the composite TES and absorber introduce noise from the TES phonon-electron and TES phonon-absorber interfaces. In the mid-frequency range the noise is dominated by these two sources. The NEP is shown in Figure 4.6, the total NEP is summed accordingly to equation (4.41) and the energy resolution for this example is 20.5 eV. The versatility of this model allows for the analysis of a multiple frequency dependent noise sources and will be used in Chapter 7 for the analysis of noise spectra from a TES operated in a liquid cryogenic dewar and pulse tube refrigeration system.

The dependence of the energy resolution on these parameters is shown in Figure 4.7. The energy resolution is normalized to the 20.5 eV for the parameters listed in Table 4.2.

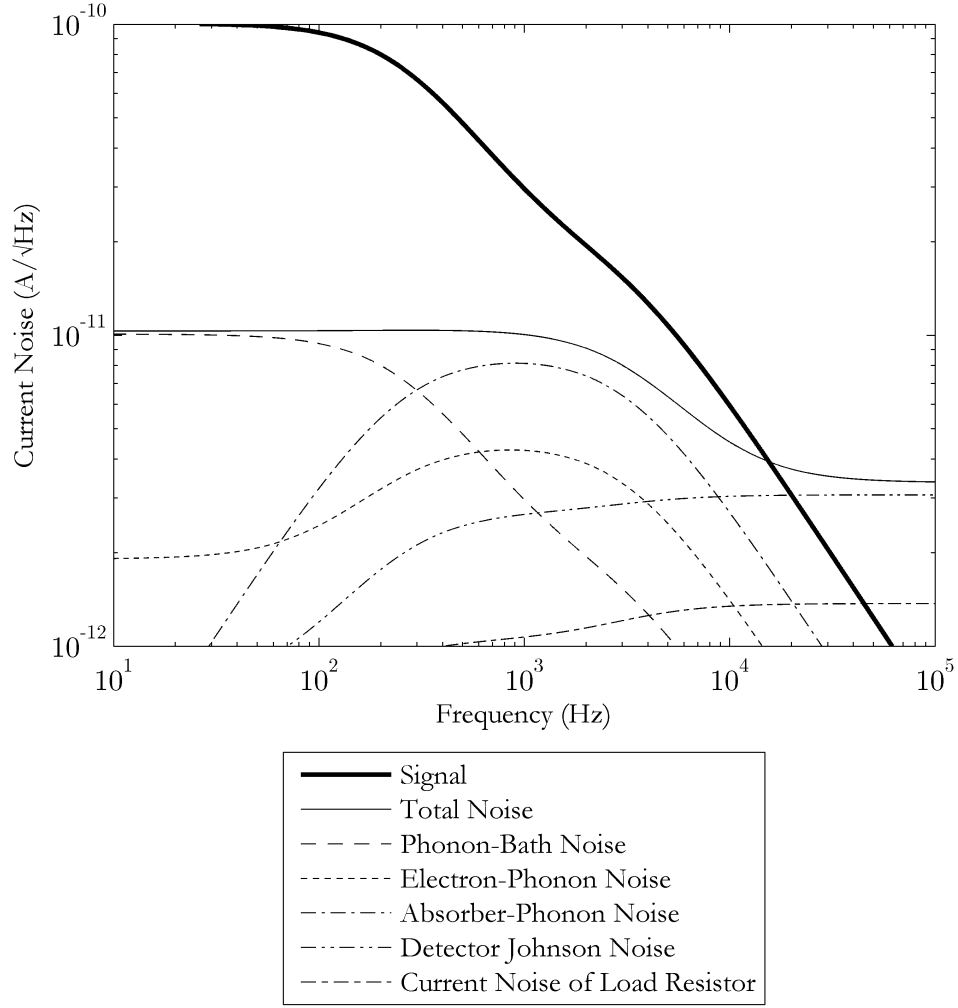


Figure 4.5: Current noise in a complex calorimeter. Sensor parameters listed in Table 4.2.

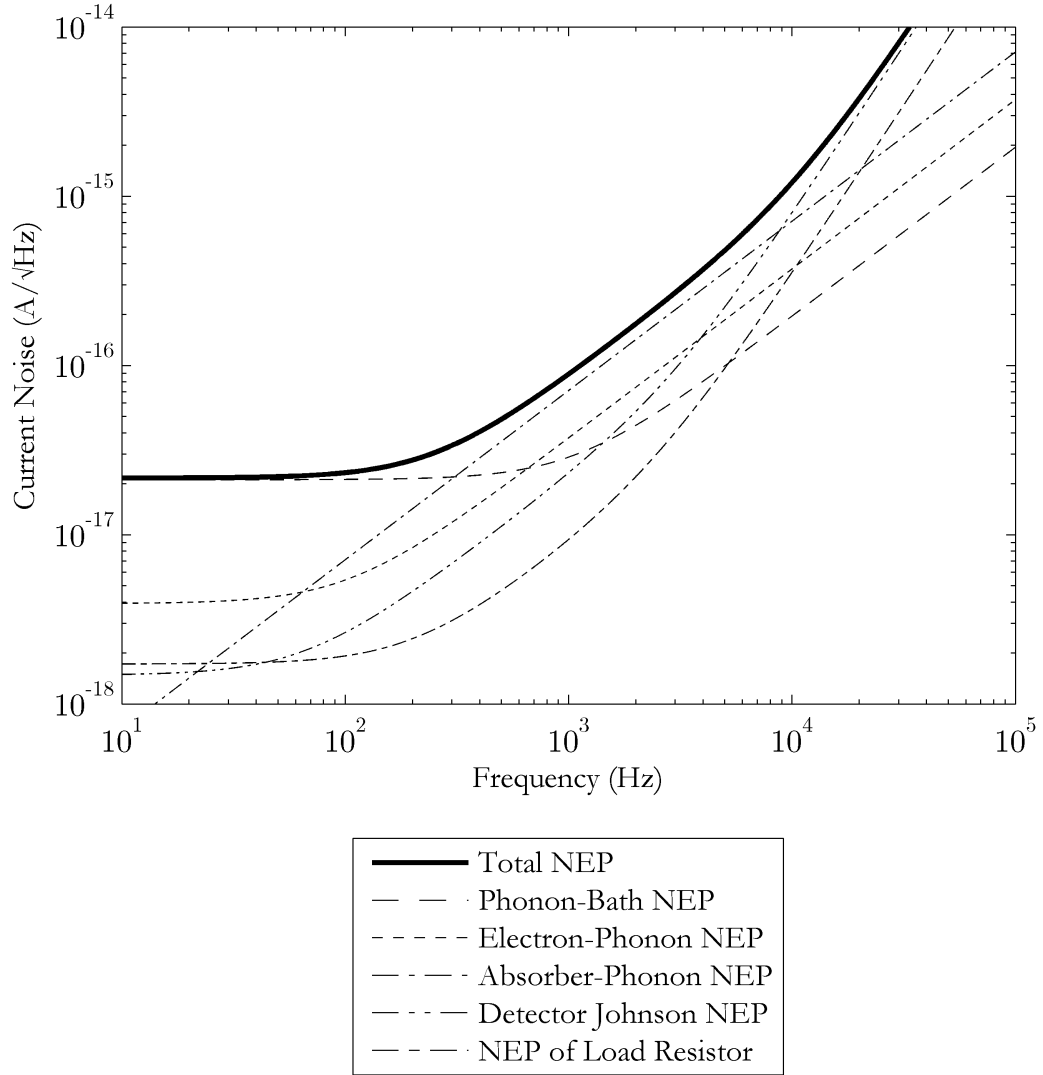


Figure 4.6: Noise equivalent power (NEP) of a complex calorimeter.

The resolution is most sensitive to variations in the absorber-phonon thermal conductance and the heat capacity of the absorber. The dependence of the absorber heat capacity and α is agreement with equation (4.45), with the energy resolution improving with decreasing C_a and increasing with α . Other parameters, such as bath temperature and TES electron-phonon thermal conductance have less of an impact on the performance of the sensor.

This model will be used to understand the performance of a TES spectrometer in Chapter 7. The remainder of this chapter will focus on assessing the feasibility of measuring ^{242}Pu with transition edge sensors.

4.7 Transition Edge Sensors for Isotopic Measurements

The following section discusses the feasibility of using transition edge sensors for measuring gamma-ray emissions from ^{242}Pu . The improved energy resolution these sensors offer in comparison to the current HPGe technology is substantial and may allow for the measurement of gamma rays that have previously been undetectable. Estimates of the noise using the complete TES model suggest that a tin based TES system can, in principle, provide an energy resolution of 50 – 90 eV, well below the line separation between ^{242}Pu gamma rays and nearest lying lines. We discuss the possibility and limitations of this measurement.

4.7.1 Sensor Performance

To estimate the sensitivity of a spectrometer, a 1 mm^3 tin absorber with an energy resolution of 100 eV at 45 keV was modeled using Geant4 [116]. The details of the modeling are discussed extensively in Chapter 6. The partial spectrum in the vicinity of the 45-keV line from decay of ^{242}Pu for a 10 mg Pu sample of 1.3% ^{238}Pu , 60.3% ^{239}Pu , 24.3% ^{240}Pu , 9.1% ^{241}Pu , and 5.0% ^{242}Pu is shown in Figure 4.8. The detection of ^{242}Pu at 44.915 keV is most affected by the close proximity of the ^{240}Pu emission line at 45.242 keV. Assuming a 24-hr data acquisition at a count rate of 10 Hz (1 detector · day), the total counts in the ^{242}Pu and ^{240}Pu peaks would be ~ 50 and 4000 counts, respectively. Although this is sufficient to detect the presence of ^{242}Pu , the limited number of counts in the peak introduces a substantial uncertainty in quantifying the ^{242}Pu concentration directly. In the following section we present a method for quantifying the statistical uncertainty of a peak measurement and estimate the uncertainty in the quantification of ^{242}Pu .

4.7.2 Quantifying Measurement Sensitivity

The following section presents a methodology to quantify the maximum precision of an isotope ratio measurement in the case where only counting statistics are considered. This fundamental statistical experimental error may be regarded as a reasonable estimate

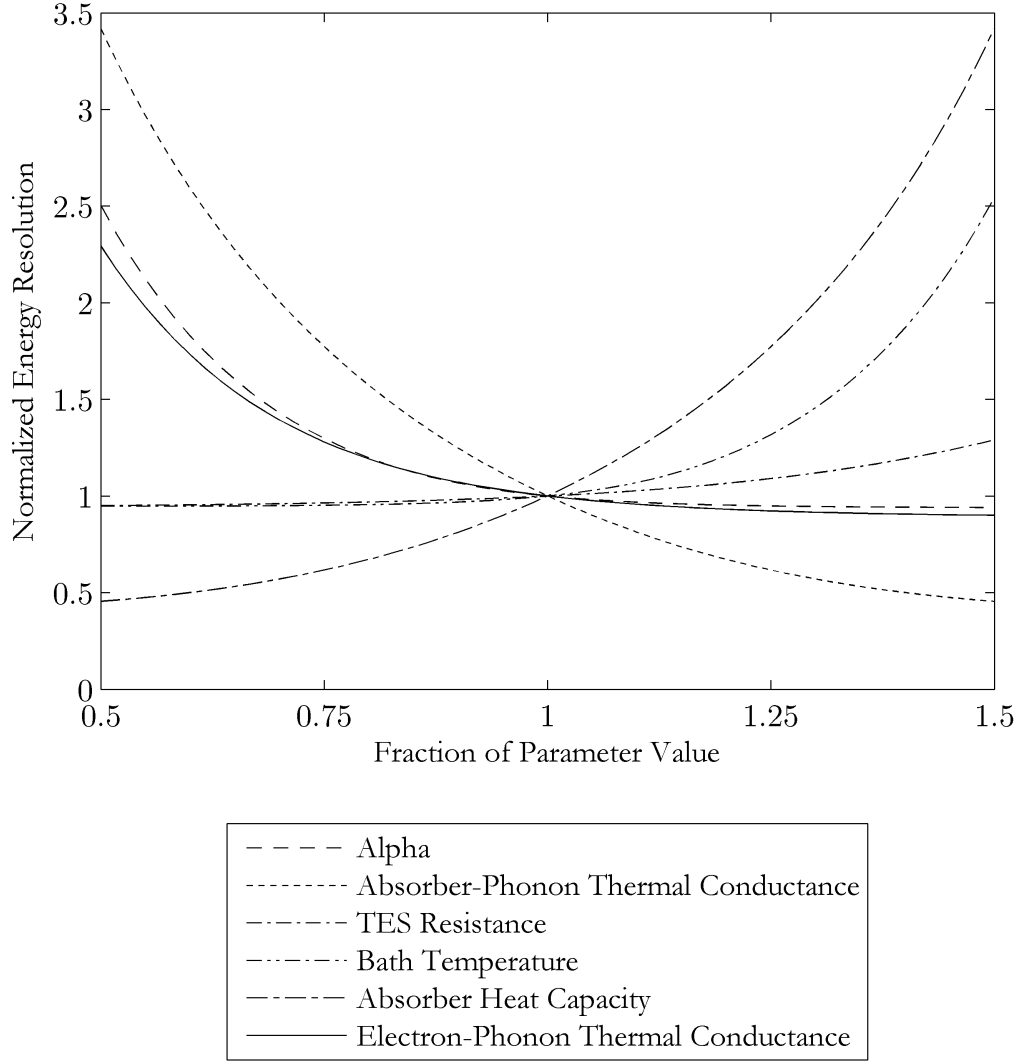


Figure 4.7: Normalized energy resolution for variations in sensor parameters. The energy resolution is most sensitive to the thermal coupling between the absorber and TES and the heat capacity of the absorber.

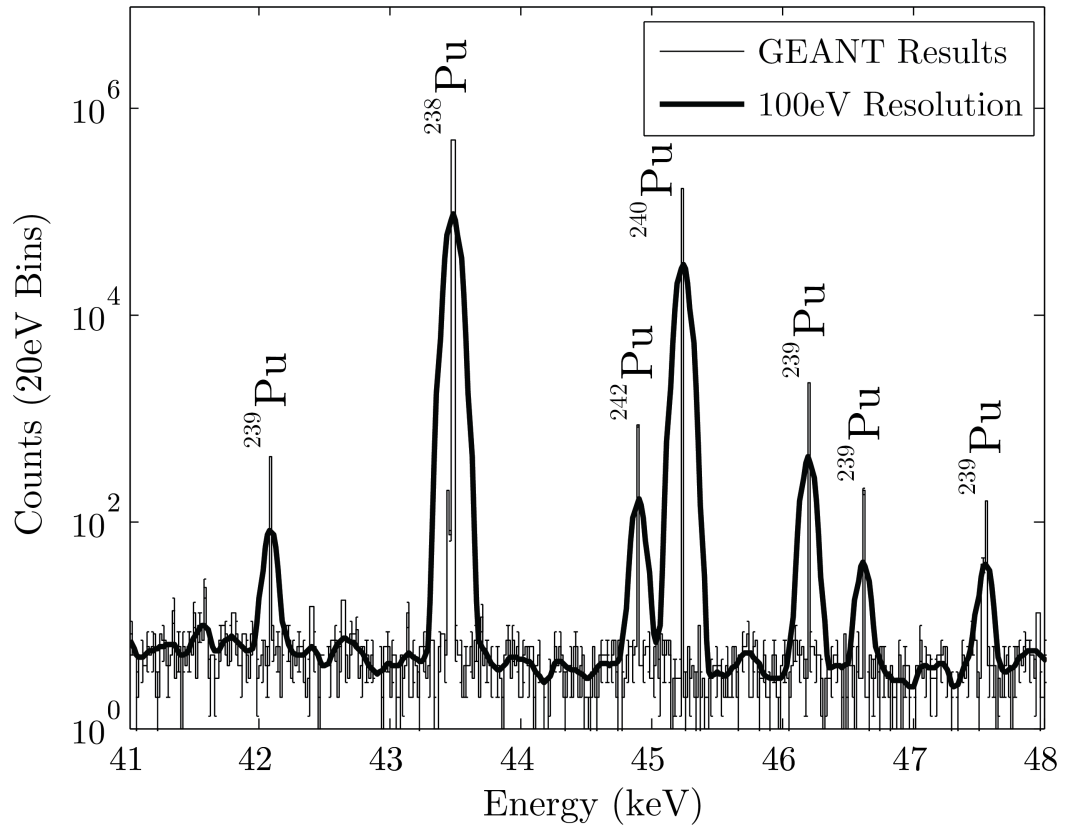


Figure 4.8: Geant4 simulation of the sensor response to a 10 mg sample of reactor grade Pu. The dark line represents the simulation results convolved with the 100 eV detector response. The ^{242}Pu line is discernible while next to the substantially stronger ^{240}Pu line.

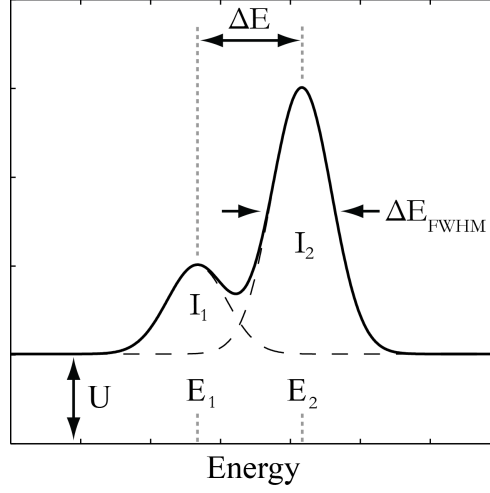


Figure 4.9: Sample case: Two γ -emissions with energies E_1 and E_2 with Gaussian width ΔE_{FWHM} and intensities I_1 and I_2 on a constant background U .

of the minimum uncertainty that can be expected. This will depend on experimental parameters which for this discussion are assumed to include the ratio of the intensities from two Gaussian shaped lines with a constant background and a detector response independent of energy. Earlier we discussed the gains in precision transition edge sensors can offer over current detection technologies; in the following section we will quantify these gains for a variety of experimental parameters, set the requirements for making a particular spectroscopic measurement and evaluate the factors limiting the accuracy of the measurement. We will use the formalism originally presented by Ryder for determining the minimum detectable mass fractions in energy-dispersive X-ray spectroscopy [117], which has recently has been applied to isotopic ratio measurements by gamma-ray spectroscopy using transition edge sensors [38] and HPGe systems [118].

To develop the analytical expressions for the line intensities and their standard deviations we consider the case shown in Figure 4.9 of two Gamma-ray emission lines at known energies E_1 and E_2 with intensities I_1 and I_2 on a constant background U (see Table 4.3). In the following discussion we define the fractional precision of a peak area σ as the one sigma estimate of the uncertainty in the net peak area divided by the net peak area I . Both these parameters are a function of the background counts per unit energy in the spectrum, the resolution of the detector, and the line separation of the interfering peaks. The analytical equations for the peak areas I_1 and I_2 are determined by least square fitting of two Gaussian curves to the observed number of signal counts N_k as shown in Figure 4.10. The mean number of expected counts in channel k is given by

$$M_k = (U + I_1 f(k\varepsilon - E_1) + I_2 f(k\varepsilon - E_2)) \varepsilon \quad (4.74)$$

where

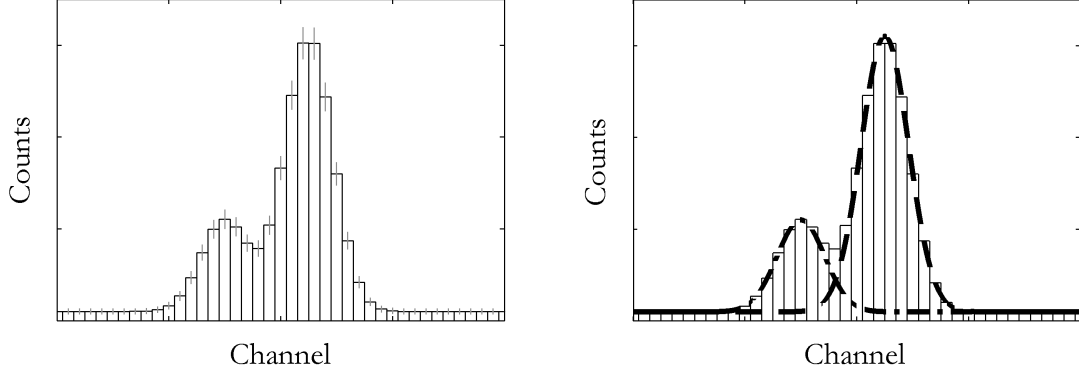


Figure 4.10: Left: A spectrum with N_k counts in channel k . The uncertainty in each channel is Poisson distributed with a standard deviation $\sqrt{N_k}$, indicated with gray vertical bars. Right: The dashed lines show the least squares fit generated using the expression in equation (4.74). The standard deviation in the total number of counts I_1 and I_2 is the total contribution from the uncertainties in each channel of the measurement.

Table 4.3: Description of symbols used for analytical peak fitting.

	Symbol	Description
Physical System	E_1, E_2	Gamma-ray energies
	ΔE	Separation between gamma-ray energies
Experimental	ΔE_{FWHM}	Detector energy resolution, 2.35σ
	k	Channel number
	N_k	Counts in channel k
	ε	Width of channel
Analytical Model	I_1, I_2	Peak areas
	σ_1, σ_2	Standard deviation
	M_k	Mean of N_k

$$f(E_i) = \frac{1}{\sigma\sqrt{2\pi}} e^{\frac{-(E-E_i)^2}{2\sigma^2}} \quad (4.75)$$

and the Gaussian width σ is assumed to be known and constant for both peaks. The quantities of I_1 and I_2 are selected to minimize the total sum of squares given by

$$T = \sum_k (M_k - N_k)^2 \quad (4.76)$$

that occurs when

$$\frac{\partial T}{\partial I_1} = \frac{\partial T}{\partial I_2} = 0 \quad (4.77)$$

The unknown intensities I_1 and I_2 can be obtained through a system of equations from applying equation (4.77) to equation (4.76). Assuming the channel bin width ε is much smaller than the detector resolution, $\varepsilon \ll \sigma$, the summations can be expressed as an integral over the two distributions and solved analytically. These are derived in Appendix E and the intensities are given by

$$I_1 = \frac{2\sigma\sqrt{\pi}}{1-b^2} (S_1 - bS_2 - (1-b)U) \quad (4.78)$$

$$I_2 = \frac{2\sigma\sqrt{\pi}}{1-b^2} (S_2 - bS_1 - (1-b)U) \quad (4.79)$$

where

$$b = e^{\frac{-(E_1-E_2)^2}{4\sigma^2}} \quad (4.80)$$

and

$$S_j = \sum_k N_k f(k\varepsilon - E_j) \quad (4.81)$$

We can now quantify uncertainty in the intensities for each peak in the fits. The standard deviation of I_1 and I_2 can be determined from equation equations (4.78) and (4.79) and recalling that for a quantity $Y(x_1, x_2, \dots)$ determined from measurements x_1, x_2, \dots the standard deviation is given by

$$\sigma^2 = \sum_i \left(\frac{\partial Y}{\partial x_i} \sigma_i \right)^2 \quad (4.82)$$

where σ_i is the standard deviation of the x_i measurement. Assuming N_k is Poisson-distributed, the standard deviation in each channel k is given by $\sqrt{M_k}$, and the total error is obtained by a summation over all channels in quadrature. Following the same approach as above (See Appendix E), we assume the channel width ε is much smaller

than the detector resolution and the standard deviation can be solved analytically and is given by

$$\sigma_1^2 = AU + BI_1 + CI_2 \quad (4.83)$$

$$\sigma_2^2 = AU + BI_2 + CI_1 \quad (4.84)$$

where

$$A = \frac{2\sqrt{\pi}}{1 - b^2} \quad (4.85)$$

$$B = \frac{2 \left(1 - 2b^{\frac{7}{3}} + b^{\frac{10}{3}}\right)}{\sqrt{3} (1 - b^2)^2} \quad (4.86)$$

$$C = \frac{2 \left(b^{\frac{4}{3}} - 2b^{\frac{7}{3}} + b^2\right)}{\sqrt{3} (1 - b^2)^2} \quad (4.87)$$

Using the equations derived above we can calculate the relative statistical error σ_1/I_1 for the measurement of the 44.915 keV lines of ^{242}Pu .

4.7.3 Direct Measurement of ^{242}Pu

Using the equations derived in the previous section we can now calculate the precision for the measurement of the 44.915-keV gamma ray of ^{242}Pu . The ^{242}Pu gamma ray is separated by 327 eV from the ^{240}Pu line at 45.242 keV. We assume an energy resolution of 100 eV and use the results of the GEANT simulation discussed in Section 4.7.1 for the values of N_{242} , N_{240} , and U .

Figure 4.11 illustrates the uncertainty in the ^{242}Pu counts as a function of the ratio of N_{242} to N_{240} for increasing number of detector days. A detector day represents the number of counts recorded in a single detector during a 24 hour period at a rate of 10 Hz or ~ 15000 counts/day. To obtain even a moderate statistical uncertainty of $\pm 10\%$ requires measurement times of one week for the single pixel detector assumed, while measurements with statistical uncertainties of a few percent, as required for many NDA applications, would require about one month of counting. Both are unacceptably long.

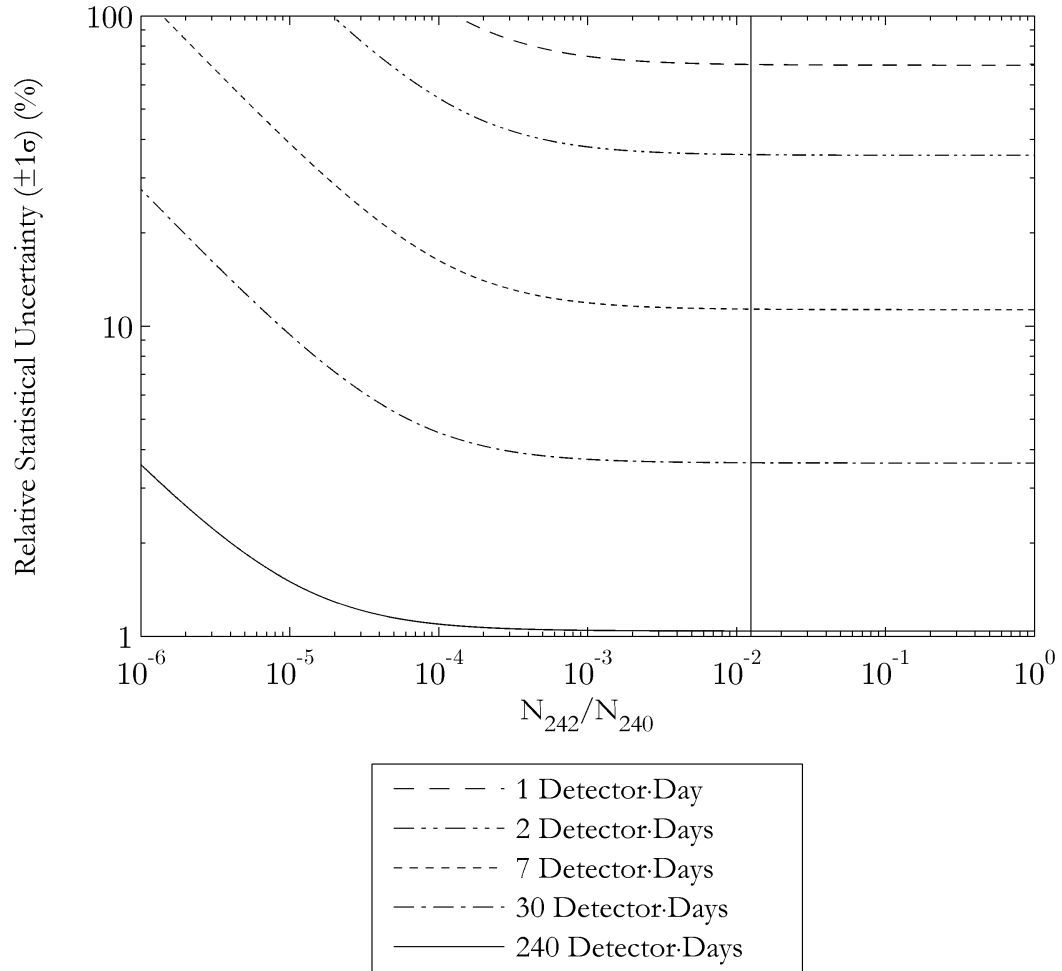


Figure 4.11: Precision of the ^{242}Pu gamma ray line at 44.915 keV as a ratio of the ^{242}Pu to ^{240}Pu counts for increasing number of detector·days. One detector·day represents the expected number of counts recorded in a single detector during a 24 hour period at a rate of 10 Hz. A background of 5 counts per channel was assumed with a detector resolution of 100 eV. The vertical line indicates the ratio of the reactor grade plutonium discussed in Section 4.7.1.

Chapter 5

Experimental Apparatus

The following chapter discusses the TES sensor fabrication and describes the cryostat used to operate the sensors at 0.1 K. The operating performance of the cryostat and the expected gamma-ray detection efficiency is also presented.

5.1 Sensor Design

In the design of a transition edge sensor we consider two important parameters which can be varied during the deposition: the thickness of the individual layers and the total thickness of the sensor. The sensor fabricated at LLNL are composed of two materials, molybdenum with a transition temperature $T_C = 0.92$ K and copper. By the proximity effect the transition temperature of the molybdenum is suppressed by the copper within a characteristic coherence length of 100 nm [119, 120]. The transition temperature of the sensor is determined by the ratio of the thicknesses of these two materials with T_C decreasing with increasing Cu thickness. A ratio of 2 nm Mo and 7 nm Cu were found to have the desired transition temperature of ~ 100 mK. For a constant ratio of Mo and Cu, T_C is independent of the total device thickness. Figure 5.1 shows the decreasing transition temperature with copper thickness and constant T_C for increasing total device thickness. The number of layers can be adjusted to set the device resistance to $1\ \Omega$ as required for use with AC biased SQUID readout systems.

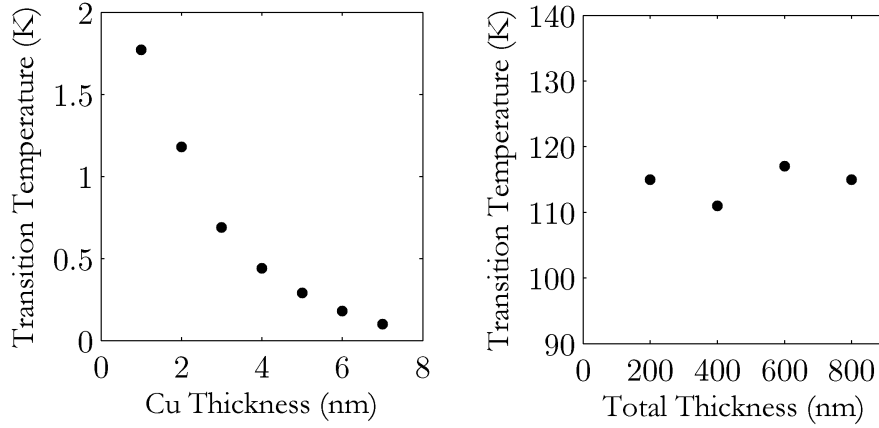


Figure 5.1: The TES transition temperature of a 2 nm Mo layer with increasing thickness of the copper layer (left) and T_C for constant Mo/Cu ratio of ratio of 2:7 with increasing total device thickness (right) [121].

5.2 Sensor Fabrication

The transition edge sensors used for this work were fabricated using standard photolithography techniques at the Lawrence Livermore National Laboratory. The fabri-

cation of a transition edge sensor begins with a 4" circular $\langle 100 \rangle$ silicon wafer. A schematic of the TES fabrication process is shown in Figure 5.4. A $0.5\ \mu\text{m}$ layer of low-stress thermally grown Si_3N_4 is formed over the entire wafer using a low pressure chemical-vapor-deposition. Measurement shown in Figure 5.2 indicate the layer is formed with a surface roughness $\sigma < 2\ \text{nm}$ RMS, necessary to ensure the sensors are uniform across the 4" wafer.

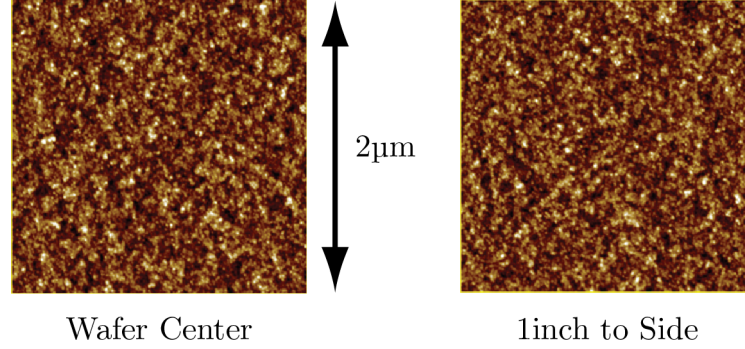


Figure 5.2: Surface roughness measurements made using a Position Sensitive Detector (PSD) on the Si_3N_4 layer. The wafer has a surface roughness of $\sigma = 0.55\ \text{nm}$ RMS, less than $2\ \text{nm}$ required for sensor fabrication.

The wafer is then coated with a positive photoresist (PR) and exposed using a mask with alignment marks for the front and the window on the back-side. The PR is then developed and the Si_3N_4 covering the Si wafer is removed using a reactive ion etch. The wafer is then placed in a wet etch solution of KOH is for several hours. This etchant preferentially etches the crystalline planes in the $\langle 100 \rangle$ Si and will preferentially create sloped side walls consisting of $\langle 111 \rangle$ planes. After the etching remains a $0.5\ \mu\text{m}$ thick SiN membrane on which the sensor will be fabricated. The thickness of this window determines the thermal conductance between the sensor and the cold bath. This is calculated in Appendix B.4 and is $0.62\ \text{nW/K}$.

The Mo/Cu layers are then deposited on the front-face of the wafer. Deposition is done using an ultra-high vacuum (UHV) sputtering system with 2 inch diameter DC magnetron sputtering targets of 99.9995% purity molybdenum and copper with the deposition pressure in the chamber maintained at 2.5 mTorr using 99.999% Ar gas. During the process 22 layers of alternating layers of 2 nm Mo and 7 nm Cu are deposited over the entire wafer, beginning with Mo as Cu does not adhere well to SiN and ending with two layers of Cu in order to protect the Mo from oxidizing. Figure 5.3 shows a cross section of a TES following the Mo/Cu deposition, the interfacial surface roughness of these layers is less than $1\ \text{\AA}$. After the multilayer deposition the wafer is coated with photoresist and patterned with the sensor mask. The excess Mo/Cu is then etched away using a strong acid solution followed by removal of the remaining photoresist. The Mo wiring layer is defined by applying a photoresist lift-off layer patterned with the wiring layer mask. After 300 nm

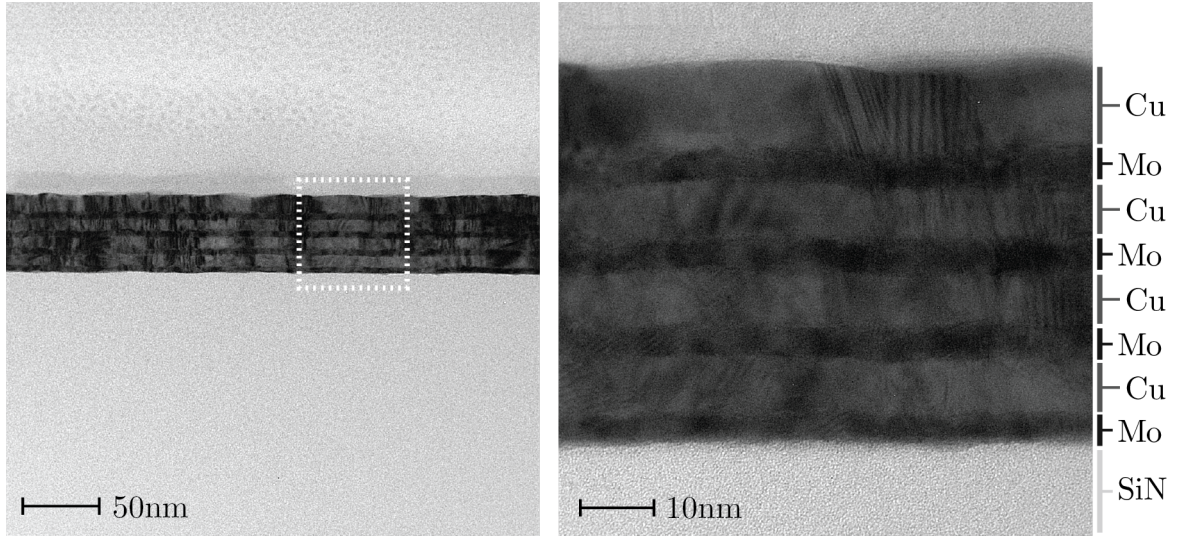


Figure 5.3: TEM image of an eight layer transition edge sensor with a 4:13 Mo:Cu ratio.

Mo layer is deposited over the photoresist the wafer is immersed in a resist stripper which leaves only the desired wiring pattern. The absorber is attached directly to the sensor by hand using a small dot of Stycast epoxy. The epoxy is ellipsoidal in shape, approximately $25\text{ }\mu\text{m}$ thick and between $100\text{ }\mu\text{m}$ and $200\text{ }\mu\text{m}$ in diameter. The variability in the cross section of the epoxy introduces an uncertainty in both the thermal conductivity and heat capacity. The range of these values are calculated in Appendix B.3 and Appendix B.2, with the thermal conductivity and heat capacity ranging from 3.1 nW/K to 12.6 nW/K , and 0.33 pJ/K and 1.32 pJ/K , respectively. Once the Stycast has cured, the sensor is ready for use, a schematic of the completed sensor is shown in Figure 5.5.

5.3 Detection Efficiency

The cryostat is optimized for gamma rays in the energy range of $5 - 100\text{ keV}$. The detector is held at 0.1 K behind four thin windows, one at 300 K , 50 K , 3 K and 0.1 K , respectively. The distance between the outermost window at 300 K and the detector is only 1 cm to ensure good solid angle coverage despite the small absorber size. The outermost window consists of $500\text{ }\mu\text{m}$ beryllium, and sets the detection efficiency at lower energies. It is designed for a transmission above 50% at 5 keV to allow measuring the actinide L X-rays in the 10 to 20 keV range. The spectrometer quantum efficiency for higher energy gamma rays is set by the thickness of the tin absorbers. Figure 5.7 shows the quantum efficiency for a $500\text{ }\mu\text{m}$ tin absorber, which is about $\sim 90\%$ in the 45 keV region for measurement of the ^{242}Pu line. Tantalum has been proposed as an absorber, and although the quantum efficiency is slightly less at 45 keV , the substantial increase in efficiency above 70 keV would be valuable for other measurements. However, tantalum




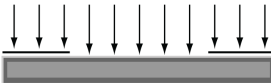


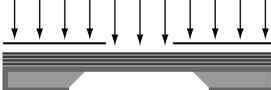


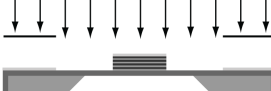



- 1  Begin with a 4" Silicon wafer, $\langle 100 \rangle$ orientation
- 2  Thermally grown SiN
- 3  Coat with photoresist
- 4  Pattern with the wiring mask
- 6  Reactive ion etch to remove SiN
- 7  Etch the Si in KOH and strip the photoresist
- 8  Deposit Mo/Cu layers over entire wafer
- 9  Cover with photoresist and pattern with the sensor mask
- 10  Etch Mo/Cu layers with 1:2:2 solution of HF:HNO₃:H₂O
- 11  Cover with photoresist and pattern with the wiring mask
- 12  Deposit 300nm Mo layer
- 13  Use lift-off to remove excess Mo
- 14  Apply dot of Stycast epoxy and attached tin absorber

Figure 5.4: Schematic of the step in TES fabrication.

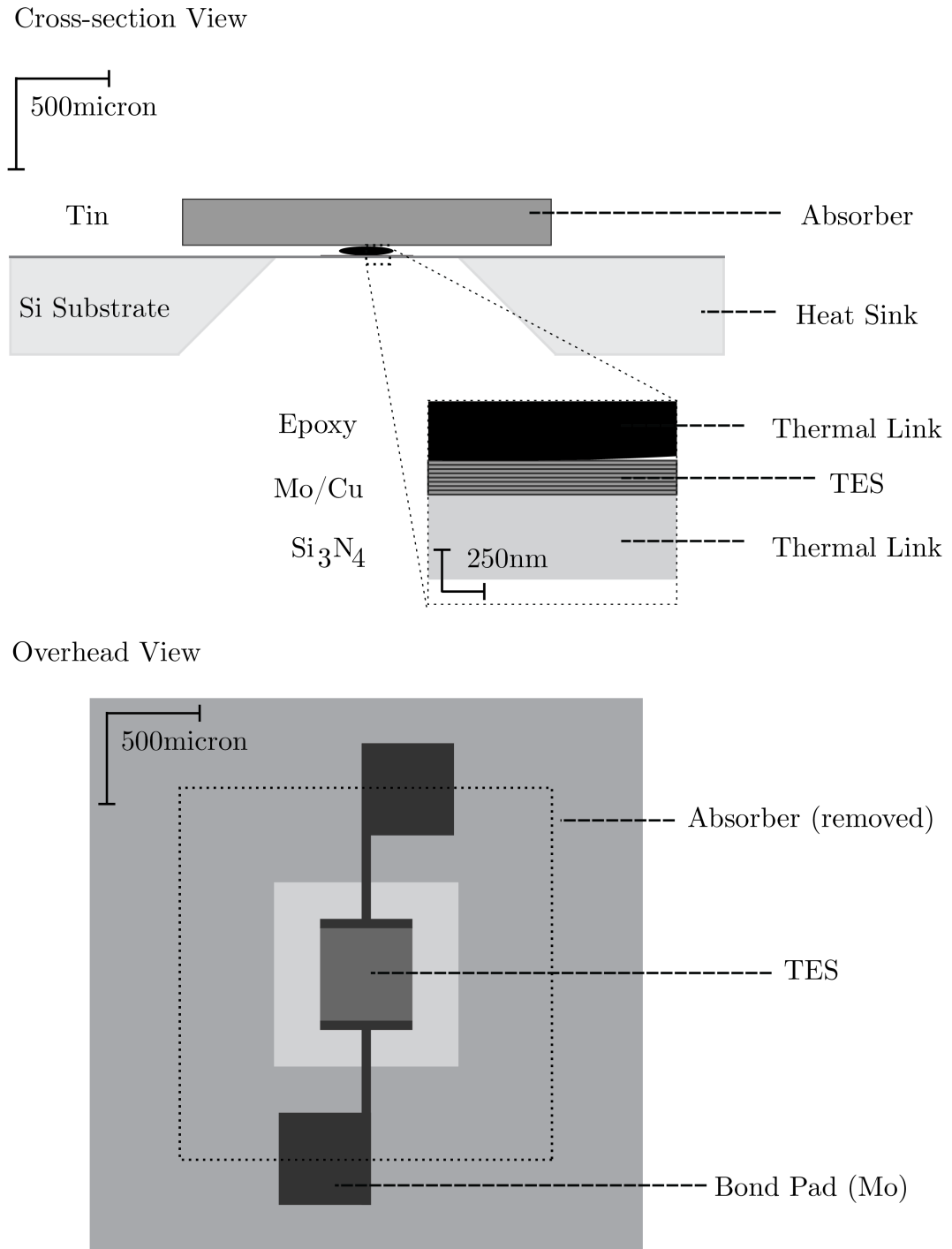


Figure 5.5: Schematic of a transition edge sensor. The cross sectional view (above) shows the TES on the thin SiN window and attached absorber. The overhead view shows the TES without attached absorber with molybdenum bond pads for wiring.

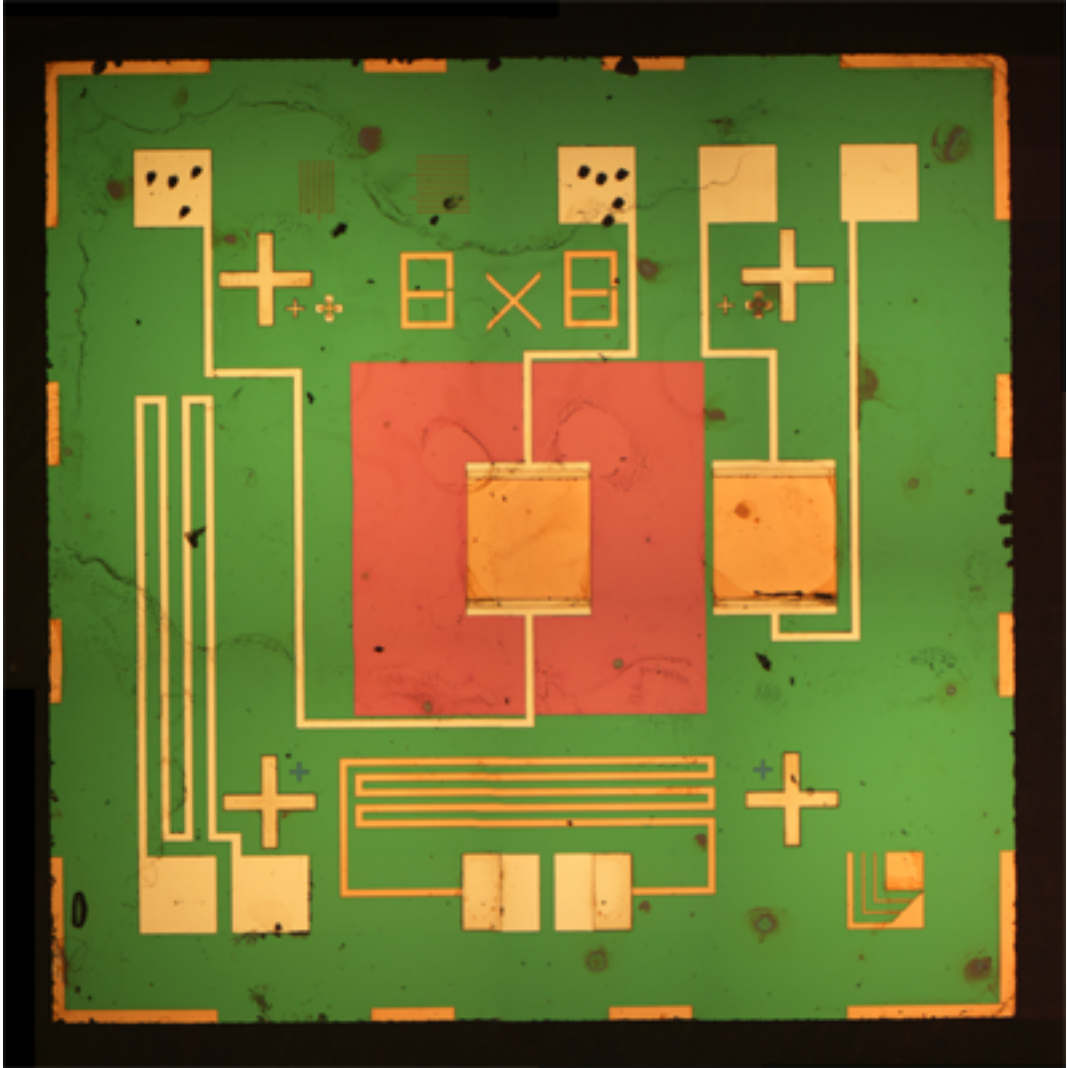


Figure 5.6: Optical micrograph of a transition edge sensor. At the center of the image is the TES on a SiN window, to the right is a TES with no window. The wiring patterns to the left and below center are for testing the deposition process.

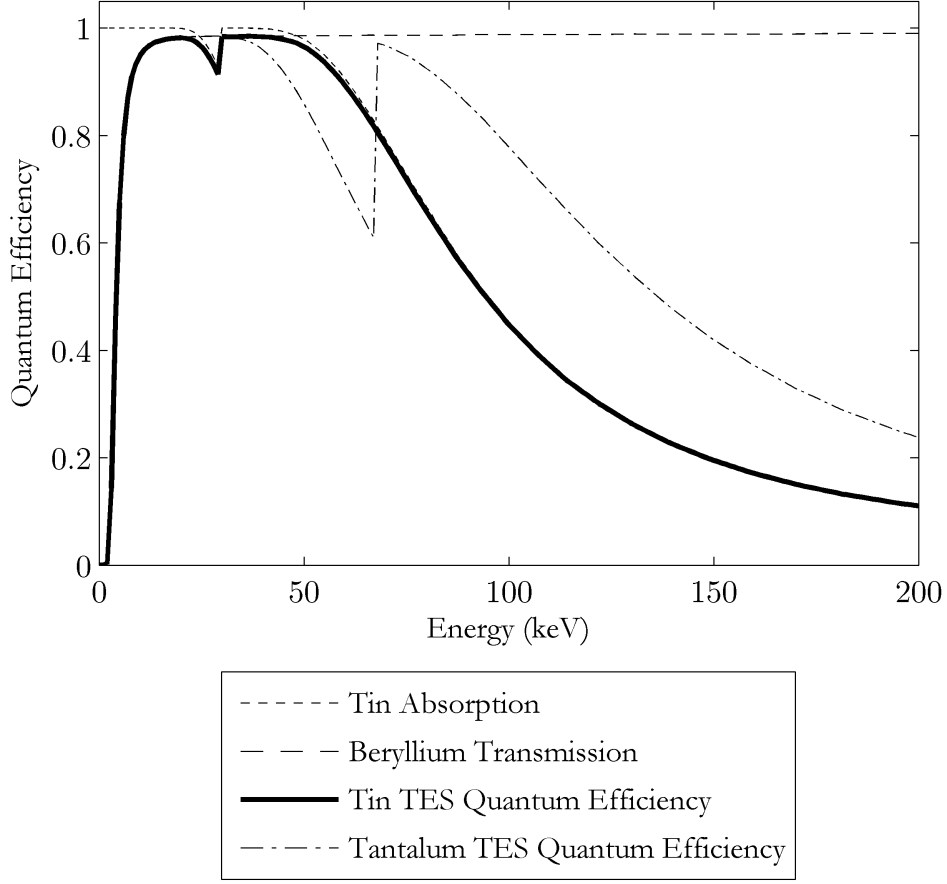


Figure 5.7: Quantum efficiency of transition edge sensor and cryostat. The quantum efficiency of the TES spectrometer with tin absorber is set by the Be window transmission at low energies, and by the absorption of the tin at high energy.

based gamma-ray TESs have not worked due to a large secondary decay time. Neither have any other absorber materials other than tin.

5.4 Cryostat Design

Transition edge sensors require a temperature ~ 100 mK for operation. Typically, this involves a precooling stage to ~ 4 K and a low temperature stage to $\lesssim 0.1$ K. Traditionally, precooling is provided by liquid nitrogen (LN_2) and liquid helium (LHe). Recently pulse tube refrigerator (PTR) have been used to provide mechanical cooling to temperatures of approximately 3 K. Both methods of precooling use a refrigeration method called adiabatic magnetization refrigeration (ADR) to reach temperatures below 100 mK. The

following discusses the operation and performance of the precooling systems and adiabatic magnetization refrigeration systems.

Earlier device characterization was performed in a liquid cryogen system. A schematic of this cryostat is shown in Figure 5.8. The system consists of three nested vessels at a temperature of 300 K, 77 K, and 4.2 K. The outermost vessel is at room temperature (300 K shield), and serves as the vacuum enclosure insulating the inner vessels. Inside is the first cold vessel (77 K shield) cooled by a liquid nitrogen tank to $T \sim 77$ K. The next vessel (4 K shield) is cooled to $T \sim 4.2$ K by a liquid helium tank. Within the liquid helium tank is volume designed to accommodate the 5T superconducting magnet and its magnetic shielding for the ADR described in Section 5.4.2. Attached to the ADR stage is the 100 mK coldplate with a detector cold finger which brings the TES closer to thin beryllium windows, increasing the solid angle coverage of the source.

5.4.1 Two-stage pulse tube refrigerator

Cooling to a temperature of ~ 3 K is achieved with a two-stage pulse tube refrigerator (PTR). Similar to the Stirling or Gifford-McMahon cryocoolers, pulse tube refrigerators use the compression and expansion of He gas to achieve cooling [122]. The main advantage of the pulse tube refrigerator over other forms of mechanical cooling is the absence of any moving components, such as the rotary valve, in direct contact with the cold stage. This substantially reduces the vibrations at the low temperature detector stage and the associated microphonic noise [123]. The two main elements of a PTR are a thin walled tube with heat exchangers located at each end and a thermal regenerator. A schematic of a PTR is shown in Figure 5.9. Additionally, a free running compressor is required to provide a continuous high and low gas pressure with a rotary valve generating pressure oscillations within the pulse tube [124]. The regenerator and heat exchangers provide thermal coupling for the working gas to the environment, while the gas inside the pulse tube is thermally isolated and therefore has a temperature that varies with pressure. The cooling is generated by the smooth and periodic pressure variations displacing the ^4He working gas in the pulse tube. By adjusting the impedance connecting the reservoir to the pulse tube and the size of the reservoir, the phase between the pressure wave from the rotary valve and the gas velocity in the pulse tube is optimized for maximum cooling efficiency [107]. In the following we will present a qualitative discussion of the thermodynamic processes for cooling in a PTR.

The cooling process in the PTR occurs in two steps, a compression and an expansion phase. The temperature evolution of gas within the PTR during these steps is shown in Figure 5.10. During the compression step the rotary valve connects the system to the high pressure output of the compressor. The heat of compression Q_0 is removed from the compressor by a heat exchanger. Inside the PTR the pressure in the pulse tube increases from the low pressure p_L to a higher pressure p_H . With the pressure in the He reservoir close to the average pressure in the system, the gas is driven from the pulse tube towards the reservoir. This compresses the gas adiabatically and results in a temperature increase.

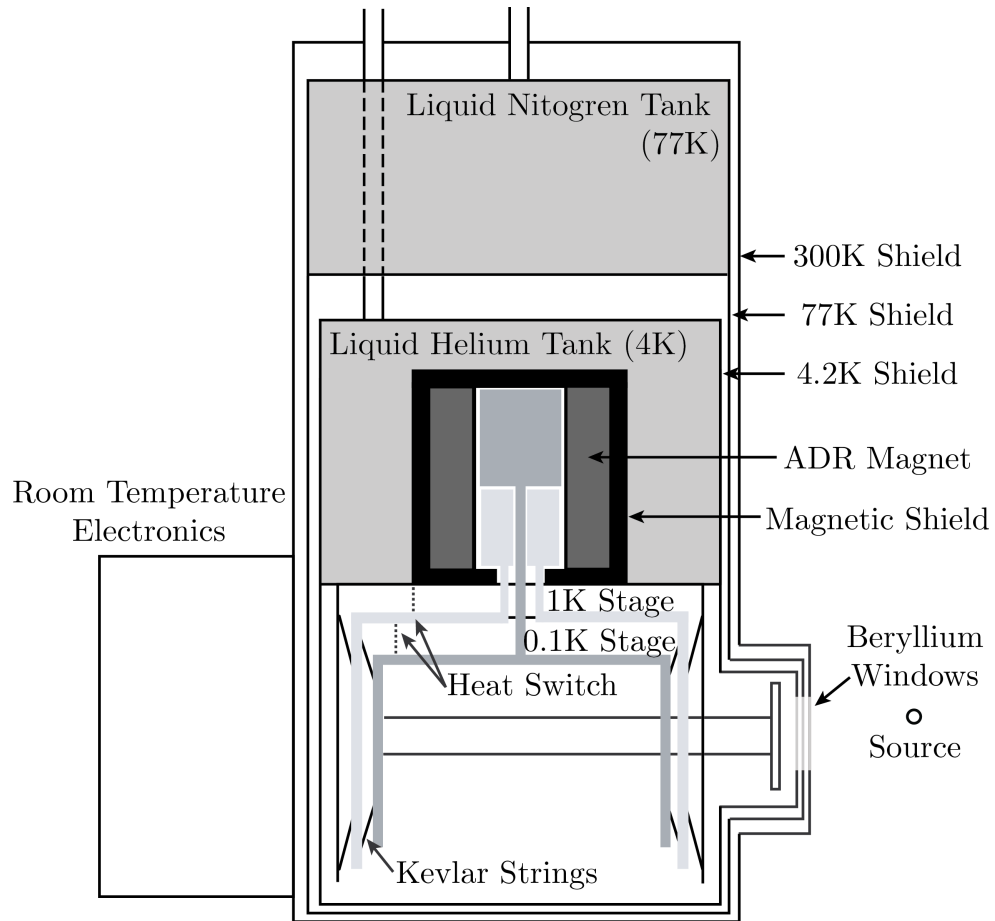


Figure 5.8: Schematic of a liquid cryogen cryostat. The liquid nitrogen and liquid helium provide precooling to 77 K and ~ 4.2 K, respectively. The ADR system is discussed in Section 5.4.2 and can be thermally isolated from the LHe bath by a mechanical heat switch. The TES sensor is located on a cold finger which can be brought within a centimeter of room temperature.

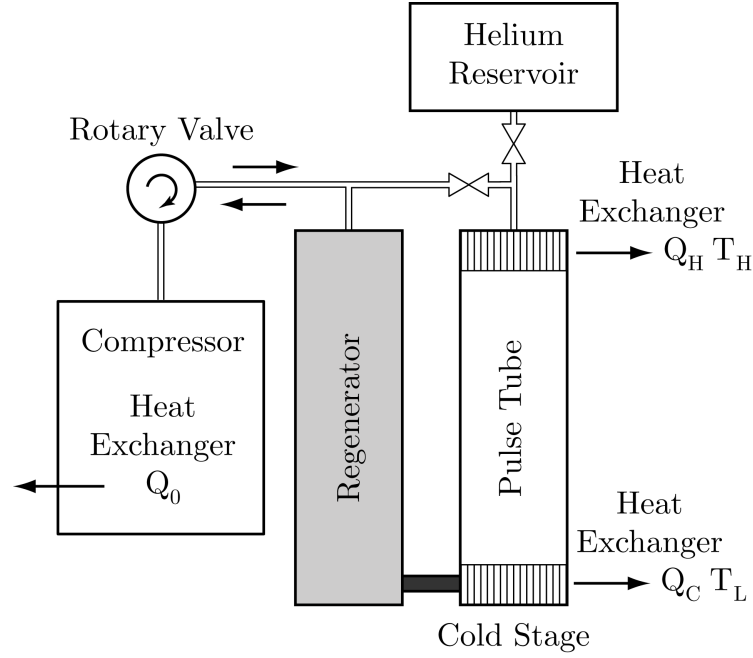


Figure 5.9: A schematic of a single-stage pulse tube refrigerator. Adiabatic compression of the ^4He occurs in the pulse tube, excess heat Q_H is removed by upper heat exchanger, and heat Q_C is absorbed from the system in the lower heat exchanger. A thermal regenerator is used provide thermal coupling of the gas to the system. A compressor and rotary valve provide the pressure oscillations within the pulse tube necessary for cooling. The heat of compression Q_0 is ultimately removed from the compressor by cooling water.

The regenerator takes up heat from the gas as it moves from the compressor into the pulse tube while the gas that flows into the reservoir gives off heat Q_H to the surroundings.

During the expansion step the system is connected to the low pressure output of the compressor, decreasing the pressure in the pulse tube from p_H to p_L . The flow is reversed and the He that has moved from the pulse tube to the compressor flows back towards the regenerator. As the system is thermally isolated, the gas temperature drops with pressure, resulting in a gas temperature that is below T_L . The gas extracts heat from the regenerator as it flows through, warming the gas to the temperature T_L . The cooling power is the amount of heat the gas removes from the heat exchanger, Q_C . At the end of each pulse the He gas is in the same place in cryostat as it was at the beginning of the cycle. This compression and expansion cycle repeats at the frequency set by the rotary valve.

The function of the pulse tube is to insulate the cooling process in the lower heat exchanger from the heat being removed from the upper heat exchanger. It is designed such that the working gas in the warm heat exchanger only moves part way into the pulse tube before the flow is reversed, so that the gas in the lower temperature heat exchanger does not reach the warmer end. During each cycle the gas in the middle portion of

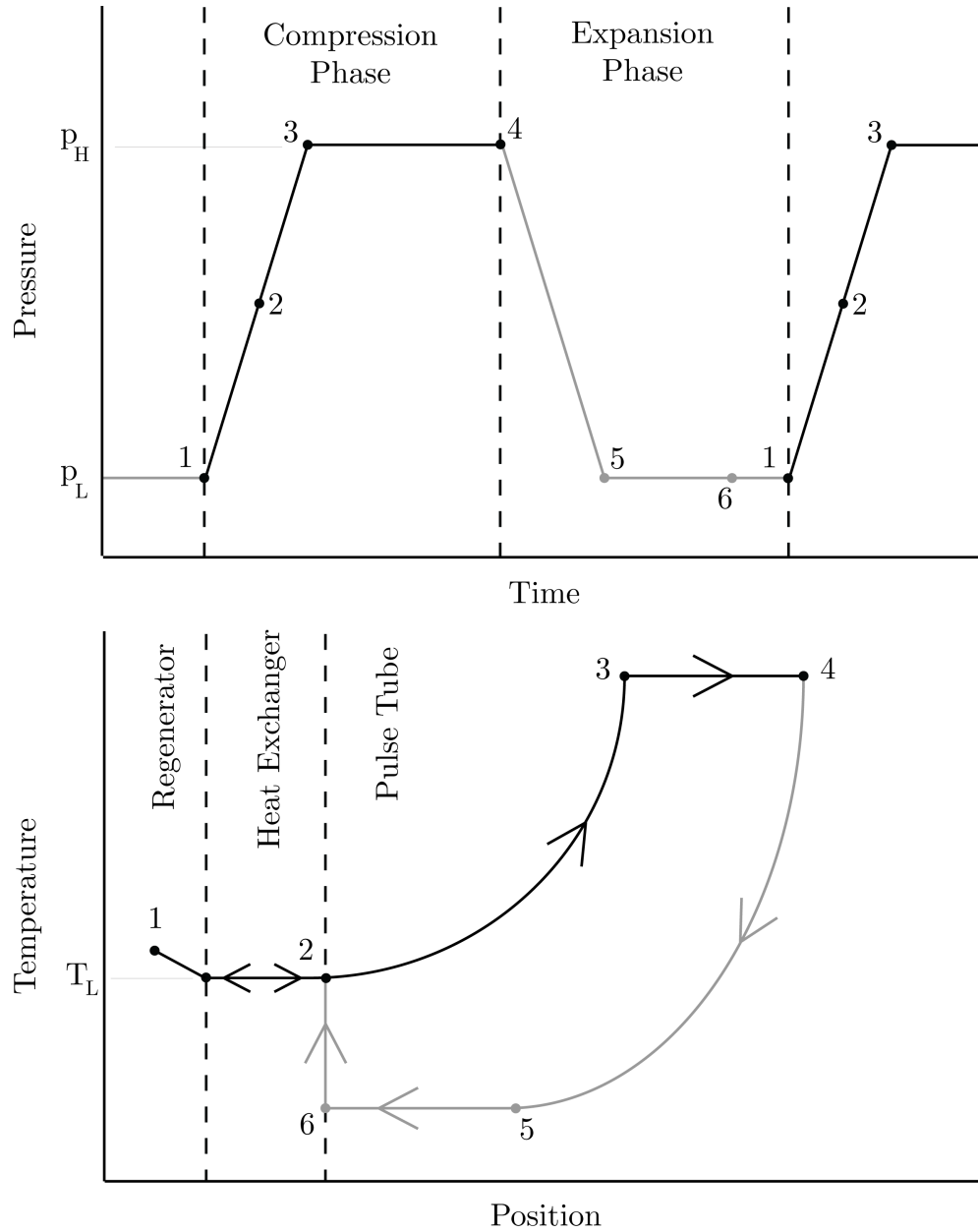


Figure 5.10: The pulse tube pressure as a function of time (above) and the temperature of the ^4He working gas as a function of position inside the PTR (below). During the compression phase (solid black line) the gas is adiabatically compressed to a pressure p_H and moves into the pulse tube with the excess heat removed by the heat exchangers at the top. The flow is reversed during expansion phase (solid gray line) and with the decreasing pressure the gas cools to a temperature below T_L . The gas warms back to a temperature T_L in the lower heat exchanger, the heat it removes cools the lower heat exchanger. Adapted from Tanaeva [125].

the pulse tube moves inside forming a temperature gradient that insulates the two ends [124]. The volume and dimensions of modern pulse tubes are designed to optimize the temperature stratification within the pulse tube and to limit gas mixing within the volume. Flow straighteners are used at the ends of the tube to reduce the turbulent gas flow.

Single stage PTR systems can achieve base temperatures close to 30 K. In order to operate at lower temperatures two PTR are used in series, with the first used to precooling the second. A schematic of a two-stage PTR is shown in Figure 5.11. Operating from the base temperature of the first PTR, the second stage can typically reach temperatures of ~ 5 K and temperatures as low as 1.3 K have been reported [126]. While a multistage PTR can reach lower temperatures, the precooling stage reduces the gas flow to the colder stages and limits the cooling power of the system. Discussions of the thermodynamics of multistage PTR can be found in the literature [127]. In each stage of a multistage PTRs the regenerators are filled with different materials to optimize heat exchange with the He gas. In current systems the 50 K regenerator uses stainless steel and phosphor bronze screens, as well as small lead spheres in the lower section. For the 4 K regenerator small Pb and ErNi spheres are used [122]. Additionally, the orifices between the pulse tubes and the He reservoir, and between the pulse tubes and the rotary valve, are designed to create a phase shift between gas compression and gas flow, limiting the injection of hot He gas into the pulse tube. For the system used at Lawrence Livermore National Laboratory, the size of these constrictions is optimized for maximum cooling power at a valve frequency of ~ 2 Hz. Without load, the pulse tube refrigerator attains a base temperature of ~ 2.5 K with a power consumption of ~ 6.5 kW set by the Leybold Coolpak 6200 compressor.

5.4.2 Adiabatic Demagnetization Refrigerator

Cooling below the base temperature of the pulse tube refrigerator is achieved by isothermal magnetization and adiabatic demagnetization of a paramagnetic salt. Adiabatic demagnetization refrigerators (ADRs) consist of paramagnetic materials coupled to the cold bath of the PTR cold stage through a heat switch.

This cooling process is illustrated in Figure 5.12 in terms of the decrease in entropy of the system. We begin with the paramagnetic salt thermally connected to the bath at temperature T_0 . We then apply an external magnetic field, aligning the magnetic moments of the electrons in the paramagnet in direction of the applied magnetic field. This increase in ordering decreases the entropy of the system. The heat of magnetization, produced as the entropy decreases, is absorbed by the bath. Once the maximum magnetic field B_f is applied, most of the magnetic moments are aligned, and the temperature is allowed to equilibrate to that of the precooling bath. The salt is subsequently thermally decoupled from the cold bath by opening the heat switch, and the magnetic field is gradually decreased, $B_f \rightarrow 0$. During this endothermic process the entropy of the paramagnet salt remains constant and as the magnetic moments return to random orientations the temperature decreases accordingly (Figure 5.12) [128, 129]. Once the system has reached its base temperature T_f , it gradually warms up due to external heat leaks [130]. As the

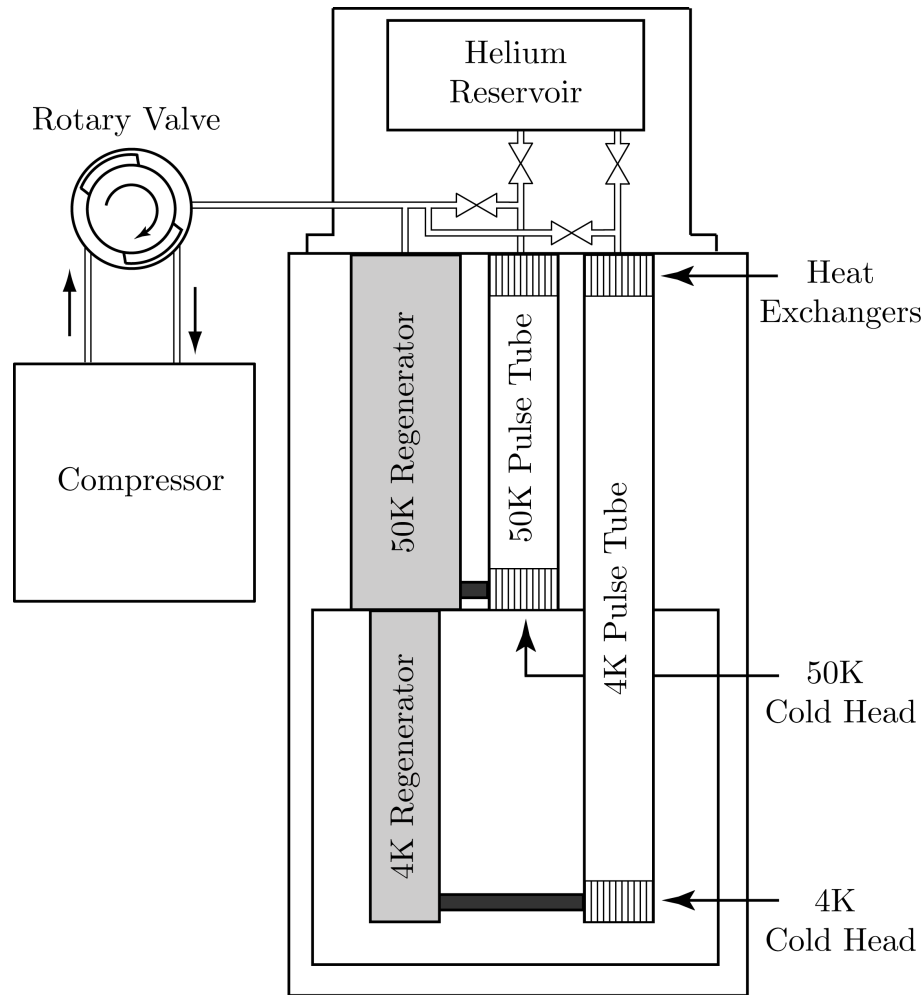


Figure 5.11: Schematic of two-stage pulse tube refrigerator. The periodic pressure cycles generated by the compressor and rotary valve move the ^4He working gas through the upper heat exchangers releasing heat into the environment while the 4K and 50K cold heads (heat exchangers) remove heat from the system.

base temperature T_f is much lower than the 100 mK required to operate the TES, a small current is applied to the ADR magnet, regulating the detector stage at a temperature slightly below the transition temperature T_C of the TES. The temperature of the detector stage is regulated using a feedback control system and can be kept stable to $\pm 10 \mu\text{K}$.

The thermodynamic process of adiabatic demagnetization can be described by considering the entropy S of non-interacting magnetic dipoles with total electronic spin J in the paramagnetic ions. At a temperature T and magnetic field B the entropy is given by [107]

$$S = \frac{x}{2} \left(\coth \left(\frac{x}{2} \right) - (2J + 1) \coth \left(\frac{x(2J + 1)}{2} \right) \right) + \ln \left(\frac{\sinh \left(\frac{2J+1}{2} \right)}{\sinh \left(\frac{x}{2} \right)} \right) \quad (5.1)$$

with

$$x = \frac{gB\mu_B}{k_B T} \quad (5.2)$$

where μ_B is the Bohr magneton, given by $\mu_B = e\hbar/2m_e = 9.27 \times 10^{-24} \text{ J/T}$ and g is the Landé g-factor. In the limit where $B \rightarrow 0$, equation (5.1) is not valid as the interactions between the moments within the salt are no longer negligible. These small interactions produce an internal field that results in spin ordering at very low temperatures. At low magnetic fields we therefore replace B in equation (5.1) with an effective magnetic field, given by

$$B_{eff} = \sqrt{B_f^2 + B_{int}^2} \quad (5.3)$$

where B_{int} is the internal field produced from the neighboring magnetic moments in the salt. The base temperature of the stage is given by [107]

$$T_f = \frac{B_{eff} T_0}{B_f} \rightarrow \frac{B_{int} T_0}{B_f} \quad (5.4)$$

Modern ADRs often use a two-stage design in which two paramagnetic salts are demagnetized simultaneously. With this design an intermediate temperature stage using a second paramagnetic material (usually referred to as the guard stage) intercepts the heat leak from the pulse tube cooler. This acts as a thermal guard to the detector stage and allows for ADR cooling to be used with a reservoir temperature of $\sim 4 \text{ K}$ [131]. For the cryostat discussed here, a gadolinium gallium garnet $\text{Gd}_3\text{Ga}_5\text{O}_{12}$ (GGG) is used for the guard stage, as it offers a comparably high heat capacity, high thermal conductivity, and a magnetic ordering temperature of 380 mK [132]. The GGG stage supports the detector stage, which uses paramagnetic iron ammonium sulfate, $\text{Fe}(\text{NH}_4)(\text{SO}_4)_2 \times 12\text{H}_2\text{O}$, commonly known as ferric ammonium alum or FAA. The low ordering temperature of FAA at $\sim 26 \text{ mK}$ sets the minimum temperature the ADR can cool down to; however, its low heat capacity requires the use of the GGG guard stage to reduce the heat load from the pulse tube cooler [133]. The material properties of FAA and GGG are summarized in 5.1. The entropies of FAA and GGG are shown in Figure 5.12 for $B = B_{int}$ and $B = 6.5 \text{ T}$, these

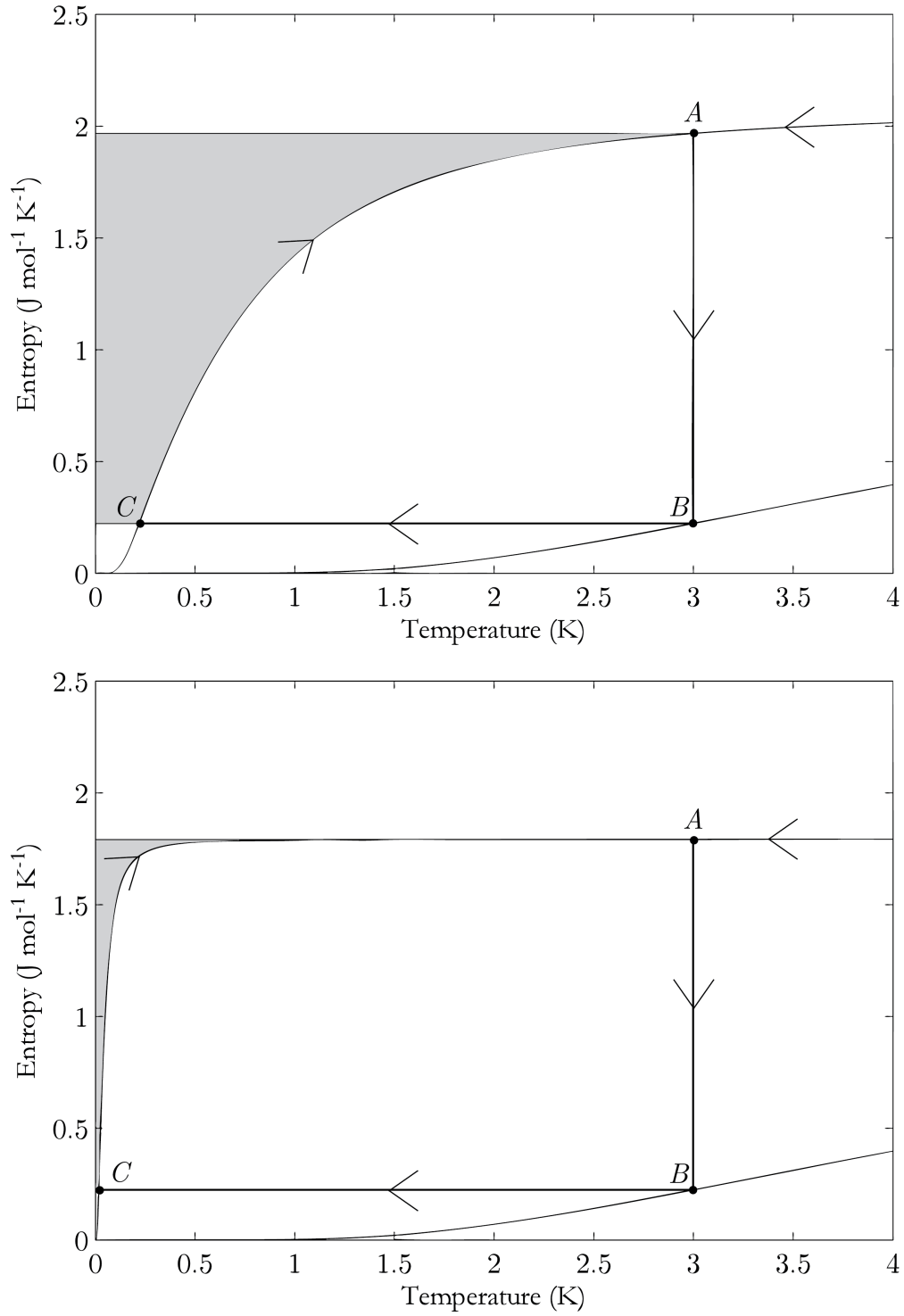


Figure 5.12: Entropy as a function of temperature for GGG (above) and FAA (below). During the refrigeration process the salt is isothermally magnetized (AB) and after coming to thermal equilibrium with the precooling bath is thermally isolated and adiabatically demagnetized (BC). The salt then warms up following the entropy curve for $B = B_{\text{eff}}$. The cooling power for each salt is given by the shaded area.

Table 5.1: Properties of iron ammonium sulfate (FAA), and Gadolinium Gallium Garnet (GGG) paramagnets.

	GGG [132]	FAA [133, 134]
Chemical Formula	$\text{Gd}_3\text{Ga}_5\text{O}_{12}$	$\text{Fe}(\text{NH}_4)(\text{SO}_4)_2 \times 12\text{H}_2\text{O}$
Spin J	$7/2$	$5/2$
Landé g Factor	2	2
Internal Field B_{int} (T)	0.48	0.038
Ordering Temperature (mK)	380	26

show the change in entropy during an ADR cooling cycle. We cycle both stages using a single superconducting 6.5 T magnet and a single mechanical heat switch. The heat switch is electrically controlled with a stepper motor inside the cryostat to avoid leaks into the vacuum at feedthroughs.

5.5 Cryostat performance

The entire cryostat cool down to < 0.1 K is automated, and takes approximately 16 – 18 hours from room temperature due to the large mass of the ADR magnet and its magnetic shielding. The ADR cycle uses a magnetizing current of 36 A for a maximum magnetization field of $B = 6.5$ T, and can be programmed ahead of time when the pulse tube has reached a temperature below 4 K. An example cooldown from room temperature is shown in Figure 5.13.

Without regulation, the ADR attains a base temperature of 30 mK, in agreement with the ordering temperature of 26 mK for the FAA paramagnet according to Table 5.1. The GGG guard stage equilibrates around 380 mK, although this number depends somewhat on the initial temperature of the demagnetization cycle, as expected from figure 5. As the cryostat base temperature is much lower than the 100 mK required for TES operation we therefore use a small current in the ADR magnet to regulate the detector stage to the desired temperature. For an operating temperature of 100 mK, the hold time between hour demagnetization cycles is greater than 48 hours with 32 signal wires connected to the TES detector stage.

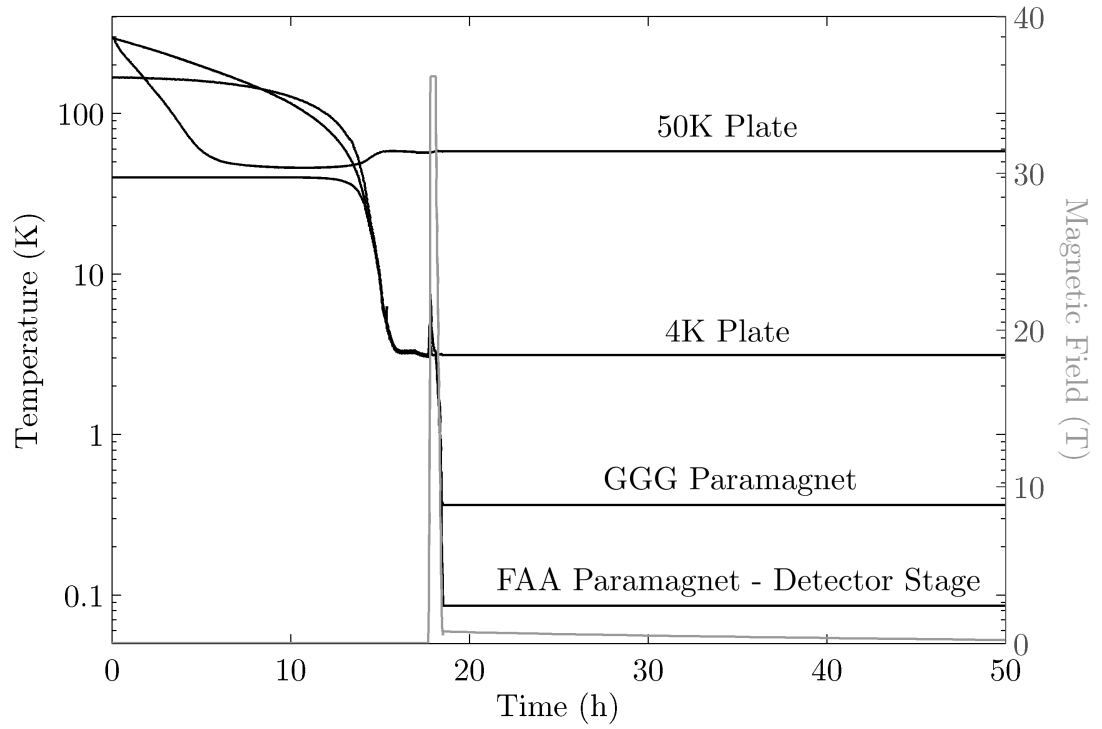


Figure 5.13: Cooldown cycle of the pulse-tube ADR for regulation at 0.1 K. Cooling from room temperature to the pulse tube cooler base temperature requires 16–18 hours. After the one hour ADR cycle the operating temperature of 100 mK can be maintained for more than 48 hours.

Chapter 6

Transition Edge Sensor Modeling

6.1 Simulation Methodology

The response of the spectrometer was modeled using Monte-Carlo simulations with Geant4. Geant4 is a versatile software toolkit implemented in C++ using object-oriented technology for modeling particle interactions in matter [116]. Although Geant4 has support for numerous physics processes, the measurements of interest will focus on photons of energies below 200keV, and the simulation exclusively uses the electromagnetic (EM) physics packages. The frameworks for the EM packages are contained in both the Low-Energy [135] and in the Standard [136] electromagnetic packages. The Low-Energy package was selected as it incorporates atomic relaxation processes including X-ray fluorescence and Auger electron emission [137] that provide an important component to the detector response. Within the Low-Energy package two models are available, the first built on data libraries, Evaluated Photon Data Library (EPDL) [138] for photons and Evaluated Electrons Data Library (EEDL) [139] for electrons and a second using the analytical models developed for the Penelope Monte Carlo code [140]. The algorithm based on Penelope was selected as it is more appropriate for low-energy calculations, showing good agreement for energies down to a few keV [141]. The simulation provides a detailed account of the radiation interactions and the energy deposited in the material for each incident photon. The deposited energy is assumed to be fully converted to heat and measured by the transition edge sensor, so that the total energy deposited in the absorber can be used to generate an energy spectrum.

Monoenergetic photon sources can be modeled sufficiently well using the default Geant4 particle engine; however, to simulate a real world sample with a single or mixture of isotopes requires a more extensive application. To account for the numerous photon energies the Geant4 simulation was integrated with RadSrc, an open source software package that determines the appropriate gamma-ray spectrum for a given isotopic composition [142]. Since the isotope database included with the software has a limited number of isotopes and decay information, it was modified to include the relevant isotopes of plutonium using decay data available from the Lawrence Berkeley National Laboratory Isotopes Project [143].

To understand the detector response two systems were modeled using Geant4. Initially only the absorber was modeled and used to understand the tradeoff between absorber thickness and area by calculating the fraction of photons absorbed for different thickness/area ratios. The second included the details of an existing liquid cryostat from LLNL and was used to determine the feasibility of measuring ^{242}Pu in mixed isotope samples.

6.2 Simplified Absorber Model

In this simplified model, only the absorber was present with the objective of determine the absorber dimensions which optimize the full energy of deposition. The desired energy

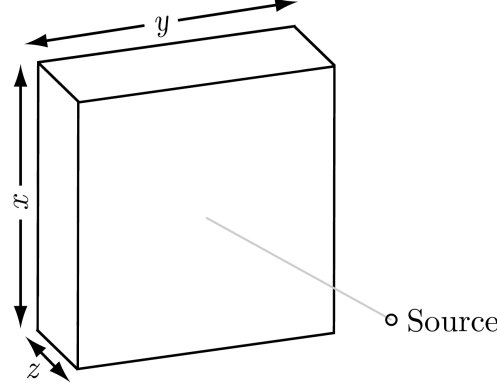


Figure 6.1: Simplified Geant4 absorber model used for determine the dimensions which optimize the full energy of deposition. The isotropic photon source, located 5 cm from the absorber, irradiated the absorber with monoenergetic photons with energy ranging from 5 to 200keV.

resolution of 100 eV requires the volume of the absorber be limited to 1 mm^3 as discussed in Chapter 3.1. For this analysis the absorber, shown in Figure 6.1, was taken as a rectangular parallelepiped with fixed volume of 1 mm^3 and variable dimensions of x , y , and z . For a constant absorber geometry, an isotropic source of monoenergetic photons with energy ranging from 5 to 200keV was placed 5 cm from the surface of the absorber. These source photons interacted with the absorber and the energy lost from electron and photon escape as well as the total energy absorbed was recorded. This idealized system neglects scattering in the radiation source, the shielding and cryostat. While not an accurate model of the experimental system this simplified model provides an understanding of how the partial energy depositions from Compton scattering in the Sn absorber and photon escape after an absorption event (as discussed in Chapter 3.2) are effected by the geometry of the absorber. In addition to tin, both lead and tantalum were simulated as absorbers. For the absorbers to have the same limiting energy resolution, $\Delta E_{\text{FWHM}} = 2.355\sqrt{k_B T^2 C}$, the heat capacities must be the same. The volumetric heat capacity of tin and tantalum are very similar, $0.015 \text{ J/m}^3\cdot\text{K}$ and $0.012 \text{ J/m}^3\cdot\text{K}$, respectively, and therefore the same absorber dimensions were used. The heat capacity of lead is substantially higher at $0.092 \text{ J/m}^3\cdot\text{K}$, requiring the volume be reduced to 0.16 mm^3 . The material properties and heat capacity calculations are discussed in Appendix B. To adequately sample the range of possible dimensions, thirty geometries were simulated for each material. For tin and tantalum absorbers, the dimensions from $0.001 \times 1 \times 1 \text{ cm}$ to $0.26 \times 0.06 \times 0.06 \text{ cm}$ were used. For lead the dimensions ranged from $0.001 \times 0.4 \times 0.4 \text{ cm}$ to $0.26 \times 0.025 \times 0.025 \text{ cm}$.

The fraction of interacted photons to total incident source photons (*attenuated* photons) with increasing absorber thickness normalized to the absorption of 5 keV photons is shown in Figure 6.2. For a constant volume V an increase in the absorber thickness z decreases the surface area perpendicular to the direction of the source photons $A = x \cdot y$.

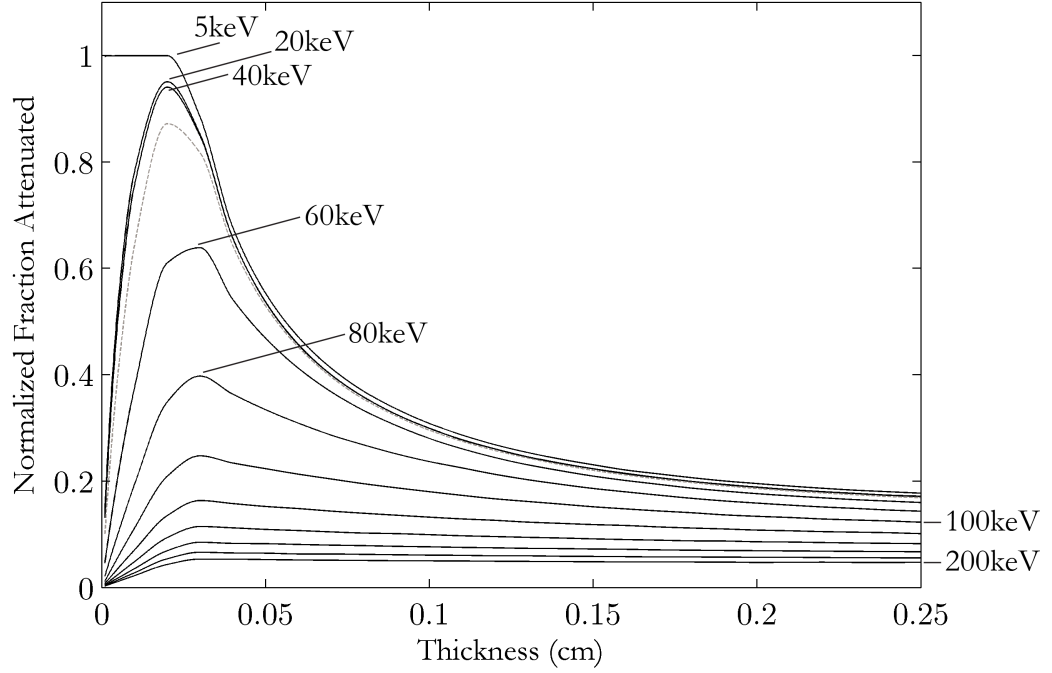


Figure 6.2: Fraction of incident photon energy deposited or lost with increasing tin absorber thickness. Above 100 keV the energy increases in 20 keV steps to the maximum of 200 keV. The dotted gray line indicates 45 keV photon energy.

The ideal thickness therefore optimizes the loss resulting from a decreased solid angle with the increase in absorption probability with larger thicknesses z . For the case of a tin absorber, the fraction attenuated increases with thickness to maximum of ~ 0.25 mm and above this value the loss in solid angle is dominates. The highlighted line of Figure 6.2 indicates 45 keV photons.

Figure 6.3 shows a simulated spectrum from a 45 keV photons source incident on a $0.25 \times 2 \times 2$ mm tin absorber. The principle components of the spectrum include the full-energy peak, the Compton scattering, and the tin escape peaks. The energies of x-ray from the principle K- and L-shell emission lines for tin are listed in Table 6.1 and the most intense are visible in the spectrum and result from the $K\alpha_1$, the $K\alpha_2$ and the $K\beta$ escape. The less intense L escape peaks also as present.

A simulated spectrum of an absorber with dimensions of $0.25 \times 2 \times 2$ mm is shown in Figure 6.4. With these dimension complete attenuation is achieved at low energies, decreasing to $\sim 80\%$ at the K-edge of tin at 29 keV . With increasing photon energy this fraction decreases with less than 20% for energies greater than 100 keV . A fraction of the photons which interact within the absorber will be absorbed entirely. The ratio of the fully absorbed to attenuated photons is the full-energy peak efficiency. The highest full-energy peak efficiency is found for low energy photons, abruptly decreasing at the K-edge

Table 6.1: Energies of x-ray from the principle K- and L-shell emission lines for tin [144, 145, 146].

Shell	Energy (eV)
$K\alpha_1$	25271.3
$K\alpha_2$	25044.3
$K\beta_1$	28486.0
$L\alpha_1$	3443.98
$L\alpha_2$	3435.42
$L\beta_1$	3662.80
$L\beta_2$	3904.86
$L\gamma_1$	4131.12

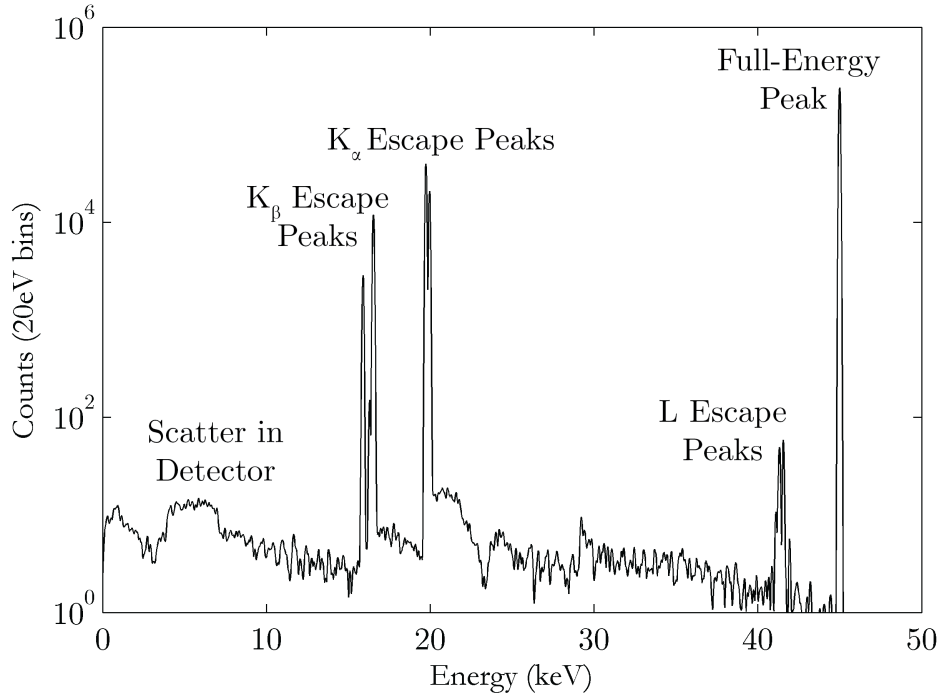


Figure 6.3: Simulation of the energy spectrum with 20 eV energy bins from a 45 keV photon source incident on a $0.25 \times 2 \times 2$ mm tin absorber.

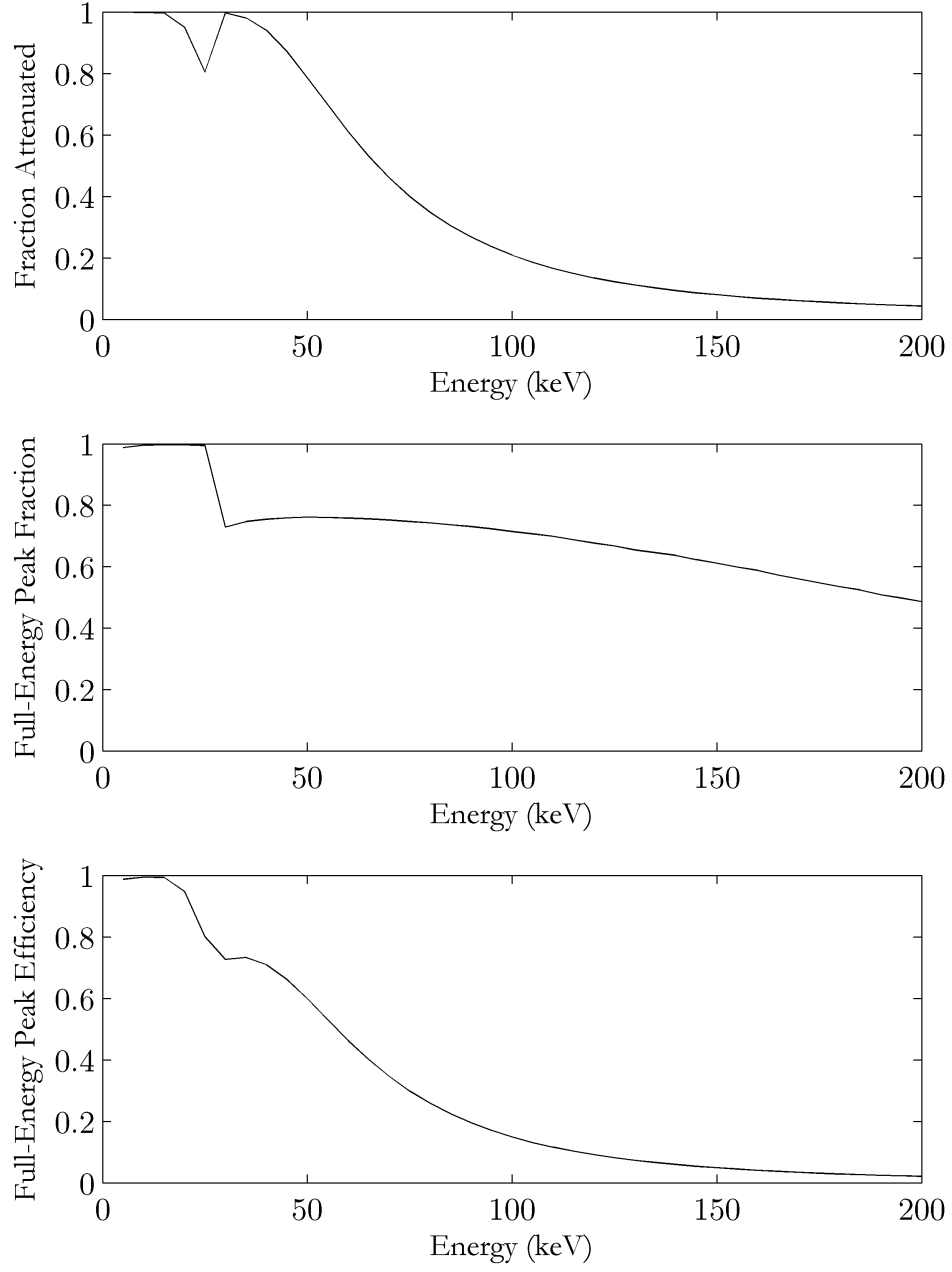


Figure 6.4: The fraction of incident photons attenuated (upper), the fraction of fully absorbed to attenuated photons (middle), and the full-energy peak efficiency (bottom) for a $0.25 \times 2 \times 2$ mm tin absorber.

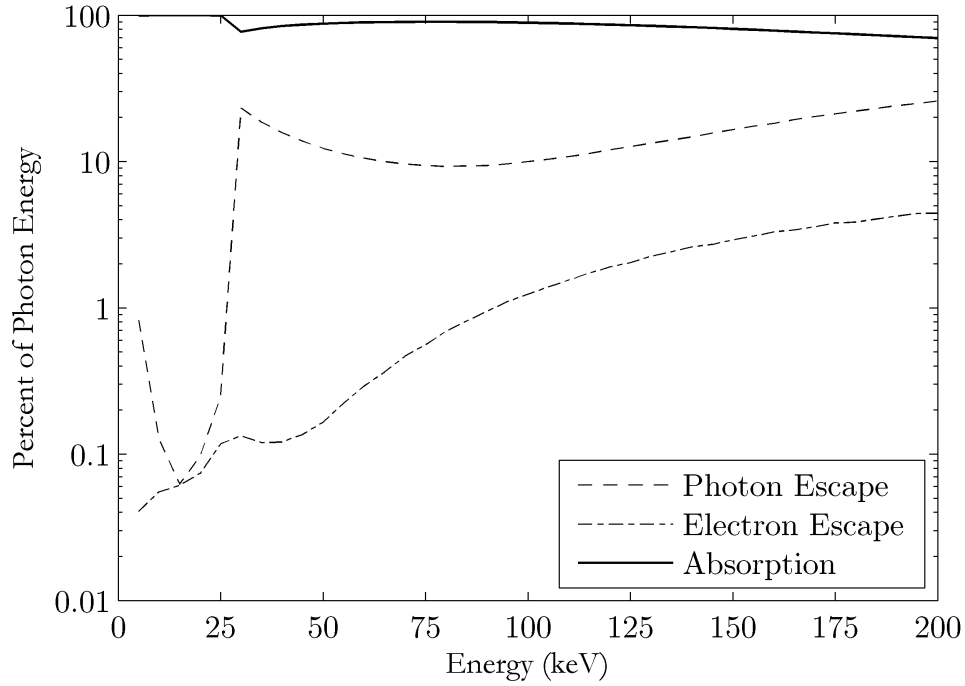


Figure 6.5: Fraction of incident photon energy deposited or lost from photon or electron escape for those photons that have been attenuated in the tin absorber. Note that the K absorption edge at 29.2 keV produces a large change in the fraction of energy loss from photon escape.

and gradually decreases with higher energies. The product of these two parameters is the probability that an incident photon will produce a full energy deposition. For 45 keV photons the total photopeak efficiency is $\sim 60\%$.

The simulation also offers insight into relative importance of the absorption and loss mechanisms with varying photon energy. The percentage of photon energy deposited in the volume or lost via photon or electron escape is shown in Figure 6.5. At energies below the tin K-edge absorption is dominant. At energies above the K-edge, the escape of X-ray fluorescence photons greatly increases the fraction of photon loss to $\sim 20\%$. For higher energies, photon and electron escape account for $\sim 20\%$ and $\sim 5\%$, respectively, of the incident photon energy.

Additional simulations were made using lead and tantalum as the absorbing material. The fraction of attenuated photons was maximized for dimensions of $0.2 \times 2.3 \times 2.3$ mm and $0.04 \times 2 \times 2$ mm for tantalum and lead, respectively. The photon attenuation fraction for these materials with optimized dimensions is shown in Figure 6.6. For energies below 40 keV tantalum absorbers show improved attenuation over tin as it is limited by the K-edge at 29 keV. Tin and tantalum have similar performance from 40 keV up to the K-edge of tantalum at 67.4 keV. Above this energy tantalum offers a substantial improvement.

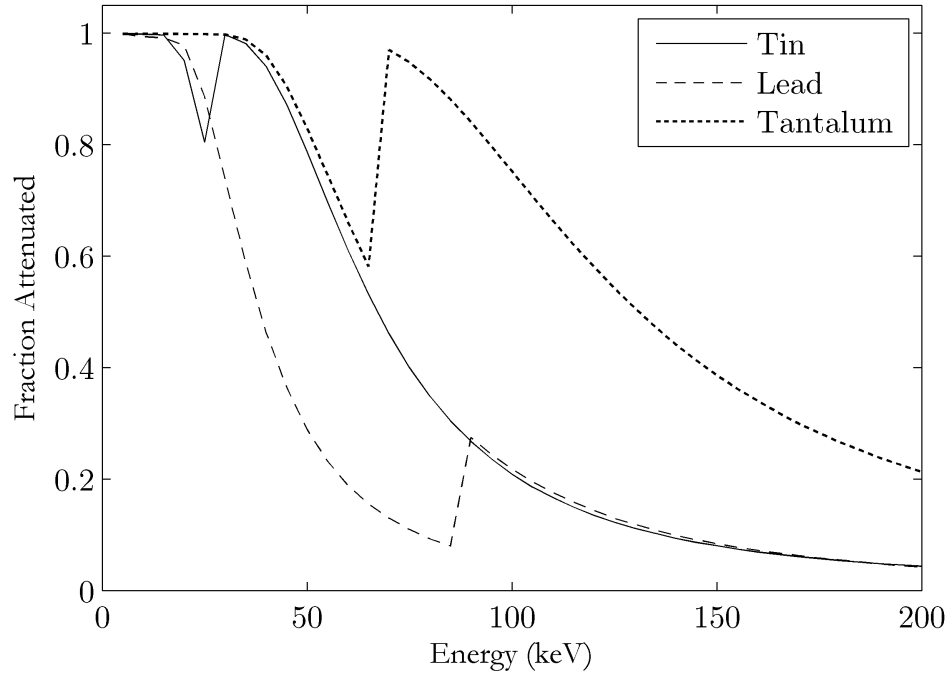


Figure 6.6: The fraction of attenuated photon from the Geant4 simulations of a $0.25 \times 2 \times 2$ mm tin, $0.2 \times 2.3 \times 2.3$ mm tantalum and $0.04 \times 2 \times 2$ mm lead absorber.

Table 6.2: Approximate isotopic composition (wt %) of various grades of plutonium [147].

	Spent fuel	Weapon
^{238}Pu	1.3	0.012
^{239}Pu	60.3	93.8
^{240}Pu	24.3	5.8
^{241}Pu	9.1	0.35
^{242}Pu	5.0	0.022

Despite having a higher cross section than both tin and tantalum, the fraction attenuated in lead is substantially reduced as a result the smaller volume. The absorption edge at 88 keV does improve the performance however it is still below that of tin. For the measurement of ^{242}Pu at 44.915 keV both tantalum and tin absorber are expected to show similar performance. Measurements of gamma rays above 70 keV would gain from the use of tantalum absorbers; however, as discussed in Chapter 5, attempts to use this material have not been successful.

6.3 Detector and Cryostat Model

A Geant4 model of an existing liquid cryostat from LLNL, described in Chapter 5, was also developed. This simulation includes all components of the device- the tin absorber, transition edge sensor, and SiN wafer. The model also included the 300 K, 77 K, and 4 K thermal shields. The outer vacuum enclosure at 300 K shield is fabricated from mumetal ($\sim 80\%$ Ni, $\sim 15\%$ Fe, $\sim 4\%$ Mo) to provide magnetic shielding. For simplicity, this outer thermal shield was modeled as nickel only. The inner 77 K and 4 K shields were modeled as Al. All three layers were 0.1 mm thick. A schematic of the system is shown in Figure 6.7.

The response of the Geant4 system was compared to experimental data using a collimated ^{241}Am point source located 8 cm from the transition edge sensor. A detailed schematic of the ^{241}Am model is shown in Figure 6.8. To determine the feasibility of directly measuring ^{242}Pu , 10 mg samples of reactor and weapons grade plutonium were modeled using the isotopic compositions listed in Table 6.2.

The Geant4 model of the simplified detector and cryostat geometry is shown in Figure 6.7. The simulated spectrum convolved with a Gaussian with a 100 eV resolution is shown along with a directly measured ^{241}Am spectrum in Figure 6.9. The contribution to the Compton background from the various spectrometer components can be seen when compared with the simulated spectrum of the absorber shown in Figure 6.3. The background below 40 keV results from scatter within the tin absorber. Scattering in the cryostat shields contributes in the 40 to 60 keV region, with a backscatter peak present around 50 keV. The simulation shows good agreement with the experimental results with the exception of 50 to 60 keV region where the magnitude of the backscatter peak is smaller

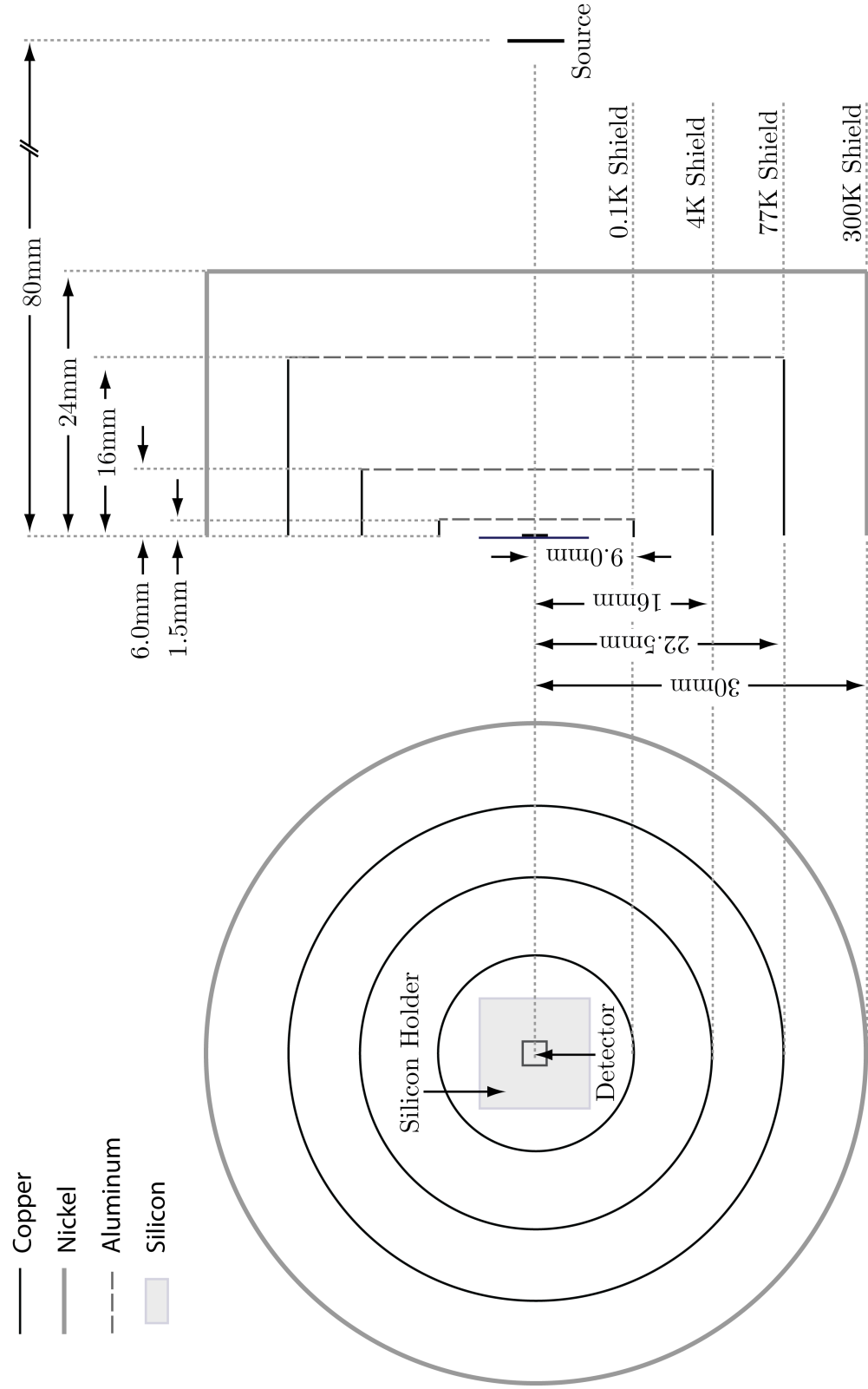


Figure 6.7: Schematic of the cryostat modeled in the Geant4 simulation.

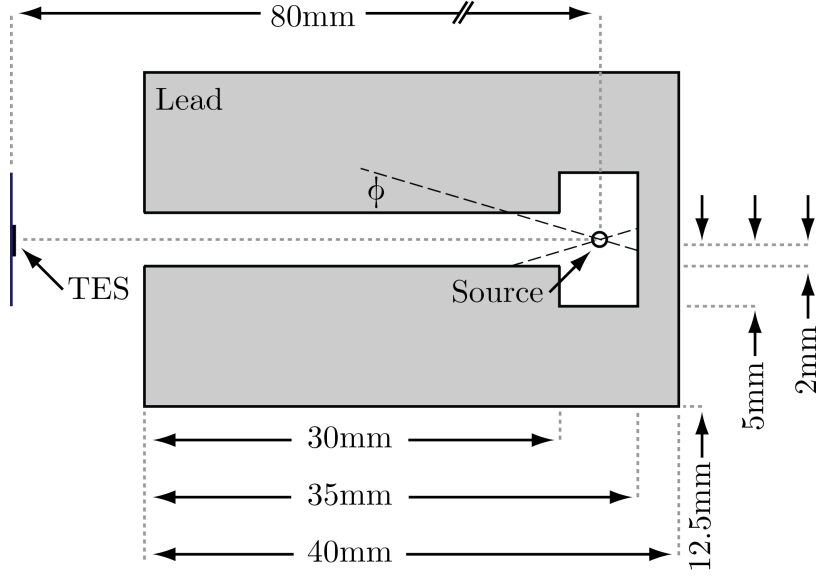


Figure 6.8: Schematic of the cylindrical encapsulated ^{241}Am used for the Geant4 simulations. The point source inside the lead was located located 8 cm from the transition edge sensor with the photon direction randomly sampled in either the forward or reverse direction within an angle $\phi = 16^\circ$ of the source-TES axis.

than measured. This discrepancy is most likely from the absence of a secondary source encapsulation in the model. The ^{241}Am was modeled as a point source suspended in the middle of the lead shield, while with actual sources the radiative material is contained within a secondary encapsulation inside of the collimation. As it was not possible to open the lead shield to investigate, this additional component was omitted. The photons which interact within the secondary encapsulation can backscatter into the spectrometer and contribute to the increased counts in the 50 keV region observed in the experimental data. As this discrepancy is not a limitation of the Geant4 framework, the simulation can be assumed to be adequate for the the simulation of plutonium samples.

The Geant4 model was then used to determine the sensitivity of the spectrometer to ^{242}Pu and assess the feasibility of a direct measurement of the isotope. This study considers two 10 mg samples of plutonium, with isotopic compositions listed in Table 6.2. These values were chosen as they are representative of the compositions found in spent fuel and nuclear weapons. The energy spectrum from the Geant4 simulation of reactor grade Pu is shown in Figure 4.8 and is reproduced for convenience in Figure 6.10. As can be seen in the figure, the ^{242}Pu full-energy peak at 44.915 keV is very close to the ^{240}Pu line at 45.242 keV, with a separation of 327 eV. The spectrometer response is assumed to be Gaussian with an energy resolution of 100 eV the ^{242}Pu signature can be resolved from the stronger ^{240}Pu line. The maximum count rate of 10Hz is set by the thermal time constant of the transition edge sensor, as discussed in Chapter 3.2.3. Under

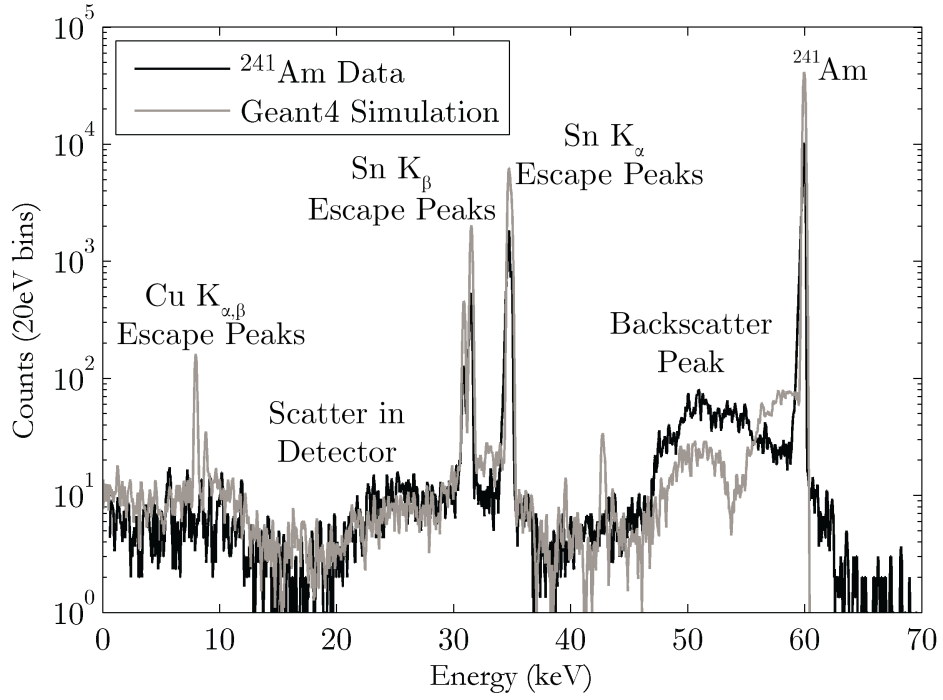


Figure 6.9: Comparison of a measured ^{241}Am spectrum and a Geant4 simulation convolved with a 100 eV Gaussian. The measured 59.5 keV full-energy peak has an energy resolution of 100 eV. The simulation geometry includes the 300 K mumetal shield, Al shielding and the Cu backing of the 100 mK stage. The small peaks at 39 and 43 keV in the Geant4 simulation are the absorption of Cu escape x-rays produced from the interaction of the tin escape x-rays in the copper located behind the TES.

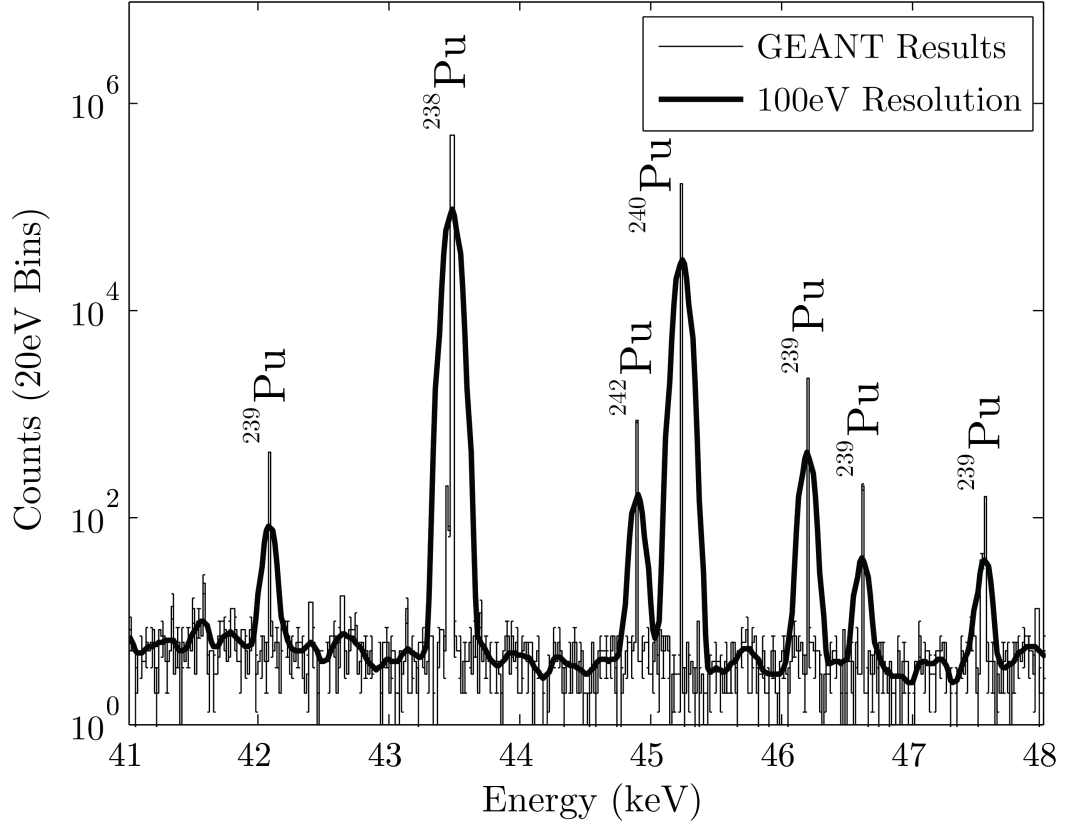


Figure 6.10: Geant4 simulation of 10 mg of reactor grade plutonium. The 44.915 keV line of ^{242}Pu is visible next to the stronger ^{240}Pu line. The simulation results convolved with a Gaussian of 100 eV FWHM is indicated by the solid line.

these conditions the ratio of ^{242}Pu to ^{240}Pu counts in a 24 hour measurement period is $\sim 47/4000$. The simulation results of the weapons grade plutonium is shown in Figure 6.11. Containing a factor of 100 less ^{242}Pu than reactor grade material, the ^{242}Pu gamma-ray line at 45.242 keV is not measurable.

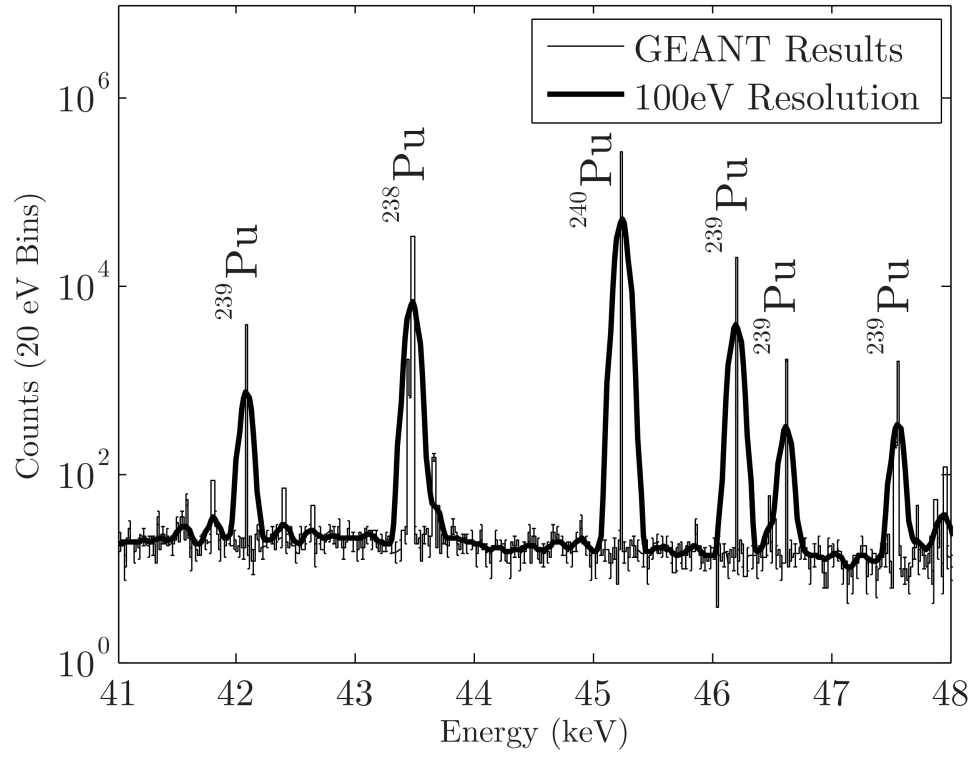


Figure 6.11: Geant4 simulation of 10 mg of weapons grade plutonium. Plutonium enriched for weapons contains a factor 100 less ^{242}Pu than that found in reactors, consequently the ^{242}Pu signature is not discernible against the background.

Chapter 7

Experimental Results

This chapter discusses the measurements made using a transition edge sensor. Results from a liquid cryogen dewar and pulse tube refrigeration system are presented and compared with the noise model from Chapter 4.

7.1 Measurements in Liquid Cryogen Dewar

The following section discusses the noise performance and gamma-ray measurements in the liquid cryogen dewar described in Section 5.4.

7.1.1 Noise Performance

The transition edge sensor noise measured with respect to the SQUID preamplifier input is shown in Figure 7.1. With the exception of the 60 Hz pickup from AC power lines, the noise is white at a level of $20 \text{ pA}/\sqrt{\text{Hz}}$. At frequencies below $\sim 1 \text{ kHz}$ it is set by the noise between the TES phonon system and the cold bath, above this frequency the noise is dominated by the coupling between the absorber and the TES phonon system.

The complex calorimeter model discussed in Chapter 4, was used to analyze the noise from a TES operated in a liquid cryostat. In this analysis an optimization procedure was performed to determine the values of the analytical model that provided optimum agreement between the model and experimental results. The initial noise spectrum was calculated using the sensor parameters calculated in Appendix B. Each parameter was then iteratively optimized using a least squares fitting routine. The parameter values were bound to within a factor of ten of the values calculated in Appendix B. The final set of parameters after optimization are listed in Table 7.1 and were all within $\pm 20\%$ of the initial values. Using these values the modeled current noise is shown in Figure 7.1. With the addition of the 60 Hz pickup as an additional circuit noise source, the model is in good agreement with the measured noise of the sensor. The antialiasing filter used for these measurements is not included in the noise model and accounts for the discrepancy in the predicted and observed noise level at higher frequencies. The limiting energy resolution can be calculated from the integral of the total noise (See equation (4.41)) and for this measurement is about 30 eV.

7.1.2 Measurements

The liquid cryogen dewar was used to make a measurement of the photons emitted from a highly enriched uranium samples from the Y-12 National Security Complex in Oak Ridge, TN. oxidized metal fragments produced during the uranium casting process. The material is a by-product from uranium fabrication, consisting of residual oxidized metal fragments formed at the interface of the refining crucible and the uranium form [148]. The composition of the sample was measured using an inductively coupled plasma mass spectrometer (ICP-MS) facility at the Savannah River National Laboratory and is listed

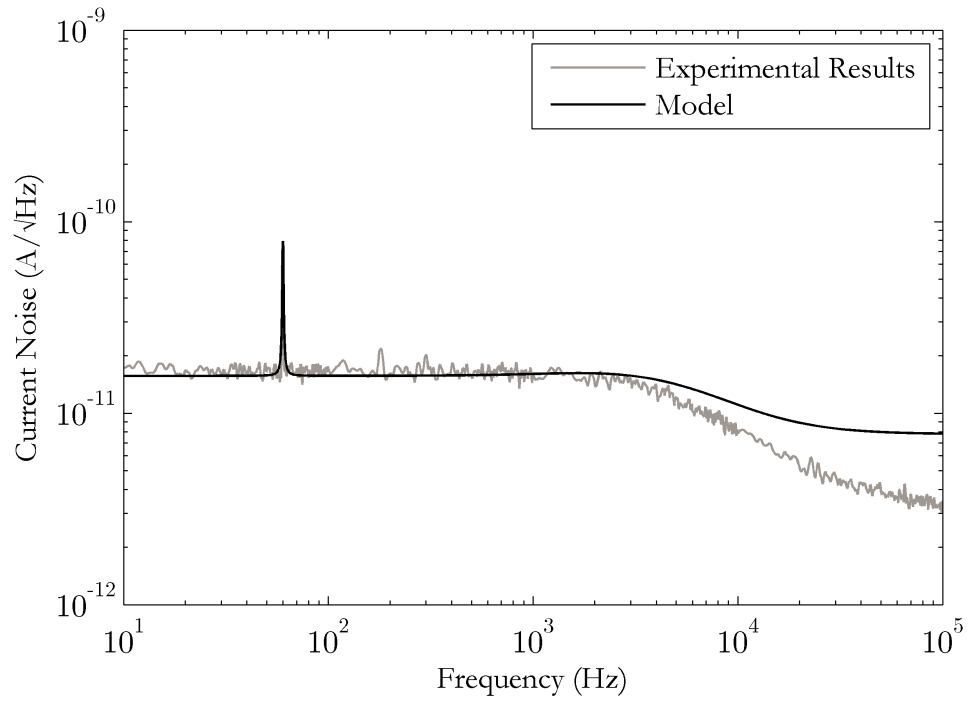


Figure 7.1: Measured current noise in a TES operated in a liquid cryostat system compared with the expected noise from the model.

Table 7.1: Complex calorimeter modeling parameters

Parameter	Symbol	Value
Temperature sensitivity	α	5
Current sensitivity	β	2
Capacitor	C_{cap}	0
Inductor	L	0
Bias Temperature	T	120 mK
Heat Sink Temperature	T_b	90 mK
Absorber Temperature	T_a	120 mK
Detector Electron System Temperature	T_e	120 mK
Detector Phonon System Temperature	T_p	120 mK
Temperature of load resistor	T_L	120 mK
Cold bath-Phonon Thermal Conductance	G_{pb}	3.1 nW/K
Electron-Phonon Thermal Conductance	G_{ep}^e and G_{ep}^p	62 nW/K
Absorber-Electron Thermal Conductance	G_{ae}^a and G_{ae}^e	0 nW/K
Absorber-Phonon Thermal Conductance	G_{ap}^a and G_{ap}^p	6.8 nW/K
Absorber Heat Capacity	C_a	2.6 pJ/K
Detector Electron Heat Capacity	C_e	5.1×10^{-3} pJ/K
Detector Phonon Heat Capacity	C_p	4.9 pJ/K
Operating point resistance	R	0.1 Ω
Load resistor	R_L	0.01 Ω
Operating point voltage	V_{bias}	3 μV
Operating point current	I	15 μA

Table 7.2: Atomic composition of uranium oxide sample obtained from Y-12 National Security Complex in Oak Ridge, TN. Composition measured using inductively coupled plasma mass spectrometry.

Isotope	Composition (%)
^{233}U	1.59
^{234}U	0.83
^{235}U	89.99
^{236}U	0.43
^{238}U	7.08

in Table 7.2. A 0.05 ml solution was evaporated unto a small platinum disk (planchet), and the residual radioactive material was fused into the disk using a propane flame. The sample was measured using a transition edge sensor with each pulse recorded for offline analysis using the optimum filter discussed in Section 4.3. As the total activity of the sample was low, approximately 1.7×10^4 Bq (45 mCi), and a single 1 mm³ sensor was used, the count rate was approximately 0.5 Hz. The warm-up of the 100 mK stage limited a single acquisition to 6 hours, and to improve statistics four separate measurements were made. For each acquisition the adiabatic magnetic refrigeration cycle was used to cool the TES to 90 mK and the sensor biased at nominally the exact same bias point in the transition. For every cooling cycle the response of the detector varies slightly as the operating point within the transition can shift and nonlinearities within the transition can appear. Thermal drifts during an acquisition also affect the detector response. Consequently, although the energy resolution for each individual spectrum ranged between 140 eV and 160 eV, the combined spectrum degraded the resolution to approximately 180 eV.

The combined spectrum measured using a single TES in comparison to two HPGe detector systems is shown in Figure 7.2. The coaxial HPGe detector has a substantial Compton continuum and lower energy resolution such that only the strongest lines are visible. Trace amounts of indium present in the lead shielding surrounding the coaxial HPGe detector produce the $K_{\alpha 1}$ line at 24.21 keV. The $^{73\text{m}}\text{Ge}$ peak at 53.53 keV is produced from neutron interactions with the ^{73}Ge detector material [149]. The 20 mm-thick, 2000 mm² semi-planar HPGe detector has a reduced Compton background; however, many of the lines are still obscured. The small sensor size of the TES allows for a substantial reduction in the background and the higher energy resolution is sufficient to resolve weak gamma-ray emissions from isotopes of plutonium, including ^{238}Pu at 43.498 keV, and ^{239}Pu at 38.661 keV and 51.624 keV in addition to previously undetectable uranium gamma-rays from ^{235}U at 34.7 keV and the ^{236}U line at 49.46 keV. Although ^{242}Pu was not present in the sample, from the sensitivity discussion in Section 4.7, an energy resolution of 180 eV is adequate to measure its gamma-ray signature.

7.2 Measurements in Pulse Tube Cryostat

7.2.1 Noise Performance

The superconducting quantum interference device (SQUID) preamplifier and TES sensor operated in the liquid cryogen system were moved to the PTR system discussed in the Chapter 5. This pulse tube system was originally designed for TES arrays and was modified to work with a single preamplifier and TES sensor. While the 300 K to 4 K wiring was unchanged, a printed circuit (PC) board was fabricated to accommodate the wiring from the 4 K stage to the detector (100 mK) stage. Additionally, the detector stage was redesigned for testing sensors and operating single TES devices. Following the modification of the cryostat and the installation of this sensor and readout electronics,

the noise performance of the device was measured. As shown in Figure 7.3, the noise contribution from the PTR system was initially several orders of magnitude greater than that in the liquid dewar. Despite having nominally similar circuits for readout, the initial measurements taken in the PTR system had an energy resolution of approximately ~ 5 keV. In order to reduce the noise numerous modifications were made to the cryostat and associated electronics. The cables used for temperature regulation and control of the heat switch motor were filtered using 220 nF and 22 nF capacitive filters, respectively. A cable shield was added to the ADR magnet and heat switch cables and were connected at a single common point ground. The rotary valve was operated using a three phase power supply and the cable connecting the two was found to produce substantial radiative noise, requiring additional cable shields and grounding. For the readout electronics, the preamplifier output was filtered with 4 μ F filters and the electrical power for both the preamplifier and bias circuitry were transferred to 12 V DC battery power. The cryostat electronics, including the magnet and heat switch power supplies, temperature controllers, and computer were moved to an isolation transformer to prevent interference caused by ground loops. The rotary valve generated substantial pickup and was separated from the other electronics and connected via a separate isolation transformer. Both isolation transformers, instrumentation racks, and cryostat were connected to a common earth ground. With these modifications, the noise floor of the SQUID preamplifier, shown in Figure 7.3, was substantially reduced and subsequently the resolution of the device improved.

In addition to the 60 Hz pickup seen in earlier measurements, additional frequencies associated with relatively high amplitude noise appear in the noise spectrum. The source of this noise has been experimentally demonstrated to arise from the cooling system. To isolate the source of this pickup, a noise measurement was made with the compressor and rotary valve turned off and another with the compressor shut off and the rotary valve on for a short period of time (< 10 s). Although both components should be operated simultaneously, the rotary valve can be operated briefly without the compressor without damaging the system. The measured noise from these two tests are shown in Figure 7.4. As can be seen the noise in the 7 kHz region is the result of the compressor operation and not from the rotary valve. Unfortunately both are needed to maintain the cooling of the cryostat and therefore it is not possible to eliminate this pickup. Potential methods to suppress this noise are discussed in Chapter 8.2. These noise sources were included in the noise model and both the model and experimental measurement are shown in Figure 7.5. The model uses the same detector properties as those in Table 7.1 with the addition of the pickup at specific frequencies. The modeled noise is in good agreement with the experiment, although at higher frequencies the model predicts a lower total noise than was measured. This is the result of feedback in the room temperature amplifiers and is not included in the complex calorimeter model.

The signal and noise spectrum from the model can be compared with a measured pulse from the TES. The results of the model can be converted to the time domain for a comparison with the measured voltage pulse from the TES during operation. A comparison

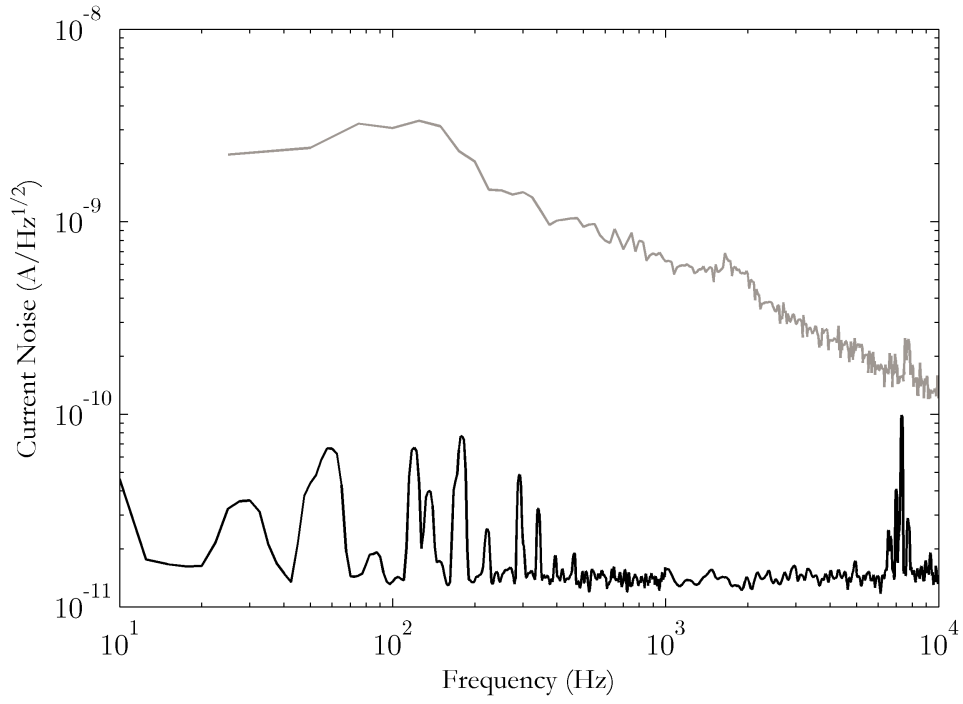


Figure 7.3: Current noise from the transition edge sensor referred to the SQUID input coil taken shortly after the sensor was operational (gray line), and after modification to the cryostat were made to reduce the noise (black line).

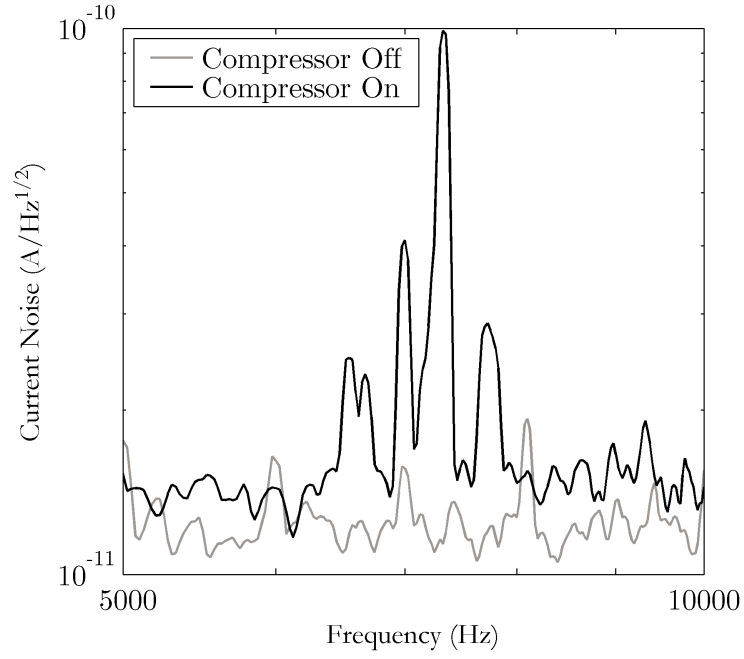


Figure 7.4: The noise measured at the input of the SQUID with the compressor on and off.

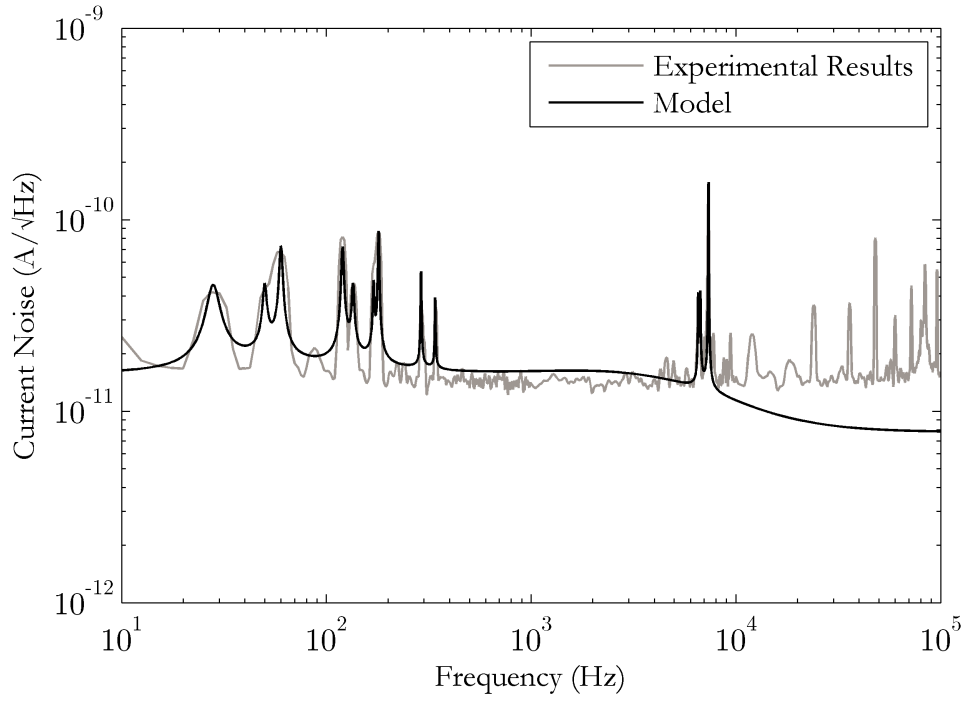


Figure 7.5: Current noise as measured at the input of the SQUID operated in PTR system.

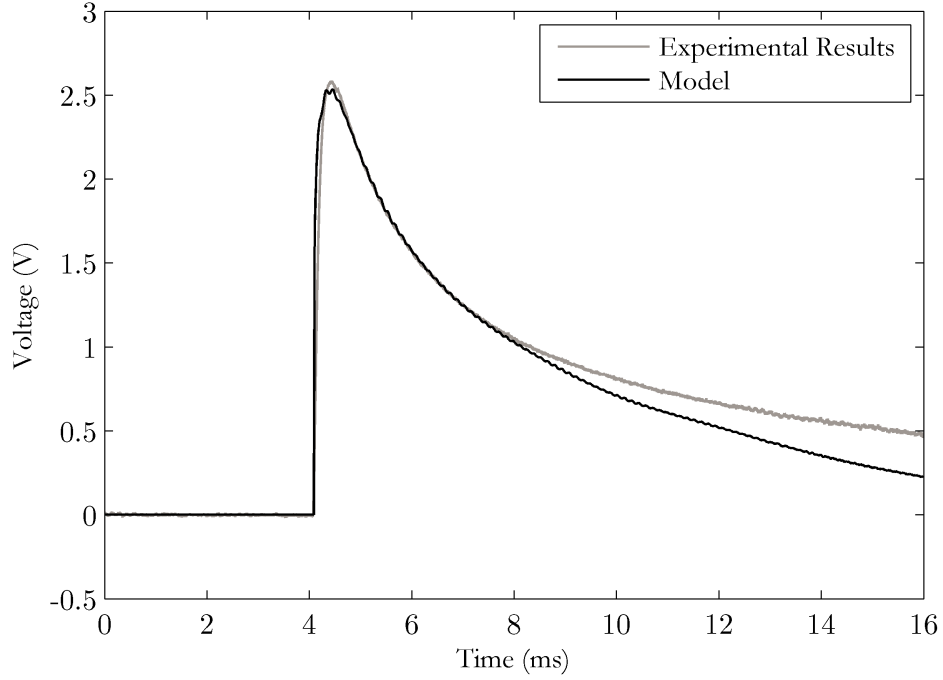


Figure 7.6: TES pulse and pulse generated from complex calorimeter model.

of the observed and modeled pulses are shown in Figure 7.6. The modeled pulse has a rise time $300 \mu\text{sec}$, as set by the thermal conductance of the Stycast connecting the absorber to the TES. The decay time of the pulse, determined by the thermal conductance of the SiN membrane is $\sim 10 \text{ ms}$. While the modeled pulse is in overall agreement with the measured pulse, the fall time is longer in the measured pulse, this long athermal decay time has been observed in other microcalorimeter systems and the origins are currently not understood [150, 151]. The inclusion of the higher frequency pickup at 7 kHz is also visible in the modeled pulse. As shown in Figure 7.7, the 7 kHz pickup can be clearly seen in both the experimental and modeled results. To understand the affect this pickup has on a spectroscopic measurement the noise profile shown in Figure 7.5 was sampled in the time domain and added to an idealized pulse from a 60 keV photon. This set of data was processed to create a energy spectrum with an energy resolution of 460 eV , in close agreement with the resolution of the measurements discussed in the following section.

7.2.2 Gamma-ray Measurements

After the reduction in noise, efforts were made to make spectroscopic measurements on ^{241}Am and ^{133}Ba sources. For this measurement, the TES was operated with a bath temperature of 95 mK . All events were recorded using a 12 bit analog-to-digital GAGE CompuScope 12100 PCI card and saved electronically for offline processing. Figure 7.6 is

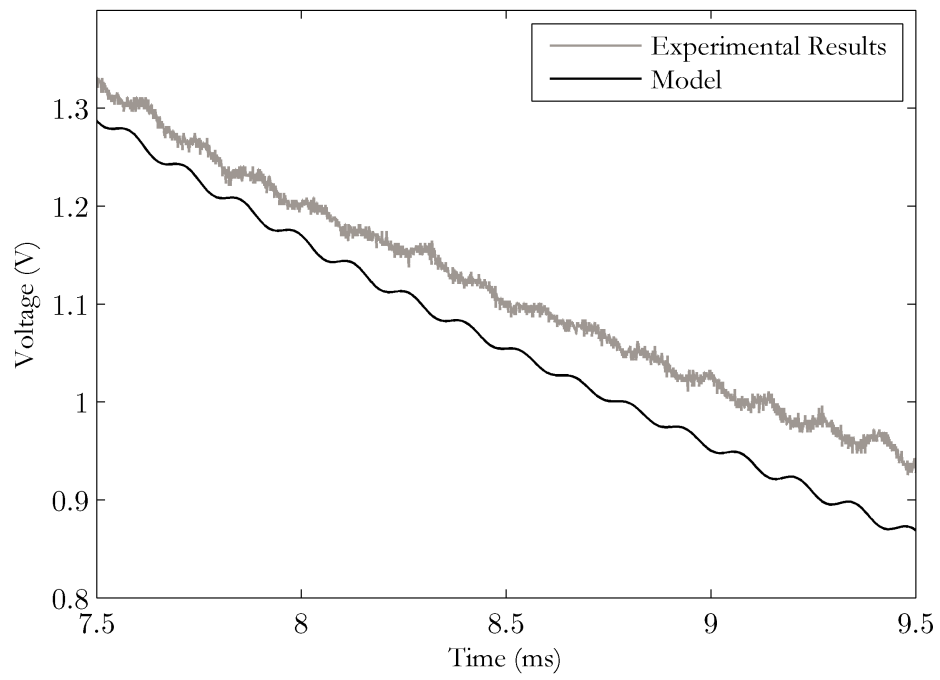


Figure 7.7: Expanded view of the TES pulse and pulse generated from complex calorimeter model with the 7 kHz pickup is clearly visible.

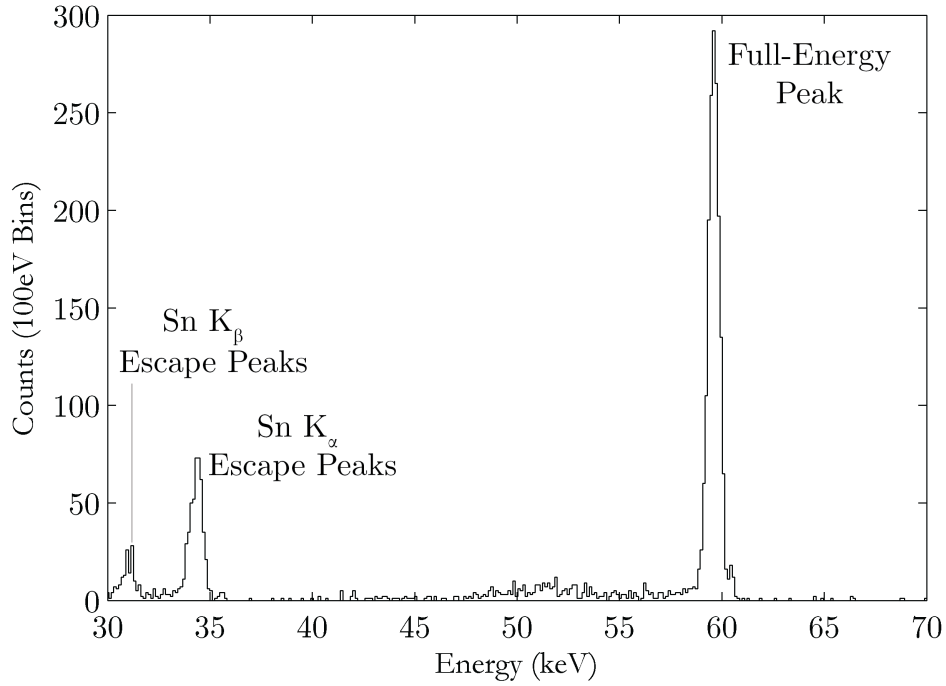


Figure 7.8: Spectrum of an ^{241}Am source taken using a single TES. The energy resolution (full width at half maximum) of the 60 keV line is 670 keV.

an example of a single event saved using the analog-to-digital system. After the acquisition, all events that appeared to be strongly affected by pickup or other anomalies were removed. The remaining pulses were then processed using an optimum (Wiener) filtering routine discussed in Appendix C. Figure 7.8 shows the spectrum from a ^{241}Am source. The photopeak at 59.5 keV and tin escape lines at 31.5 keV and 34.541 keV are visible. The energy resolution of the 59.5 keV line is 668 eV.

An additional measurement was made of ^{133}Ba , the spectrum is shown in Figure 7.9. Visible in the spectrum are the photopeak at 80.997 keV. The two large peaks at 30 and 35 keV are the result of the $K_{\alpha 2}$ and $K_{\alpha 1}$ cesium x-ray lines at 30.62 keV and 30.97 keV, and the $K_{\beta 3}$ and $K_{\beta 1}$ lines at 34.92 keV and 34.99 keV. Tin escape peaks around 52.5 keV and 55.7 keV can also be seen. The energy resolution of the 81 keV full-energy peak is 1.0 keV.

7.3 Discussion

The noise pickup in the PTR system is substantial and limits the performance of the sensor. Although the noise reduction techniques helped improved the energy resolution from ~ 5 keV to 668 eV at 60 keV, the performance is still insufficient for the direct mea-

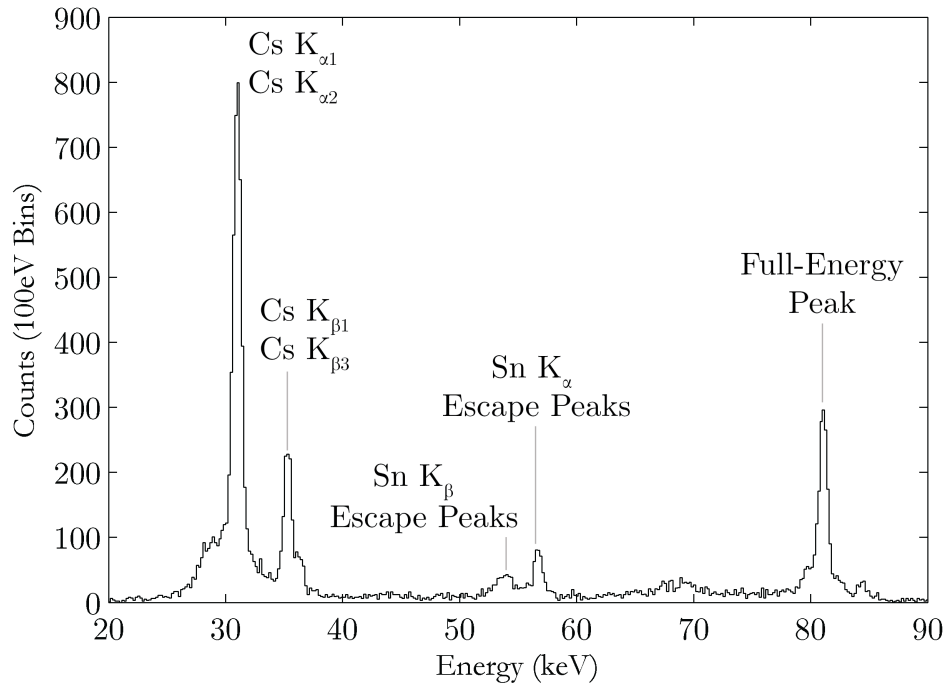


Figure 7.9: Spectrum of a ^{133}Ba source. The two low energy peaks are the result of close lying cesium $K_{\alpha 2}$ and $K_{\alpha 1}$ lines at 30.62 keV and 30.97 keV, respectively and the cesium $K_{\beta 3}$ and $K_{\beta 1}$ lines at 34.92 keV and 34.99 keV, respectively. The energy resolution (full width at half maximum) of the 80.99 keV line is 1.0 keV.

surement of ^{242}Pu . As both the compressor and rotary valve must be operated for cooling, it is not possible to remove this pickup entirely and can only be suppressed to limit the effect on the signal. The expected noise performance can be predicted using the noise model used in Section 7.1.1. The 7 kHz pickup can be removed from the model, and the resulting signal and noise can be processed in the time domain for an estimate of the energy resolution without this noise contribution. Removal of the 7 kHz pickup improves the energy resolution to approximately 370 eV. This is still higher than the energy resolution calculated in Section 7.1.1 as the pickup in the ~ 100 Hz region degrades the performance.

An estimate also can be made of the energy resolution that can be achieved in the measurement of ^{242}Pu if the 7 kHz pickup could be removed. Using the measurement precision modeled developed in Chapter 4.7 with the same detector parameters, i.e. a background of 5 counts per channel with a detector count rate of 10 Hz, the precision in the ^{242}Pu measurement can be determined and for various energy resolutions is shown in Figure 7.10. With an energy resolution of 350 eV a total uncertainty of $\sim 6\%$ in the intensity of the 44.915 – keV peak from decay of ^{242}Pu would require over 100 detector \cdot days. Multiple month measurements are prohibitive, especially when compared with existing NDA techniques that require only one day (See Table 1.1) and as discussed in Chapter 2, energy resolutions below 350 eV are necessary for direct measurements of ^{242}Pu . To obtain higher precision the energy resolution will need to be improved by at least 100 eV and multiple sensors would be needed to obtain adequate statistics on a time scale of less than one week.

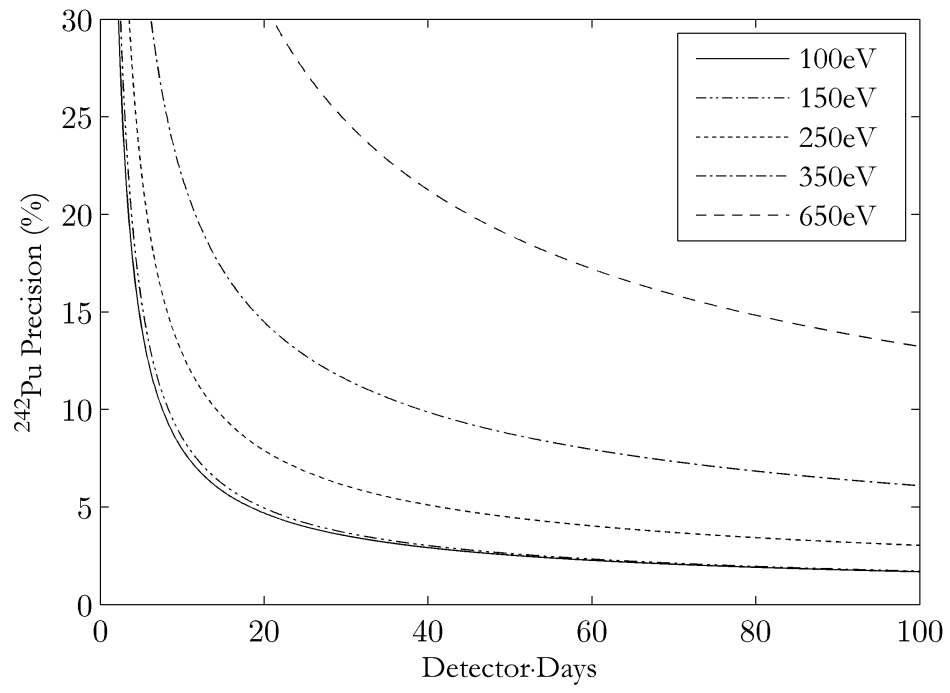


Figure 7.10: Precision in the measurement of ^{242}Pu with a single pixel detector operated at 10 Hz per pixel for different sensor energy resolutions.

Chapter 8

Summary and Conclusions

8.1 Findings

Current nondestructive analysis methods cannot measure the ^{242}Pu gamma ray signature directly, and therefore rely on correlations to infer the amount present. The uncertainty in these correlations, particularly in the case of materials of unknown origin, can be substantial and affects the overall quality of the plutonium analysis. The isotopic composition of plutonium varies with the reactor type and operating conditions and consequently is useful in determining the origin of the material. In the study of nuclear fuel from a BWR, a factor of ~ 4 improvement in the measurement of the $^{238}\text{Pu}/^{242}\text{Pu}$ atom ratio would reduce the uncertainty in the initial ^{235}U enrichment by a factor of ~ 3 . Such an improvement would prove invaluable in nuclear safeguards. This thesis has investigated the possibility of measuring gamma ray emissions from ^{242}Pu using high resolution transition edge sensors based on tin absorbers with superconducting Mo/Cu multilayer transition edge sensors.

The first part of the thesis has examined the detector requirements for measuring ^{242}Pu . To understand the limits of performance and characterize the dependence these detectors have on a variety of design parameters, an analytical model was developed. The model shows that transition edge sensors can be built to meet the performance requirements for the measurement of ^{242}Pu . From this model it was found that with nominal characteristics these devices have a limiting energy resolution of approximately 30 eV, provided the operating temperature is $< 100\text{ mK}$ and the device is limited in size to 1 mm^3 . Ideally the noise is limited by the coupling between the absorber and the transition edge sensor; however, in practice additional noise sources from pick-up and other non-idealities degrade the performance.

The dependence on the energy resolution, acquisition time and sensor volume for this measurement were discussed and quantified the accuracy and precision that can be obtained with particular sensor characteristics. From this analysis it was shown that the direct detection of the 44.915 keV gamma-ray line of ^{242}Pu is possible assuming nominal TES characteristics with 100 eV resolution and can be quantified in the presence of a ^{240}Pu gamma-ray line at 45.242 keV, even if the emission is ~ 1000 times stronger. The accuracy and precision of the measurement depends on the percentage of the ^{242}Pu in the sample, on the energy resolution of the TES detector and the total acquisition time. Based on the limitations of currently available TES fabrication techniques and the intrinsically low efficiency of the small tin absorber, it can be inferred that for concentrations of ^{242}Pu found in reactor fuel, a detector with an energy resolution of about 100 eV would have to be operated for several weeks to obtain a precision in ^{242}Pu measurement of $\sim 4\%$. To reduce the total measurement time, multiple well-characterized, high quality sensors would be required.

The second part of this thesis discussed the efforts to implement such a detector. Measurements made using a liquid cryogen system of a uranium oxide sample had an energy resolution of 180 eV for a single TES operated for six hours. To obtain better statistics, four acquisitions were made and the spectra summed. Small nonlinearities

in the detector response and drift in the signal height over days of operation degraded the energy resolution to ~ 200 eV. Although this resolution is well above the 30 eV theoretical limit, it is still sufficient to measure ^{242}Pu as the peak separation is 324 eV and it is reasonable to assume that currently available spectral analysis programs can extract the intensity of the low energy peak without significant error above that of counting statistics. To operate this sensor without the use of expensive liquid cryogenics, we have designed and built, in collaboration with VeriCold Technologies, a liquid cryogen free PTR system. This system uses pressurized helium for precooling to 3 K and an ADR stage to cool to < 100 mK. The mechanical cooling system introduced significant noise requiring substantial modifications to the cryostat and support electronics to reduce. With these improvements the best performance obtained with this TES was 670 eV at 60 keV. At present the performance of the sensor is limited by the pickup from the compressor required to maintain the precooling stage. To suppress this significant pickup will require additional modifications to the compressor and rotary valve.

Transition edge sensors have achieved energy resolution of 60 – 90 eV for gamma-rays up to 100 keV. This energy resolution is sufficient for the measurement of the ^{242}Pu gamma ray. Simulations have indicated that the increased resolution combined with the decreased Compton continuum allows for the detection of this isotope in reactor grade plutonium samples. However, this gamma-signature is weak and with the low count rate of the TES long acquisition times and/or multiple sensors are required to obtain sufficiently small total uncertainties. Measurements made using the liquid cryogen system have shown an energy resolution of approximately 180 eV at 60 keV. Operation of this sensor in the pulse tube refrigeration system had higher noise due to the pickup from the compressor used for cooling. Despite signal filtering and additional shielding the sensor could not provide the energy resolution necessary for the direct measurement of the 44.915 keV gamma ray of ^{242}Pu . Despite this, the data can be accurately reproduced using a numerical noise model. If the noise contributions from the mechanical cooling could be suppressed, the performance of the device would be ~ 250 eV, adequate to demonstrate the feasibility of this measurement.

8.2 Future Efforts

Through this research questions have arisen that require further investigation. To precisely measure low-intensity gamma-ray signatures, arrays of well-characterized sensors must be fabricated. Liquid cryogen systems are expensive to operate; however, the additional noise from PTR systems must be reduced in order for practical measurements to be made. Further reduction in the noise level will require additional modifications to the cryostat. The helium lines provide an electrical connection from the compressor to the rotary valve and cryostat, and are a coupling path for the compressor noise into the system. Nonconductive fittings should be added to these lines to electrically isolate the cryostat from the compressor and prevent this pickup. As the helium lines are ~ 50 ft in

length, the compressor can also be relocated to another room and powered from an electrical distribution panel on a circuit separate from the cryostat and readout electronics to reduce the interference from the magnetic fields emitted from the compressor. If these improvements are successful in removing the excess noise, this work has shown that these sensors hold promise for high resolution spectroscopic measurements in nuclear safeguards.

Bibliography

- [1] Office Of Technology Assessment. *Nuclear Safeguards and the International Atomic Energy Agency*. AD-a338 840. Office of Technology Assessment, Washington DC, 1995.
- [2] National Security Strategy, May 2010.
- [3] J. Doyle. *Nuclear Safeguards, Security and Nonproliferation: Achieving Security with Technology and Policy*. Butterworth-Heinemann homeland security series. Butterworth-Heinemann, 2008.
- [4] G. Perkovich. The Plutonium Genie. *Foreign Affairs*, 72(3):pp. 153–165, 1993.
- [5] Frank von Hippel, Rodney Ewing, Richard Garwin, and Allison Macfarlane. Nuclear proliferation: Time to bury plutonium. *Nature*, 485(7397):167–168, May 2012.
- [6] G. Cameron. *Nuclear Terrorism: A Threat Assessment for the 21st Century*. Palgrave Macmillan, 1999.
- [7] M. Bunn. *Securing the Bomb 2010*. Cambridge, Mass., and Washington, D.C., April 2010.
- [8] International Panel on Fissile Materials. *Global Fissile Material Report 2007*. Princeton, NJ, 2007.
- [9] OECD-NEA. Nuclear Energy Outlook 2008. Technical Report 6348, 2008.
- [10] K. Fukuda, Y. Peryoga, H. Sagara, M. Saito, and M. Ceyhan. Perspectives of inventories of secondary nuclear materials generated in the nuclear energy production and mass balance in PPP cycle. *Progress in Nuclear Energy*, 50:654 – 659, 2008. Innovative Nuclear Energy Systems for Sustainable Development of the World. Proceedings of the Second COE-INES International Symposium, INES-2, November 26-30, 2006, Yokohama, Japan.
- [11] D. Holdstock and F. Barnaby. *Hiroshima and Nagasaki: Retrospect and Prospect*. F. Cass, 1995.

- [12] T. B. Taylor. Nuclear Safeguards. *Annual Review of Nuclear Science*, 25(1):407–421, 1975.
- [13] Office of Technology Assessment U.S. Congress. *Technologies underlying weapons of mass destruction*. U.S. Government Printing Office, 1993.
- [14] P. Lettow. *Strengthening the Nuclear Nonproliferation Regime*. Council on Foreign Relations Press, 2010.
- [15] International Atomic Energy Agency. Against the Spread of Nuclear Weapons: IAEA Safeguards in the 1990s, December 1993. 93-04459, IAEA/PI/A38E.
- [16] International Atomic Energy Agency. IAEA Safeguards Glossary 2001 Edition. International Nuclear Verification Series 3, International Atomic Energy Agency, 2001.
- [17] E. A. Hakkila and T. Burr. Safeguards considerations in the study of proliferation resistance of plutonium disposition options. Technical Report LA-UR-97-2676, Los Alamos National Lab, NM (United States), November 1997.
- [18] International Atomic Energy Agency. *Safeguards Techniques and Equipment (International Nuclear Verification Series)*. IAEA, 2011.
- [19] R. Avenhaus. *Verifying Treaty Compliance: Limiting Weapons of Mass Destruction And Monitoring Kyoto Protocol Provisions*. Springer, 2006.
- [20] A. Vértes, S. Nagy, Z. Klencsár, R.G. Lovas, and F. Rösch. *Handbook of Nuclear Chemistry*. Number v. 5. Springer, 2010.
- [21] C. Grupen and I. Buvat. *Handbook of Particle Detection and Imaging*. Number v. 1 in Springer reference. Springer, 2012.
- [22] M.A. Levi and Council on Foreign Relations. *On Nuclear Terrorism*. Harvard University Press, 2007.
- [23] G. B. Dudder, S. Niemeyer, D. K. Smith, and M. J. Kristo. Model Action Plan for Nuclear Forensics and Nuclear Attribution. Technical Report UCRL-TR-202675, Lawrence Livermore National Lab., Livermore, CA (US), March 2004.
- [24] International Atomic Energy Agency. *Nuclear Forensics Support*. Vienna, 2006.
- [25] K. Mayer. Activities of the Working Group for Destructive Analysis. *ESARDA Bulletin*, 30:26–27, 2000.
- [26] M. Sturm. Destructive Analysis: Effective Analytical Support to Nuclear Safeguards and Non-Proliferation. *ESARDA Bulletin*, 45:56–65, 2010.

- [27] M. May, R. Abedin-Zadeh, D. Barr, et al. Nuclear Forensics: Role, State of the Art, Program Needs. Technical report, Nuclear Forensics Working Group of the American Physical Society's Panel on Public Affairs and the American Association for the Advancement of Science., 2008.
- [28] J. Svedkauskaite-LeGore, G. Rasmussen, C. Vincent, P. van Belle, and S. Abousahl. Importance of the impurity spectrum in nuclear materials for nuclear safeguards. In IAEA, editor, *Proceedings of an International Safeguards Symposium Vienna*,, pages 533–539, Vienna, October 2006.
- [29] F. Simon. Application of Low Temperature Calorimetry to Radioactive Measurements. *Nature*, 135:763, May 1935.
- [30] D. H. Andrews, W. F. Brucksch, W. T. Ziegler, and E. R. Blanchard. Attenuated Superconductors I. For Measuring Infra-Red Radiation. *Review of Scientific Instruments*, 13(7):281 –292, jul 1942.
- [31] D.H. Andrews, R.D. Fowler, and M.C. Williams. The Effect of Alpha-particles on a Superconductor. *Physical Review*, 76:154–155, July 1949.
- [32] S. H. Moseley, J. C. Mather, and D. McCammon. Thermal detectors as x-ray spectrometers. *Journal of Applied Physics*, 56:1257–1262, September 1984.
- [33] B. Cabrera, L. M. Krauss, and F. Wilczek. Bolometric detection of neutrinos. *Phys. Rev. Lett.*, 55:25–28, Jul 1985.
- [34] E. Fiorini and T.O. Niinikoski. Low-temperature calorimetry for rare decays. *Nuclear Instruments and Methods in Physics Research*, 224(1-2):83–88, 1984.
- [35] D.T Chow, M.A Lindeman, M.F Cunningham, et al. Gamma-ray spectrometers using a bulk Sn absorber coupled to a Mo/Cu multilayer superconducting transition edge sensor. *Nuclear Instruments and Methods in Physics Research Section A: Accelerators, Spectrometers, Detectors and Associated Equipment*, 444(1-2):196–200, 2000.
- [36] D.T. Chow, M.L. van den Berg, A. Loshak, et al. Gamma-ray spectrometers using superconducting transition edge sensors with external active feedback bias. *Applied Superconductivity, IEEE Transactions on*, 11(1):743 –746, mar 2001.
- [37] S. Terracol, T. Miyazaki, U. Morita, et al. The non-equilibrium response of a high-resolution Ti/Au X-ray microcalorimeter. *Nuclear Instruments and Methods in Physics Research Section A: Accelerators, Spectrometers, Detectors and Associated Equipment*, 520(1-3):300–302, 2004. Proceedings of the 10th International Workshop on Low Temperature Detectors.

- [38] S. F. Terracol, S. Ali, I. Niedermayr, et al. Ultra-high resolution gamma-ray spectrometer development for nuclear attribution and non-proliferation applications. In *Proc. IEEE Nuclear Science Symp. Conf. Record*, volume 2, pages 1006–1013, 2004.
- [39] S Friedrich, M Velazquez, O Drury, and S Salaymeh. Report on Ultra-high Resolution Gamma- / X-ray Analysis of Uranium Skull Oxide. Technical Report LLNL-TR-419842, Lawrence Livermore National Laboratory (LLNL), Livermore, CA, November 2009.
- [40] M.W. Rabin. National and International Security Applications of Cryogenic Detectors-Mostly Nuclear Safeguards. In B. Young, B. Cabrera, and A. Miller, editors, *American Institute of Physics Conference Series*, volume 1185 of *American Institute of Physics Conference Series*, pages 725–732, December 2009.
- [41] S. Friedrich. Nuclear diagnostics with cryogenic spectrometers. *Nuclear Instruments and Methods in Physics Research Section A: Accelerators, Spectrometers, Detectors and Associated Equipment*, 579(1):157 – 160, 2007. Proceedings of the 11th Symposium on Radiation Measurements and Applications.
- [42] M. F. Cunningham, J. N. Ullom, T. Miyazaki, et al. High-resolution operation of frequency-multiplexed transition-edge photon sensors. *Applied Physics Letters*, 81(1):159 –161, jul 2002.
- [43] J.N. Ullom, M.F. Cunningham, T. Miyazaki, et al. A frequency-domain read-out technique for large microcalorimeter arrays demonstrated using high-resolution gamma;-ray sensors. *Applied Superconductivity, IEEE Transactions on*, 13(2):643 – 648, june 2003.
- [44] M.K. Bacrania, A.S. Hoover, P.J. Karpus, et al. Large-Area Microcalorimeter Detectors for Ultra-High-Resolution X-Ray and Gamma-Ray Spectroscopy. *Nuclear Science, IEEE Transactions on*, 56(4):2299 –2302, aug. 2009.
- [45] S. Friedrich, S. F. Terracol, T. Miyazaki, et al. Design of a multichannel ultra-high-resolution superconducting gamma-ray spectrometer. In A. Burger, R.B. James, and L.A. Franks, editors, *Society of Photo-Optical Instrumentation Engineers (SPIE) Conference Series*, volume 5540 of *Society of Photo-Optical Instrumentation Engineers (SPIE) Conference Series*, pages 156–164, Oct 2004.
- [46] N. Jethava, J.N. Ullom, D.A. Bennett, et al. Improved Isotopic Analysis With a Large Array of Gamma-Ray Microcalorimeters. *Applied Superconductivity, IEEE Transactions on*, 19(3):536 –539, june 2009.
- [47] G. T. Seaborg. The Plutonium Story. Technical Report LBL-13492, Lawrence Berkeley Nat. Lab., Berkeley, CA, Sep 1981.

- [48] E. McMillan and Philip H. Abelson. Radioactive Element 93. *Phys. Rev.*, 57:1185–1186, Jun 1940.
- [49] J. W. Kennedy, G. T. Seaborg, E. Segrè, and A. C. Wahl. Properties of 94(239). *Phys. Rev.*, 70:555–556, Oct 1946.
- [50] J. Emsley. *Nature's Building Blocks: Everything You Need to Know About the Elements*. Oxford University Press, 2011.
- [51] D.C. Hoffman, F.O. Lawrence, J.L. Mewherter, and F.M. Rourke. Detection of Plutonium-244 in Nature. *Nature*, 234:132–134, Nov 1971.
- [52] K.S. Krane. *Introductory Nuclear Physics*. Wiley, 1987.
- [53] L. A. Carillo P. A. Hypes C. R. Rudy C. M. Schneider M. K. Smith D. S. Bracken, R. S. Biddle. *Application Guide to Safeguards Calorimetry*. LA-13867-M, January 2002.
- [54] J. J. Duderstadt and L. J. Hamilton. *Nuclear reactor analysis*. Wiley, New York :, 1976.
- [55] M. Benedict, T.H. Pigford, and H.W. Levi. *Nuclear chemical engineering*. McGraw-Hill series in nuclear engineering. McGraw-Hill, 1981.
- [56] G. Kessler. *Proliferation-Proof Uranium/ Plutonium Fuel Cycles: Safeguards and Non-Proliferation*. KIT Scientific Publishing, 2011.
- [57] S. Guardini. Performance values for non-destructive assay (NDA) techniques applied to safeguards: the 2002 evaluation by the ESARDA NDA Working Group. *ESARDA Bulletin*, 1(32):12–54, March 2004.
- [58] D. Bodansky. *Nuclear Energy: Principles, Practices, and Prospects*. Springer, 2004.
- [59] J.R. Phillips, G.E. Bosler, J.K. Halbig, et al. Neutron measurement techniques for the nondestructive analysis of irradiated fuel assemblies. Technical Report LA-9002-MS, Los Alamos National Lab., NM (USA), Nov 1981.
- [60] International Atomic Energy Agency. Nuclear Fuel Cycle Simulation System (VISTA). Technical report, International Atomic Energy Agency, 2007.
- [61] S. Sanatani. Applications of Isotopic Correlation Technique (ICT) to International Safeguards. *ESARDA Symp. on Isotopic Correlation and Its Application to the Nuclear Fuel Cycle*, ICT-19, May 1978.
- [62] B. Brandalise, L. Koch, C. Rijkeboer, and D. Romkowsk. The Application of Isotope Correlations in Verifying Automatic Analyses of Irradiated Fuels. *ESARDA Symp. on Isotopic Correlation and Its Application to the Nuclear Fuel Cycle*, ICT-19, 1978.

- [63] M. Wallenius and K. Mayer. Age determination of plutonium material in nuclear forensics by thermal ionisation mass spectrometry. *Fresenius' Journal of Analytical Chemistry*, 366:234–238, 2000.
- [64] G. Nicolaou. Determination of the origin of unknown irradiated nuclear fuel. *Journal of Environmental Radioactivity*, 86(3):313 – 318, 2006.
- [65] M. Robel and M. J. Kristo. Discrimination of source reactor type by multivariate statistical analysis of uranium and plutonium isotopic concentrations in unknown irradiated nuclear fuel material. *Journal of Environmental Radioactivity*, 99(11):1789 – 1797, 2008.
- [66] M. Wallenius, P. Peerani, and L. Koch. Origin Determination of Plutonium Material in Nuclear Forensics. *Journal of Radioanalytical and Nuclear Chemistry*, 246:317–321, 2000.
- [67] T.S. Reilly and M-L. Evans. *Measurements reliability for nuclear materials assay*. LA-6574, January 1977.
- [68] F. X. Haas and W. W. Strohm. Gamma-Ray Spectrometry for Calorimetric Assay of Plutonium Fuels. *Nuclear Science, IEEE Transactions on*, 22(1):734 –738, February 1975.
- [69] M. S. Krick D. G. Langner M. M. Pickrell J. E. Stewart N. Ensslin, W. C. Harker. *Application Guide to Neutron Multiplicity Counting*. LA-13422-M, November 1998.
- [70] S. Croft P.M.J. Chard L.C.-A. Bourva U. Blohm-Hieber H. Ottmar, P. Van Belle. An empirical measurement of the specific ^{240}Pu -effective mass of ^{238}Pu and ^{242}Pu . In *Proceedings of the 21st ESARDA Symposium on Safeguards and Nucl. Mater. Manage.*, May 1999.
- [71] S. Croft and P.M.J. Chard. Neutronic characterisation of plutonium reference samples at Harwell. *ESARDA Symp. on Safeguards and Nuclear Materials Management*, (EUR 15214EN):511–519, 1993.
- [72] D.M. Cifarelli and W. Hage. Models for a three-parameter analysis of neutron signal correlation measurements for fissile material assay. *Nuclear Instruments and Methods in Physics Research Section A: Accelerators, Spectrometers, Detectors and Associated Equipment*, 251(3):550 – 563, 1986.
- [73] T. E. Sampson. Plutonium isotopic composition by gamma-ray spectroscopy: A review. Technical Report LA-10750-MS, Los Alamos National Laboratory, September 1986.
- [74] G. Tokcan and C.R. Cothorn. Efficiency Determinations for a Ge (Li) Detector. *The Ohio Journal of Science*, 69:92–100, March 1969.

- [75] H. Seyfarth, A.M. Hassan, B. Hrastnik, P. Gottel, and W. Delang. Efficiency determination for some standard type Ge(Li) detectors for gamma-rays in the energy range from 0.04 to 11 MeV. *Nuclear Instruments and Methods*, 105(2):301 – 310, 1972.
- [76] T.K. Li, T.E. Sampson, and S.S. Johnson. Plutonium isotopic measurement for small product samples. Technical Report LA-UR-83-1115, Los Alamos National Lab, NM (USA), January 1983.
- [77] P.A. Russo, S.T. Hsue, J.K. Jr. Sprinkle, et al. In-plant measurements of gamma-ray transmissions for precise K-edge and passive assay of plutonium concentration and isotopic fractions in product solutions. Final report on TASTEX Task G. Technical report, Los Alamos National Lab., NM (USA), 1982.
- [78] R. Gunnink. MGA: A Gamma Ray Spectrum Analysis Code for Determining Plutonium Isotopic Abundances. Technical Report UCRL LR 03220, Lawrence Livermore National Laboratory, 1990.
- [79] T.E. Sampson, G.W. Nelson, and T.A. Kelley. FRAM: A versatile code for analyzing the isotopic composition of plutonium from gamma-ray pulse height spectra. Technical Report LA-11720-MS, Los Alamos National Laboratory, 1989.
- [80] R. Gunnink. Status of Plutonium Isotopic Measurements by Gamma-ray Spectrometry. Technical Report UCRL 76418, Lawrence Livermore National Laboratory, 1975.
- [81] R. Gunnink. An algorithm for fitting Lorentzian-broadened, K-series X-ray peaks of the heavy elements. *Nuclear Instruments and Methods*, 143(1):145 – 149, 1977.
- [82] R. Gunnink. Use of isotope correlation techniques to determine ^{242}Pu abundance. Technical Report UCRL-84096, Lawrence Livermore National Laboratory, 1980.
- [83] C.L. Timmerman. Isotopic safeguards data bank (ISTLIB) and control program (MISTY). Technical Report ISPO-34; PNL-2726, Battelle Pacific Northwest Labs, Richland, WA (USA), September 1978.
- [84] C.L. Timmerman, G.P. Selby, B.A. Napier, et al. *Selected Isotopic Functions: A Description and Demonstration of Their Uses*. Pacific Northwest Laboratory, 1978.
- [85] H. Natsume, H. Okashita, H. Umezawa, et al. Gamma-Ray Spectrometry and Chemical Analysis Data of JPDR-I Spent Fuel. *Journal of Nuclear Science and Technology*, 14(10):745–761, 1977.
- [86] H. Ottmar. MGA in K-edge gamma and neutron-gamma counters. In *Proceedings of the MGA User's Workshop*, September 1994.

- [87] W.O. Ruhter, R. Gunnink, S. Baumann, S. Abeynaike, and J. Verplancke. MGA and Passive Neutron Measurements. In *Proceedings ESARDA International Workshop on Passive Neutron Coincidence Counting*, August 1993.
- [88] G. Bignan, W. Ruhter, H. Ottmar, A. Schubert, and C. Zimmerman. Plutonium Isotopic Determination By Gamma Spectrometry: Recommendations for the ^{242}Pu content evaluation using a new algorithm. *ESARDA BULLETIN*, 28:1–6, 1998.
- [89] J. Morel, M. Bickel, C. Hill, and A. Verbruggen. Results of the international Pu-2000 exercise for plutonium isotopic composition measurements. *Applied Radiation and Isotopes*, 60(2-4):607–614, 2004. Proceedings of the 14th International Conference on Radionuclide Metrology and its Applications, ICRM 2003.
- [90] P. van Belle T. van Vuure-K. Burke J. Mason-A. Tolchard A. Towner H. Ottmar, S. Abousahl. A combined calorimetry, neutron coincidence counting and gamma spectrometry system (CANEGA) for enhanced plutonium mass and isotopic assay. In *Addressing Verification Challenges*, number IAEA-CN-148/84, pages 495–520, 2006.
- [91] Oak Ridge National Laboratory. SCALE: A Modular Code System for Performing Standardized Computer Analyses for Licensing Evaluations. Technical Report ORNL/TM-2005/39, Oak Ridge National Laboratory, 2009.
- [92] G. Ilas, I. C. Gauld, and V. Jodoin. LWR Cross Section Libraries for ORIGEN-ARP in SCALE 5.1. *Transactions - American Nuclear Society*, 95:706–708, 2006.
- [93] C. Kittel. *Introduction to solid state physics*. John Wiley & Sons, Inc., 2005.
- [94] R.D. Evans. *The Atomic Nucleus*. McGraw-Hill, Inc., New York, 1955.
- [95] J.R. Olson. Thermal conductivity of some common cryostat materials between 0.05 and 2 K. *Cryogenics*, 33(7):729 – 731, 1993.
- [96] L. N. Cooper. Bound Electron Pairs in a Degenerate Fermi Gas. *Phys. Rev.*, 104:1189–1190, Nov 1956.
- [97] J. Bardeen, L. N. Cooper, and J. R. Schrieffer. Theory of Superconductivity. *Phys. Rev.*, 108:1175–1204, Dec 1957.
- [98] T.J. Sumner, S.M. Grant, D. Alexiev, and K.S.A. Butcher. LPE GaAs as an X-ray detector for astronomy. *Nuclear Instruments and Methods in Physics Research Section A: Accelerators, Spectrometers, Detectors and Associated Equipment*, 348:518–521, 1994.

- [99] M. Kurakado and H. Mazaki. Possibility of a high-resolution nuclear radiation detector using a superconductor: II. Tunnel junction. *Nuclear Instruments and Methods in Physics Research*, 185(1-3):149 – 155, 1981.
- [100] R. S. Collier and R. A. Kamper. Energy Gap of Superconducting Tin Films in a Magnetic Field. *Phys. Rev.*, 143:323–328, Mar 1966.
- [101] S. B. Kaplan, C. C. Chi, D. N. Langenberg, et al. Quasiparticle and phonon lifetimes in superconductors. *Phys. Rev. B*, 14:4854–4873, Dec 1976.
- [102] W.H. Parker. Effective quasiparticle lifetime in superconducting Sn. *Solid State Communications*, 15(6):1003 – 1006, 1974.
- [103] A. Zehnder. Response of superconductive films to localized energy deposition. *Phys. Rev. B*, 52:12858–12866, Nov 1995.
- [104] J. Chang and D. J. Scalapino. Kinetic-equation approach to nonequilibrium superconductivity. *Phys. Rev. B*, 15:2651–2670, Mar 1977.
- [105] H. J. Maris and S. Tamura. Anharmonic decay and the propagation of phonons in an isotopically pure crystal at low temperatures: Application to dark-matter detection. *Phys. Rev. B*, 47:727–739, Jan 1993.
- [106] K. D. Irwin. An application of electrothermal feedback for high resolution cryogenic particle detection. *Applied Physics Letters*, 66(15):1998–2000, 1995.
- [107] F. Pobell. *Matter and Methods at Low Temperatures 2nd ed.* Springer, New York, New York, 1996.
- [108] W.S. Boyle and Jr. K.F. Rodgers. Performance Characteristics of a New Low-Temperature Bolometer. *J. Opt. Soc. Am.*, 49(1):66–69, Jan 1959.
- [109] J. C. Mather. Bolometer noise: nonequilibrium theory. *Applied Optics*, 21:1125–1129, 1982.
- [110] K. Irwin and G. Hilton. *Cryogenic Particle Detection*, chapter Transition-edge sensors, pages 63–149. Berlin: Springer, July 2005.
- [111] M. A. Lindeman. *Microcalorimetry and the Transition-Edge Sensor*. PhD thesis, University of California Davis, March 2000.
- [112] E. F. Feliciano. *Theory and Development of Position-Sensitive Quantum Calorimeters*. PhD thesis, Stanford University, October 2001.
- [113] P. L. Richards. Bolometers for infrared and millimeter waves. *Journal of Applied Physics*, 76(1):1 –24, jul 1994.

- [114] H. Spieler. *Semiconductor Detector Systems*. Series on Semiconductor Science and Technology. Oxford University Press, 2005.
- [115] D. McCammon. *Cryogenic Particle Detection*, chapter Thermal Equilibrium Calorimeters - An Introduction, pages 1–34. Berlin: Springer, July 2005.
- [116] S. Agostinelli, J. Allison, K. Amako, et al. Geant4 - a simulation toolkit. *Nuclear Instruments and Methods in Physics Research Section A: Accelerators, Spectrometers, Detectors and Associated Equipment*, 506(3):250–303, 2003.
- [117] P. L. Ryder. Theoretical Analysis of Statistical Limitations to the Accuracy and Spectral Resolution in Energy Dispersive X-ray Analysis. In *Proceedings of the Workshop on Analytical Electron Microscopy*, volume 1, pages 273–280, Chicago, IL, March 1977.
- [118] R. Keyser and T. Twomey. Detector resolution required for accurate identification in common gamma-ray masking situations. *Journal of Radioanalytical and Nuclear Chemistry*, 282:841–847, 2009. 10.1007/s10967-009-0233-1.
- [119] P. G. De Gennes. Boundary Effects in Superconductors. *Rev. Mod. Phys.*, 36:225–237, Jan 1964.
- [120] L. N. Cooper. Superconductivity in the Neighborhood of Metallic Contacts. *Phys. Rev. Lett.*, 6:689–690, Jun 1961.
- [121] Z.A. Ali, O.B. Drury, M.F. Cunningham, et al. Fabrication of Mo/Cu multilayer and bilayer transition edge sensors. *Applied Superconductivity, IEEE Transactions on*, 15(2):526 – 529, june 2005.
- [122] C. Wang, G. Thummes, and C. Heiden. A two-stage pulse tube cooler operating below 4 K. *Cryogenics*, 37(3):159 – 164, 1997.
- [123] R. Radebaugh. Development of the Pulse Tube Refrigerator as an Efficient and Reliable Cryocooler. In *Proceedings of the Institute of Refrigeration*, volume 96, pages 11–31, London, 2001.
- [124] R. N. Richardson and B. E. Evans. A review of pulse tube refrigeration. *International Journal of Refrigeration*, 20(5):367 – 373, 1997.
- [125] I. A. Tanaeva. *Low-temperature cryocooling*. PhD thesis, Eindhoven University of Technology, 2004.
- [126] N. Jiang, U. Lindemann, F. Giebeler, and G. Thummes. A ^3He pulse tube cooler operating down to 1.3 K. *Cryogenics*, 44(11):809 – 816, 2004.

- [127] A. T. A. M. de Waele, I. A. Tanaeva, and Y. L. Ju. Multistage pulse tubes. *Cryogenics*, 40(7):459 – 464, 2000.
- [128] D. De Klerk and M.J. Steenland. Chapter XIV Adiabatic Demagnetization. volume 1 of *Progress in Low Temperature Physics*, pages 273 – 335. Elsevier, 1955.
- [129] A.T Serlemitsos, M SanSebastian, and E Kunes. Design of a spaceworthy adiabatic demagnetization refrigerator. *Cryogenics*, 32(2):117 – 121, 1992. Space Cryogenics Workshop.
- [130] G. K. White. *Experimental Techniques in Low-Temperature Physics*. Oxford University Press, USA, 1987.
- [131] C. Hagmann and P.L. Richards. Two-stage magnetic refrigerator for astronomical applications with reservoir temperatures above 4 K. *Cryogenics*, 34(3):221–226, 1994.
- [132] E. W. Hornung, R. A. Fisher, G. E. Brodale, and W. F. Giauque. Magnetothermodynamics of gadolinium gallium garnet. II. Heat capacity, entropy, magnetic moment from 0.5 to 4.2°K, with fields to 90 kG, along the [111] axis. *The Journal of Chemical Physics*, 61:282–291, 1974.
- [133] J. A. Sauer. On the Adiabatic Demagnetization of Iron Alum. *Phys. Rev.*, 64(3-4):94, Aug 1943.
- [134] O. E. Vilches and J. C. Wheatley. Measurements of the Specific Heats of Three Magnetic Salts at Low Temperatures. *Phys. Rev.*, 148(2):509–516, Aug 1966.
- [135] J. Apostolakis, S. Giani, M. Maire, et al. GEANT4 low energy electromagnetic models for electrons and photons. oai:cds.cern.ch:397049. Technical Report CERN-OPEN-99-034, CERN, Geneva, Aug 1999.
- [136] V.N. Ivanchenko P. Gumplinger R.P. Kokoulin-M. Maire L. Urban H. Burkhardt, V.M. Grichine. Geant4 Standard Electromagnetic Package. In *Proc. 2005 Conf. on Monte Carlo Method: Versatility Unbounded in a Dynamic Computing World*, 2005.
- [137] S. Guatelli, A. Mantero, B. Mascialino, P. Nieminen, and M.G. Pia. Geant4 Atomic Relaxation. *Nuclear Science, IEEE Transactions on*, 54(3):585 –593, June 2007.
- [138] D. Cullen, J. Hubbell, and L. Kissel. EPDL97: the Evaluated Photon Data Library. Technical Report UCRL-50400, Vol. 6, Rev. 5, University of California, Lawrence Livermore National Laboratory, September 1997.

- [139] S.T. Perkins, D.E. Cullen, and S.M. Seltzer. Tables and Graphs of Electron-Interaction Cross Sections from 10 eV to 100 GeV Derived from the LLNL Evaluated Electron Data Library (EEDL). Technical Report UCRL-50400 Vol. 31, University of California, Lawrence Livermore National Laboratory, 1997.
- [140] F. Salvat, J. M. Fernandez-Varea, and J. Sempau. PENELOPE-2008: A Code System for Monte Carlo Simulation of Electron and Photon Transport. In *Nuclear Energy Agency Workshop Proceedings*, June 2008.
- [141] J. Baró, J. Sempau, J.M. Fernández-Varea, and F. Salvat. PENELOPE: An algorithm for Monte Carlo simulation of the penetration and energy loss of electrons and positrons in matter. *Nuclear Instruments and Methods in Physics Research Section B: Beam Interactions with Materials and Atoms*, 100(1):31 – 46, 1995.
- [142] L. Hiller, T. Gosnell, J. Gronberg, and D. Wright. Calculating gamma-ray signatures from aged mixtures of heavy nuclides. In *Nuclear Science Symposium Conference Record, 2007. NSS 2007. IEEE*, volume 2, pages 1138 –1142, November 2007.
- [143] L.P. Ekström and R.B. Firestone. WWW Table of Radioactive Isotopes. URL. database version 2/28/99.
- [144] J. A. Bearden. X-Ray Wavelengths. *Rev. Mod. Phys.*, 39:78–124, Jan 1967.
- [145] M.O. Krause and J.H. Oliver. Natural widths of atomic K and L levels, Ka X-ray lines and several KLL Auger lines. *J. Phys. Chem. Ref. Data*, 8:329–338, 1979.
- [146] A. Thompson, D. Attwood, E. Gulikson, et al. X-ray Data Booklet. Lawrence Berkeley National Laboratory, Berkeley, CA, 2009.
- [147] J.C. Mark, F. Von Hippel, and E. Lyman. Explosive Properties of Reactor-Grade Plutonium. *Science & Global Security*, 17(2-3):170–185, 2009.
- [148] Argonne National Laboratory. Chemical Engineering Division and U.S. Atomic Energy Commission. *Chemical engineering division research highlights*. Argonne National Laboratory, 1964.
- [149] R.L. Bunting and J.J. Kraushaar. Short-lived radioactivity induced in Ge(Li) gamma-ray detectors by neutrons. *Nuclear Instruments and Methods*, 118(2):565 – 572, 1974.
- [150] M. L. van den Berg, D. T. Chow, A. Loshak, et al. High-resolution hard x-ray and gamma-ray spectrometers based on superconducting absorbers coupled to superconducting transition edge sensors. *Proc. SPIE 4140, X-Ray and Gamma-Ray Instrumentation for Astronomy XI*, pages 436–444, 2000.

- [151] B. L. Zink, J. N. Ullom, J. A. Beall, et al. Array-compatible transition-edge sensor microcalorimeter gamma-ray detector with 42eV energy resolution at 103keV. *Applied Physics Letters*, 89(12):124101–124101–3, Sep 2006.
- [152] C. A. Swenson. Linear thermal expansivity (1.5-300K) and heat capacity (1.2-90K) of Stycast 2850FT. *Review of Scientific Instruments*, 68(2):1312–1315, 1997.
- [153] D. Katze. Stycast 2850FT Thermally Conductive Epoxy. Technical report, Emerson & Cuming, 46 Manning Road Billerica, MA 01821, January 2007.
- [154] A.C. Anderson and R.E. Peterson. Selection of a thermal bonding agent for temperatures below 1 K. *Cryogenics*, 10(5):430 – 433, 1970.
- [155] W. Holmes, J. M. Gildemeister, P. L. Richards, and V. Kotsubo. Measurements of thermal transport in low stress silicon nitride films. *Applied Physics Letters*, 72(18):2250–2252, 1998.
- [156] M.J. O’Neil. *The Merck Index: An Encyclopedia of Chemicals, Drugs, and Biologicals*. Number v. 2 in MERCK INDEX. Merck, 2006.
- [157] A. E. Szymkowiak, R. L. Kelley, S. H. Moseley, and C. K. Stahle. Signal processing for microcalorimeters. *Journal of Low Temperature Physics*, 93:281–285, 1993.
- [158] W.H. Press. *Numerical Recipes: The Art of Scientific Computing*. Cambridge University Press, 2007.

Appendix A

Derivations

A.1 Temperature Response of a Simple Transition Edge Sensor

The thermal equation governing the response of the transition edge sensor is given by

$$C \frac{dT(t)}{dt} = P_{\text{bath}}(T, T_b) + E_\gamma \delta(t - t_\gamma) \quad (\text{A.1})$$

where

$$P_{\text{bath}}(T, T_b) = G(T - T_b) \quad (\text{A.2})$$

substituting equation (A.2) into equation (A.1) we arrive at

$$C \frac{dT(t)}{dt} = G(T(t) - T_b) + E_\gamma \delta(t - t_\gamma) \quad (\text{A.3})$$

rearranging

$$\frac{dT(t)}{dt} + \frac{G}{C}T(t) = \frac{1}{C}(GT_b) + \frac{E_\gamma}{C}\delta(t - t_\gamma) \quad (\text{A.4})$$

This is an ordinary differential equation of the form

$$y' + P(x)y = Q(x) \quad (\text{A.5})$$

whose solution is

$$y = \frac{\int Q(x)M(x)dx}{M(x)} \quad (\text{A.6})$$

where $M(x)$ is the integrating factor, given by

$$M(x) = e^{\int P(x)dx} \quad (\text{A.7})$$

Solving for $T(t)$

$$\begin{aligned} \left(e^{\int \frac{G}{C} dt} T(t) \right)' &= \left(e^{\int \frac{G}{C} dt} \left(\frac{1}{C}(GT_b) + \frac{E_\gamma}{C}\delta(t - t_\gamma) \right) \right) \\ T(t) &= \frac{\int e^{\int \frac{G}{C} dt} \left(\frac{1}{C}(GT_b) + \frac{E_\gamma}{C}\delta(t - t_\gamma) \right) dt}{e^{\int \frac{G}{C} dt}} \\ &= \frac{\int e^{\frac{G}{C}t} \left(\frac{1}{C}(GT_b) + \frac{E_\gamma}{C}\delta(t - t_\gamma) \right) dt}{e^{\frac{G}{C}t}} \\ &= \frac{\int e^{\frac{G}{C}t} \frac{1}{C}(GT_b) dt + \int e^{\frac{G}{C}t} \frac{E_\gamma}{C}\delta(t - t_\gamma) dt}{e^{\frac{G}{C}t}} \end{aligned}$$

Recall $\int f(x)\delta(x) = f(0)$, for $t_\gamma = 0$

$$\begin{aligned}
 T(t) &= \frac{\frac{C}{G} \frac{1}{C} (GT_b) e^{\frac{G}{C}t} + \frac{E_\gamma}{C}}{e^{\frac{G}{C}t}} \\
 &= T_b + \frac{E_\gamma}{C} e^{-\frac{G}{C}t} \\
 &= T_b + \frac{E_\gamma}{C} e^{-\frac{t}{\tau_0}}
 \end{aligned} \tag{A.8}$$

A.2 Simplification of the Simple Calorimeter Phonon and Johnson Noise

From equation (3.36) the phonon noise can be expressed as

$$\begin{aligned}
 \langle |\Delta I_{ph}(\omega)|^2 \rangle &= 2k_b (T_b^2 + T^2) G \left| \frac{-I\alpha}{(G_{ETF} + G + j\omega C) T} \right|^2 \\
 &= 2k_b (T_b^2 + T^2) G \left| \frac{-I\alpha}{\frac{C}{\tau_{eff}} (1 + j\omega\tau_{eff}) T} \right|^2 \\
 &= 2k_b (T_b^2 + T^2) G \frac{I^2 \alpha^2 \tau_{eff}^2}{C^2 T^2} \frac{1}{1 + \omega^2 \tau_{eff}^2}
 \end{aligned}$$

Recall $P = \frac{V^2}{R} = IV$

$$\begin{aligned}
 &= 2k_b (T_b^2 + T^2) \cdot \frac{GP}{R} \frac{\alpha^2 \tau_{eff}^2}{C^2 T^2} \cdot \frac{1}{1 + \omega^2 \tau_{eff}^2} \\
 &= 2k_b (T_b^2 + T^2) \cdot \frac{G}{PR} \left(\frac{\alpha P}{TG} \right)^2 \left(\frac{\tau_{eff}}{\tau_0} \right)^2 \frac{1}{1 + \omega^2 \tau_{eff}^2}
 \end{aligned}$$

We arrive at

$$\langle |\Delta I_{ph}(\omega)|^2 \rangle = 2k_b (T_b^2 + T^2) \cdot \frac{G}{V^2} \left(\frac{\alpha P}{TG} \right)^2 \left(\frac{\tau_{eff}}{\tau_0} \right)^2 \frac{1}{1 + \omega^2 \tau_{eff}^2}$$

The Johnson noise from equation (3.39) is given by

$$\langle |\Delta I_{jh}(\omega)|^2 \rangle = 4k_b T R \left| \frac{1}{R} + \frac{-I^2 \alpha}{(G_{ETF} + G + j\omega C) T} \right|^2$$

Simplifying

$$\begin{aligned}
\langle |\Delta I_{jh}(\omega)|^2 \rangle &= 4k_b T R \left| \frac{1}{R} + \frac{-I^2 \alpha}{\frac{TC}{\tau_{eff}} (1 + j\omega \tau_{eff})} \right|^2 \\
&= 4k_b T R \left| \frac{1}{R} + \frac{-I^2 \alpha \tau_{eff}}{TC (1 + j\omega \tau_{eff})} \right|^2 \\
&= 4k_b T R \left| \frac{TC (1 + j\omega \tau_{eff}) - RI^2 \alpha \tau_{eff}}{RTC (1 + j\omega \tau_{eff})} \right|^2 \\
&= 4k_b T R \left| \frac{C (1 + j\omega \tau_{eff}) - \frac{P\alpha}{T} \tau_{eff}}{RC (1 + j\omega \tau_{eff})} \right|^2 \\
&= 4k_b T R \left| \frac{\tau_0 (1 + j\omega \tau_{eff}) - \tau_{eff} \frac{G_{ETF}}{G}}{R\tau_0 (1 + j\omega \tau_{eff})} \right|^2 \\
&= 4k_b T R \left| \frac{\tau_{eff} \left(\frac{\tau_0}{\tau_{eff}} + j\omega \tau_0 - \frac{G_{ETF}}{G} \right)}{R\tau_0 (1 + j\omega \tau_{eff})} \right|^2 \\
&= 4k_b T R \left| \frac{\tau_{eff} \left(\frac{G+G_{ETF}}{G} - \frac{G_{ETF}}{G} + j\omega \tau_0 \right)}{R\tau_0 (1 + j\omega \tau_{eff})} \right|^2 \\
&= 4k_b T R \left| \frac{\tau_{eff} (1 + j\omega \tau_0)}{R\tau_0 (1 + j\omega \tau_{eff})} \right|^2
\end{aligned}$$

we arrive at

$$\langle |\Delta I_{jh}(\omega)|^2 \rangle = \frac{4k_b T}{R} \left(\frac{\tau_{eff}}{\tau_0} \right)^2 \frac{1 + \omega^2 \tau_0^2}{1 + \omega^2 \tau_{eff}^2}$$

A.3 Power Spectrum of TES Signal Current

To calculate the frequency spectrum of the signal current in a TES we begin with equation (3.16)

$$\Delta T(t) = \frac{E_\gamma}{C} e^{-\frac{t}{\tau_{eff}}} \quad (\text{A.9})$$

Recalling equation (3.31)

$$\Delta I = -\frac{V}{R^2} \frac{\partial R}{\partial T} \Delta T \quad (\text{A.10})$$

$$\Delta I = -\frac{\alpha I}{T} \Delta T \quad (\text{A.11})$$

Substituting equation (3.16) into equation (A.11) the current variation from the absorption of a photon will be

$$\Delta I(t) = -\frac{\alpha I}{T} \frac{E_\gamma}{C} e^{-\frac{t}{\tau_{\text{eff}}}} \quad (\text{A.12})$$

$$= -\frac{G}{C} \left(\frac{\alpha P}{TG} \right) \frac{I}{P} e^{-\frac{t}{\tau_{\text{eff}}}} \quad (\text{A.13})$$

$$= -\frac{1}{\tau_0} \left(\frac{\alpha P}{TG} \right) \frac{1}{V} e^{-\frac{t}{\tau_{\text{eff}}}} \quad (\text{A.14})$$

$$= -\left(\frac{1 + \frac{\alpha P}{TG}}{\tau_0} - \frac{1}{\tau_0} \right) \frac{1}{V} e^{-\frac{t}{\tau_{\text{eff}}}} \quad (\text{A.15})$$

$$= -\left(\frac{1}{\tau_{\text{eff}}} - \frac{1}{\tau_0} \right) \frac{E_\gamma}{V} e^{-\frac{t}{\tau_{\text{eff}}}} \quad (\text{A.16})$$

The frequency power spectrum resulting from a photon absorption is given by

$$\Delta I(\omega) = \int_0^\infty \Delta I(t) e^{-j\omega t} d\omega \quad (\text{A.17})$$

Substituting equation (A.16) into equation (A.17)

$$\Delta I(\omega) = \int_0^\infty -\left(\frac{1}{\tau_{\text{eff}}} - \frac{1}{\tau_0} \right) \frac{E_\gamma}{V} e^{-\frac{t}{\tau_{\text{eff}}}} e^{-j\omega t} d\omega \quad (\text{A.18})$$

where $j^2 = -1$.

$$\Delta I(\omega) = -\left(\frac{1}{\tau_{\text{eff}}} - \frac{1}{\tau_0} \right) \frac{E_\gamma}{V} \frac{1}{\frac{1}{\tau_{\text{eff}}} + j\omega} \quad (\text{A.19})$$

The magnitude of the signal frequency power spectrum is

$$|\Delta I(\omega)| = \left(\frac{1}{\tau_{\text{eff}}} - \frac{1}{\tau_0} \right) \frac{E_\gamma}{V} \frac{\tau_{\text{eff}}}{\sqrt{1 + \omega^2 \tau_{\text{eff}}^2}} \quad (\text{A.20})$$

A.4 Thevenin Equivalent Bias Circuit

A schematic of the experimental bias circuit used to operate a TES is shown in Figure A.1. A power supply is used to provide a voltage V_b through the bias resistor R_b . The voltage is applied to in parallel to shunt resistor R_S and the TES $R(T, I)$ with inductor L . To simplify the analysis, this can be expressed as a Thevenin equivalent circuit. For this example, the Thevenin equivalent voltage is given by

$$V_{th} = \frac{V_b R_S}{R_S + R_b} \quad (\text{A.21})$$

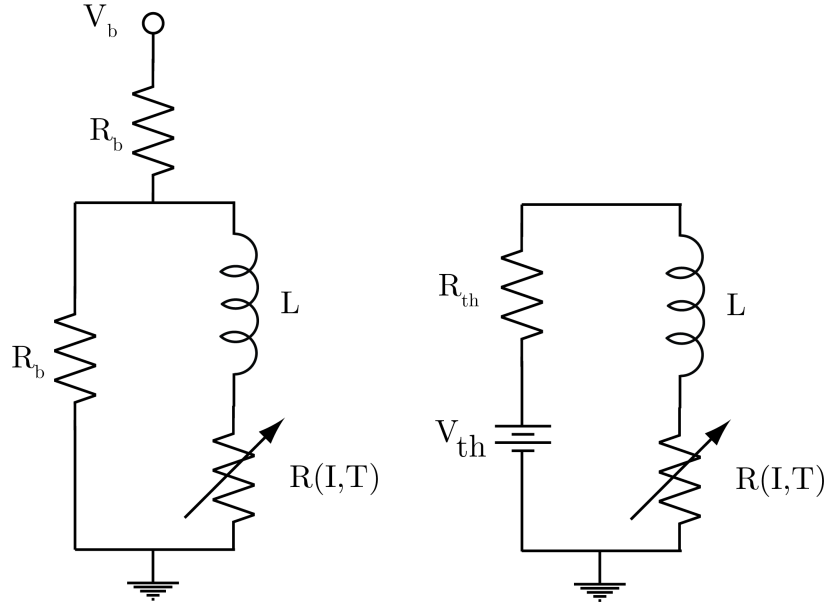


Figure A.1: A schematic of the experimental bias circuit used to operate a TES (left) and the Thevenin equivalent circuit (right).

For typical values of R_S and R_b , $V_{th} \sim \mu\text{V}$. The equivalent resistance is given as

$$R_{th} = \frac{R_S R_b}{R_S + R_b} \quad (\text{A.22})$$

for $R_b \gg R_S$, $R_{th} \rightarrow R_S$. This equivalent circuit is used in the basic and complex calorimeter derivations [111].

A.5 Simplification of the Basic Calorimeter Thermal and Current Response

The following is the derivation of the basic calorimeter discussed in Section 4.1 with the addition of a circuit noise source, $i_{cn}(t)$. The circuit is shown in Figure A.2. Starting with the thermal equation

$$C \frac{d}{dt} \Delta T = I_0 v_{dn}(t) + p_{ph}(t) + P_\gamma(t) + V (2 + \beta) \Delta I + \left(\frac{P\alpha}{T_0} - G \right) \Delta T \quad (\text{A.23})$$

and

$$\Delta T = \frac{T_0}{\alpha V} (v_{cn}(t) - R_L i_{cn}(t) - v_{dn}(t)) - \frac{T_0}{\alpha I_0} \left(1 + \beta + \frac{R_L}{R_0} \right) \Delta I \quad (\text{A.24})$$

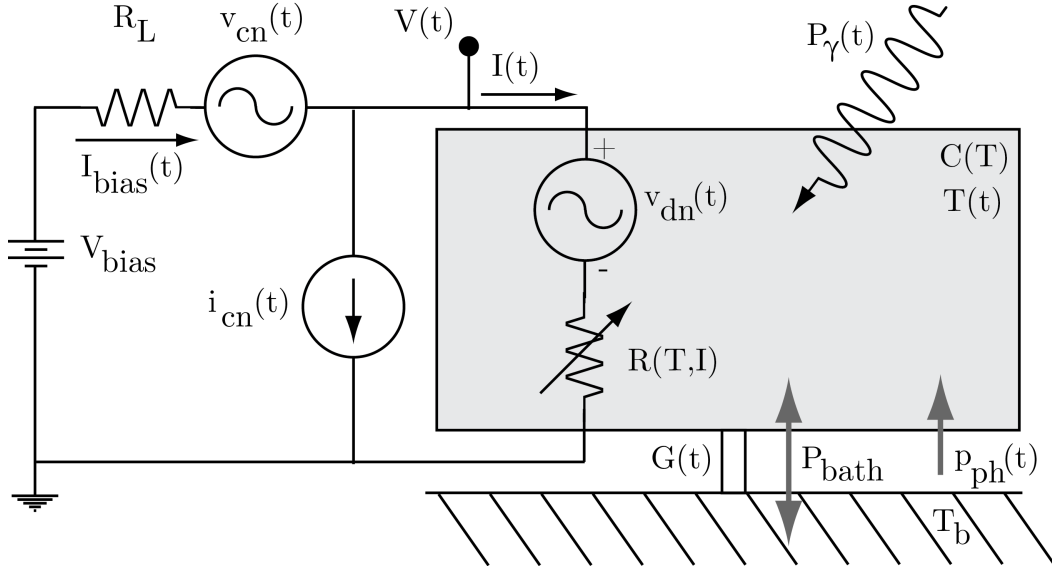


Figure A.2: Schematic of a basic calorimeter. The components are the same as that in Figure 4.1 with the addition of a variable current noise source $i_{cn}(t)$.

rearranging (A.24)

$$\begin{aligned}
 \Delta T &= -\frac{T_0}{\alpha I_0 R_0} (R_0 (1 + \beta) + R_L) \Delta I + \frac{T_0}{\alpha V} (v_{cn}(t) - R_L i_{cn}(t) - v_{dn}(t)) \\
 &= -\frac{T_0}{\alpha V} ((R_0 (1 + \beta) + R_L) \Delta I + v_{cn}(t) - R_L i_{cn}(t) - V_{dn}(t)) \\
 &= -\frac{T_0 (R_0 (1 + \beta) + R_L)}{\alpha V} \left(\Delta I + \frac{-v_{cn}(t) + R_L i_{cn}(t) + V_{dn}(t)}{(R_0 (1 + \beta) + R_L)} \right) \quad (A.25)
 \end{aligned}$$

Substituting equation (A.25) into equation (A.23) and simplifying

$$\begin{aligned}
 C \frac{d}{dt} \left(-\frac{T_0 (R_0 (1 + \beta) + R_L)}{\alpha V} \left(\Delta I + \frac{-v_{cn}(t) + R_L i_{cn}(t) + v_{dn}(t)}{(R_0 (1 + \beta) + R_L)} \right) \right) = \\
 I_0 V_{dn}(t) + p_{ph}(t) + P_\gamma(t) + V (2 + \beta) \Delta I \\
 + \left(\frac{P\alpha}{T_0} - G \right) \left(-\frac{T_0 (R_0 (1 + \beta) + R_L)}{\alpha V} \left(\Delta I + \frac{-v_{cn}(t) + R_L i_{cn}(t) + V_{dn}(t)}{(R_0 (1 + \beta) + R_L)} \right) \right) \quad (A.26)
 \end{aligned}$$

$$\begin{aligned}
& -C \left(\frac{T_0 (R_0 (1 + \beta) + R_L)}{\alpha V} \right) \frac{d}{dt} \left(\Delta I + \frac{-v_{cn}(t) + R_L i_{cn}(t) + V_{dn}(t)}{(R_0 (1 + \beta) + R_L)} \right) = \\
& \quad V (2 + \beta) \Delta I + I_0 v_{dn}(t) + p_{ph}(t) + P_\gamma(t) \\
& \quad + \left(\frac{P\alpha}{T_0} - G \right) \left(-\frac{T (R_0 (1 + \beta) + R_L)}{\alpha V} \Delta I \right. \\
& \quad \left. + \left(\frac{T_0 (R_0 (1 + \beta) + R_L)}{\alpha V} \right) \left(\frac{v_{cn}(t) + R_L i_{cn}(t) + V_{dn}(t)}{(R_0 (1 + \beta) + R_L)} \right) \right) \quad (A.27)
\end{aligned}$$

$$\begin{aligned}
& -C \left(\frac{T_0 (R_0 (1 + \beta) + R_L)}{\alpha V} \right) \frac{d}{dt} \left(\Delta I + \frac{-v_{cn}(t) + R_L i_{cn}(t) + V_{dn}(t)}{(R_0 (1 + \beta) + R_L)} \right) = \\
& \quad V (2 + \beta) \Delta I + I_0 v_{dn}(t) + p_{ph}(t) + P_\gamma(t) \\
& \quad + \left(\frac{P\alpha}{T_0} - G \right) \left(-\frac{T_0 (R_0 (1 + \beta) + R_L)}{\alpha V} \right) \Delta I \\
& \quad + \left(\frac{P\alpha}{T_0} - G \right) \left(\frac{T_0 (R_0 (1 + \beta) + R_L)}{\alpha V} \right) \left(\frac{v_{cn}(t) + R_L i_{cn}(t) + V_{dn}(t)}{(R_0 (1 + \beta) + R_L)} \right) \quad (A.28)
\end{aligned}$$

$$\begin{aligned}
& -C \left(\frac{T_0 (R_0 (1 + \beta) + R_L)}{\alpha V} \right) \frac{d}{dt} \left(\Delta I + \frac{-v_{cn}(t) + R_L i_{cn}(t) + V_{dn}(t)}{(R_0 (1 + \beta) + R_L)} \right) = \\
& \quad V (2 + \beta) \Delta I + I_0 v_{dn}(t) + p_{ph}(t) + P_\gamma(t) \\
& \quad + \left(\frac{P\alpha}{T} - G \right) \left(-\frac{T_0 (R_0 (1 + \beta) + R_L)}{\alpha V} \right) \Delta I \\
& \quad + \left(\frac{P\alpha}{T_0} - G \right) \left(\frac{T_0 (R_0 (1 + \beta) + R_L)}{\alpha V} \right) \left(\frac{v_{cn}(t) + R_L i_{cn}(t) + V_{dn}(t)}{(R_0 (1 + \beta) + R_L)} \right) \quad (A.29)
\end{aligned}$$

$$\begin{aligned}
& -C \left(\frac{T_0 (R_0 (1 + \beta) + R_L)}{\alpha V} \right) \frac{d}{dt} \left(\Delta I + \frac{-v_{cn}(t) + R_L i_{cn}(t) + V_{dn}(t)}{(R_0 (1 + \beta) + R_L)} \right) = \\
& \quad V (2 + \beta) \Delta I + \left(\frac{P\alpha}{T} - G \right) \left(-\frac{T_0 (R_0 (1 + \beta) + R_L)}{\alpha V} \right) \Delta I \\
& \quad + I_0 v_{dn}(t) + p_{ph}(t) + P_\gamma(t) \\
& \quad + \left(\frac{P\alpha}{T_0} - G \right) \left(\frac{-T_0 (R_0 (1 + \beta) + R_L)}{\alpha V} \right) \left(\frac{-v_{cn}(t) + R_L i_{cn}(t) + V_{dn}(t)}{(R_0 (1 + \beta) + R_L)} \right) \quad (A.30)
\end{aligned}$$

$$\begin{aligned}
C \frac{d}{dt} \left(\Delta I + \frac{-v_{cn}(t) + R_L i_{cn}(t) + V_{dn}(t)}{(R_0(1+\beta) + R_L)} \right) &= \left(\frac{-\alpha V}{T_0(R_0(1+\beta) + R_L)} \right) \\
&\left(V(2+\beta) + \left(\frac{P\alpha}{T_0} - G \right) \left(-\frac{T_0(R_0(1+\beta) + R_L)}{\alpha V} \right) \right) \Delta I \\
&+ \left(\frac{-\alpha V}{T_0(R_0(1+\beta) + R_L)} \right) \left(I_0 v_{dn}(t) + p_{ph}(t) + P_\gamma(t) + \right. \\
&\left. \left(\frac{P\alpha}{T_0} - G \right) \left(\frac{-T_0(R_0(1+\beta) + R_L)}{\alpha V} \right) \left(\frac{-v_{cn}(t) + R_L i_{cn}(t) + V_{dn}(t)}{(R_0(1+\beta) + R_L)} \right) \right) \quad (A.31)
\end{aligned}$$

We will solve each each component piecewise

$$C \frac{d}{dt} \left(\Delta I + \frac{-v_{cn}(t) + R_L i_{cn}(t) + V_{dn}(t)}{(R_0(1+\beta) + R_L)} \right) = A \Delta I + B \quad (A.32)$$

where

$$A = \left(\frac{-\alpha V}{T_0(R_0(1+\beta) + R_L)} \right) \left(V(2+\beta) + \left(\frac{P\alpha}{T_0} - G \right) \left(-\frac{T_0(R_0(1+\beta) + R_L)}{\alpha V} \right) \right) \quad (A.33)$$

and

$$\begin{aligned}
B &= \left(\frac{-\alpha V}{T_0(R_0(1+\beta) + R_L)} \right) \left(I_0 v_{dn}(t) + p_{ph}(t) + P_\gamma(t) \right. \\
&\left. + \left(\frac{P\alpha}{T_0} - G \right) \left(\frac{-T_0(R_0(1+\beta) + R_L)}{\alpha V} \right) \left(\frac{-v_{cn}(t) + R_L i_{cn}(t) + V_{dn}(t)}{(R_0(1+\beta) + R_L)} \right) \right) \quad (A.34)
\end{aligned}$$

Start with A

$$\begin{aligned}
A &= \left(\frac{-\alpha V}{T_0(R_0(1+\beta) + R_L)} \right) \\
&\left(V(2+\beta) + \left(\frac{P\alpha}{T_0} - G \right) \left(-\frac{T_0(R_0(1+\beta) + R_L)}{\alpha V} \right) \right) \quad (A.35)
\end{aligned}$$

$$\begin{aligned}
&= \left(\frac{-\alpha}{T_0(R_0(1+\beta) + R_L)} \right) \\
&\left(V^2(2+\beta) - \frac{T_0 G}{\alpha} \left(\frac{P\alpha}{TG} - 1 \right) (R_0(1+\beta) + R_L) \right) \quad (A.36)
\end{aligned}$$

$$= \frac{-\alpha}{T_0(R_0(1+\beta) + R_L)} \frac{2V^2 + V^2\beta}{TG} + G \left(\frac{P\alpha}{TG} - 1 \right) \quad (A.37)$$

Recall that $V^2 = PR$

$$A = \frac{-2PR_0\alpha - PR_0\alpha\beta}{T_0(R_0(1+\beta) + R_L)} + \frac{P\alpha}{T_0} - G \quad (\text{A.38})$$

$$= \frac{-2PR_0\alpha T_0}{T_0^2(R_0(1+\beta) + R_L)} - \frac{T_0PR_0\alpha\beta}{T_0^2(R_0(1+\beta) + R_L)} + \frac{P\alpha T(R_0(1+\beta) + R_L)}{T_0^2(R_0(1+\beta) + R_L)} - \frac{GT^2(R_0(1+\beta) + R_L)}{T_0^2(R_0(1+\beta) + R_L)} \quad (\text{A.39})$$

$$= \frac{-2PR_0\alpha T_0 - TPR_0\alpha\beta + (P\alpha - GT)(T_0(R_0(1+\beta) + R_L))}{T_0^2(R_0(1+\beta) + R_L)} \quad (\text{A.40})$$

$$= \frac{-2PR_0\alpha T_0 - T_0PR_0\alpha\beta + (PT_0R_0\alpha - GR_0T_0^2)\left(1 + \beta + \frac{R_L}{R_0}\right)}{R_0T_0^2\left(1 + \beta + \frac{R_L}{R_0}\right)} \quad (\text{A.41})$$

$$= \frac{-2PR_0\alpha T_0 - T_0PR_0\alpha\beta + PT_0R_0\alpha + PT_0R_0\alpha\beta + PT_0R_L\alpha - GR_0T_0^2 - \beta GR_0T_0^2 - GR_LT_0^2}{RT_0^2\left(1 + \beta + \frac{R_L}{R}\right)} \quad (\text{A.42})$$

$$= \frac{-PT_0R_0\alpha + PT_0R_L\alpha - GR_0T_0^2 - \beta GR_0T_0^2 - R_0G\frac{R_L}{R_0}T_0^2}{R_0T_0^2\left(1 + \beta + \frac{R_L}{R_0}\right)} \quad (\text{A.43})$$

$$= \frac{PT_0\alpha}{R_0T_0^2}\frac{(-R_0 + R_L)}{\left(1 + \beta + \frac{R_L}{R_0}\right)} + \frac{-GR_0T_0^2\left(1 + \beta + \frac{R_L}{R_0}\right)}{R_0T_0^2\left(1 + \beta + \frac{R_L}{R_0}\right)} \quad (\text{A.44})$$

$$= \frac{P\alpha}{R_0T_0}\frac{R\left(-1 + \frac{R_L}{R_0}\right)}{\left(1 + \beta + \frac{R_L}{R_0}\right)} - G \quad (\text{A.45})$$

$$A = -G\left(L\frac{\left(1 - \frac{R_L}{R_0}\right)}{\left(1 + \beta + \frac{R_L}{R_0}\right)} + 1\right) \quad (\text{A.46})$$

where the low frequency loop gain L is given by

$$L \equiv \frac{P\alpha}{GT_0} \quad (\text{A.47})$$

Simplifying B

$$B = \left(\frac{-\alpha V}{T_0(R_0(1+\beta) + R_L)}\right)\left(I_0v_{dn}(t) + p_{ph}(t) + P_\gamma(t) + \left(\frac{P\alpha}{T_0} - G\right)\left(\frac{-T_0(R_0(1+\beta) + R_L)}{\alpha V}\right)\left(\frac{-v_{cn}(t) + R_Li_{cn}(t) + V_{dn}(t)}{(R_0(1+\beta) + R_L)}\right)\right) \quad (\text{A.48})$$

$$= \left(\frac{-\alpha V}{T_0 (R_0 (1 + \beta) + R_L)} \right) \left(I_0 v_{dn}(t) + p_{ph}(t) + P_\gamma(t) + \left(\frac{P\alpha}{T_0} - G \right) \left(\frac{-T_0}{\alpha V} \right) (-v_{cn}(t) + R_L i_{cn}(t) + V_{dn}(t)) \right) \quad (\text{A.49})$$

$$= \left(\frac{-\alpha V}{T_0} \frac{1}{(R_0 (1 + \beta) + R_L)} \right) \left(\left(-\frac{GT_0}{\alpha V} \right) (L - 1) (-v_{cn}(t) + R_L i_{cn}(t) + V_{dn}(t)) + (I v_{dn}(t) + p_{ph}(t) + P_\gamma(t)) \right) \quad (\text{A.50})$$

$$= \left(\frac{-1}{(R_0 (1 + \beta) + R_L)} \right) \left(G (L - 1) (v_{cn}(t) - R_L i_{cn}(t) - V_{dn}(t)) + \frac{\alpha V}{T_0} (I_0 v_{dn}(t) + p_{ph}(t) + P_\gamma(t)) \right) \quad (\text{A.51})$$

$$= \left(\frac{-G (L - 1) (v_{cn}(t) - R_L i_{cn}(t) - V_{dn}(t))}{(R_0 (1 + \beta) + R_L)} - \frac{\alpha V}{T_0} \frac{(I_0 v_{dn}(t) + p_{ph}(t) + P_\gamma(t))}{(R_0 (1 + \beta) + R_L)} \right) \quad (\text{A.52})$$

$$= \frac{G (1 - L) (v_{cn}(t) - R_L i_{cn}(t) - v_{dn}(t))}{(R_0 (1 + \beta) + R_L)} - \frac{\alpha V}{T_0} \frac{I_0 v_{dn}(t)}{(R_0 (1 + \beta) + R_L)} - \frac{\alpha V}{T_0} \frac{(p_{ph}(t) + P_\gamma(t))}{(R_0 (1 + \beta) + R_L)} \quad (\text{A.53})$$

$$B = \frac{\overbrace{G (1 - L) (v_{cn}(t) - R_L i_{cn}(t))}^C}{\left(R_0 \frac{GT}{n} (1 + \beta) + R_L \right)} - \overbrace{\frac{G (1 - L) v_{dn}(t)}{(R_0 (1 + \beta) + R_L)} - \frac{\alpha V}{T_0} \frac{I_0 v_{dn}(t)}{(R_0 (1 + \beta) + R_L)} - \frac{\alpha V}{T_0} \frac{(p_{ph}(t) + P_\gamma(t))}{(R_0 (1 + \beta) + R_L)}}^E \quad (\text{A.54})$$

Simplifying C

$$C = \frac{G (1 - L) (v_{cn}(t) - R_L i_{cn}(t))}{(R_0 (1 + \beta) + R_L)} \quad (\text{A.55})$$

$$= G (1 - L) \frac{v_{cn}(t) - R_L i_{cn}(t)}{R_0 (1 + \beta) + R_L} \quad (\text{A.56})$$

Simplifying D

$$D = - \left(\frac{G (1 - L)}{(R_0 (1 + \beta) + R_L)} + \frac{\alpha IV}{T_0} \frac{1}{(R_0 (1 + \beta) + R_L)} v_{dn} \right) (t) \quad (\text{A.57})$$

Recall $P = IV$

$$D = -G \left(\frac{(1-L)}{(R_0(1+\beta) + R_L)} + \frac{\alpha P}{GT_0} \frac{1}{(R_0(1+\beta) + R_L)} \right) v_{dn}(t) \quad (\text{A.58})$$

$$= -G \left(\frac{(1-L) + \frac{\alpha P}{GT_0}}{(R_0(1+\beta) + R_L)} \right) v_{dn}(t) \quad (\text{A.59})$$

$$= \frac{-G}{(R_0(1+\beta) + R_L)} v_{dn}(t) \quad (\text{A.60})$$

Simplifying E

$$E = -\frac{\alpha V}{T_0} \frac{(p_{ph}(t) + P_\gamma(t))}{(R_0(1+\beta) + R_L)} \quad (\text{A.61})$$

$$= -\frac{\alpha IV}{T_0 I_0} \frac{(p_{ph}(t) + P_\gamma(t))}{(R_0(1+\beta) + R_L)} \quad (\text{A.62})$$

$$= -GL \frac{(p_{ph}(t) + P_\gamma(t))}{I_0 (R_0(1+\beta) + R_L)} \quad (\text{A.63})$$

Substituting C , D , and E (equations (A.56), (A.60), and (A.63)) for B (equation (A.54)) we find

$$B = G(1-L) \frac{v_{cn}(t) - R_L i_{cn}(t)}{R_0(1+\beta) + R_L} + \frac{-G}{(R_0(1+\beta) + R_L)} v_{dn}(t) - GL \frac{(p_{ph}(t) + P_\gamma(t))}{I_0 (R_0(1+\beta) + R_L)} \quad (\text{A.64})$$

Substituting A (A.46) and B (A.64) into (A.32) we arrive at

$$\begin{aligned} C \frac{d}{dt} \left(\Delta I + \frac{-v_{cn}(t) + R_L i_{cn}(t) + v_{dn}(t)}{(R_0(1+\beta) + R_L)} \right) &= -G \left(L \frac{\left(\frac{R_L}{R_0} - 1 \right)}{\left(1 + \beta + \frac{R_L}{R_0} \right)} + 1 \right) \Delta I + \\ G(1-L) \frac{v_{cn}(t) - R_L i_{cn}(t)}{R_0(1+\beta) + R_L} &+ \frac{-G}{(R_0(1+\beta) + R_L)} v_{dn}(t) - GL \frac{(p_{ph}(t) + P_\gamma(t))}{I (R_0(1+\beta) + R_L)} \end{aligned} \quad (\text{A.65})$$

Simplifying

$$\begin{aligned} \frac{C}{G} \frac{d}{dt} \left(\Delta I + \frac{-v_{cn}(t) + R_L i_{cn}(t) + v_{dn}(t)}{(R_0(1+\beta) + R_L)} \right) &= - \left(L \frac{\left(1 - \frac{R_L}{R_0} \right)}{\left(1 + \beta + \frac{R_L}{R_0} \right)} + 1 \right) \Delta I + \\ (1-L) \frac{v_{cn}(t) - R_L i_{cn}(t)}{R_0(1+\beta) + R_L} &- \frac{v_{dn}(t)}{(R_0(1+\beta) + R_L)} - L \frac{(p_{ph}(t) + P_\gamma(t))}{I_0 (R_0(1+\beta) + R_L)} \end{aligned} \quad (\text{A.66})$$

Setting $i_{cn}(t) = 0$ we arrive at equation (4.19).

A.6 Calculation of Energy Resolution from Noise Equivalent Power

Calculation of Energy Resolution

From equation (4.41) the energy resolution is given by [32]

$$\Delta E_{FWHM} = 2\sqrt{2\ln 2} \left(\int_0^\infty \frac{4}{\text{NEP}^2(f)} df \right)^{-\frac{1}{2}} \quad (\text{A.67})$$

where $f = \omega/2\pi$ and the total NEP is given by equation (4.42). The integral can be solved as

$$\int_0^\infty \frac{1}{a + b \cdot (2\pi x^2)} dx = \frac{\sqrt{b/a}}{4b} = \frac{1}{4b\sqrt{a/b}} = \frac{1}{4\sqrt{ab}} \quad (\text{A.68})$$

Total NEP can be expressed as

$$\text{NEP}^2(2\pi f) = p_{tn}^2 + \frac{1 + (2\pi f)^2 \tau_0^2}{L^2} \cdot I_0^2 v_{dn}^2 + \frac{(1-L)^2 + (2\pi f)^2 \tau_0^2}{L^2} \cdot I_0^2 (v_{cn}^2 + R_L^2 i_{cn}^2) \quad (\text{A.69})$$

Solving for a and b we find

$$a = p_{tn}^2 + \frac{I_0^2}{L^2} (v_{dn}^2 + (1-L)^2 (v_{cn}^2 + R_L^2 i_{cn}^2)) \quad (\text{A.70})$$

$$b = \frac{\tau_0^2 I_0^2}{L^2} (v_{dn}^2 + v_{cn}^2 + R_L^2 i_{cn}^2) \quad (\text{A.71})$$

Substituting equations (A.70) and (A.71) into (A.68)

$$\frac{1}{4\sqrt{ab}} = \frac{1}{4 \frac{\tau_0 I_0}{L} \sqrt{\left(p_{tn}^2 + \frac{I_0^2}{L^2} (v_{dn}^2 + (1-L)^2 (v_{cn}^2 + R_L^2 i_{cn}^2)) \right) (v_{dn}^2 + v_{cn}^2 + R_L^2 i_{cn}^2)}} \quad (\text{A.72})$$

The energy resolution is given by

$$\Delta E_{FWHM} = 2\sqrt{2\ln 2} \sqrt{\frac{\tau_0 I_0}{L} \sqrt{\left(p_{tn}^2 + \frac{I_0^2}{L^2} (v_{dn}^2 + (1-L)^2 (v_{cn}^2 + R_L^2 i_{cn}^2)) \right) (v_{dn}^2 + v_{cn}^2 + R_L^2 i_{cn}^2)}} \quad (\text{A.73})$$

Comparison with Strong Electrothermal Feedback

For zero load resistance $R_L = 0$ the equation (A.73) becomes

$$\Delta E_{FWHM} = 2\sqrt{2\ln 2} \sqrt{\frac{\tau_0}{L^2} \sqrt{L^2 p_{tn}^2 \cdot I_0^2 v_{dn}^2 + I_0^4 v_{dn}^4}} \quad (\text{A.74})$$

$$= 2\sqrt{2\ln 2} \sqrt{\frac{\tau_0}{L^2} \cdot L \cdot I_0 \sqrt{p_{tn}^2 v_{dn}^2 + \frac{I_0^2 v_{dn}^4}{L^2}}} \quad (\text{A.75})$$

For $L \ll 1$ we find

$$\Delta E_{FWHM} = 2\sqrt{2\ln 2} \sqrt{\frac{I_0 \cdot \tau_0}{L} \sqrt{p_{tn}^2 v_{dn}^2}} \quad (\text{A.76})$$

We define p_{tn} and v_{dn} by equations (3.21) and (3.22).

$$\Delta E_{FWHM} = 2\sqrt{2\ln 2} \sqrt{\frac{I_0 \cdot \tau_0}{L} \sqrt{(2k_B (T_b^2 + T_0^2) G) (4k_b T_0 R)}} \quad (\text{A.77})$$

For $T_b \ll T_0$ and $\tau_0 = C/G$

$$\Delta E_{FWHM} = 2\sqrt{2\ln 2} \sqrt{\frac{C I_0}{G L} \sqrt{(2k_B T_0^2 G) (4k_b T_0 R)}} \quad (\text{A.78})$$

Rearranging

$$\Delta E_{FWHM} = 2\sqrt{2\ln 2} \sqrt{2k_B T_0 \frac{C I_0}{G L} \sqrt{2G T_0 R}} \quad (\text{A.79})$$

$$= 2\sqrt{2\ln 2} \sqrt{\frac{2k_B C T_0}{L} \sqrt{\frac{2G T_0 R I_0^2}{G^2} \cdot \frac{4T_0}{4T_0}}} \quad (\text{A.80})$$

$$= 2\sqrt{2\ln 2} \sqrt{4k_B C T_0^2 \sqrt{\frac{R I^2}{2T_0 L^2 G}}} \quad (\text{A.81})$$

Recall $P = IR^2$ and

$$\Delta E_{FWHM} = 2\sqrt{2\ln 2} \sqrt{4k_B C T_0^2 \sqrt{\frac{P}{2T_0 G} \left(\frac{GT_0}{P\alpha}\right)^2}} \quad (\text{A.82})$$

$$= 2\sqrt{2\ln 2} \sqrt{4k_B C T_0^2 \sqrt{\frac{1}{2T_0 G P} \left(\frac{GT_0}{\alpha}\right)^2}} \quad (\text{A.83})$$

Substituting $P = GT_0/n$

$$\Delta E_{FWHM} = 2\sqrt{2\ln 2} \sqrt{4k_B C T_0^2 \cdot \frac{1}{\alpha} \sqrt{\frac{1}{2T_0 G} \frac{n}{GT_0} (GT_0)^2}} \quad (\text{A.84})$$

$$\Delta E_{FWHM} = 2\sqrt{2\ln 2} \sqrt{4k_B C T_0^2 \cdot \frac{1}{\alpha} \sqrt{\frac{n}{2}}} \quad (\text{A.85})$$

In agreement with the expression found in [106].

Appendix B

Calculation of Sensor Parameters

In the following we calculate the heat capacities, thermal conductivities for various materials used in transition edge sensors. Material properties used for these calculations are listed in Section B.6.

B.1 Heat Capacity of Tin and Transition Edge Sensor

For normal metals at temperatures well below the Debye temperature θ_D , $T < \theta_D/10$, the heat capacity is given by the sum of the electron and phonon heat capacities, C_{el} and C_{ph} , respectively. The electronic heat capacity scales linearly with temperature and the phonon heat capacity scales by T^3 , this can be expressed as [107, 110]

$$C_{\text{total}} = C_{\text{el}} + C_{\text{ph}} \quad (\text{B.1})$$

$$= \gamma T + \beta T^3 \quad (\text{B.2})$$

where

$$\beta = \frac{12}{5} \pi^4 k_B N_0 \left(\frac{1}{\theta_D} \right)^3 \quad (\text{B.3})$$

N_0 is the atom number density and γ is the Sommerfeld constant. For a material of density ρ , atomic mass A , and volume V , equation (B.2) can be expressed as

$$C_{\text{total}} = \frac{\rho}{A} \gamma T + \frac{12}{5} \pi^4 k_B N_0 \left(\frac{T}{\theta_D} \right)^3 \quad (\text{B.4})$$

At the superconducting transition temperature T_C , the heat capacity increases by $1.43\gamma T$ above its normal-state value, where γT is the normal state electronic specific heat. Below T_C the electronic specific heat decreases exponentially and at temperatures $T \ll T_C$, the heat capacity of the system is dominated by the phonon system

$$C_{\text{total}} \cong C_{\text{ph}} = \frac{12}{5} \pi^4 k_B N_0 \left(\frac{T}{\theta_D} \right)^3 \quad (\text{B.5})$$

B.1.1 Heat Capacity of Tin Absorber

The operating temperature of $T = 100$ mK is substantially below the 3.72 K transition temperature of tin. The heat capacity of the tin absorber can be calculated using equation (B.5)

$$\begin{aligned} C_{\text{ph}} &= \frac{12}{5} \pi^4 \left(3.7 \times 10^{28} \text{ m}^{-3} \right) \left(1.38 \times 10^{-23} \text{ J/K} \right) \left(\frac{0.1 \text{ K}}{200 \text{ K}} \right)^3 \\ &= 0.015 \text{ J/m}^3 \cdot \text{K} \end{aligned} \quad (\text{B.6})$$

Using an optical micrograph, the dimensions of the absorber were measured to be approximately $0.55 \text{ mm} \times 0.7 \text{ mm} \times 0.5 \text{ mm} = 0.19 \text{ mm}^3$. This corresponds to a heat capacity of

$$\begin{aligned} C_{\text{tin}} &= (0.015 \text{ J/m}^3 \cdot \text{K}) (0.19 \times 10^{-9} \text{ m}^3) \\ &= 2.9 \text{ pJ/K} \end{aligned} \quad (\text{B.7})$$

B.1.2 Heat Capacity of Molybdenum-Copper Transition Edge Sensor

The transition edge sensor is composed of 15 layers of 4 nm thick molybdenum and 16 layers of 9 nm thick copper. The total heat capacity of the sensor will be the sum of the heat capacities of the individual layers given by equation (B.4). As the complex calorimeter model requires both the electronic C_{el} and phonon C_{ph} heat capacities, each will be calculated separately. Results of these calculations are given in Table B.1. The heat capacity for copper is

$$\begin{aligned} C_{\text{Cu,el}} &= 0.1407 \text{ mol/cm}^3 \cdot 0.695 \text{ mJ/mol} \cdot \text{K}^2 \cdot 0.1 \text{ K} \\ &= 9.78 \times 10^{-6} \text{ J/cm}^3 \cdot \text{K} \end{aligned}$$

$$\begin{aligned} C_{\text{Cu,ph}} &= \frac{12}{5} \pi^4 (0.084 \times 10^{24} \text{ cm}^{-3}) (1.38 \times 10^{-23} \text{ J/K}) \left(\frac{0.1 \text{ K}}{200 \text{ K}} \right)^3 \\ &= 3.39 \times 10^{-8} \text{ J/cm}^3 \cdot \text{K} \end{aligned}$$

A single layer of copper within the transition edge sensor has dimensions of $9 \text{ nm} \times 500 \text{ } \mu\text{m} \times 500 \text{ } \mu\text{m} = 2.25 \times 10^{-9} \text{ cm}^3$, the total heat capacity is

$$\begin{aligned} C_{\text{Cu,el}} &= (9.78 \times 10^{-6} \text{ J/cm}^3 \cdot \text{K}) (2.25 \times 10^{-9} \text{ cm}^3) \\ &= 2.2 \times 10^{-2} \text{ pJ/K} \end{aligned}$$

$$\begin{aligned} C_{\text{Cu,ph}} &= (3.39 \times 10^{-8} \text{ J/cm}^3 \cdot \text{K}) (2.25 \times 10^{-9} \text{ cm}^3) \\ &= 7.6 \times 10^{-5} \text{ pJ/K} \end{aligned}$$

$$C_{\text{Cu,total}} = 2.2 \times 10^{-2} \text{ pJ/K}$$

Similarly for the molybdenum,

$$\begin{aligned} C_{\text{Mo,el}} &= 0.107 \text{ mol/cm}^3 \cdot 2.0 \text{ mJ/mol} \cdot \text{K}^2 \cdot 0.1 \text{ K} \\ &= 2.14 \times 10^{-5} \text{ J/cm}^3 \cdot \text{K} \end{aligned}$$

$$\begin{aligned}
C_{\text{Mo,ph}} &= \frac{12}{5} \pi^4 (0.064 \times 10^{24} \text{ cm}^{-3}) (1.38 \times 10^{-23} \text{ J/K}) \left(\frac{0.1 \text{ K}}{200 \text{ K}} \right)^3 \\
&= 2.58 \times 10^{-8} \text{ J/cm}^3 \cdot \text{K}
\end{aligned}$$

A single layer of molybdenum has dimensions of $4 \text{ nm} \times 500 \mu\text{m} \times 500 \mu\text{m} = 1.0 \times 10^{-9} \text{ cm}^3$, and total a heat capacity of

$$\begin{aligned}
C_{\text{Mo,el}} &= (2.14 \times 10^{-5} \text{ J/cm}^3 \cdot \text{K}) (1.0 \times 10^{-9} \text{ cm}^3) \\
&= 2.14 \times 10^{-2} \text{ pJ/K}
\end{aligned}$$

$$\begin{aligned}
C_{\text{Mo,ph}} &= (2.58 \times 10^{-8} \text{ J/cm}^3 \cdot \text{K}) (1.0 \times 10^{-9} \text{ cm}^3) \\
&= 2.58 \times 10^{-5} \text{ pJ/K}
\end{aligned}$$

$$C_{\text{Mo,total}} = 2.14 \times 10^{-2} \text{ pJ/K}$$

The Mo-Cu TES is comprised of 15 layers of 4 nm Mo and 16 layers of 9 nm Cu. The normal state heat capacity of the sensor is

$$\begin{aligned}
C_{\text{TES,normal}} &= 15 (2.14 \times 10^{-2} \text{ pJ/K}) + 16 (2.2 \times 10^{-2} \text{ pJ/K}) \\
&= 0.67 \text{ pJ/K}
\end{aligned} \tag{B.8}$$

The Bardeen, Cooper, Schrieffer (BCS) theory of superconductivity states that at the transition temperature the heat capacity increases by 1.43 times the normal state electronic heat capacity [107]. For the Mo-Cu TES this is

$$\begin{aligned}
C_{\text{TES,SC}} &= C_{\text{TES,normal}} + 1.43 C_{\text{el, total}} \\
&= 0.67 \text{ pJ/K} + 1.43 (0.67 \text{ pJ/K})
\end{aligned} \tag{B.9}$$

$$= 1.63 \text{ pJ/K} \tag{B.10}$$

As the resistance of the TES varies from its normal to superconducting state, the heat capacity of the TES will vary between 0.67 pJ/K and 1.63 pJ/K, respectively. Since the sensor is biased at approximately 20% of the normal resistance, we will take

$$C_{\text{TES}} = 1.44 \text{ pJ/K} \tag{B.11}$$

Table B.1: Phonon and electron heat capacities of a TES.

	Copper		Molybdenum		Total
	Phonon	Electron	Phonon	Electron	
Normal State					
Single Layer [pJ/K]	7.60×10^{-5}	2.2×10^{-2}	2.58×10^{-5}	2.14×10^{-2}	
Total [pJ/K]	1.22×10^{-3}	3.52×10^{-1}	3.87×10^{-4}	3.21×10^{-1}	0.67
Superconducting					
Single Layer [pJ/K]	7.60×10^{-5}	5.35×10^{-2}	2.58×10^{-5}	5.20×10^{-2}	
Total [pJ/K]	1.22×10^{-3}	8.55×10^{-1}	3.87×10^{-4}	7.80×10^{-1}	1.64
At Operating Point [pJ/K]	1.22×10^{-3}	7.55×10^{-1}	3.87×10^{-4}	6.88×10^{-1}	1.44

B.2 Heat Capacity of Stycast Epoxy

The heat capacity of Stycast 2850FT is given by [152]

$$C_{\text{Stycast}} = \rho_{\text{Stycast}} V_{\text{Stycast}} (B_1 T + B_3 T^3 + B_5 T^5 + \dots) \quad (\text{B.12})$$

where

$$\begin{aligned} B_1 &= 7 \times 10^{-6} \text{ J/g}\cdot\text{K}^2 \\ B_3 &= 4.56 \times 10^{-6} \text{ J/g}\cdot\text{K}^4 \\ B_5 &= 1.67 \times 10^{-6} \text{ J/g}\cdot\text{K}^6 \end{aligned}$$

and

$$V = L\pi r^2$$

The manufacturer [153] lists the nominal density of Stycast as 2.40 g/cm^3 . The epoxy is approximately $25 \mu\text{m}$ thick with a radius between $50 \mu\text{m}$ and $100 \mu\text{m}$. Using equation (B.12) the heat capacity of the Stycast can range from 0.33 pJ/K and 1.32 pJ/K at the operating temperature of $T = 100 \text{ mK}$.

B.3 Thermal Conductance of Stycast Epoxy

The tin absorber is attached to the TES using a small amount of epoxy (Stycast 2850FT). The epoxy is approximately $25 \mu\text{m}$ thick and can range between $100 \mu\text{m}$ and $200 \mu\text{m}$ in diameter. The thermal resistance of Stycast is the sum of the bulk thermal resistance of the Stycast R_{Stycast} and the Kapitza boundary resistance R_{Kap} at the two interfaces. This effective thermal resistance is given by [154]

$$R_{\text{Eff}} = R_{\text{Stycast}} + 2(R_{\text{Kap}}) \quad (\text{B.13})$$

Recall that the reciprocal of thermal resistivity is thermal conductivity, $R_{\text{Eff}} = 1/G_{\text{Eff}}$. To calculate the bulk thermal conductance we first calculate the Stycast the thermal conductivity Λ , given by [95]

$$\Lambda = AT^B \left[\frac{\mu\text{W}}{\text{cm} \cdot \text{K}} \right] \quad (\text{B.14})$$

where $A = 92 \mu\text{W} \cdot \text{cm}^{-1} \cdot \text{K}^{-1}$, $B = 2.65$ for Stycast 2850FT. The bulk thermal resistance with a cross sectional area A , and a thickness L is given by [154]

$$R_{\text{Stycast}} = \frac{L}{\Lambda A} \quad (\text{B.15})$$

The cross sectional area of the Stycast dot can range from $A = 7.8 \times 10^3 \mu\text{m}^2 - 3.1 \times 10^4 \mu\text{m}^2$ with a constant thickness of $25 \mu\text{m}$. The range of the bulk thermal conductance at 100 mK is

$$\begin{aligned} G_{\text{Stycast}}(7.8 \times 10^3 \mu\text{m}^2) &= \left(9.2 \cdot 0.1^{2.65} \frac{\text{nW}}{\mu\text{m} \cdot \text{K}} \right) \frac{7.8 \times 10^3 \mu\text{m}^2}{25 \mu\text{m}} = 6.4 \text{ nW/K} \\ G_{\text{Stycast}}(3.1 \times 10^4 \mu\text{m}^2) &= 25.6 \text{ nW/K} \end{aligned}$$

The Kapitza interface conductance at Stycast-Tin and Stycast-TES boundary can be estimated from [154]

$$G_{\text{Kap}} = 1.6 \left[\frac{\text{nW}}{\mu\text{m}^2 \cdot \text{K}^4} \right] AT^3 \quad (\text{B.16})$$

where T is the temperature at the interface, and A is the area perpendicular to the flow of phonons. With the range of cross sectional area and using equation (B.16) we find

$$\begin{aligned} G_{\text{Kap}}(7.8 \times 10^3 \mu\text{m}^2) &= 1.6 \left[\frac{\text{nW}}{\mu\text{m}^2 \cdot \text{K}^4} \right] (7.8 \times 10^3 \mu\text{m}^2) (0.1\text{K})^3 = 12.5 \text{ nW/K} \\ G_{\text{Kap}}(3.1 \times 10^4 \mu\text{m}^2) &= 50.2 \text{ nW/K} \end{aligned}$$

Using equation (B.13) the effective thermal conductance of the Stycast can range from 3.1 nW/K to 12.6 nW/K . The total, bulk, and Kapitza conductances for several epoxy dot sizes are summarized in Table B.2.

Table B.2: Heat capacity and effective thermal conductance of Stycast epoxy dots

Epoxy Dot Diameter [μm]	100	150	200
Heat Capacity [pJ/K]	0.33	0.75	1.32
Thermal Conductivity [nW/K]	6.4	14.5	25.6
Kapitza Interface Conductivity [nW/K]	12.5	28.3	50.2
Effective Thermal Conductance [nW/K]	3.1	7.2	12.7

B.4 Thermal Conductance of Silicon Nitride Membrane

At low temperatures the thermal conductance of the silicon nitride membrane is dominated by surface scattering of phonons, and as a result only an upper limit on this value can be determined. The thermal conductance of the SiN membrane can be calculated using [155]

$$G_{\text{SiN}} = 4\sigma AT^3\xi \quad (\text{B.17})$$

with [108]

$$\sigma = \sum_i \frac{\pi^5 k_B^4}{15h^3 v_i^2} = 15.7 \frac{\text{mW}}{\text{cm}^2 \text{K}^4} = 157 \frac{\text{W}}{\text{m}^2 \text{K}^4} \quad (\text{B.18})$$

where A is the cross sectional area of the membrane perpendicular to the direction of heat flow and ξ is a numerical value equaling one for the case of specular scattering and less than one for cases of diffuse scattering. We will take $\xi = 1$ and the cross sectional area A to be the perimeter P_{SiN} of the SiN membrane multiplied by the membrane thickness T_{SiN} .

$$\begin{aligned} A &= P_{\text{SiN}} T_{\text{SiN}} \\ &= 2000 \mu\text{m} \cdot 0.5 \mu\text{m} \\ &= 10^{-9} \text{m}^2 \end{aligned} \quad (\text{B.19})$$

The conductivity is therefore

$$\begin{aligned} G_{\text{SiN}} &= 4 \left(157 \frac{\text{W}}{\text{m}^2 \text{K}^4} \right) (10^{-9} \text{m}^2) (0.1 \text{K})^3 \\ &= 0.62 \text{ nW/K} \end{aligned} \quad (\text{B.20})$$

B.5 Electron-Phonon Coupling

The coupling between electrons and phonon in a superconducting material is given by

$$G_{\text{ep}} = 5\Sigma VT^4 \quad (\text{B.21})$$

where Σ is a material dependent constant, $\sim 10^9 \text{ W} \cdot \text{m}^{-3} \cdot \text{K}^{-5}$ and V is the volume of the transition edge sensor [110]. For a Molybdenum-Copper Transition Edge Sensor discussed in Section B.1.2, the electron to phonon coupling is

$$\begin{aligned} G_{\text{ep}} &= 5 \left(10^9 \text{ W} \cdot \text{m}^{-3} \cdot \text{K}^{-5} \right) (10^{-9} \text{m}^3) (0.1 \text{K})^4 \\ &= 5 \times 10^{-4} \text{ W/K} \end{aligned} \quad (\text{B.22})$$

B.6 Material Properties of Transition Edge Sensors

Table B.3: Material properties of tin, copper, molybdenum, tantalum, and lead

Parameter	Symbol	Tin	Copper	Molybdenum	Tantalum	Lead
Atomic Number	Z	50	29	42	73	82
Density $[\text{g}/\text{cm}^3]$ [156]	ρ	7.31	8.94	10.28	16.69	11.34
Atomic Mass $[\text{g}/\text{mol}]$ [156]	A	118.710	63.546	95.94	180.948	207.2
Atom Number Density $(\times 10^{24})[\text{mol}/\text{cm}^3]$	N_0	0.037	0.084	0.064	0.055	0.033
Transition Temperature $[\text{K}]$ [93]	T_C	3.72	Not SC	0.92	4.483	7.193
Debye Temperature $[\text{K}]$ [93]	θ	200	343	450	240	105
Sommerfeld Constant $[\text{mJ}/\text{mol}\cdot\text{K}^2]$ [93]	γ	1.78	0.695	2.0	5.9	2.98

Appendix C

Optimum Filtering

In the following we present an overview of the optimum (also called Wiener) filtering technique used for TES signal processing. Optimum filtering is a method of signal processing used to filter the pulses generated by an absorption event in a TES. The analysis method is described in the literature [157, 158], here we discuss the technique and the limitations. Optimum filtering assumes that the detector response can be characterized by a single pulse shape $s(t)$, scaled by a linear factor A where the spectral shape and amplitude of the noise remains constant. With these conditions each pulse can be described by

$$As(t)$$

where $s(t)$ is the pulse shape scaled by an amplitude factor A . The optimal estimate of the pulse height H is the least squares minimum between the experimental data $d(t)$ and the idealized pulse shape. In the frequency domain we find

$$\chi^2 = \sum \frac{(D(f) - H \cdot S(f))^2}{N^2(f)} \quad (\text{C.1})$$

where $N^2(f)$ is the power spectrum of the noise. Setting the derivatives of equation (C.1) to zero the optimal estimate of the pulse shape is given by

$$H(f) = \sum \frac{D(f) \cdot S^*(f)}{N^2(f)}$$

this can be expressed in the time domain as

$$h(t) = \sum d(t) \cdot f(t)$$

where

$$f(t) = \mathcal{F}^{-1} \left(\frac{S^*(f)}{N^2(f)} \right)$$

This filtering method is convenient in that once $f(t)$ is determined filtering of each pulse can be done in the time domain, reducing the computation cost; however, calculating the average pulse and noise spectra requires all the processing be done after the acquisition. Another important consideration is the fact that the sensor response is not linear and variations can arise with the position of the initial interaction and can saturate at higher incident energies. Also this method requires that the acquired pulse be free of pile up as this will adversely effect the average pulse. The noise is also not constant throughout the acquisition as the Johnson noise of the sensor scales with the resistance which increases during an absorption event. These nonidealities limit the performance of the optimal filter.

Appendix D

Sensor Modeling

The following provides the MATLAB code used for sensor modeling. This code was written using MATLAB 7.10.0 (R2010a).

D.1 Simple Calorimeter

The simple calorimeter model is derived in Chapter 3.5.

```

1 clear all
2 %Boltzmann constant (J/K)
3 k_B=1.3806504e-23;
4 %Energy of the incident gamma
5 E_gamma=1.60217646e-16*0.50;
6 %Bias Temperature (K)
7 T=100e-3;
8 %Bath Temperature (K)
9 T_b=50e-3;
10 n=3.2;
11 %Absorber Heat Capacity (J/K)
12 C=5e-12;
13 %Thermal Conductance (W/K)
14 G=1e-9;
15 %Equation (3.7)
16 alpha=10;
17 %Operating point resistance (Constant) (Ohm)
18 R=0.2;
19 %Operating point voltage (V)
20 %Equation (3.12)
21 V=sqrt(R*G*(T-T_b));
22 %Current (Amps)
23 I=V/R;
24 %Power (W) V^2/R
25 P=V^2/R;
26 %Decay constant
27 tau_0=C/G;
28 %Equation (3.18)
29 tau_eff=tau_0/(1+alpha/n*(1-T_b^n/T^n));
30
31 %Range of frequency space for calculation [Hz]
32 FrequencyOmega=logspace(1, 5, 35);
33
34 for i=1:length(FrequencyOmega)
35     omega=FrequencyOmega(i); %[Hz]
36
37     phi=(alpha*P/(T*G)); %[Unitless]
38     sigma=1+omega^2*tau_eff^2; %[Unitless]
39     nu=1+omega^2*tau_0^2; %[Unitless]
40     chi=tau_eff/tau_0; %[Unitless]
41

```

```

42      %Equation (3.37)
43      PhononNoise=2*k_B*G*(T^2+T_b^2)/V^2*phi^2*chi^2/sigma;
44
45      %Equation (3.40)
46      JohnsonNoise=4*k_B*T/R*chi^2*nu/sigma;
47
48      %Total Noise
49      I_noise(i,:)=[sqrt(PhononNoise) sqrt(JohnsonNoise) ...
50                  sqrt(JohnsonNoise+PhononNoise)];
51
52      %Signal from absorption
53      %Equation (3.41)
54      S(i)=phi^2*chi^2*1/(1+omega^2*tau_eff^2)*(E_gamma/V)^2;
55      S(i)=sqrt(S(i));
56 end

```

D.2 Basic Calorimeter

The basic calorimeter model is derived in Chapter 4.1.

```

1 clear all
2
3 %Boltzmann constant (J/K)
4 k_B=1.3806504e-23;
5 %Bias Temperature (K)
6 T=100e-3;
7 %Bath Temperature (K)
8 T_b=50e-3;
9 %Temperature of load resistor (K)
10 T_L=100e-3;
11 n=3.2;
12 %Absorber Heat Capacity (J/K)
13 C=5.4e-12;
14 %Thermal Conductance (W/K)
15 G=0.63e-9;
16 %Equation (3.7)
17 alpha=10;
18 %Equation (4.11)
19 beta=0;
20 %Operating point resistance (Constant) (Ohm)
21 R=0.2;
22 %Load resistor (Ohm)
23 R_L=0.01;
24 %Operating point voltage (V)
25 %Equation (3.12)
26 V=sqrt(R*G*(T-T_b));
27 %Current (Amps)
28 I=V/R;

```

```

29 %Power (J)
30 P=V^2/R;
31 %Decay constant [sec]
32 tau_0=C/G;
33 %Equation (4.23) [sec]
34 tau_eff=tau_0/(1+alpha/n*(1-T_b^n/T^n)*((1-(R_L/R))/(1+beta+R_L/R)));
35
36 %General power noise input to absorber
37 %Equation (3.21)
38 P_tn=sqrt(2*k_B*(T^2+T_b^2)*G);
39 %Equation (3.22) [V/sqrt(Hz)]
40 V_dn=sqrt(4*k_B*T*R);
41 %Equation (4.43) [V/sqrt(Hz)]
42 V_cn=sqrt(4*k_B*T_L*R_L);
43
44 %Range of frequency space for calculation [Hz]
45 FrequencyOmega=logspace(1, 5, 35);
46
47 for i=1:length(FrequencyOmega)
48     omega=FrequencyOmega(i); %[Hz]
49     phi=(alpha*P/(T*G)); %[Unitless]
50     psi=1+beta+R_L/R; %[Unitless]
51     sigma=1+omega^2*tau_eff^2; %[Unitless]
52     nu=1+omega^2*tau_0^2; %[Unitless]
53     chi=tau_eff/tau_0; %[Unitless]
54     %Equation (4.33) [A^2/Hz]
55     I_tn=phi^2/psi^2*chi^2*1/(sigma)*(P_tn/V)^2;
56     %Equation (4.34) [A^2/Hz]
57     I_dn=1/psi^2*chi^2*(nu/sigma)*(V_dn/R)^2;
58     %Equation (4.35) [A^2/Hz]
59     I_cn=1/psi^2*chi^2*((1-phi)^2-1+nu)/(sigma)*(V_cn^2+R_L^2)/R^2;
60
61     I_noise(i,:)=[sqrt(I_tn) sqrt(I_dn) sqrt(I_cn) sqrt(I_tn+I_dn+I_cn)];
62
63     P_gamma(i)=1.5e-16;
64     S(i)=phi^2/psi^2*chi^2*1/sigma*P_gamma(i)^2/V^2;
65     S(i)=sqrt(S(i));
66     %=====
67     % Noise Equivalent Power (NEP)
68     %=====
69     %Equation (4.38)
70     NEP_tn=P_tn^2;
71     %Equation (4.39)
72     NEP_dn=nu/phi^2*I^2*V_dn^2;
73     %Equation (4.40)
74     NEP_cn=((1-phi)^2+nu-1)/phi^2*I^2*(V_cn^2+R_L^2*I_cn^2);
75     I_NEP(i,:)=[sqrt(NEP_tn) sqrt(NEP_dn) sqrt(NEP_cn) ...
76         sqrt(NEP_tn+NEP_dn+NEP_cn)];
77 end
78 %Energy resolution

```



```

78 r=R_L*T_L/(R*T);
79 EfwhmPart2=T*G/P*(1+r)*(1/2*(1+T_b^2/T^2)+...
80 T*G/(P*alpha^2)*(1+r*(1-((alpha*P)/(T*G))^2));
81 Efwhm=2.355*sqrt(4*k_B*T^2*C/alpha*sqrt(EfwhmPart2))*6.24150974e18;
82 fprintf('FWHM for this case is: %feV\n' , Efwhm);

```

D.3 Complex Calorimeter

The complex calorimeter model is derived in Chapter 4.5.

```

1 clear all
2
3 R=0.2;
4 R_L=0.01;
5 alpha=25;
6 beta=0;
7 L=0;
8
9 C_cap=0;
10
11 %Heat capacities
12 C_a=5.4e-12;
13 C_e=1.44e-12;
14 C_p=2.7824e-16;
15
16 %Temperatures
17 T_L=150e-3;
18 T=150e-3;
19 T_b=50e-3;
20 T_p=150e-3;
21 T_e=150e-3;
22 T_a=150e-3;
23
24 %Thermal Conductances.
25 G_pb=0.62e-9;
26 Ge_ep=31.2e-9;
27 Gp_ep=31.2e-9;
28 Ga_ae=0;
29 Ge_ae=0;
30 Ga_ap=7.2e-9;
31 Gp_ap=7.2e-9;
32
33 %Bias System
34 V=sqrt(R*G_pb*(T_e-T_b));
35 I=V/R;
36 P=R*I^2;
37
38 %Boltzmann constant (J/K)

```

```

39 k_B=1.3806504e-23;
40
41 %Range of frequency space for calculation [Hz]
42 FrequencyOmega=logspace(1, 5, 4001);
43
44 %Preallocate Noise and NEP matrix
45 Noise=zeros(7,length(FrequencyOmega));
46 NEP=zeros(7,length(FrequencyOmega));
47
48 %Pickup [Power, Frequency, Bandwidth]
49 NoiseParameters=[12e-12, 60, 0.5];
50
51 %=====
52 for i=1:length(FrequencyOmega)
53     omega=FrequencyOmega(i); %[Hz]
54
55     AdditonalNoise=0;
56     for l=1:size(NoiseParameters,1)
57         AdditonalNoise=AdditonalNoise+(NoiseParameters(l,1)*...
58             NoiseParameters(l,3)*1i*omega/((1i*omega)^2+NoiseParameters(l,3)...
59             *(1i*omega)+NoiseParameters(l,2)^2));
60     end
61
62     V_cn=sqrt(4*k_B*T_L*R_L)+AdditonalNoise;
63     V_dn=sqrt(4*k_B*T_e*R);
64
65     I_cn=0;
66     P_ae=0;
67     P_ep=sqrt(2*k_B*(T_e^2+T_p^2)*Gp_ep);
68     P_ap=sqrt(2*k_B*(T_a^2+T_p^2)*Gp_ap);
69     P_ta=0;
70     P_te=0;
71     P_tp=sqrt(2*k_B*(T_p^2+T_b^2)*G_pb);
72
73     %Equation (4.61)
74     X(1,:)=[R*(1+beta)+1i*omega*L, -1, alpha*V/T, 0, 0];
75     X(2,:)=[R_L, 1+1i*omega*R_L*C_cap, 0, 0, 0];
76     X(3,:)=[-(2+beta)*V, 0, Ge_ep+Ge_ae-alpha*P/T+1i*omega*C_e, -Gp_ep ...
77         ,-Ga_ae];
78     X(4,:)=[0,0,-Ge_ep, Gp_ep+Gp_ap+G_pb+1i*omega*C_p, -Ga_ap];
79     X(5,:)=[0,0,-Ge_ae, -Gp_ap, Ga_ae+Ga_ap+1i*omega*C_a];
80
81     %Equation (4.63)
82     N(1,:)=V_dn;
83     N(2,:)=V_cn-R_L*I_cn;
84     N(3,:)=P_te-I*V_dn+P_ep+P_ae;
85     N(4,:)=P_tp-P_ep+P_ap;
86     N(5,:)=P_ta-P_ae-P_ap;
87
88     %Solve the matrix. Can be done using  $\Delta=\text{inv}(M)*N$ ; however, for speed

```

```

88      %and accuracy using  $\Delta=X\backslash N$ , as recommended on MathWorks site.
89       $\Delta(i,:)=(X\backslash N)$ ;
90      a=inv(X);
91
92      %=====
93      % Current Noise
94      %=====
95      Noise(1,i)=abs(a(1,4)*P_tp);
96      Noise(2,i)=abs(a(1,3)*P_ep-a(1,4)*P_ep);
97      Noise(3,i)=abs(a(1,4)*P_ap-a(1,5)*P_ap);
98      Noise(4,i)=abs(a(1,1)*V_dn-a(1,3)*I*V_dn);
99      Noise(5,i)=abs(a(1,2)*V_cn);
100     Noise(6,i)=abs(a(1,2)*R_L*I_cn);
101
102     Noise(1,i)=(sqrt(Noise(1,i).^2));
103     Noise(2,i)=(sqrt(Noise(2,i).^2));
104     Noise(3,i)=(sqrt(Noise(3,i).^2));
105     Noise(4,i)=(sqrt(Noise(4,i).^2));
106     Noise(5,i)=(sqrt(Noise(5,i).^2));
107     Noise(6,i)=(sqrt(Noise(6,i).^2));
108     Noise(7,i)=sqrt(sum(Noise(:,i).^2));
109     %Signal component
110     S(i)=10*abs(a(1,4)*P_tp);
111     S(i)=(sqrt(S(i))).^2;
112
113     %=====
114     % Noise Equivalent Power (NEP)
115     %=====
116     NEP(1,i)=abs(1/a(1,5)*(a(1,3)*P_tp));
117     NEP(2,i)=abs(1/a(1,5)*(a(1,3)*P_ep-a(1,4)*P_ep));
118     NEP(3,i)=abs(1/a(1,5)*(a(1,4)*P_ap-a(1,5)*P_ap));
119     NEP(4,i)=abs(1/a(1,5)*(a(1,1)*V_dn-a(1,3)*I*V_dn));
120     NEP(5,i)=abs(1/a(1,5)*(a(1,2)*V_cn));
121     NEP(6,i)=abs(1/a(1,5)*(a(1,2)*R_L*I_cn));
122     NEP(7,i)=sqrt(sum(NEP(:,i).^2));
123     %=====
124     %Compute Other Parameters
125     D(i,:)=a*N;
126 end
127
128 %Energy resolution
129 Efwhm=2*sqrt(2*log(2))/sqrt(trapz(FrequencyOmega./(2*pi),...
130     (4./(NEP(7,:).^2))))*6.24150974e18;
131 fprintf('%4.0f : FWHM for this case is: %f eV\n' , ...
    length(FrequencyOmega), Efwhm);

```

Appendix E

Precision of Isotopic Ratio Measurement

In the following we derive the analytical equations used to determine the precision in measuring two Gamma rays of similar energy in a energy histogram.

$$M(k) = (U + I_1 f(k\varepsilon - E_1) + I_2 f(k\varepsilon - E_2)) \varepsilon \quad (\text{E.1})$$

The quantities of I_1 and I_2 are selected to minimize the total sum of squares given by

$$T = \sum_k (M_k - N_k)^2 \quad (\text{E.2})$$

where the minimum occurs at

$$\frac{\partial T}{\partial I_1} = 0 \quad (\text{E.3})$$

$$\frac{\partial T}{\partial I_2} = 0 \quad (\text{E.4})$$

Applying equation (E.3) to equation (E.2)

$$\frac{\partial}{\partial I_1} \left(\sum_k (M_k - N_k)^2 \right) = 0 \quad (\text{E.5})$$

Substituting equation (E.1) into equation (E.5)

$$\frac{\partial}{\partial I_1} \left(\sum_k ((U + I_1 f(k\varepsilon - E_1) + I_2 f(k\varepsilon - E_2)) \varepsilon - N_k)^2 \right) = 0 \quad (\text{E.6})$$

and defining

$$f_{jk} = f(k\varepsilon - E_j) \quad (\text{E.7})$$

equation E.6 becomes

$$\frac{\partial}{\partial I_1} \left(\sum_k ((U + I_1 f_{1k} + I_2 f_{2k}) \varepsilon - N_k)^2 \right) = 0 \quad (\text{E.8})$$

Expanding equation E.8 and taking the derivative with respect to I_1 we arrive at

$$\sum_k f_{1k} (U\varepsilon + I_1 \varepsilon f_{1k} + I_2 \varepsilon f_{2k} - N_k) = 0 \quad (\text{E.9})$$

Similiarly, solving equation (E.4) we find

$$\sum_k f_{2k} (U\varepsilon + I_1 \varepsilon f_{1k} + I_2 \varepsilon f_{2k} - N_k) = 0 \quad (\text{E.10})$$

The system of equations from (E.9) and (E.10) can be solved to determine I_1 and I_2 . As the channel width is smaller than the detector resolution $\varepsilon \ll s$ the sums over the Gaussian functions can be expressed as the following integrals

$$\sum_k f_{2jk} \varepsilon \approx \int_{-\infty}^{\infty} f(E - E_j) dE = 1 \quad (\text{E.11})$$

$$\begin{aligned} \sum_k f_{jk} f_{ik} \varepsilon &\approx \int_{-\infty}^{\infty} f(E - E_j) \cdot f(E - E_i) dE \\ &= \frac{1}{2s\sqrt{\pi}} e^{-\frac{(E_j - E_i)^2}{4s^2}} \end{aligned} \quad (\text{E.12})$$

To simplify the discussion we define the following

$$b = e^{-\frac{(E_j - E_i)^2}{4s^2}} \quad (\text{E.13})$$

$$\alpha = \frac{1}{2s\sqrt{\pi}} \quad (\text{E.14})$$

$$S_j = \sum_k N_k f_{jk} \quad (\text{E.15})$$

With equations (E.11) and (E.12) we can simplify equation (E.9)

$$\sum_k f_{1k} (U\varepsilon + I_1\varepsilon f_{1k} + I_2\varepsilon f_{2k} - N_k) = 0 \quad (\text{E.16})$$

$$\int_{-\infty}^{\infty} (f_{1k}U + I_1 f_{1k}^2 + I_2 f_{1k} f_{2k}) dE - \sum_k f_{1k} N_k = 0 \quad (\text{E.17})$$

$$U + \alpha I_1 + \alpha b I_2 - S_1 = 0 \quad (\text{E.18})$$

This simplification can be repeated for (E.10) to obtain

$$U + \alpha b I_1 + \alpha I_2 - S_1 = 0 \quad (\text{E.19})$$

To solve for I_1 , multiply equation (E.19) by b and subtract from equation (E.18)

$$U(1 - b) + \alpha I_1 - \alpha b^2 I_1 - S_1 + b S_2 = 0 \quad (\text{E.20})$$

$$\alpha I_1 (1 - b^2) = S_1 - b S_2 - U(1 - b) \quad (\text{E.21})$$

$$I_1 = \frac{1}{\alpha(1 - b^2)} (S_1 - b S_2 - U(1 - b)) \quad (\text{E.22})$$

Substituting equation (E.22) into either equation (E.19) or equation (E.18) to solve for I_2

$$I_2 = \frac{1}{\alpha(1 - b^2)} (S_2 - b S_1 - U(1 - b)) \quad (\text{E.23})$$

Standard Deviation

The standard deviation of I_1 and I_2 can be determined from equations (E.22) and (E.23) by recalling that for a quantity $Y(x_1, x_2, \dots)$ determined from measurements x_1 and x_2, \dots the standard deviation is given by

$$\sigma^2 = \sum_i \left(\frac{\partial Y}{\partial x_i} \sigma_i \right)^2 \quad (\text{E.24})$$

where σ_i is the standard deviation of the x_i measurement. Assuming N_k is Poisson-distributed, the standard deviation in each channel k is given by $\sqrt{M_k}$, and the total error is obtained by summation over all channels in quadrature. Following the same approach as above and assuming the channel width ε is much smaller than the detector resolution.

$$\sigma_1^2 = \sum_i \left(\frac{\partial I_1}{\partial N_k} \sqrt{M_k} \right)^2 \quad (\text{E.25})$$

Substituting equation (E.22) and $\sigma_i = \sqrt{M_k}$ into equation (E.24)

$$\sigma_1^2 = \sum_i \left(\frac{\partial}{\partial N_k} \left(\frac{1}{\alpha(1-b^2)} (S_1 - bS_2 - U(1-b)) \right) \sqrt{M_k} \right)^2$$

Recalling that $S_j = \sum_k N_k f_{jk}$

$$\sigma_1^2 = \left(\frac{1}{\alpha(1-b^2)} \right)^2 \sum_k M_k (f_{1k} - bf_{2k})^2 \quad (\text{E.26})$$

Substituting equation (E.1) for M_k into equation (E.26)

$$\sigma_1^2 = \frac{1}{\alpha^2(1-\beta^2)^2} \sum_i \varepsilon (U + I_1 f(k\varepsilon - E_1) + I_2 f(k\varepsilon - E_2)) (f_{1k} - \beta f_{2k})^2 \quad (\text{E.27})$$

$$= \frac{1}{\alpha^2(1-\beta^2)^2} \sum_i \varepsilon (U + I_1 f_{1k} + I_2 f_{2k}) (f_{1k}^2 - \beta^2 f_{2k}^2 + 2\beta f_{1k} f_{2k}) \quad (\text{E.28})$$

$$\begin{aligned} \sigma_1^2 = \frac{1}{\alpha^2(1-b^2)^2} \sum_i \varepsilon \left(U (f_{1k}^2 + \beta^2 f_{2k}^2 - 2\beta f_{1k} f_{2k}) + I_1 (f_{1k}^3 + \beta^2 f_{1k} f_{2k}^2 + 2\beta f_{1k}^2 f_{2k}) \right. \\ \left. - I_2 (2\beta f_{2k}^2 + f_{2k} f_{1k}^2 + \beta f_{1k} f_{2k}^2) \right) \quad (\text{E.29}) \end{aligned}$$

As in the previous section we express the Gaussian sums as integrals given in equations (E.11) and (E.12). We define the following

$$\beta = e^{\frac{-(E_j - E_i)^2}{3s^2}} = b^{\frac{4}{3}} \quad (\text{E.30})$$

$$\varphi = \frac{1}{2\pi s^2 \sqrt{3}} = \frac{\alpha}{s\sqrt{3\pi}} \quad (\text{E.31})$$

and evaluate equation (E.29)

$$\begin{aligned} \sigma_1^2 = \frac{1}{\alpha^2 (1-b^2)^2} \int_{-\infty}^{\infty} & \left(U \left(\overbrace{f_{1k}^2}^{\alpha} + b^2 \overbrace{f_{2k}^2}^{\alpha} - 2b \overbrace{f_{1k} f_{2k}}^{\alpha b} \right) + I_1 \left(\overbrace{f_{1k}^3}^{\varphi} + b^2 \overbrace{f_{1k} f_{2k}^2}^{\varphi \beta} - 2b \overbrace{f_{1k}^2 f_{2k}}^{\varphi \beta} \right) \right. \\ & \left. + I_2 \left(\underbrace{f_{2k} f_{1k}^2}_{\varphi \beta} - 2b \underbrace{f_{1k} f_{2k}^2}_{\varphi \beta} + b^2 \underbrace{f_{2k}^3}_{\varphi} \right) \right) dE \quad (\text{E.32}) \end{aligned}$$

$$\begin{aligned} \sigma_1^2 = \frac{1}{\alpha^2 (1-b^2)^2} & \left(U \left(\alpha + b^2 \alpha - 2\alpha b^2 \right) + I_1 \left(\varphi + b^2 \varphi \beta - 2b \varphi \beta \right) \right. \\ & \left. + I_2 \left(\varphi \beta - 2b \varphi \beta + b^2 \varphi \right) \right) \quad (\text{E.33}) \end{aligned}$$

$$\begin{aligned} \sigma_1^2 = \frac{1}{\alpha^2 (1-b^2)^2} & \left(U \alpha \left(1 - b^2 \right) + I_1 \varphi \left(1 + b^2 \beta - 2b \beta \right) \right. \\ & \left. + I_2 \varphi \left(\beta - 2b \beta + b^2 \right) \right) \quad (\text{E.34}) \end{aligned}$$

Using equation (E.30) and equation (E.31)

$$\begin{aligned} \sigma_1^2 = \frac{1}{\alpha^2 (1-b^2)^2} & \left(U \alpha \left(1 - b^2 \right) + I_1 \varphi \left(1 + b^{\frac{10}{3}} - 2b^{\frac{7}{3}} \right) \right. \\ & \left. + I_2 \varphi \left(b^{\frac{4}{3}} - 2b^{\frac{7}{3}} + b^2 \right) \right) \quad (\text{E.35}) \end{aligned}$$

$$\begin{aligned} \sigma_1^2 = U \frac{1}{\alpha (1-b^2)} + I_1 \frac{1}{\alpha^2 (1-b^2)^2} \frac{\alpha}{s\sqrt{3\pi}} & \left(1 + b^{\frac{10}{3}} - 2b^{\frac{7}{3}} \right) \\ & + I_2 \frac{1}{\alpha^2 (1-b^2)^2} \frac{\alpha}{s\sqrt{3\pi}} \left(b^{\frac{4}{3}} - 2b^{\frac{7}{3}} + b^2 \right) \quad (\text{E.36}) \end{aligned}$$

$$\begin{aligned} \sigma_1^2 = \frac{1}{\alpha (1-b^2)} U + \frac{1}{\alpha s \sqrt{3\pi} (1-b^2)^2} & \left(1 + b^{\frac{10}{3}} - 2b^{\frac{7}{3}} \right) I_1 \\ & + \frac{1}{\alpha^2 (1-b^2)^2} \frac{\alpha}{s\sqrt{3\pi}} \left(b^{\frac{4}{3}} - 2b^{\frac{7}{3}} + b^2 \right) I_2 \quad (\text{E.37}) \end{aligned}$$

Substituting equation (E.14) for α

$$\sigma_1^2 = \frac{2s\sqrt{\pi}}{(1-b^2)}U + \frac{2}{\sqrt{3}} \frac{\left(1 + b^{\frac{10}{3}} - 2b^{\frac{7}{3}}\right)}{(1-b^2)^2}I_1 + \frac{2}{\sqrt{3}} \frac{\left(b^{\frac{4}{3}} - 2b^{\frac{7}{3}} + b^2\right)}{(1-b^2)^2}I_2 \quad (\text{E.38})$$

The equation for σ_1^2 can be obtained by following the same procedure as above and is given by

$$\sigma_1^2 = \frac{2s\sqrt{\pi}}{(1-b^2)}U + \frac{2}{\sqrt{3}} \frac{\left(1 + b^{\frac{10}{3}} - 2b^{\frac{7}{3}}\right)}{(1-b^2)^2}I_2 + \frac{2}{\sqrt{3}} \frac{\left(b^{\frac{4}{3}} - 2b^{\frac{7}{3}} + b^2\right)}{(1-b^2)^2}I_1 \quad (\text{E.39})$$

The results can be expressed more concisely as

$$\sigma_1^2 = AU + BI_1 + CI_2 \quad (\text{E.40})$$

$$\sigma_2^2 = AU + BI_2 + CI_1 \quad (\text{E.41})$$

where

$$\begin{aligned} A &= \frac{2s\sqrt{\pi}}{1-b^2} \\ B &= \frac{2\left(1 - 2b^{\frac{7}{3}} + b^{\frac{10}{3}}\right)}{\sqrt{3}(1-b^2)^2} \\ C &= \frac{2\left(b^{\frac{4}{3}} - 2b^{\frac{7}{3}} + b^2\right)}{\sqrt{3}(1-b^2)^2} \end{aligned} \quad (\text{E.42})$$

in agreement with the results derived in Ryder [117].